Springer Series in

OPTICAL SCIENCES **105**

Founded by H.K.V. Lotsch

Springer Series in

OPTICAL SCIENCES

The Springer Series in Optical Sciences, under the leadership of Editor-in-Chief *William T. Rhodes*, Georgia Institute of Technology, USA, and Georgia Tech Lorraine, France, provides an expanding selection of research monographs in all major areas of optics: lasers and quantum optics, ultrafast phenomena, optical spectroscopy techniques, optoelectronics, quantum information, information optics, applied laser technology, industrial applications, and other topics of contemporary interest.

With this broad coverage of topics, the series is of use to all research scientists and engineers who need up-to-date reference books.

The editors encourage prospective authors to correspond with them in advance of submitting a manuscript. Submission of manuscripts should be made to the Editor-in-Chief or one of the Editors. See also http://www.springer.de/phys/books/optical_science/

Mikhail A. Noginov

Solid-State Random Lasers

With 131 Figures

Foreword by V.S. Letokhov

Springer

Mikhail A. Noginov
Center for Materials Research
Dept. of Physics
Norfolk State University
Norfolk, VA 23504
USA

Library of Congress Control Number: 2005924132

ISBN-10: 0-387-23913-8 e-ISBN 0-387-25105-7 Printed on acid-free paper.
ISBN-13: 978-0387-23913-2

Printed in the United States of America. (TC/MV)

9 8 7 6 5 4 3 2 1

springeronline.com

To Natalia, Maxim, and Julia

Foreword

This book reminded me of the unforgettable creative atmosphere in the late 1960s in the laboratory of my Ph.D. advisor N.G. Basov (at that time already a Nobel laureate in physics, who shared the prize in 1964 with A.M. Prokhorov and C.H. Townes). One of the experimental groups at that time included V.S. Zuev, P.G. Kryukov, and R.V. Ambartsumyan, who were working on an exceptionally important problem of amplifying nanosecond pulses in a cascade of ruby amplifiers to ignite a nuclear fusion reaction. I collaborated with this group trying to understand the challenging problems and questions that arose in the process of the experiments. One such problem, related to the strange behavior of a nanosecond pulse in a chain of amplifying crystals, led to the discovery of nonlinear propagation of a front of amplified pulse with a speed greater than the speed of light. A simpler problem, self-excitation of stimulated emission in a cascade of amplifiers by examination of its output with a paper white card, led to the concept of nonresonant intensity feedback without conservation of a phase. At the same time, I realized that this effect takes place in a medium with distributed amplification and scattering if the photon scattering length is significantly smaller than the gain length. In such a medium, there exists an effect of self-confinement of light, which is characterized by a stimulated emission threshold and many other properties of regular lasers, but without spatial coherence of radiation.

Today, I would call such a laser a *laser with incoherent feedback*. These early results and ideas were forgotten. However, 20 years later they were revived in laser-pumped powders of laser crystals. Today the achieved level of understanding of such lasers is high enough to have the results of numerous original publications reviewed in a book. This precise work was done by M.A. Noginov. I believe that this book, useful for many researchers working in the field of quantum electronics, will be a valuable addition to existing books describing different types of lasers.

Moreover, I foresee in the future important applications of random lasers including not only the search for novel laser materials and their express-testing, but also the development of random lasers based on thin scattering films excited by low-energy electrons produced by field-emission cathodes. In this way, one can anticipate the development of new high-brightness displays with an isotropic angular diagram of emission. Possibly, the progress will reach the level of designing

thin-layer illumination systems, which can take different shapes on room and building walls, and so on. Future illumination devices probably will be based on controllable stimulated emission rather than noncontrollable or poorly controllable spontaneous emission. Any new effect sooner or later becomes very useful. This surely can be said about solid-state random lasers, and the book presented by M.A. Noginov will facilitate this progress.

Lund-Troitsk, Russia Professor V.S. Letokhov

Preface

I turn the knob to increase the power of my pumping laser, I turn it further, I turn it a little bit more, and . . . Yes! A red splash crosses the screen of the streak camera. Another splash comes, one more pulse, again and again . . . . It is lasing! The beauty of this moment is irresistible. Those who experienced it will agree with me. Those who did not . . . well, come visit my lab (please, not all at once) and I will show it to you.

But wait a second. *What* is lasing? Does this small amount of powder the size of a cubic millimeter produce a laser emission without any cavity or mirrors? Is this possible?

Yes, it is possible, and the name of this miniature source of stimulated emission is the *random laser* or *powder laser*. First proposed by Letokhov in 1968, the effect of stimulated emission in a scattering medium with gain was studied by a large number of researchers. The wavelengths of random lasers span from ultraviolet to mid-infrared. Random laser materials (in the form of powders and polycrystalline ceramics) include inorganic dielectrics, semiconductors, polymers, and liquids. Some random lasers are based on liquid solutions of dyes with scatterers. The size of random lasers can vary from a cubic micrometer to hundreds of cubic millimeters, their radiation can be pulsed or cw, the coherence of emission can be high or low, and so on. The list of different varieties is long, and in a number of years it may become endless. Similar to the case of regular lasers, which range from semiconductor diode lasers to free electron lasers, various random lasers are extremely different from each other. So, what is a random laser? In this book I answer this question, emphasizing the similarities among various types of random lasers and discussing the differences.

The majority of random lasers are solid-state. Correspondingly, the focus of this book is on solid-state random lasers. However, random lasers based on liquid dyes with scatterers, which were discovered in the early 1990s initiating a renaissance in this field of study, are described as well. The discussion in this book is centered on experimental observations. A large number of extremely diverse theoretical models, which have been proposed over a number of recent years, indicate that the time for a conclusive review of theories describing random lasers has not yet come.

Over the last decade, random lasers have become a rapidly growing field of research. This is evidenced by the chart below showing the numbers of papers on random lasers published in different years. The search was done in INSPEC database using the keywords "random laser," "powder laser," and "plaser." (A number of articles, including nearly a dozen papers published between the late 1960s and mid 1990s, were not found by the search engine.) The review of such a field presents a challenge, inasmuch as interesting new publications appear every month in a constantly increasing rate. To get the book done, I had to finalize its scope at some point. However, I included the latest results that were published when the book was in proof stage.

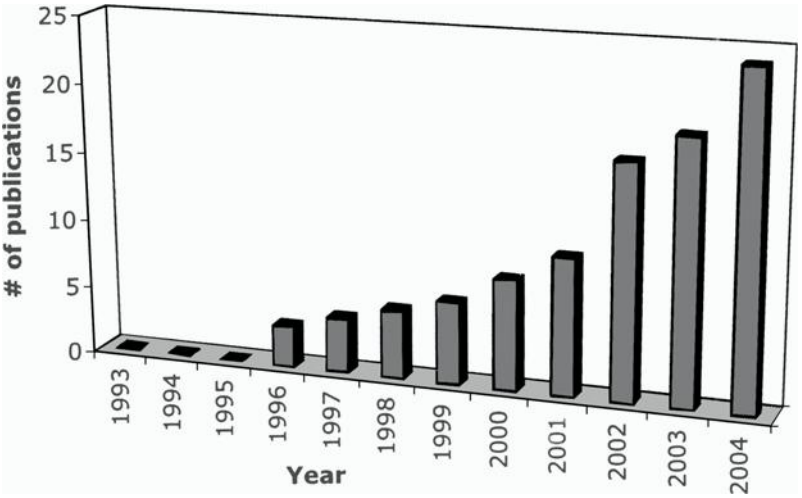

The book is organized as follows. The early theoretical and experimental studies of random lasers are presented in Chapter 1. The stimulated emission experiments with neodymium-doped powders and ceramics, the materials of choice in our group, are described in Chapter 2. The propagation of pumping light in neodymium random lasers is studied in Chapter 3. The theoretical modeling of stimulated emission in neodymium random lasers, the results of which are applicable to most random lasers with incoherent feedback, is discussed in Chapter 4. Some engineering aspects of the random laser design are exemplified in Chapter 5. Chapter 6 is devoted to random lasers pumped with an electron beam. Random lasers based on semiconductor powders and films, primarily ZnO, are discussed in Chapter 7. Stimulated emission in liquid dyes with scatterers is described in Chapter 8. The rest of Chapter 8 is devoted to polymer film random lasers. Random lasers and relevant phenomena (including cooperative emission in scattering media), which do not fall in any of the categories above, are discussed in Chapter 9. Potential applications of random lasers are discussed in Chapter 10.

The references, which, I believe, include most of the important publications, are aimed to support the discussion of experimental results and theoretical concepts

presented in the course of the book. The task of referring to all publications on random lasers has not been attempted. The omission of any particular reference should not be interpreted as a lack of my regard to its merit.

The chapters of the book are almost independent of one another. So, scientists, engineers, and students interested in any particular aspect of random lasers can read the relevant section directly. New researchers and students entering the field of random lasers will find in the book an overview of the research area. Scientists working in this and relevant fields can use the book as a reference source.

In conclusion, it is a pleasure to thank many friends and colleagues for their help and advice at different stages of the research and writing. First of all, I would like to acknowledge Prof. H. John Caulfield, my co-author on many papers and a permanent source of advice, who strongly encouraged me to write this book. I want to express my gratitude to Profs. Vladilen S. Letokhov, Vladislav V. Zolin, and Stephen C. Rand for reviewing the manuscript or its parts and returning comments to me. Prof. Stephen C. Rand contributed some of his unpublished results to Chapter 6. Prof. Letokhov, the founder of the field of random lasers, kindly accepted my invitation to write a foreword for this book. I would also like to thank Dr. Ch. M. Briskina, Prof. Alexander L. Burin, Prof. Hui Cao, Dr. Vladimir P. Drachev, Prof. George B. Loutts, Dr. Andrey K. Sarychev, and Profs. Vladimir M. Shalaev, Diederik S. Wiersma, and Vladisalav S. Zolin for many stimulating discussions.

Several chapters of this book are based on the original research of myself and my colleagues, collaborators, and students. I would like to acknowledge the help of many of my co-authors in different random laser-related papers, especially Dr. Messaoud Bahoura, Dr. Stephen U. Egavievwe, Ichesia N. Fowlkes, Dr. Milan R. Kokta, Prof. Sergey B. Mirov, Kaleem J. Morris, Jakub Novak, Dr. Joseph Paitz, Dr. Irina T. Sorokina, Starre M. Williams, and Guohua Zhu.

My special thanks are due to the editor, Dr. Hans Koelsch, for his great care and support in preparing this book.

This book could not have been possible without the help, advice, encouragement, love, and patience of my wife and co-author of many publications, Prof. Natalia Noginova.

Norfolk, Virginia
USA

Mikhail A. Noginov

Color Plate 1

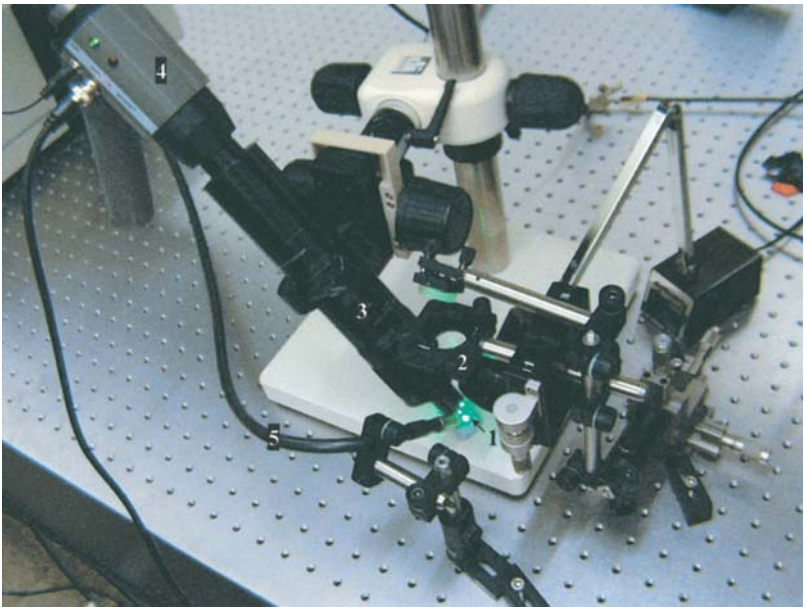

FIGURE 2.23. Experimental setup used for the measurements at small pumped spot: (1) $Nd_{0.5}La_{0.5}Al_3(BO_3)_4$ ceramic sample; (2) focusing lens; (3) microscope; (4) Visible/Infrared CCD camera; (5) fiber optic bundle. (After [16].)

Color Plate 2

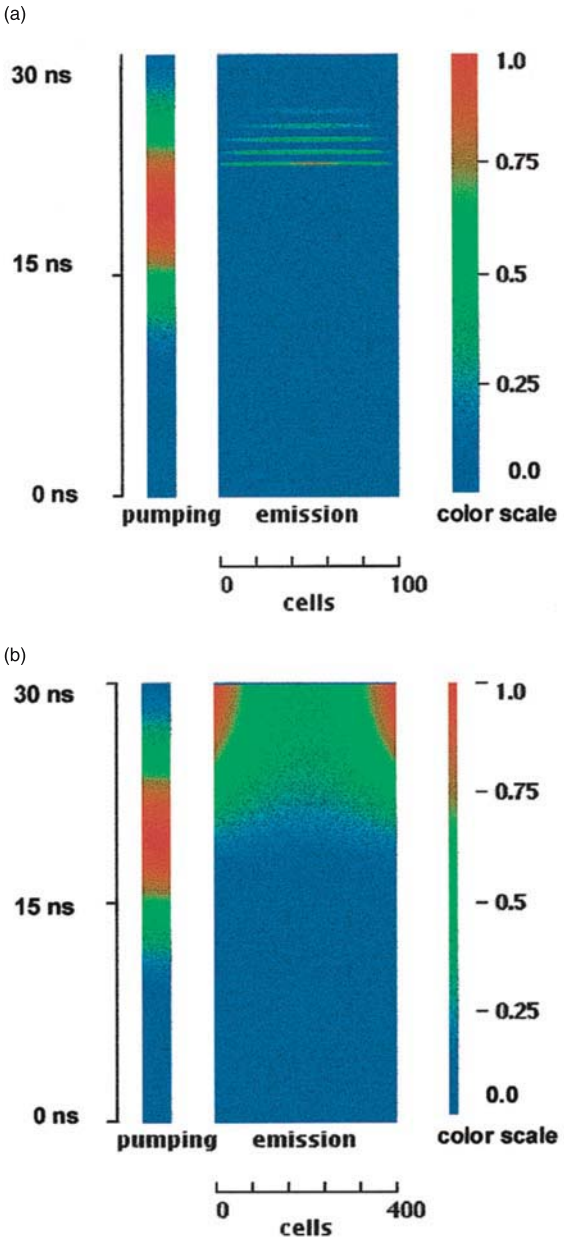

FIGURE 4.9. Calculated emission dynamics in (a) strip of 100 cells; pumping intensity corresponds to 1 J/cm^2 of absorbed energy, $r_{aver} = 8\%$, the residence time τ_{res} is calculated to be 0.43 ps, the maximum emission intensity is equal to 24,566 rel. units. (b) Strip of 400 cells pumped with the same intensity, with no reflection at the boundaries of the cells, the residence time is calculated to be 0.67 ps and the maximum emission intensity is equal to 16 rel. units. Loss is neglected in both (a) and (b). (*Source*: Ref. [30].)

Color Plate 3

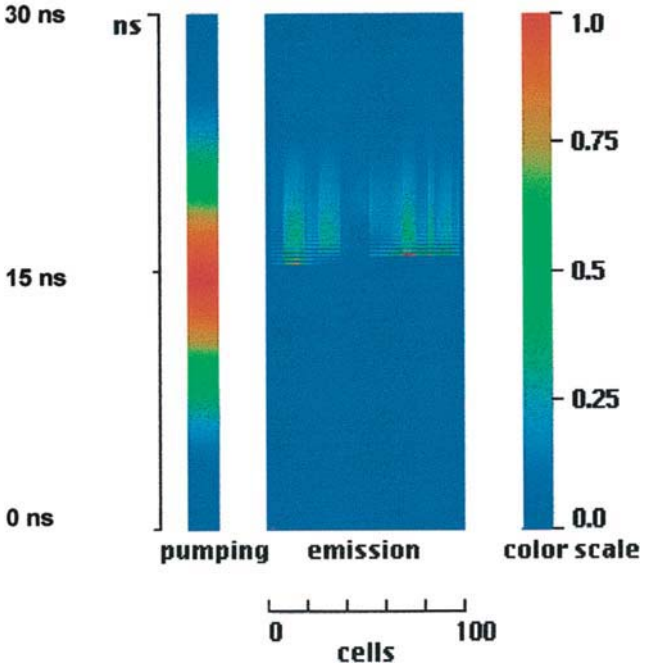

FIGURE 4.10. Calculated emission dynamics in a 100-cell strip with loss introduced to the system, $l_{aver} = 4\%$, pumping intensity corresponds to $10\,\mathrm{J/cm^2}$ of absorbed energy. Multiple regions of light localization are seen in the figure. (*Source*: Ref. [30].)

Contents

Foreword vii

Preface ix

Color Insert . . . . . (**facing page 78**)

1 Lasers with Nonresonant Feedback and Laserlike Emission from Powders: Early Ideas and Experiments 1
1.1 Idea of Laser with Nonresonant Feedback and Random Laser 1
1.2 Early Experiments 4
References 7

2 Neodymium Random Lasers: Experimental Studies of Stimulated Emission 10
2.1 First Observation of Stimulated Emission in Powders of Neodymium-Doped Materials 10
2.2 Basic Properties of Neodymium-Doped Random Lasers . . . 11
2.2.1 Emission Kinetics 12
2.2.2 Spectrum of Laserlike Emission 12
2.2.3 Input–Output Dependence 14
2.2.4 Angular Distribution of Stimulated Emission 15
2.3 Stimulated Emission in Different Materials and Types of Samples 16
2.4 Stimulated Emission in Mixtures of Powders 23
2.5 Stimulated Emission Supported by Large Regularly Shaped Particles 25
2.6 Quantum Yield of Stimulated Emission 27
2.7 Coherence Studies 30
2.7.1 Interferometric Measurements of Longitudinal Coherence 30
2.7.2 Speckle Pattern Analysis 33
2.7.3 Interferometric Studies of Transversal Coherence . . . 35

2.8 Dependence of the Stimulated Emission Threshold on the Diameter of the Pumped Spot 39
2.9 Dependence of the Stimulated Emission on the Powder Volume Density 41
2.10 Dependence of the Stimulated Emission on the Powder Particle Size 44
References 47

3 Propagation of Light in Neodymium Random Lasers 52
3.1 Propagation of Pumping Light 52
3.1.1 Model 52
3.1.2 Transmission and Reflection Measurements in Powders 54
3.1.3 Comparison of the Model Predictions with the Experimental Results 55
3.2 Determination of the Transport Mean Free Path in Random Laser Material 57
3.2.1 Experimental Samples and Absorption Spectra 58
3.2.2 Idea of Coherent Backscattering 59
3.2.3 Experimental Setup 59
3.2.4 Experimental Results 60
3.2.5 Correlation Between Transport Mean Free Path l_t and Particle Size s: Comparison with Experiment 61
References 66

4 Theoretical Modeling of Neodymium Random Lasers 68
4.1 Diffusion Model 69
4.1.1 Prediction of Stimulated Emission 69
4.1.2 Spectrum Narrowing 70
4.1.3 Application of the Diffusion Model to Stimulated Emission in a Mixture of Powders 71
4.2 Modeling of Stimulated Emission Dynamics 72
4.3 Invariance of the Threshold Pumping Energy in Different Pumping Regimes 75
4.3.1 Random Laser Threshold in cw Regime 78
4.3.2 Random Laser Threshold in Pulsed Regime 79
4.4 Spectral Dynamics of Neodymium Random Lasers 82
4.5 Stimulated Emission in One-Dimensional Array of Coupled Lasing Volumes 83
4.6 Calculation of Random Laser Threshold in Diffusion Approximation 86
4.7 Application of the Diffusion Model: Comparison with Experiment 89
4.8 Dependence of the Random Laser Threshold on the Diameter of the Pumped Spot 91

4.8.1 Model and Monte Carlo Simulation of the Residence Time . . . 92
4.8.2 Calculation Results . . . 93
4.9 Model of Coupled Intraparticle Resonators . . . 95
References . . . 97

5 Engineering Aspects of Neodymium Random Lasers: External Seeding, Design, and Second Harmonic Generation . . . 101
5.1 Control of Neodymium Random Laser Emission with External Seeding Light . . . 101
5.2 Effect of External Mirror on Stimulated Emission . . . 101
5.3 Fiber-Coupled Random Laser . . . 105
5.4 Demonstration of a Second-Harmonic Powder Laser . . . 107
5.4.1 Experimental Samples . . . 107
5.4.2 Experimental Results . . . 108
5.4.3 Modeling: Comparison of Theory and Experiment . . . 109
References . . . 118

6 Random Lasers Pumped with Electron Beam . . . 120
6.1 Rare-Earth Random Lasers Directly Pumped with Electron Beam . . . 120
6.1.1 Ce:δ-Alumina Random Laser . . . 120
6.1.2 Pr:δ-Alumina Random Laser . . . 125
6.1.3 Nd:δ-Alumina Random Laser . . . 126
6.1.4 Discussion of Experiments with Electron Beam-Pumped δ-Alumina Powders . . . 130
6.2 Nd:YAG Pumped with an Electron Beam via Scintillator . . . 131
References . . . 132

7 Semiconductor Random Lasers . . . 135
7.1 ZnO Random Laser: Phenomenological Description and Intuitive Model . . . 135
7.2 Study of Angular Distribution of Stimulated Emission in ZnO Random Laser . . . 137
7.3 Effect of External Feedback in ZnO Random Laser . . . 140
7.4 ZnO Microlaser and Strong Spatial Confinement of Simulated Emission . . . 140
7.5 Photon Statistics in ZnO Random Laser . . . 143
7.6 Effect of the Pumped Area on the Operation of ZnO Random Laser . . . 145
7.7 Study of the Dynamics of ZnO Random Laser . . . 148
7.8 Spectrally Resolved Speckle Studies in ZnO Random Laser . . . 149
7.9 Stimulated Emission from 3D Photonic Crystals Made of Self-Assembled ZnO Colloidal Spheres . . . 151
7.10 Quasi cw Stimulated Emission in ZnO Pellet . . . 151

7.11 New Technological Realizations of ZnO Random Lasers . . . 153
7.12 Random Lasing in Epitaxially Grown GaAsN 154
7.13 GaAs Random Laser 155
References 159

8 Dye and Polymer Random Lasers 164
8.1 Liquid Dye Random Lasers 164
8.1.1 Liquid Dye Random Lasers with Nonresonant Feedback 164
8.1.2 Transition from Incoherent Regime of Operation to Coherent Regime of Operation 168
8.2 Solid-State Polymer Random Lasers with Nonresonant Feedback 171
8.2.1 Photonic Fibers 171
8.2.2 Random Laser Action from Semiconducting Polymers with TiO_2 Nanoparticles 171
8.2.3 Laserlike Emission in a Variety of Conjugated Polymers 172
8.2.4 Time-Resolved Studies of Stimulated Emission in Polymer Film 173
8.3 Polymer Random Lasers with Resonant Feedback 178
8.3.1 Transition from Incoherent Regime of Operation to Coherent Regime of Operation 178
8.3.2 Photon Statistics of Polymer Random Lasers 180
8.3.3 Fourier Transform of the Emission Spectra of Polymer Random Laser 182
8.3.4 Uniformity of Random Laser Cavities in Polymer Random Lasers 184
8.3.5 Coherent Polymer Random Lasers Based on PMMA Films Doped with Rhodamine 640 Dye and TiO_2 Particles 186
8.4 Other Random Lasers Based on Dyes and Polymers 190
References 191

9 Other Types of Solid-State Random Lasers 198
9.1 Praseodymium-Doped Oxisulfide Powder Lasers 198
9.2 Ti-Sapphire Random Laser 198
9.2.1 Experimental Observation of Stimulated Emission in Ti-Sapphire Powder 198
9.2.2 Qualitative Explanation of the Influence of a Channel Formation on Stimulated Emission in Powders 200
9.2.3 Studies of Light Amplification in Ti-Sapphire Powders 201
9.3 Color Center Powder Laser 202
9.3.1 Experimental Samples and Setup 202

9.3.2 Experimental Results 203
9.3.3 Stimulated Emission in CC:LiF Powder 210
9.4 Mid-Infrared Eye-Safe Random Lasers Based on Cr^{2+}:ZnS and Cr^{2+}:ZnSe 212
9.5 Superradiance and Superfluorescence in Random Laser Materials 215
9.5.1 Properties of Cooperative Emission 215
9.5.2 Experimental Observations of Superradiance and Superfluorescence in Random Laser Materials 216
References 219

10 Applications of Random Lasers 222

Additional Notes and References 228

Index 230

1
Lasers with Nonresonant Feedback and Laserlike Emission from Powders: Early Ideas and Experiments

1.1 Idea of Laser with Nonresonant Feedback and Random Laser

In a laser with a Fabry–Perot cavity and resonant feedback [1,2], stimulated emission is spatially coherent and its frequencies are primarily determined by eigenmodes of the resonator. Coherence of a laser emission and its strong dependence on the properties of the cavity present a severe drawback for certain applications where high spatial uniformity of illumination and high stability of the emission wavelength are desired. For example, the speckle pattern, which is due to a high coherence of laser radiation, makes intensity distribution of scattered laser light strongly nonuniform. The frequency of the laser emission mode is sensitive to optical alignment, thermal expansion of the resonator, mechanical vibration, and so on. In order to overcome these and other disadvantages caused by spatial coherence of a laser beam, Ambartsumyan et al. (in 1966) proposed a new type of laser where a nonresonant feedback occurred via reflection off a highly scattering medium used in place of the back laser mirror [3–6] (Figure 1.1a). Alternative possible realizations of multimode cavities in which nonresonant feedback conditions can be fulfilled are (i) a cavity with rough reflecting inner walls and a small pinhole opening (Figure 1.1b) and (ii) a quasi-concentric resonator formed by two concave mirrors (Figure 1.1c) [6]. (The resonator conceptually similar to that shown in Figure 1.1b, a piece of fiber with optical gain and rough walls, has been studied in [7].) A laser with nonresonant feedback is an extreme case of a multimode laser with very strong interactions between modes [6]. According to References [8–11], the central emission frequency of such a laser is determined by the resonant frequency of a gain medium rather than eigenmodes of the cavity. The dynamics of the line narrowing in a laser with nonresonant feedback is typically much slower than that in a conventional laser with an open Fabry–Perot resonator [8]. The laser with nonresonant feedback has no spatial coherence, it is not stable in phase, and its photon statistics (Bose–Einstein) is strongly different from that of a regular single-mode laser (Poisson) [12–16].

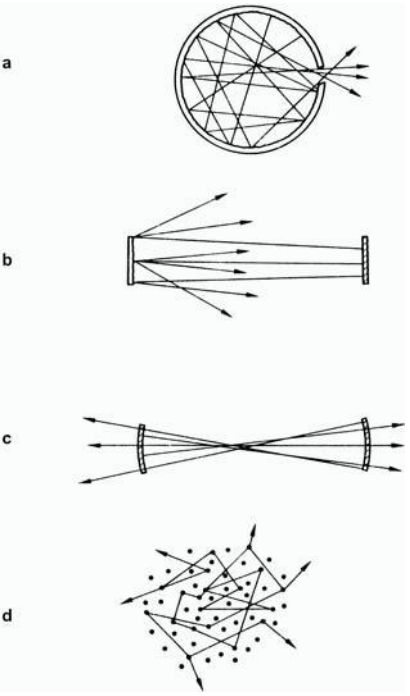

FIGURE 1.1. Examples of different configurations of multimode cavities in which nonresonant feedback conditions can be fulfilled: (a) scattering surface and mirror; (b) cavity with scattering walls and small outlet hall; (c) quasi-concentric resonator; (d) combination of scattering particles in an amplifying medium. (*Source*: Ref. [6].)

In 1967, Letokhov took one step further and theoretically predicted the possibility of generating laserlike light by scattering particles with negative absorption in the case when the mean free path of the photon due to scattering was much smaller than the dimensions of the system, that is, when the photon motion was diffuse [17]. In the proposed system, the scattering material at the same time played the role of an active laser medium and an effective resonator providing for nonresonant feedback. Letokhov found [17] that the solution of the diffusion equation for propagation of emitted photons in an amplified medium diverges at some critical value of gain g depending on the characteristic size of the pumped medium B (different for different shapes of the pumped volume) and the diffusion coefficient D,

$$g = DB^2, \tag{1.1}$$

(In Ref. [17] and in a more detailed Ref. [18], a homogeneous distribution of pumping in the absence of any reflection from the boundary of the scattering medium has been assumed.) This critical value of g was associated with the threshold of stimulated emission in a medium with gain and scatterers. That was probably the first report of what we now call the *random laser* or *powder laser*. The proposed applications of an incoherent random laser included a highly stable optical frequency

standard and express-testing of laser materials, which could not be easily produced in the form of homogeneous large crystals.

In Reference [18], Letokhov studied the same system in more detail, including in the consideration the rate equation for population inversion. In particularly, he predicted slow kinetics of the spectral line narrowing in a random laser (which is typical of nonresonant feedback lasers) and damped oscillations in the emission dynamics, which preceded the establishment of the stationary generation regime [18]; see Figure 1.2. These oscillations are known in the modern literature as *relaxation oscillations*.

Note that in contrast with an open Fabry–Perot resonator, the effective cavity formed by scatterers in a *volume* of a random laser is, by nature, a closed three-dimensional resonator with losses. (Resonators of some thin film random lasers are effectively two-dimensional.) This suggests that in macroscopic volume V, the number of modes N per frequency interval $\Delta\nu$ around optical frequency ν can be very large. According to the Rayleigh–Jeans formula,

$$N = 4\pi \frac{V}{c^3}\nu^2 \Delta\nu = 4\pi \frac{V}{\lambda^4}\Delta\lambda, \tag{1.2}$$

where $\lambda = c/\nu$ is the wavelength, $\Delta\lambda = \Delta\nu\lambda^2/c$ is the frequency interval, and c is the speed of light. At $V = 1\,\text{mm}^3$ and $\lambda = 1\,\mu\text{m}$, the number of modes per $\Delta\lambda = 1\,\text{nm}$ is equal to $N = 1.25 \times 10^7$ (!) and a large fraction of these modes can be nondegenerate. As stated in Reference [18], a "stochastic resonator" in the form of a scattering medium (as in Figure 1.1d) constitutes a system with a large number of modes, which are strongly coupled by scattering and which have large radiation losses. The large radiation losses and the strong interaction of the modes lead to a complete overlap of their frequency spectra. The concept of "mode" loses its usual meaning here and the spectrum becomes a continuum.

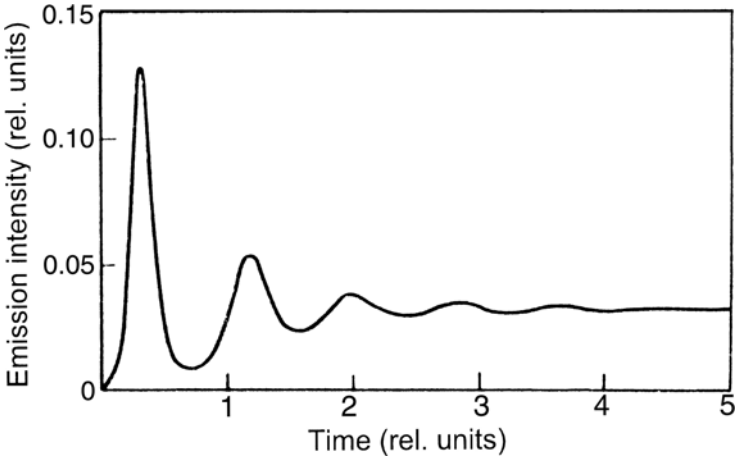

FIGURE 1.2. Dynamics of establishment of stationary generation regime in a spherical scattering region with negative absorption. (*Source*: Ref. [18].)

If the number N of interacting modes is sufficiently large, the feedback becomes nonresonant.

In the case where the photon mean free path l^* is larger than the characteristic size of the pumped medium L, only a small fraction of the emitted radiation is scattered in the ensemble of particles and lasing can occur only when the amplification g is large enough. It was shown [6,19] that the laser threshold in this case can be described as

$$e^{gL}\frac{\chi}{g} > 1, \tag{1.3}$$

where $\chi = 1/l^*$ is the backscattering coefficient. As argued in Reference [19], this case is possibly realized in cosmic clouds of optically pumped HO radicals with dust particles and electrons acting as scattering centers. Stimulated emission effect in such natural masers ($\lambda = 18.5\,\text{cm}$) was used to explain emission pulsations registered in radio astronomy experiments. The possibility of the laser effect in stellar atmospheres was predicted in [20], where OI-oxygen was considered to be an active laser medium and the scattering (providing for nonresonant feedback) was assumed to be due to amplifying transitions of excited atoms. The early studies of nonresonant feedback in space masers and stellar lasers are summarized in Reference [21]. More recent reports of ultrabright galaxy masers include [22,23] and many others.

1.2 Early Experiments

In 1971, Varsanyi experimentally observed optically excited stimulated emission ("superradiant emission" as he called it) at the $^3P_0 \rightarrow {}^3F_2\,Pr^{3+}$ transition in individual powder particles of $PrCl_3$ and $PrBr_3$ [24]. The stimulated emission, which was not supported by any cavity, occurred in the volumes where linear size exceeded $1\,\mu\text{m}$. The direction of the emitted light was determined by the shape of the pumped volume. At reasonably small pumping energies, <1 mJ, when the penetration depth of pumping, $h \approx 1\,\mu\text{m}$, was smaller than the diameter of the pumped spot d, stimulated emission was generated along the surface of the sample. At larger pumping energies, when the penetration depth h increased significantly due to the saturation of ground state absorption and became greater than d, the emitted light suddenly changed its direction and started propagating along the normal to the sample surface. Accordingly, two different thresholds have been observed in the input–output dependence. To describe the miniature source of stimulated emission, Varsanyi used, probably for the first time, the term *powder laser*. In the modern literature, this term is primarily used to describe emission supported by an ensemble of particles. It was proposed that miniature light sources, *powder lasers*, could find applications in integrated circuit networks [24].

In the 1970s, Fork et al. observed unusual optical properties in microcrystals of different luminophosphors containing Eu^{2+} [25–28]. The anomalously efficient and fast emission occurred in single microcrystals, the dimensions of which were

on the order of several optical wavelengths, $\lambda \approx 0.37\,\mu m$. The emission spectrum, which slightly changed from sample to sample, was attributed to the transitions between one of the Stark levels of the excited state $^6I(4f^7)$ Eu^{2+} and the ground state $^8S_{7/2}(4f^7)$ Eu^{2+}. A threshold for nonlinear emission behavior and a nonlinear competition between the wavelength components have been observed with the increase of the pumping intensity. The nature of this emission has never been clearly understood. Although several features of emission behavior were close to those of lasers (selective enhancements of certain spectral components, frequency shifts, and so on), the authors of [27] concluded that the emission was not due to the laser effect because (a) the emission line did not narrow above the threshold, (b) emission was not highly directional, and (c) the enhancement of certain spectral components occurred both below and above the threshold for nonlinear dependence of emission on pumping intensity, and so on.

In 1981, Nikitenko et al. studied spectroscopic properties and stimulated emission of ZnO at high levels of single-photon excitation [28]. Experimental samples, which included monocrystals, epitaxial layers, and powders of ZnO, were excited with the N_2 laser at $T \geq 80\,K$ (and below the room temperature). It was reported [28] that at proper (unspecified) conditions, laser action could be obtained in a powder of ZnO. The wavelength of this emission (374.7 nm) was ascribed to the first phonon-induced line corresponding to a free A-exciton [28]. The first report on the experimental observation of stimulated emission in ZnO powder was very brief [28]. In particular, Nikitenko et al. did not discuss whether this was a collective lasing effect occurring in an ensemble of excited particles or if the laser action could also exist in individual particles, as in Reference [24].

In 1986, Markushev et al., conducting routine emission spectroscopy experiments with powders of neodymium-activated luminophosphors (Nd:La_2O_3 [29], Nd:La_2O_2S [29], and $Na_5La_{1-x}Nd_x(MoO_4)_4$ [30]), found that above a certain pumping energy threshold, the duration of the emission pulse shortened by approximately four orders of magnitude. (Most of the experiments in Refs. [29,30] were carried out at liquid nitrogen temperature and some at liquid helium temperature.) An approximately equally strong enhancement was found in the intensity of the strongest spectral component of the $^4F_{3/2} - {}^4I_{11/2}$ emission transition ($\approx 1.06 - 1.08\,\mu m$), the linewidth of which narrowed significantly [29–31]. Only one narrow emission line was observed in the spectrum above the threshold; see Figure 1.3. The intensity of this emission line plotted versus pumping energy resembled input–output dependence in conventional lasers; see Figure 1.4. Inasmuch as the experimental behavior of the observed radiation was characteristic of lasers, Markushev et al. explained it in terms of stimulated emission from excited powders [29,30]. The results of References [29,30] and other publications of the same research group, which undoubtedly holds credit for the first detailed experimental study of a random (powder) laser and its qualitative and quantitative description, are discussed in detail in Chapters 2 and 4.

The focus of this book is primarily on the emission enhancements occurring in *ensembles* of excited particles or random lasers. However, as evidenced by the experiments of Varsanyi [24] and Fork [25–27], stimulated emission and

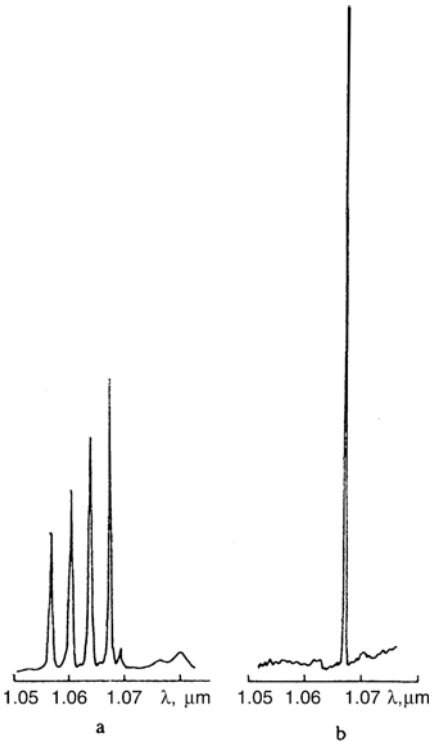

FIGURE 1.3. Emission spectrum of Nd^{3+} ($^4F_{3/2} - {}^4I_{11/2}$ transition, $T = 77\,K$) below (a) and above (b) the threshold. (*Source*: Ref. [30].)

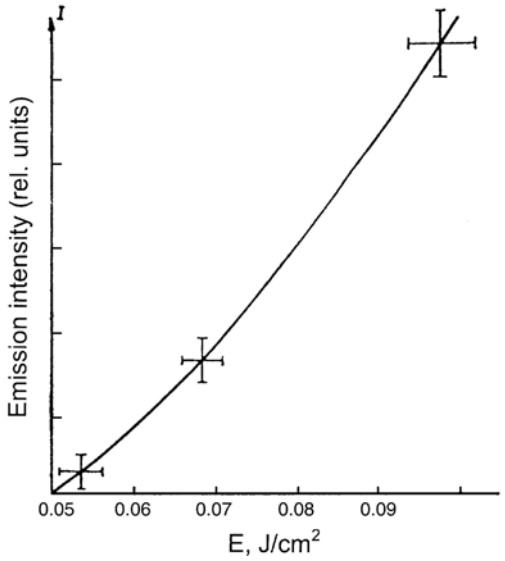

FIGURE 1.4. Input–output curve of stimulated emission in $Na_5La_{1-x}\ Nd_x(MoO_4)_4$ powder. (*Source*: Ref. [30].)

unusual optical effects, which remotely resemble stimulated emission, can also take place in individual particles constituting ensembles. The discovery and study of powder (random) lasers was done in parallel with the development of other micron-scale sources of laser emission [32], including microchip lasers [33,34], microsphere lasers [35–37], and microdisk lasers [37]. What makes random (powder) lasers principally different from all other micron-sized lasers listed above is that powder particles, as a rule, have irregular shapes and lack morphology-dependent resonances supporting stimulated emission.

References

1. A.M. Prokhorov, Molecular amplifier and generator for submillimeter waves, *Sov. Phys. JETP*, **7**: 1140–1141 (1958).
2. A.L. Shawlow and C.H. Townes, Infrared and optical masers, *Phys. Rev.*, **112**: 1940–1949 (1958).
3. R.V. Ambartsumyan, N.G. Basov, P.G. Kryukov, and V.S. Letokhov, Laser with nonresonant feedback [*Pis'ma Zh. Eksp. i Teor. Fiz.*, **3**: 261–264 (1966) Russian] *JETP Lett.*, **3**: 167–169 (1966).
4. R.V. Ambartsumyan, N.G. Basov, P.G. Kryukov, and V.S. Letokhov, A laser with nonresonant feedback [*Zh. Eksp. i Teor. Fiz.*, **51**: 724–729 (1966) Russian] *Sov. Phys. JETP*, **24**: 481–485 (1967).
5. R.V. Ambartsumyan, N.G. Basov, P.G. Kryukov, and V.S. Letokhov, A laser with a non-resonant feedback, *IEEE J. Quantum Electron.*, QE-**2**: 442–446 (1966).
6. R.V. Ambartsumyan, N.G. Basov, P.G. Kryukov, and V.S. Letokhov, Non-resonant feedback in lasers. In *Progress in Quantum Electronic*, Vol. 1, J.H. Sanders and K.W.H. Stevens, eds. Pergamon: New York (1970), pp. 107–185.
7. M. Kretschmann, A.A. Maradudin, Lasing action in waveguide systems and the influence of rough walls, *J. Opt. Soc. Am. B*, **21**: 150–158 (2004).
8. R.V. Ambartsumyan, P.G. Kryukov, and V.S. Letokhov, Dynamics of emission line narrowing for a laser with nonresonant feedback [*Zh. Eksp. i Teor. Fiz.*, **51**: 1669–1675 (1966) Russian] *Sov. Phys. JETP*, **24**: 1129–1134 (1967).
9. R.V. Ambartsumyan, N.G. Basov, and V.S. Letokhov, Investigation of frequency characteristics of a He-Ne laser with a diffuse mirror [*Pis'ma Zh. Eksp. i Teor. Fiz.*, **7**: 88–91 (1966) Russian] *JETP Lett.*, **7**: 66–68 (1968).
10. R.V. Ambartsumyan, N.G. Basov, and V.S. Letokhov, Frequency stability of a He-Ne laser with nonresonant feedback, *IEEE Trans. Instrum. Measure.*, **IM-17**: 338–343 (1968).
11. R.V. Ambartsumyan, S.P. Bazhunin, N.G. Basov, and V.S. Letokhov, Emission spectrum of an He-Ne laser with nonresonant feedback [*Zh. Eksp. i Teor. Fiz.*, **58**: 441–445 (1970) Russian] *Sov. Phys. JETP*, **31**: 234–241 (1970).
12. R.V. Ambartsumyan, P.G. Kryukov, V.S. Letokhov, and Yu.A. Matveets, Emission statistics of a laser with nonresonant feedback [*Pis'ma Zh. Eksp. i Teor. Fiz.*, **5**: 378–382 (1967) Russian] *JETP Lett.*, **5**: 312–314 (1967).
13. R.V. Ambartsumyan, P.G. Kryukov, V.S. Letokhov, and A. Yu Matveets Statistical emission properties of a nonresonant feedback laser [*Zh. Eksp. i Teor. Fiz.*, **53**: 1955–1966 (1967) Russian] *Sov. Phys. JETP*, **26**: 1109–1114 (1968).

14. V.S. Letokhov, Quantum statistics of multi-mode radiation from an ensemble of atoms [*Zh. Eksp. i Teor. Fiz.*, **53**: 2210–2222 (1967) Russian] *Sov. Phys. JETP*, **26**: 1246–1251 (1968).
15. J.W. Goodman, *Statistical Optics*, Wiley: New York (2000).
16. R. Loudon, *The Quantum Theory of Light*, 2nd ed., Oxford University Press: Oxford, (1983).
17. V.S. Letokhov, Stimulated emission of an ensemble of scattering particles with negative absorption [*Pis'ma Zh. Eksp. i Teor. Fiz.*, **5**: 262–265 (1967) Russian] *JETP Lett.*, **5**: 212–215, (1967).
18. V.S. Letokhov, Generation of light by a scattering medium with negative resonance absorption [*Zh. Eksp. i Teor. Fiz.*, **53**: 1442–1452 (1967) Russian] *Sov. Phys. JETP*, **26**: 835–840 (1968).
19. V.S. Letokhov, Stimulated radio emission of the interstellar medium [*Pis'ma Zh. Eksp. i Teor. Fiz.*, **4**: 477–481 (1966) Russian] *JETP Lett.*, **4**: 321–323 (1966).
20. N.N. Lavrinovich and V.S. Letokhov, The possibility of the laser effect in stellar atmospheres [*Zh. Eksp. i Teor. Fiz.*, **67**: 1609–1620 (1974) Russian] *Sov. Phys. JETP*, **40**: 800–805 (1975).
21. V.S. Letokhov, Noncoherent feedback in space masers and stellar lasers. In *Amazing Light, A Volume Dedicated to Charles Hard Townes on His 80th Birthday*, R.Y. Chiao, ed., Springer-Verlag: New York (1996), p. 409.
22. A.D. Haschick and W.A. Baan, A very bright water vapor maser source in the galaxy NGC3079, *Nature* (London), **314**: 144–146 (1985).
23. L. Staveley-Smith, D.A. Allen, J.M. Champan, R.P. Norris, and J.B. Whiteoak, Ultraluminous OH maser emission from an IRAS galaxy, *Nature* (London), **337**: 625–627 (1989).
24. F. Varsanyi, Surface lasers, *Appl. Phys. Lett.*, **19**: 169–171 (1971).
25. R.L. Fork, D.W. Taylor, K.R. German, A. Kiel, and E. Buehler, Unusual luminescence from small europium chalcogenide crystals, *Bull. Am. Phys. Soc.*, **19**: 308–309 (1974).
26. R.L. Fork, D.W. Taylor, K.R. German, A. Kiel, and E. Buehler, Unusual luminescence from crystals containing Eu^{2+}, *Phys. Rev. Lett.*, **32**: 781–783 (1974).
27. R.L. Fork and D.W. Taylor, Unusual optical emission from microcrystals containing Eu^{2+}: Experiment, *Phys. Rev. B*, **19**: 3365–3398 (1979).
28. V.A. Nikitenko, A.I. Tereschenko, I.P. Kuz'mina, and A.N. Lobachev, Stimulated emission of ZnO at high level of single photon excitation, *Optika i Spektroskopiya*, **50**: 605–607 (1981) Russian.
29. V.M. Markushev, V.F. Zolin, and Ch.M. Briskina, Powder laser, *Zh. Prikl. Spektr.*, **45**: 847–850 (1986) Russian.
30. V.M. Markushev, V.F. Zolin, and Ch.M. Briskina, Luminescence and stimulated emission of neodymium in sodium lanthanum molybdate powders, *Sov. J. Quantum Electron.*, **16**: 281–283 (1986).
31. V.F. Zolin, The nature of plaser-powdered laser, *J. Alloys Compounds*, **300–301**: 214–217 (2000).
32. Y. Yamamoto and R.E. Slusher, Optical properties in microcavities, *Phys. Today*, 66–73 (June 1993).
33. M.S. Brodin, N.I. Vitrikhovskii, A.A. Kypen, S.G. Shevel, and N.I. Yanushevskii, Spatial and spectral characteristics and a new model of laser generation for CdS-type single crystals under one-photon excitation, *Phys. Status. Solidi A*, **78**: 349–363 (1983).
34. J.J. Zayhowski and A. Mooradian, Frequency-modulated Nd:YAG microchip lasers, *Opt. Lett.*, **14**: 618–620 (1989).

35. H.-M. Tzeng, K.F. Wall, M.B. Long, and R.K. Chang, Laser emission from individual droplets at wavelengths corresponding to morphology-dependent resonances, *Opt. Lett.*, **9**: 499–501 (1984).
36. H.-B. Lin, A.L. Huston, B.L. Justus, and A.L. Campillo, Some characteristics of a droplet whispering-gallery-mode laser, *Opt. Lett.*, **11**: 614–616 (1986).
37. A. Biswas, H. Latifi, R.L. Armstrong, and R.G. Pinnick, Time-resolved spectroscopy of laser emission from dye-doped droplets, *Opt. Lett.*, **14**: 214–216 (1989).
38. S.L. McCall, A.F.J. Levi, R.E. Slusher, S.J. Pearton, and R.A. Logan, Whispering-gallery mode microdisk lasers, *Appl. Phys. Lett.*, **60**: 289–291 (1992).

2
Neodymium Random Lasers: Experimental Studies of Stimulated Emission

2.1 First Observation of Stimulated Emission in Powders of Neodymium-Doped Materials

As discussed in Chapter 1, the results of the first detailed experimental study of random laser emission (in $Na_5La_{1-x}Nd_x(MoO_4)_4$ powder) were reported by Markushev et al. in Reference [1]. In this experiment, the particle sizes varied between 1 and 10 μm, and the concentration of neodymium ions in different $Na_5La_{1-x}Nd_x(MoO_4)_4$ samples ranged between $x = 0.01$ and $x = 0.9$ [1]. The samples were pumped with ≈30 ns pulses of Rhodamine 6G laser between $\lambda \approx 575$ and 590 nm. The spontaneous emission decay time of the metastable state $^4F_{3/2}$ Nd^{3+} was equal to 140 μs at $x = 0.01$ and decreased to 60 μs at $x = 0.9$.

The stimulated emission experiment was carried out at liquid nitrogen temperature ($T = 77$ K). Above the characteristic threshold energy density of the order of ≈50 mJ/cm^2, the duration of the emission pulse shortened approximately four orders of magnitude [1]. About the same large enhancement was found in the intensity of the strongest emission line at the transition $^4F_{3/2}$–$^4I_{11/2}$ Nd^{3+} (≈1.066 μm), the linewidth of which narrowed significantly [1] (Figure 1.3). (The energy-level diagram of the Nd^{3+} ion is shown in Figure 2.1.) The intensity of this amplified spectral line plotted versus pumping energy resembled an input–output dependence in regular lasers (Figure 1.4). Based on the results of the spectroscopic, kinetics, and input–output measurements above, Markushev et al. concluded that the observed phenomenon was a laser emission from excited powder [1].

Similar laserlike emission was observed in neodymium-doped powders of lanthanum oxide La_2O_3 and lanthanum oxysulfide La_2O_2S (with neodymium concentration n_{Nd} equal to 3–7%, $T = 77$ K) [2], double barium gadolinium molybdate $BaGd_2(MoO_4)_4$ ($n_{Nd} = 2$–10%, $T = 77$ K) [1], and ytterbium selenogallate $YbGa_2Se_4$ ($n_{Nd} \approx 1\%$, $T = 4.2$ K) [3]. At the same time, no lasing effect was observed in bulk optically clear single crystals of $BaGd_2(MoO_4)_4$ at the pumping energy density ≈100 mJ/cm^2 [2]. That is why it was concluded that scattering in an ensemble of particles, providing for diffuse reflection of photons back to the pumped volume, played a significant role in the stimulated emission

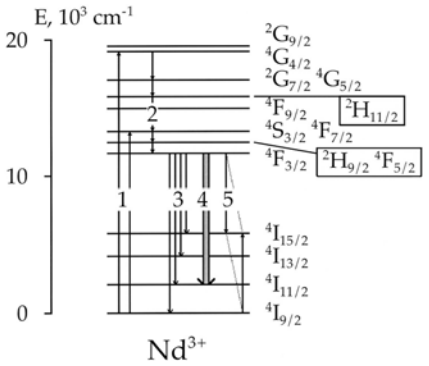

FIGURE 2.1. Nd^{3+} energy level diagram and the most important excitation and relaxation processes: (1) pumping; (2) multiphonon relaxation populating the metastable level $^4F_{3/2}$; (3) spontaneous radiation and multiphonon relaxation of the level $^4F_{3/2}$; (4) stimulated emission at the transition $^4F_{3/2}$–$^4I_{9/2}$; (5) cross relaxation. The Stark splitting of the energy levels is not shown in the figure. (*Source*: Ref. [14].)

process [2]. The history of the discovery of the neodymium random (powder) laser is described in the review paper [4].

It was concluded in Reference [1] that it is possible to construct a monochromatic bright source of radiation using fine-grained powders of transparent luminescent media (powder lasers), similar to those predicted by Letokhov in [5,6]. It was predicted that other scattering media with gain, such as luminescent ceramics, zeolites embedded with dye, and frozen or emulsion solutions of luminescent dyes, could generate stimulated emission as well [1,2]. The proposed applications of random (powder) lasers [1,2] included express-testing of novel laser materials and simulation and study in the laboratory environment of the cosmic laser effect [7–9].

2.2 Basic Properties of Neodymium-Doped Random Lasers

In the series of studies following the pioneering works [1,2], the list of neodymium-activated random lasers was extended to include a large number of pulverized materials discussed in Section 2.3. It has been found that many of these materials demonstrate qualitatively similar behavior. The basic properties of neodymium random lasers, such as emission kinetics, emission spectrum, threshold input–output dependence, and angular distribution of stimulated emission are discussed in this section. Other characteristics of neodymium random lasers are described in different sections of this chapter as well as Chapters 3 through 5.

Note that the authors of References [1,2] and their coworkers (see, e.g., Refs. [10–12]) conducted their experiments at cryogenic temperature. However, after Gouedard et al. [13], random laser emission was predominantly studied at room temperature.

2.2.1 Emission Kinetics

In different experiments with neodymium random lasers, the duration of the pumping pulse was varied between approximately 10 and 30 ns [1,10,13,14]. At weak pumping, only regular spontaneous emission of neodymium ions can be observed experimentally. [Note that the spontaneous emission kinetics can be shortened and the emission quantum yield can be reduced due to "concentration self-quenching" ($^4F_{3/2} \rightarrow {}^4I_{15/2}$, $^4I_{9/2} \rightarrow {}^4I_{15/2}$ cross-relaxation) known in neodymium-doped laser materials [15]; see Figure 2.1.]

With the increase of the pumping energy, the regime of amplified spontaneous emission (ASE) predominates over the regular spontaneous emission, causing (a) gradual increase of the peak emission intensity, (b) narrowing of the strongest emission spectral line, and (c) shortening of the emission decay kinetic (from 120 μs to ≈10 μs in the example of Nd:LaP_5O_{14} [13]). The ASE regime is especially pronounced in the materials with a relatively long luminescence lifetime ($\tau > 10^{-5}$–10^{-4} s) and, respectively, small nonradiative decay. It has been observed in scattering polycrystalline $Nd_{0.75}La_{0.25}P_5O_{14}$ [13] as well as $NdSc_3(BO_3)_4$, $NdAl_3(BO_3)_4$, and $Nd_{0.5}La_{0.5}Al_3(BO_3)_4$ powders and ceramics studied in our group. In the materials with strongly quenched luminescence, such as $NdCl_3 \cdot 6H_2O$ ($\tau \approx 16$ ns), the ASE regime is practically absent [13]. (In $NdCl_3 \cdot 6H_2O$, laserlike emission, described below, emerges above a certain pumping energy threshold without any noticeable ASE preceding it [13].)

As the pumping energy is increased further (above the ASE range), one short and very intense emission pulse appears close to the end of the pumping pulse [10,13,14]. The duration of this pulse varies in different experiments between approximately 0.3 and 3 ns. The pumping energy corresponding to the appearance of this short emission pulse, which is accompanied by a dramatic narrowing of the emission spectrum and increase of the peak emission intensity, is regarded as the threshold of laserlike emission. As the pumping energy is increased above the threshold, the intensity of the emission pulse also increases.

At stronger pumping, the second emission pulse, separated from the first one by several nanoseconds, emerges in the kinetics. As the pumping energy is increased further, the number of pulses increases, the pulses get shorter, and the time delay between the first emission pulse and the beginning of the pumping pulse becomes smaller [10,13,14]. As a rule, the time intervals between pulses are shorter in the beginning of the series of pulses than in the end of the series. The emission kinetics recorded in different pumping regimes in $Nd_{0.5}La_{0.5}Al_3(BO_3)_4$ ceramic and $NdAl_3(BO_3)_4$ powder are depicted in Figures 2.2 and 2.3 (Refs. [14,16]).

2.2.2 Spectrum of Laserlike Emission

The spectrum of spontaneous emission of Nd^{3+} ions at the $^4F_{3/2} \rightarrow {}^4I_{11/2}$ transition consists of 12 partially overlapped Stark-split components (in the sites with symmetry higher than cubic [17]). In most laser crystals, these spectral lines are positioned between 1.0 and 1.1 μm. The widths of individual emission lines

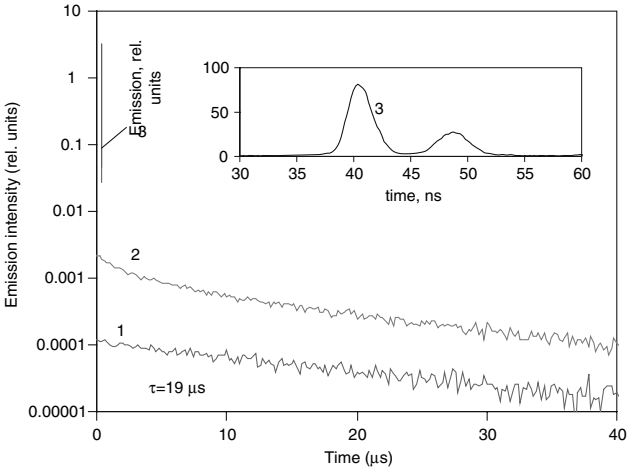

FIGURE 2.2. Evolution of the emission kinetics in $Nd_{0.5}La_{0.5}Al_3(BO_3)_4$ scattering ceramic with the increase of the pumping energy ($\lambda_{pump} = 532$ nm, $t_{pump} = 10$ ns): (1) 0.02 mJ—spontaneous regime; (2) 0.5 mJ—ASE regime; (3) 0.6 mJ—short-pulsed stimulated emission regime. Inset: high-resolution kinetics above the threshold, approximately corresponding to that shown by trace 3. The diameter of the pumped spot ≈0.21 mm. (*Source*: Ref. [16]).

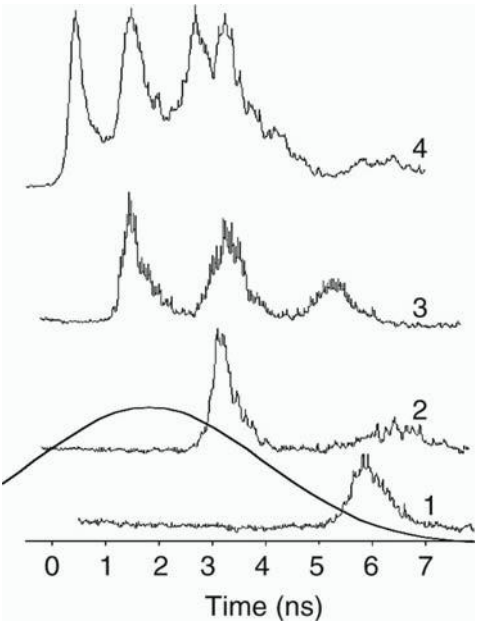

FIGURE 2.3. Pulses of stimulated emission in $NdAl_3(BO_3)_4$ powder: (1) near the threshold ($200\,mJ/cm^2$); (2) at $x = 1.6$ times threshold energy; (3) at $x = 1.9$; and (4) at $x = 3.9$. The bell-shaped line at the bottom of the figure shows approximate position and shape of the pumping pulse ($\lambda_{pump} = 532$ nm). The average (mean) linear size of the powder particles in this particular experiment was equal to 3.6 μm. (After [14].)

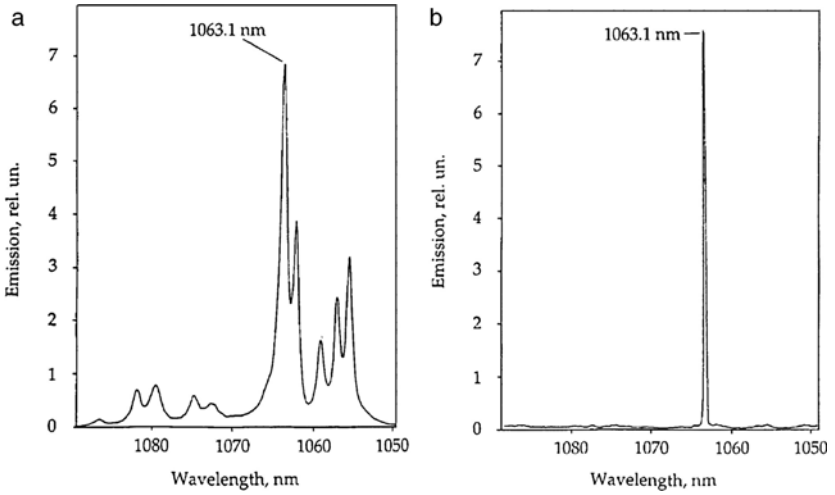

FIGURE 2.4. Emission spectrum of $NdAl_3(BO_3)_4$ powder (a) below the threshold, pumping density $\approx 30\,mJ/cm^2$, and (b) above the threshold, pumping density $\approx 240\,mJ/cm^2$. $\lambda_{pump} = 532\,nm$, $t_{pump} \approx 10\,ns$. (*Source*: Ref. [14].)

(dependent on the temperature) typically range between 0.5 and 3 nm. Above the random laser threshold, the intensity of the strongest line in the spontaneous emission spectrum is increased by two to four orders of magnitude and its width is reduced to approximately 1 Å. Thus, in $Na_5La(MoO_4)_4$ powder, the width of the laser spectrum above the threshold did not exceed $\delta\nu = 1\,cm^{-1}$ ($\approx$1Å) [10]. In $NdCl_3 \cdot 6H_2O$, the reported value of $\delta\lambda$ was equal to 1.5Å [13], and in $Nd_{0.5}La_{0.5}Al_3(BO_3)_4$ ceramic $\delta\nu$ was equal to 0.66Å [18]. Only one narrow line is observed in the emission spectrum above the threshold. The transformation of the neodymium emission spectrum when the pumping energy increases the threshold value in $Na_5La_{1-x}Nd_x(MoO_4)_4$ powder at 77 K is shown in Figure 1.3 [1]. A qualitatively similar pattern is observed at room temperature. The emission spectra of $NdAl_3(BO_3)_4$ powder before and after threshold at $T = 296\,K$ are depicted in Figure 2.4 [14].

2.2.3 *Input–Output Dependence*

The input–output dependence in neodymium random lasers, measured at the wavelength of stimulated emission, is very similar to that in regular lasers. A dramatic increase of the emission intensity just above the threshold makes the threshold sharp and well defined; see Figure 1.4.

The input–output curves obtained in $NdAl_3(BO_3)_4$ powder at the laser wavelength, ($\lambda = 1063.1\,nm$) and another, weaker, spectral line ($\lambda = 1054.4\,nm$), originating at the same upper laser level $^4F_{3/2}$, are depicted in Figure 2.5. One can see that although a characteristic laser input–output curve is observed at

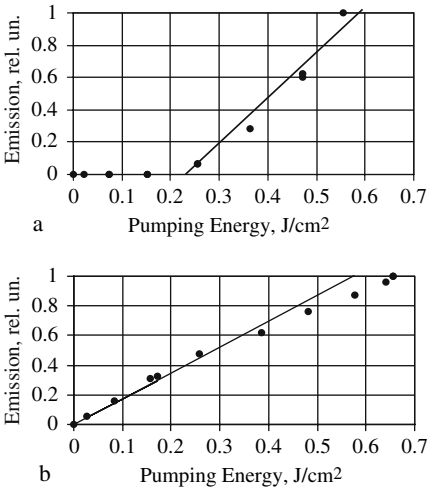

FIGURE 2.5. Experimental input–output emission curves in $NdAl_3(BO_3)_4$ powder: (a) stimulated emission at $\lambda = 1063.1$ nm; (b) luminescence at $\lambda = 1054.4$ nm registered in the maximum of kinetics (at $t = 0$). Both transitions $^4F_{3/2} - {}^4I_{11/2}$ and $^4F_{3/2} - {}^4I_{9/2}$ originate from the same metastable state $^4F_{3/2}$. Pumping: $\lambda_{pump} = 532$ nm, $t_{pump} \approx 10$ ns. (*Source*: Ref. [14].)

$\lambda = 1063.1$ nm (Figure 2.5a), the energy dependence of the emission intensity at 1054.4 nm does not exhibit any noticeable change of the slope at the threshold energy (Figure 2.5b). This result can be used as evidence that only a small fraction of excited ions contributed to the stimulated emission or that the lasing volume was much smaller than the pumped volume.

2.2.4 *Angular Distribution of Stimulated Emission*

The angular distribution diagram of $NdAl_3(BO_3)_4$ powder laser emission is shown in Figure 2.6 [19]. It resembles that for scattering off a rough surface and can be fitted with the function $I(\Theta) \propto \cos(\Theta)$, where Θ is the angle measured starting from the normal to the sample surface. Each data point in Figure 2.6 was obtained as the result of averaging over many laser pulses. In a separate set of measurements, it was found that the shape of the angular distribution diagram remains almost the same from pulse to pulse. (Note that the distribution diagram above is very different from that of ZnO random lasers (discussed in Chapter 7), where different spectra of stimulated emission can be observed at different angles [20–22].)

In the particular experiment depicted in Figure 2.6, no data were taken in the vicinity of the exact backscattering direction for the pumping beam. According to Reference [23], the angular distribution of emission in the random laser based on liquid dye with TiO_2 scatterers had a characteristic cone shape, which is typically observed in coherent backscattering (CBS) [24–26] (surprisingly, the cone in the

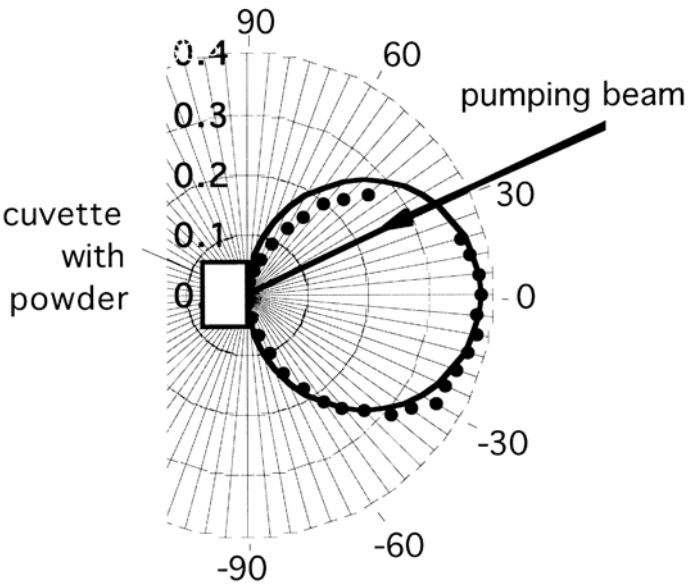

FIGURE 2.6. Angular distribution of the stimulated emission intensity in $NdAl_3(BO_3)_4$ powder sample under 532 nm pumping. Circles: experimental data; solid line: fitting with $\cos(\Theta)$. (*Source*: Ref. [19].)

angular distribution was not "seeded" by any probe beam at the emission wavelength). When the intensity distribution of stimulated emission in $NdAl_3(BO_3)_4$ and $Nd_{0.5}La_{0.5}Al_3(BO_3)_4$ random lasers has been studied in a narrow range of angles centered at the exact backscattering direction for pumping, no angular enhancement of emission exceeding $\approx$4% noise level has been observed.

2.3 Stimulated Emission in Different Materials and Types of Samples

Random laser emission has been obtained in more than a dozen neodymium-doped materials. A summary of properties of neodymium random lasers is given in Table 2.1. The detailed list of spectroscopic parameters of $NdAl_3(BO_3)_4$, $NdSc_3(BO_3)_4$, $Nd_xLa_{1-x}Sc_3(BO_3)_4$, and $Nd:Sr_5(PO_4)_3$ (Nd:SFAP) powder (random) lasers is given in Table 2.2 [14].

Most of the samples listed in Table 2.1 are powders of laser materials. A typical Scanning Electron Microscope (SEM) picture of the $NdSc_3(BO_3)_4$ powder sample and the corresponding distribution of powder particles by their sizes are given in Figure 2.7 [48]. However, the lasing effect similar to that illustrated in Figures 2.3 and 2.4 is not unique to pulverized media. Thus, an apparently similar

(*continued on page 22*)

TABLE 2.1. Summary of neodymium-activated random laser materials

Material	Granule size	Pumping type	Temperature	Threshold pumping	Threshold gain	Comment	Ref.
$Na_5La_{1-x}Nd_x(MoO_4)_4$ $x = 0.01–0.7$	Powder size: ≈1–10 μm	$^4I_{9/2} \rightarrow {}^4G_{5/2}, {}^4G_{7/2}$ transition: ≈575–595 nm; ≈Rhodamine 6G (R6G) laser; ≈30 ns	77 K	0.05 J/cm^2		First observation of powder (random) laser emission in neodymium doped material.	[1]
Nd:$Na_5La(MoO_4)_4$ $n_{Nd} = 15\%$ and $n_{Nd} = 45\%$	Powder 3–20 μm	R6G laser; ≈12 ns 575–595 nm	77 K	0.1 J/cm^2 (at $n_{Nd} = 15\%$)	≈10 cm^{-1}		[10]
Nd:$Na_5La(MoO_4)_4$	Mixture of two powders, with $n_{Nd} = 15\%$ and $n_{Nd} = 85\%$ and with $n_{Nd} = 15\%$ and $n_{Nd} = 95\%$; ≈10 μm	R6G laser 575–595 nm	77 K			The emission wavelength depends on the relative concentrations of the two powders in the mixture.	[11], [27]
Nd:$BaGd(MoO_4)_4$ $n_{Nd} = 1\%, 2\%$	Powder	$^4I_{9/2} \rightarrow {}^4G_{5/2}, {}^4G_{7/2}$ transition: 575–595 nm; R6G laser; ≈30 ns	77 K				[1]
Nd:$YbGa_2Se_4$ $n_{Nd} \approx 1\%$	Powder	$^4I_{9/2} \rightarrow {}^4G_{5/2}, {}^4G_{7/2}$ transition: 575–595 nm; R6G laser; ≈30 ns	4.2 K				[3]
Nd:La_2O_3 $n_{Nd} = 1\%$ and $n_{Nd} = 10\%$	Powder 3–20 μm	R6G laser; ≈12 ns; 575–595 nm	77 K				[1,2,10]
Nd:La_2O_2S	Powder 3–20 μm	R6G laser; ≈12 ns; 575–595 nm	77 K				[1,2,10]
Nd:$LaNbO_7$ $n_{Nd} = 8\%$	Powder 3–20 μm	R6G laser; ≈12 ns; 575–595 nm	77 K				[10]
Nd:$LaNbO_7$, $n_{Nd} = 5\%$	Powder	R6G laser; ≈585 nm	77 K				[28]
Nd:$SrLa_2WO_7$	Powder 3–20 μm	R6G laser; ≈12 ns; 575–595 nm	77K				[10]
Nd:$BaLa_2WO_7$	Powder	R6G laser; ≈585 nm	77 K				[28]
La_3TaO_7, $n_{Nd} = 20\%$		R6G laser; ≈585 nm	77 K				[28]

(*continued*)

TABLE 2.2. Continued

$LiNd(PO_3)_4$	Powder particles of regular shapes (hexagonal prisms and rectangular plates) 50–200 μm	R6G laser; ≈20 ns	77 K			A single narrow laser line corresponds to the maximum of the gain at relatively low pumping. Multiple laser lines and the shift of their frequencies are observed at stronger pumping.	[12]
NdP_5O_{14}	–Large regularly shaped particles: (50–250 μm wide) × (10–20 μm thick) platelets and prisms 20–50 μm. –Medium-size powder: 20–50 μm, partially irregular shapes. –Small-size powder: 1–30 μm, irregular shapes.	R6G laser; ≈20 ns	77 K	$<0.4\,J/cm^2$ in medium-size powder. $1.4\,J/cm^2$ in small-size powder	$200\,cm^{-1}$–$250\,cm^{-1}$	Small-size powder: one laser line corresponding to the maximum of the gain spectrum is observed at both high and low pumping. Medium-size and large-size powder: one laser line corresponding to the maximum of the gain is observed at the relatively low pumping. Multiple laser lines and shifts of their frequencies are observed at stronger pumping.	[12]
$Nd_{0.75}La_{0.25}P_5O_{14}$	Scattering polycrystalline	*Q*-switched Nd:YAG 6 ns, 532 nm	Room temperature	30 mJ, spot: ≈0.3 mm × 3 mm ≈$3\,J/cm^2$		Observation of the ASE regime followed by the short-spiked lasing regime at higher pumping. Low degree of coherence (8%) is deducted from the analysis of the speckle pattern.	[13]

Material	Granule size	Pumping type	Temperature	Threshold pumping	Threshold gain	Comment	Ref.
NdP_5O_{14}	Powder 4–40 μm	R6G laser	80 K and 300 K			From the analysis of the speckle pattern, the relatively low degree of coherence, 10–20%, is found in the majority of samples. In some samples, the degree of coherence was rather high, 40–50%. Bright spots are observed in the near-field emission above the threshold.	[29], [30], [31]
Nd:CdS	Small-size powder	R6G laser	77 K				[12]
$NdCl_3 \cdot 6H_2O$	Compressed powder	Q-switched Nd:YAG 6 ns, 532 nm	Room temperature	30 mJ in multi-mode fiber.	$\approx 800\,cm^{-1}$	Strongly quenched luminescence ($\tau = 16$ ns). No ASE regime is observed. Low degree of coherence (14%) is deducted from the analysis of the speckle pattern.	[13,32]
$NdAl_3\,(BO_3)_4$	Powder 4–20 μm	R6G laser	80 K and 300 K			Relatively low degree of coherence, 10–20%, is deducted from the analysis of the speckle pattern. Bright spots are observed in the near-field emission above the threshold.	[29], [30], [31]
$NdAl_3(BO_3)_4$	Powder ≈3 μm	Q-switched Nd:YAG laser; 532 nm, 10 ns	Room temperature	$0.2\,J/cm^2$	$7.5\,cm^{-1}$		[14]

(*continued*)

TABLE 2.1. Continued

$Nd_{0.5}La_{0.5}Al_3(BO_3)_4$	Powder (≈3–5 μm) and scattering ceramic	*Q*-switched Nd:YAG laser; 532 nm, 10 ns	Room temperature			Powders of different volume densities have been studied. The lowest threshold absorbed energy was found in the powder with the lowest volume density.	[33]
$Nd_{0.5}La_{0.5}Al_3(BO_3)_4$	Powder ≈3–5 μm	*Q*-switched Nd:YAG laser; 532 nm, 10 ns	Room temperature			The effects of external seeding and external mirror have been studied.	[34]
$Nd_{0.5}La_{0.5}Al_3(BO_3)_4$	Scattering ceramic	*Q*-switched Nd:YAG laser; 532 nm, 10 ns	Room temperature			Longitudinal and transversal coherence have been studied using interferometric techniques.	[18]
$Nd_{0.5}La_{0.5}Al_3(BO_3)_4$	Scattering ceramic	*Q*-switched Nd:YAG laser; 532 nm, 10 ns	Room temperature	0.1 J/cm^2 at d = 4.5 mm		The threshold and the output efficiency have been studied at different diameters of the pumped spot.	[16,35]
$NdSc_3(BO_3)_4$	Powder ≈3 μm	*Q*-switched Nd:YAG laser; 532 nm, 10 ns	Room temperature	0.56 J/cm^2	2.5 cm^{-1}		[14]
$Nd_xLa_{1-x}Sc_3(BO_3)_4$ x = 0.5	Powder ≈3 μm	*Q*-switched Nd:YAG laser; 532 nm, 10 ns	Room temperature				[14]
$NdAl_3(BO_3)_4$ and $NdSc_3(BO_3)_4$	Mixture of two powders ≈3 μm	*Q*-switched Nd:YAG laser; 532 nm, 10 ns	Room temperature			The stimulated emission started at 1063.1 nm (the wavelength of the maximum gain in $NdAl_3(BO_3)_4$) and then hopped to 1061.5 nm (the wavelength of the maximum gain in $NdSc_3(BO_3)_4$).	[14]

Material	Granule size	Pumping type	Temperature	Threshold pumping	Threshold gain	Comment	Ref.
Nd:$Sr_5(PO_4)_3F$ $n_{Nd} = 2\%$	Powder	Q-switched Cr:LICAF laser; 805 nm, ≈100 ns	Room temperature	0.17 J/cm^2	15.7 cm^{-1}		[15]
$Nd_{0.5}La_{0.5}Al_3(BO_3)_4$ and 2-methyl-4-nitroaniline (MNA)	Mixture of lasing powder (≈3–5 μm) and frequency doubling powder	Dye laser (580 nm) pumped with frequency doubled Q-switched Nd:YAG laser; ≈10 ns	Room temperature			Second harmonic generation was observed in a powder laser.	[36]
Nd:$Y_3Al_5O_{12}$		Cathodoluminophore (scintillator) was pumped with an electron beam. It then excited Nd:$Y_3Al_5O_{12}$ optically	77 K			When the pumping energy was changed from 18 keV to 20 keV, the ratio of the emission intensities at 1064 nm and 1081 nm increased in a threshold manner from 2 to 3. The effect is explained in terms of superluminescence (ASE). Electron beam pulse duration: 0.7 μs.	[30,31]
Nd:δ-alumina n_{Nd}=1000–10000 ppm	Nano-powder ≈30 nm	Electron beam				Change in the slope of the dependence of the luminescence intensity ($\lambda = 469$ nm) on the electron beam current is interpreted as lasing.	[37], [38], [39]

TABLE 2.2. Spectroscopic properties of $NdAl_3(BO_3)_4$, $Nd_xLa_{1-x}Sc_3(BO_3)_4$, and $Nd:Sr(PO_4)_3F$ powder (random) lasers [14]

	$NdAl_3(BO_3)_4$	$NdSc_3(BO_3)_4$/ $Nd_xLa_{1-x}Sc_3(BO_3)_4$	Nd:S-FAP
Nd concentration in 100% doped sample	5.3×10^{21} cm^{-3}, Ref. [40]	5.1×10^{21} cm^{-3} in $NdSc_3(BO_3)_4$, Refs. [43,44]	1.68×10^{22} cm^{-3}, Ref. [46]
$^4F_{3/2}$ life-time	20 μs, Ref. [40]	Nd(1–10%): $LaSc_3(BO_3)_4$ 118 μs $NdSc_3(BO_3)_4$ 24 μs, Refs. [43,44]	298 μs, Ref. [47]
Wavelength of the maximum emission cross section	≈1.063 μm Ref. [41]	1.0615 μm, (our measurements)	1.059 μm, Refs. [46,47]
$^4F_{3/2} - {}^4I_{11/2}$ emission cross section	10×10^{-19} cm^2, Ref. [40]	$Nd_{0.1}La_{0.9}Sc_3(BO_3)_4$ Ell**x**,13×10^{-20} cm^2, Ell**y**, 9×10^{-20} cm^2, Ell**z**, 5×10^{-20} cm^2, Ref. [43], averaged over different polarizations: 9×10^{-20} cm^2	Ell**c**, 5.4×10^{-19} cm^2, E⊥**c**, 2.4×10^{-19} cm^2 Refs. [46,47]; averaged over different polarizations: 3.9×10^{-19} cm^2
Absorption cross section at the pump wavelength	Ell**c** 3.3×10^{-21} cm^2, Ell**c**, 2.6×10^{-21} cm^2 ($\lambda = 532$ nm) Ref. [42]	Ell**x**, 5.1×10^{-21} cm^2, Ell**y**, 4.2×10^{-21} cm^2, Ell**z**, 2.4×10^{-21} cm^2 ($\lambda = 532$ nm) Ref. [45][a]	Ell**c**, 2.26×10^{-19} cm^2, E⊥**c**, 0.7×10^{-19} cm^2 ($\lambda = 805$ nm) Ref. [46]
Threshold pumping density (in the powder)	200 mJ/cm^2 ($\lambda = 532$ nm)	560 mJ/cm^2 ($\lambda = 532$ nm)	170 mJ/cm^2 ($\lambda = 805$ nm)
Threshold Nd excited state concentration	7.5×10^{18} cm^{-3}	2.8×10^{19} cm^{-3}	3.64×10^{19} cm^{-3}
Threshold gain	≈7.5 cm^{-1}	≈2.5 cm^{-1}	≈15.7 cm^{-1}

[a] $Nd_{0.1}La_{0.9}Sc_3(BO_3)_4$ is a trigonal crystal, whereas $NdSc_3(BO_3)_4$ is a monoclinic crystal, Ref. [43].

stimulated emission was observed in polished and unpolished bulk laser crystals without cavity [14,40,44]. As follows from Table 2.3, where the behavior of stimulated emission in powders is compared with that in single crystals, the factors reducing the lasing threshold are: (1) reasonably large pumped volume, (2) pulverization of the material (strong scattering providing for nonresonant feedback), and (3) polished plane-parallel surfaces in optically clear bulk crystals (providing for resonant feedback).

It is important to note that stimulated emission could not be obtained in a monolayer of irregularly shaped powder particles (average particle size ≈3.6 μm) [14]. This suggests that stimulated emission in fine (irregularly shaped) powder is a collective effect occurring in an ensemble of particles where scattering provides for feedback.

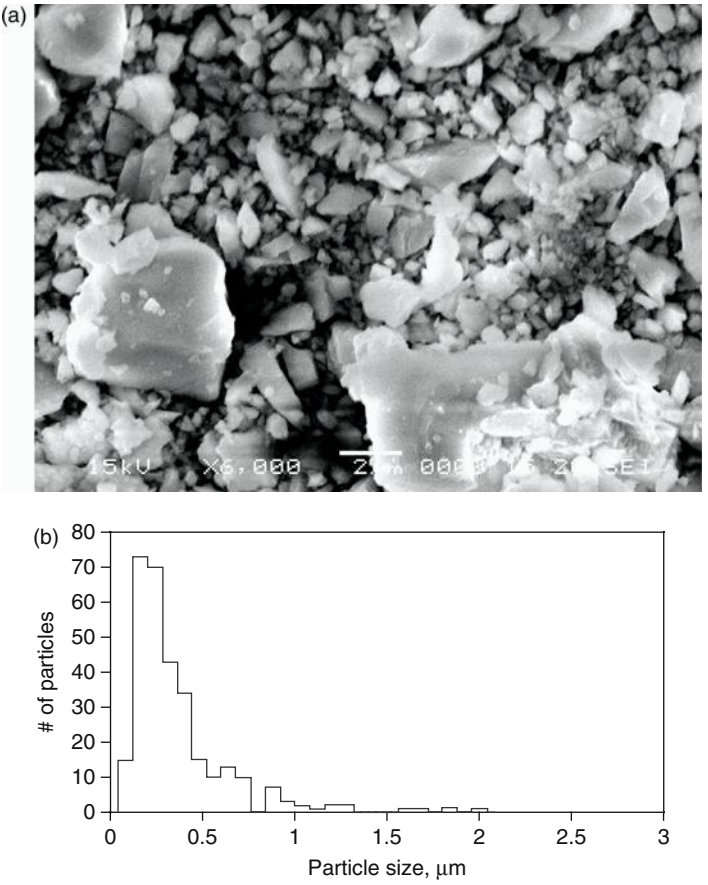

FIGURE 2.7. Scanning electron microscope image of (a) the $NdSc_3(BO_3)_4$ powder sample and (b) the corresponding distribution of particles by their sizes. (*Source*: Ref. [48].)

2.4 Stimulated Emission in Mixtures of Powders

In Reference [11], stimulated emission was studied in the mixture of powders of $Na_5Nd_{0.15}La_{0.85}(MoO_4)_4$ and $Na_5Nd_{0.85}La_{0.15}(MoO_4)_4$. The powders in the compound were mixed in equal proportion. The wavelength of the strongest spontaneous emission line at the $^4F_{3/2} \rightarrow {}^4I_{11/2}$ transition slightly changed with the change of the crystal composition: at $n_{Nd} = 0.15$ it was equal to 1067.11 nm and at $n_{Nd} = 0.85$ it was equal to 1067.27 nm. The excitation spectra of stimulated emission in the two individual components were very different as well. Thus, by scanning the pumping wavelength, it was possible to change the relative contributions of the two powders to the stimulated emission of the mixture.

Only one spectral line was observed in stimulated emission of the mixture of the two components [11]. The emission wavelength of the mixture was

TABLE 2.3. Thresholds of the stimulated emission in the powders and single crystals of $NdAl_3(BO_3)_4$, $Nd_xLa_{1-x}Sc_3(BO_3)_4$, and $Nd:Sr(PO_4)_3F$ [14]

	$NdAl_3(BO_3)_4$ $\lambda_{pump} = 532\,nm$	$NdSc_3(BO_3)_4$ $\lambda_{pump} = 532\,nm$	$Nd:Sr(PO_4)_3F$ $\lambda_{pump} = 805\,nm$	
Powder $V \geq 1\,mm^3$ $\approx 3\,\mu m$	Threshold: $200\,mJ/cm^2$	Threshold: $560\,mJ/cm^2$	Threshold: $170\,mJ/cm^2$	
Monolayer of powder $\approx 3\,\mu m$	At $\leq 1\,J/cm^2$ threshold was not achieved			
Single crystals	Irregularly shaped; $V \approx 1\,mm^3$; Threshold = $600\,mJ/cm^2$		8 mm polished plate	Thresh = $625\,mJ/cm^2$
			1.5 mm polished plate	Thresh = $920\,mJ/cm^2$
			0.8 mm unpolished plate	Thresh = $1080\,mJ/cm^2$

always larger than that in $Na_5Nd_{0.15}La_{0.85}(MoO_4)_4$ and smaller than that in $Na_5Nd_{0.85}La_{0.15}(MoO_4)_4$. It could be tuned, within approximately 0.07 nm, by the tuning of the excitation wavelength. This experiment proved that stimulated emission in powder was a collective effect where powder particles in an ensemble strongly influenced each other via radiation. An almost similar result was observed in Reference [27], where different values of neodymium-doping concentrations and different proportions between powders in the mixtures were used.

A qualitatively different result was obtained in the mixture of $NdAl_3(BO_3)_4$ and $NdSc_3(BO_3)_4$ powders [14]. In $NdAl_3(BO_3)_4$, the peak emission cross section at 1063.1 nm is equal to $10 \times 10^{-19}\,cm^2$ [40], and in $NdSc_3(BO_3)_4$, the peak emission cross section at 1061.5 nm (averaged over different polarizations) is equal to $9 \times 10^{-20}\,cm^2$ [43]. The most interesting result was obtained when $NdAl_3(BO_3)_4$ and $NdSc_3(BO_3)_4$ powders were mixed in the proportion approximately equal to 1:5 (by volume). At low pumping energy (below the threshold), the luminescence spectrum of the mixture closely resembled that of the dominant material, $NdSc_3(BO_3)_4$. However, at strong pumping, two narrow emission lines appeared approximately at 1063.1 and 1061.5 nm. Their thresholds and relative intensities were strongly dependent on very small variations of the concentrations of the components. Attaching the streak camera (Hamamatsu C4334) to a widely open output slit of the monochromator, one could record two-dimensional (wavelength–time) patterns of stimulated emission in the mixture of powders [13]. In the particular mixture, the time–wavelength pattern of which is depicted in Figure 2.8, the line at 1063.1 nm had a lower threshold (E_1) than the line at 1061.5 nm (E_2). Thus, at $E_1 < E < E_2$, only one stimulated emission line at 1063.1 nm has been observed. When the pumping energy was increased above the second threshold value (E_2), required for the both lines to emerge in the spectrum, several short pulses of emission appeared at $\approx$1063.1 nm first. Then the emission "jumped" to the wavelength $\approx$1061.5 nm, which produced one or several short pulses, depending on the pumping energy.

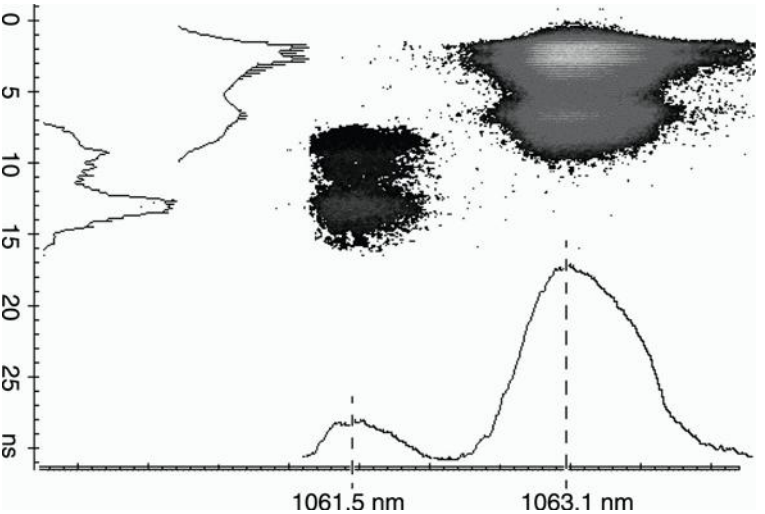

FIGURE 2.8. Image of stimulated emission from the mixture of $NdAl_3(BO_3)_4$ ($\approx 1/6$) and $NdSc_3(BO_3)_4$ ($\approx 5/6$) as it appears on the screen of streak camera (Hamamatsu C4334) connected to widely open output slit of a monochromator. (*Source*: Ref. [14].)

In a single-component medium, the first pulse in the series was always the strongest one (Figure 2.3). In contrast, in the mixture of two powders, where the first pulse in the $\approx$1061.5 nm series overlapped in time with the last pulse in the $\approx$1063.1 nm series, the first 1061.5 nm pulse was strongly damped and weaker than succeeding pulses of the same series. This was another clear indication that particles of different materials in the mixture emitted collectively as an ensemble.

In the mixture of $NdAl_3(BO_3)_4$ and $NdSc_3(BO_3)_4$ powders, the emission wavelengths were not exactly equal to their values in the pure constituents, 1063.1 and 1061.5 nm, but were slightly shifted toward each other. Depending on the composition of the mixture, the shift could be as large as 0.2 nm. However, in contrast to the mixture of $Na_5Nd_{0.15}La_{0.85}(MoO_4)_4$ and $Na_5Nd_{0.85}La_{0.15}(MoO_4)_4$ powders [11], the mixture of $NdAl_3(BO_3)_4$ and $NdSc_3(BO_3)_4$ powders never produced a single laser line that was approximately centered between the emission wavelengths of the pure powders [14]. Apparently, the major reason for the difference between the results of the two works is the spectral distance between the emission lines in the individual components, 1.6 nm in [14] and 0.16 nm in [11].

2.5 Stimulated Emission Supported by Large Regularly Shaped Particles

Several examples discussed in the preceding sections clearly demonstrate that stimulated emission in neodymium random lasers composed of small irregularly shaped granules is a collective effect occurring in an ensemble of particles.

However, the situation may change dramatically if powder particles are large and have regular shapes. In Reference [12], three different types of $LiNd(PO_3)_4$ and NdP_5O_{14} powders have been studied: powders consisting of large, up to 250 μm, regularly shaped particles (prisms and plane-parallel plates); powders consisting of medium sized, 20 to 50 μm, particles, many of which were regularly shaped; and powders consisting of small, 1 to 30 μm, particles of irregular shapes (Table 2.1).

Only one narrow (<0.1 nm) emission line corresponding to the maximum of the gain profile was observed above the threshold in small-sized irregularly shaped powders. Its wavelength was stable, within <0.1 nm, during the whole series of the emission pulses. This behavior, previously observed in other fine powders [10], is typical of random lasers with diffusive incoherent feedback provided by scatterers [6].

The spectral dynamics in large- and medium-size powders at pumping energies slightly exceeding the threshold was almost similar to that in fine irregular powders. At larger pumping energies, several (up to four) narrow spectral lines, fitting the gain band, could be found in the emission spectra [12]. The separation

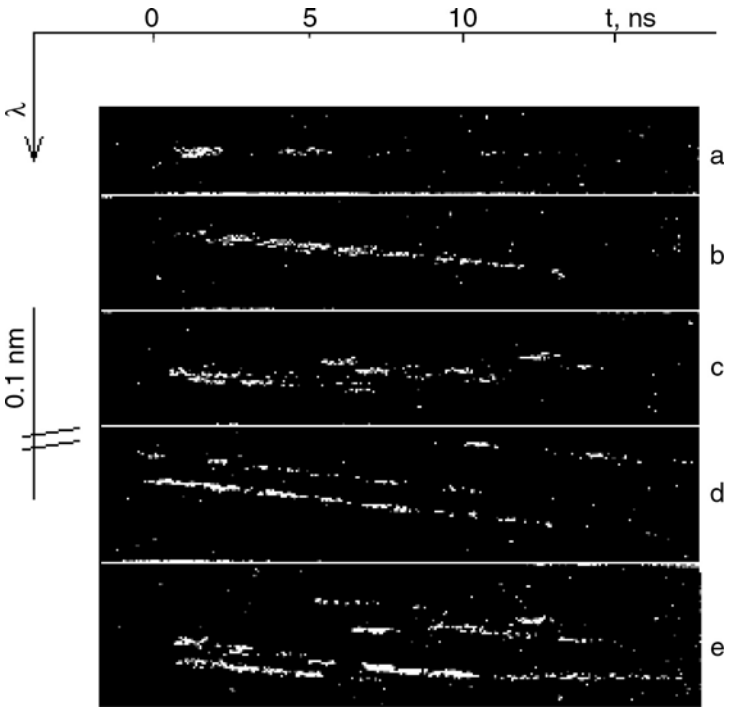

FIGURE 2.9. Time-wavelength patterns recorded with a streak camera attached to an output slit of a monochromator in $LiNd(PO_3)_4$ large-granule powders. The series of traces a to d has been obtained by gradually increasing the pumping rate; series e is the superposition of several realizations (shots). The samples are pumped and the emission is delivered through an optical fiber. (After [12].)

between lines was of the order of 0.1 nm. The spectral positions of these lines shifted to longer wavelengths within one series of stimulated emission pulses, semicontinuously or by hopping from pulse to pulse ("staircase"); see Figure 2.9 [4,12]. The narrow emission lines in reasonably large regularly shaped particles were associated with resonator modes supported by individual granules [12]. The wavelength shifts were explained by (a) thermal expansion of particles during the laser pulse and (b) change of the refraction index via thermal or nonlinear optical mechanisms (obviously, both factors could change the effective optical length of the cavity). This suggests that powders composed of large, regularly shaped particles can be regarded as random collections of individual microlasers. The fact that a reasonably small number of individual narrow lines were observed in the experiment (instead of an inhomogeneously broadened semi-continuous spectrum that could be expected in the case of a large number of uncorrelated laser lines contributing to the net emission signal) was explained by a very small number of particles situated in the vicinity of the end of the optical fiber used for pumping and delivery of random laser emission [12].

To summarize, the results of Sections 2.3 through 2.5 suggest that powder laser emission is a collective effect in ensembles of small irregularly shaped particles and can be due to intraparticle resonances when granules are large and have regular shapes.

2.6 Quantum Yield of Stimulated Emission

It was shown in a number of publications that the quantum yield of neodymium random lasers pumped through the surface is typically very low. In Reference [14], the $^4F_{3/2} \rightarrow {}^4I_{11/2}$ emission kinetics in $NdAl_3(BO_3)_4$ powder was recorded at strong pumping (I_1) above the threshold (Figure 2.10a), and at very low pumping (I_0) below the threshold, (Figure 2.10b). The area under the former emission kinetics trace (S_1) is proportional to the number of photons that went to the stimulated emission channel, and the area under the latter one (S_0) is proportional to the number of photons emitted spontaneously below the threshold. Assuming that the quantum efficiency of population of the state $^4F_{3/2}$ is independent of pumping energy (at the pumping densities used in the experiment, the depopulation of the ground state $^4I_{9/2}$ was negligibly small), the fraction of the $^4F_{3/2}$ excitation going to the stimulated emission channel can be calculated as

$$\varepsilon = \frac{S_1}{S_0}\frac{I_0}{I_1}\eta, \tag{2.1}$$

where η is the quantum yield of spontaneous emission. The value of η, which is determined by the rates of cross relaxation, multiphonon quenching, and spontaneous emission, is not known in $NdAl_3(BO_3)_4$. In the material of the same family, $NdSc_3(BO_3)_4$, η can be estimated as $0.2 < \eta < 1$ [42,43]. At $\eta = 1$, the calculated value of ε is equal to $\approx 0.2\%$ at the pumping energy twice exceeding the threshold

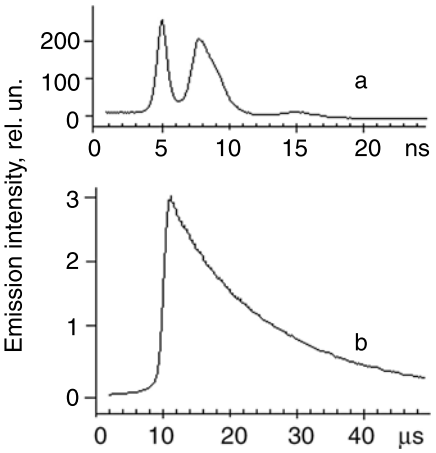

FIGURE 2.10. (a) Kinetics of stimulated emission above the threshold in $NdAl_3(BO_3)_4$ powder at the pumping density $\approx 400\,mJ/cm^2$; (b) kinetics of spontaneous emission below the threshold at the pumping density $\approx 55\,mJ/cm^2$, $\lambda_{pump} = 532\,nm$. (*Source*: Ref. [14].)

energy [14]. Thus, according to this experiment, only very small fraction of energy stored in the state $^4F_{3/2}$ was emitted in form of short laser pulses.

In $Nd_{0.5}La_{0.5}Al_3(BO_3)_4$ ceramic, the input–output curves of random laser emission were studied at different diameters of the pumped spot [35]. Experimentally, the sample was pumped through the surface, and the diameter of the pumped spot was controlled with the position of the focusing lens. The light pulse energy was assumed to be proportional to the area under the recorded emission kinetics trace. In order to calibrate the output energy, the kinetics of scattered pumping light was recorded in the same geometry. This calibration required the knowledge of the pumping pulse energy, the reflection coefficient of powder at the pumping wavelength [32], and the spectral sensitivity of the photodetector at the pumping and the emission wavelengths. Additionally, it was assumed that the random laser emission and the scattered pumping light had the same angular distribution diagrams (Figure 2.6). Figure 2.11 shows the input–output curves measured this way. The dependence of slope efficiency on the size of the pumped spot is shown in Figure 2.12. As follows from this figure, the slope efficiency increases with the increase of the size of the pumped spot at small diameters d and saturates at the value $\approx 1\%$ at large values of d [35].

In References [29–31], one or several 20 to 30 μm bright emission spots positioned inside the 300 to 350 μm pumped spot were observed on the surface of $NdAl_3(BO_3)_4$ powder above the threshold. These bright spots were interpreted as localized regions of stimulated emission in small ensembles of optically coupled particles. The ratio of the emission intensity integrated over those small bright spots to the emission intensity integrated over the whole pumped area was of the order of 0.005 [29]. Thus, the value of the random laser output efficiency was equal to 0.5%.

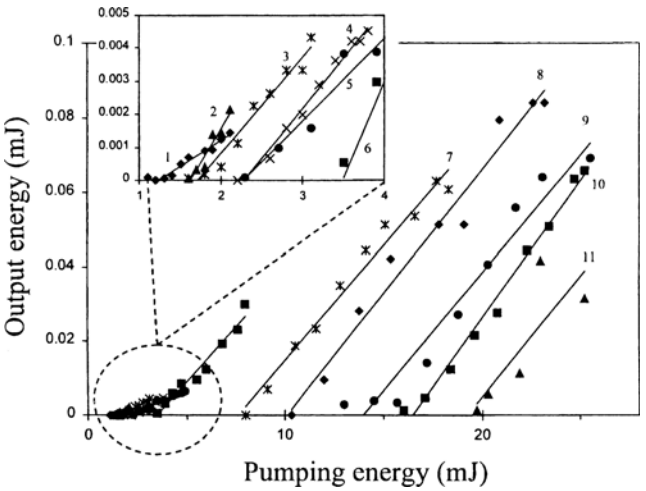

FIGURE 2.11. Output energy of the stimulated emission from $Nd_{0.5}La_{0.5}Al_3(BO_3)_4$ ceramic plotted versus absorbed pumping energy. The diameter of the pumped area is equal to (1) $d = 0.050$ cm, (2) $d = 0.062$ cm, (3) $d = 0.071$ cm, (4) $d = 0.088$ cm, (5) $d = 0.097$ cm, (6) $d = 0.101$ cm, (7) $d = 0.146$ cm, (8) $d = 0.213$ cm, (9) $d = 0.286$ cm, (10) $d = 0.357$ cm, (11) $d = 0.415$ cm. (*Source*: Ref. [35].)

Random lasers pumped through the surface of a scattering medium have an obvious disadvantage: a fraction of the pumping energy, sometimes very large, is reflected by the sample and, thus, wasted. This increases the threshold energy and reduces the slope efficiency of stimulated emission.

The slope efficiency (as well as the threshold) can be improved if a random laser is excited through an optical fiber that delivers pumping energy deep inside the scattering medium. In Reference [10], where $Na_5La(MoO_4)_4$ powder was pumped

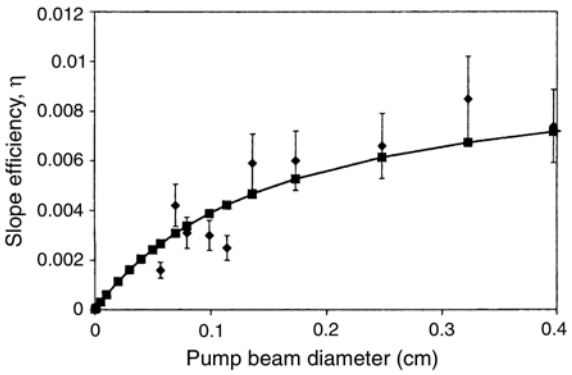

FIGURE 2.12. Slope efficiency plotted versus diameter of the pumped area. (*Source*: Ref. [35].)

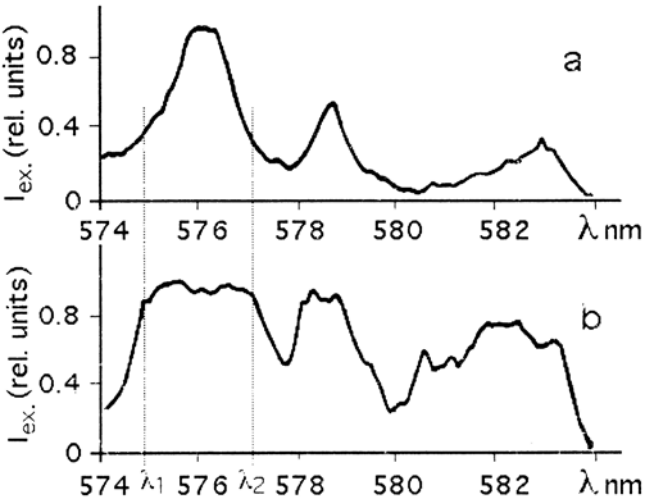

FIGURE 2.13. Excitation spectra of luminescence in Nd (15%):$Na_5La(MoO_4)_4$ powder (a) below and (b) above the lasing threshold. The samples are pumped with dye laser through an optical fiber. Luminescence of $^4F_{3/2} \rightarrow {}^4I_{9/2}$ is registered $\sim$0.9 μm. (After [10].)

through a fiber, the excitation spectrum of the $^4F_{3/2} \rightarrow {}^4I_{9/2}$ emission (originating at the upper laser level; Figure 2.1) has been studied below and above the lasing threshold. From the fact that the tops of the strongest peaks in the excitation spectrum flattened above the threshold (Figure 2.13), the authors of Reference [10] concluded that a significant fraction of excitation stored at the upper laser level $^4F_{3/2}$ went to the stimulated emission channel. Following this argument, one can roughly estimate from Figure 2.13 the quantum yield of stimulated emission to be equal to 20 to 25%.

A fiber-pumped random laser [49] is discussed in detail in Section 5.3.

2.7 Coherence Studies

Coherence is one of the important laser parameters. Knowledge of the coherence properties helps to understand better the mechanisms of the operation of random lasers and to optimize their performance. Several studies of coherence in random lasers are presented in this section.

2.7.1 Interferometric Measurements of Longitudinal Coherence

In Reference [18], a piece of highly scattering $Nd_{0.5}La_{0.5}Al_3(BO_3)_4$ ceramic was pumped with a Q-switched second harmonic Nd:YAG laser ($\lambda = 532$ nm)

operating at a 10 Hz repetition rate. The experimental setup for the longitudinal coherence measurements was based on a Twyman–Green interferometer (Figure 2.14a). The $Nd_{0.5}La_{0.5}Al_3(BO_3)_4$ sample was placed close to the focal plane of lens 9. The set of characteristic concentric rings was observed in screen 7. When mirror 4 was slowly moved, fringes moved as well. The dynamics of light intensity in the center of the concentric ring pattern was recorded when a fast Si photodetector with a small pinhole aperture was positioned in the place of screen 4. The fringe dynamics at 1.06 μm (random laser emission, Figure 2.14b) and at 532 nm (scattered pumping light) could be recorded separately by choosing a proper color filter (6).

When the fringe dynamics was recorded at different positions of mirror (4), the minimum and maximum values of the fringe light intensity were plotted as a function of the mirror displacement (Figure 2.15a) [18]. If one assumes a Gaussian form of the spectral line,

$$P(\nu) = \frac{1}{\Delta\nu} \exp\left(-\pi\left(\frac{\nu - \nu_0}{\Delta\nu}\right)^2\right),$$

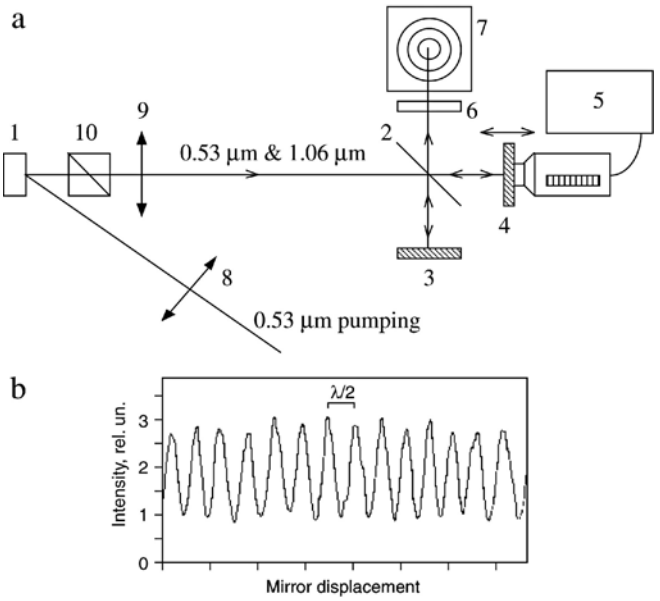

FIGURE 2.14. (a) Setup for longitudinal coherence measurements: (1) $Nd_{0.5}La_{0.5}Al_3(BO_3)_4$ sample, (2) beamsplitter, (3) mirror, and (4) movable mirror compose an interferometer; (5) control unit for the motor driven mirror; (6) spectral filter; (7) screen; (8) pumping focusing lens; (9) collimating lens; (10) polarizer; (b) fringe intensity as a function of displacement of mirror 4 (recorded for 1.06 μm random laser emission). (*Source*: Ref. [18].)

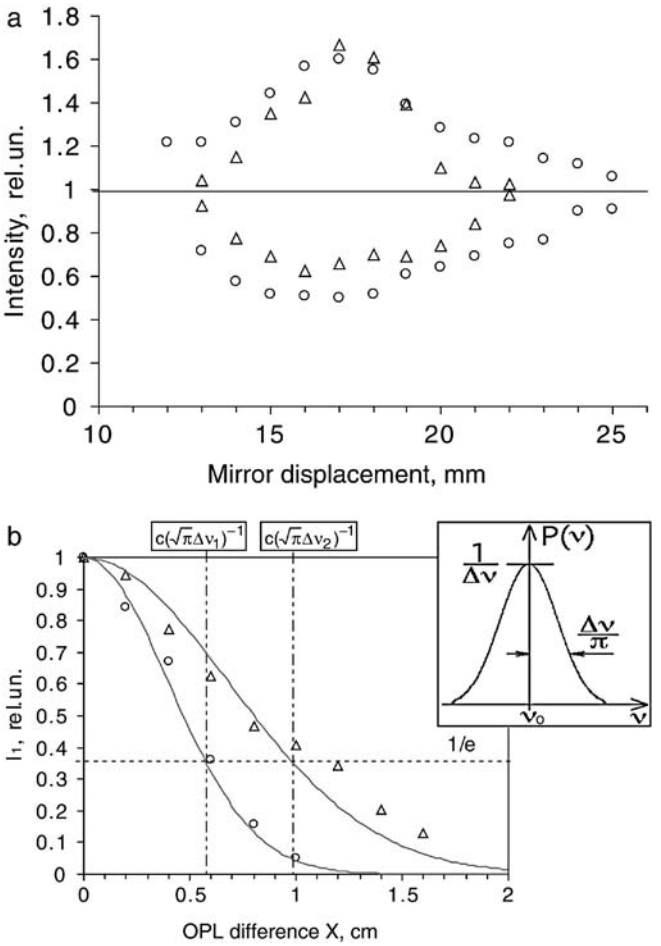

FIGURE 2.15. (a) Maximum and minimum fringe light intensity $I_{\max,\min}$ of the oscillating interference pattern (Figure 2.14b) recorded in the setup of Figure 2.14a. Circles: 1.06 μm random laser emission; triangles: scattered 532 nm light; (b) Fit of experimental data points $I_1(X)$ with the function $\exp[-\pi(\Delta\nu X/c)^2]$. Triangles: 1.06 μm random laser emission; circles: scattered 532 nm light; solid line: theoretical fit. Inset: quasimonochromatic line with a Gaussian shape. (*Source*: Ref. [18].)

where ν_0 is the central frequency and $\Delta\nu$ is the linewidth (Figure 2.15b inset), then the data points in Figure 2.15a, $I_{\max,\min}(X)$, can be fitted with the envelope $\{1 \pm \exp[-\pi(\Delta\nu X/c)^2]\}$, where X is the optical path length difference between the two branches of the interferometer and c is the speed of light [50].

In order to estimate the linewidth $\Delta\nu$, the experimental data of Figure 2.15a were recalculated as $I_1(X) = |I_{\max,\min}(X) - 1|$, averaged over the left and right-hand side parts of the bell-shape distribution $I_{\max,\min}(X)$, normalized to unity, and plotted against X (Figure 2.15b). The fitting of the experimental dependence

$I_1(X)$ with the function $\exp[-\pi(\Delta\nu X/c)^2]$ yielded the bandwidth of the 532 nm laser emission to be equal to $\Delta\nu_1 = 3 \times 10^{10}$ Hz ($\Delta\lambda_1 = \Delta\nu_1\lambda_1^2/c = 0.28$ Å) and that of the 1.06 μm random laser emission to be equal to $\Delta\nu_2 = 1.8 \times 10^{10}$ Hz ($\Delta\lambda_2 = \Delta\nu_2\lambda_2^2/c = 0.66$ Å). (In the experiment, the pumping energy exceeded the threshold value approximately twice [18].)

The determined value $\Delta\lambda_2$ is in good agreement with the linewidths measured in different neodymium random lasers with the use of spectrographs or monochromators, ≤0.5 Å [30], <1 Å [10], <2 Å [14], and ≈1.5 Å [13].

The fact that the radiation of the solid-state random laser can be studied in a conventional interferometric experiment [18] clearly demonstrates that random lasers (equipped with a simple optics) can produce high-quality collimated beams of stimulated emission. This conclusion is of great importance for applications of random lasers.

2.7.2 *Speckle Pattern Analysis*

The contrast of a speckle pattern is an important parameter characterizing the coherence of a light source [51]. In order to evaluate the degree of coherence of the emission of $NdCl_3{:}H_2O$ and $Nd_{0.75}La_{0.25}P_5O_{14}$ random lasers, their speckle patterns have been analyzed in Reference [13]. Figure 2.16a depicts the polarized speckle pattern of the 1.06 μm fundamental line of the pumping laser scattered in the powder. Its intensity distribution histogram $P(I)$ corresponds to that of a highly coherent light source with the contrast close to unity [13]. The corresponding degree of coherence was calculated to be equal to $\sigma/\langle I\rangle = 0.98$. (Here $\langle I\rangle$ is the mean intensity and σ is the variance of distribution.)

The analogous speckle patterns from 0.3 ns emission pulses of the $NdCl_3{:}6H_2O$ random laser and 1 ns pulses of the $Nd_{0.75}La_{0.25}P_5O_{14}$ (Nd:LaPP) random laser had much smaller contrasts. The corresponding intensity histogram is shown in Figure 2.16b. The degrees of coherence of neodymium random laser emission were calculated to be equal to $\sigma/\langle I\rangle = 0.14$ in $NdCl_3{:}6H_2O$ and $\sigma/\langle I\rangle = 0.08$ in Nd:LaPP.

To explain the low degree of coherence of random laser emission, it has been hypothesized [13] that (a) grains of powder emit collectively with a distributed feedback provided by multiple scattering, and (b) emission within the lasing volume is uncorrelated owing to multiple scattering. Correspondingly, the low contrast of a speckle pattern of random laser emission can be due to an effective averaging over $N = t_{\text{pulse}}/t_c$ high-contrast speckle patterns changing one another during the pulse (or train of pulses) of laserlike emission [13]. Here t_{pulse} is the duration of the random laser pulse and t_c is the emission coherence time.

This interpretation is in line with that of Letokhov [6], who has proposed that a "stochastic resonator" in the form of a scattering medium constitutes a system with a large number of modes (waves of different directions), which are strongly coupled by scattering and have large radiation losses. If the number N of interacting modes is sufficiently large, the feedback becomes nonresonant. Accordingly the emission

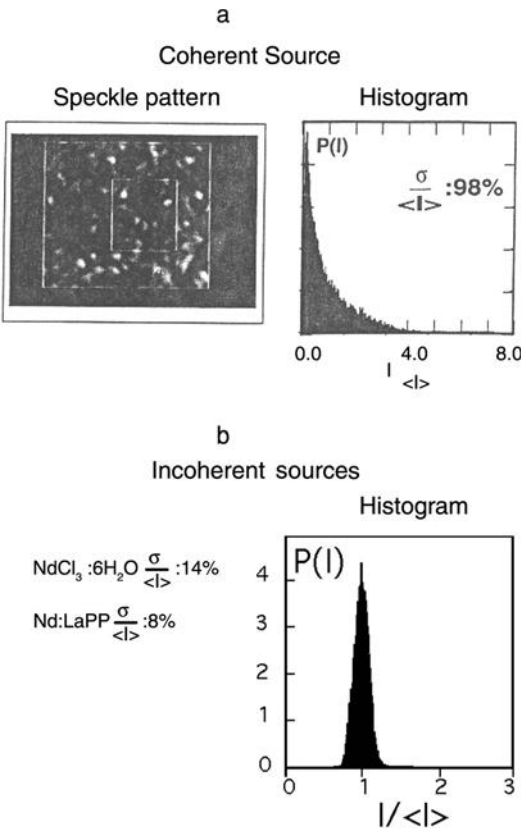

FIGURE 2.16. (a) Speckle pattern of 1.06 μm light of the pumping laser scattered in the powder (left) and the corresponding intensity distribution histogram (right); (b) intensity distribution histogram of the speckle pattern of the $NdCl_3{:}6H_2O$ random laser emission. (After [13].)

of such a "supermultimode" laser with frequent photon exchange between modes has low coherence.

In References [29–31], similar studies of the contrast of a speckle pattern were done in $NdAl_3(BO_3)_4$ and NdP_5O_{14} powder lasers. In the majority of powder samples studied, the degree of coherence $\sigma/\langle I\rangle$ was between 10 and 20%, in agreement with the results of Reference [13]. However, in some NdP_5O_{14} samples the degree of coherence was as large as 40 or 50%. About the same high degree of coherence was found in the emission of a pulsed dye laser that was used to pump the random laser [30]. The example of a high-coherence intensity distribution histogram in a neodymium random laser is shown in Figure 2.17. Evidently, the shape of this distribution is much closer to that in Figure 2.16a than that in Figure 2.16b.

Another finding of Reference [29] was that the degree of coherence of random laser emission decreased with the increase of the pumping power. Following [6],

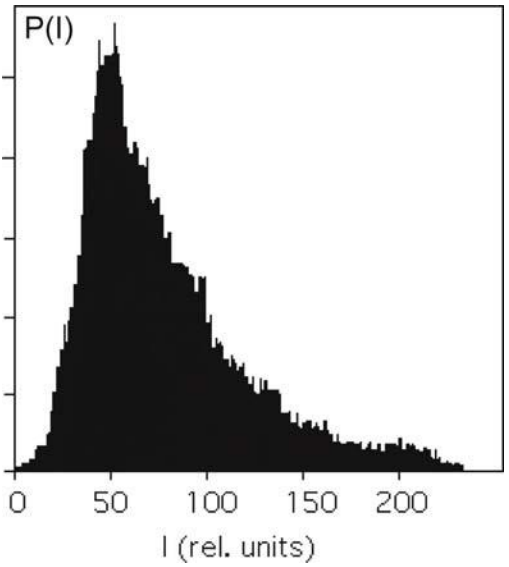

FIGURE 2.17. Distribution histogram of light intensity in the speckle pattern of NdP_5O_{14} random laser with high degree of coherence. (After [29].)

this result can be interpreted as the increase of the number of mixed strongly coupled modes above the threshold with the increase of the pumping power. (Note that the coherence of ZnO random laser emission [52] increased with the increase of the pumping energy above the threshold; see Section 7.5.)

The authors of References [29–31] did not believe that the feedback in their random lasers was due to the diffuse scattering, because the number of powder particles, which could fit the size of the bright spot of stimulated emission (see Section 2.6), was not large enough. Instead, they explained the experimental results in terms of coupled intraparticle resonators [27]. Another argument against the diffusion model was a relatively high degree of coherence observed in some of the samples.

2.7.3 Interferometric Studies of Transversal Coherence

The transversal coherence of emission of a $Nd_{0.5}La_{0.5}Al_3(BO_3)_4$ ceramic random laser was studied in [18] using a Young interferometer. Experimentally, the magnified real image of a random laser surface was projected to the slit plane of the Young interferometer and the fringe pattern was examined in the far field using a CCD camera or a scanning low-aperture Si detector (Figure 2.18). The fringe pattern at 0.53 μm (scattered light of frequency-doubled Nd:YAG laser), used as a reference, was compared to that at 1.06 μm (random laser emission). Experimentally, the distance between the two local areas on the sample surface, which were imaged onto the two slits, was equal to ≈86 μm (measured between

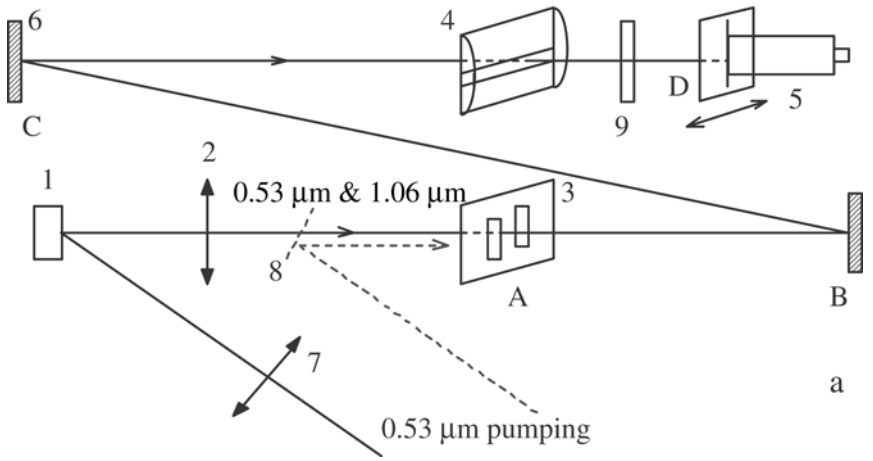

FIGURE 2.18. Setup for transversal coherence measurements: (1) $Nd_{0.5}La_{0.5}Al_3(BO_3)_4$ ceramic sample; (2) imaging lens; (3) opaque screen with slits; (4) cylindrical lens with masking screens that was used in some measurements; (5) scanning small-aperture Si detector or a CCD camera; (6) steering mirrors; (7) pumping focusing lens; (8) mirror was used to illuminate the slits with direct 532 nm laser beam; (9) long-path color filter. (*Source*: Ref. [18].)

the centers). The resolution of the imaging system was better than 40 μm, so the two images were well resolved.

When mirror (8) was introduced to the scheme and the slits were illuminated with 532 nm light of the frequency-doubled Nd:YAG laser, the profile of the fringe pattern, as expected, was described by the product $\{\cos^2[\pi ya/(\lambda d)]\}\{\mathrm{sinc}^2[\pi yb/(\lambda d)]\}$, where a was the distance between the centers of the slits, b was the slit width, d was the distance between the slit plane and the observation screen, λ was the wavelength, and y was the coordinate in the horizontal direction in the observation plane [50].

When mirror (8) was removed and the pumped spot on the ceramic surface was imaged to the slits ($\lambda = 532$ nm), the phase distribution in the slit plane was randomly scrambled due to scattering. As a result, although the periodical fringe pattern still had an expected period $\lambda d/a$, its envelope was not shaped by $\mathrm{sinc}^2[\pi yb/(\lambda d)]$ (Figure 2.19a). On the contrary, the fringe pattern was widely spread, arbitrarily modulated, and had low peak intensity. In addition, the sets ("layers") of fringes at different heights were shifted relative to each other. (One such layer is marked in Figure 2.19b with a dashed box).

To simulate this type of light distribution, each slit was divided into 51 sections and cross interference between all 102 subareas was calculated. To account for scattering, a random initial phase angle ϕ_0 was attributed to each of 102 components. When all phase shifts ϕ_0 were set equal to zero, the expected distribution $\{\cos^2[\pi ya/(\lambda d)]\}\{\mathrm{sinc}^2[\pi yb/(\lambda d)]\}$ was obtained (Figure 2.20a). However, when the nonzero random phase shifts (caused by scattering) were

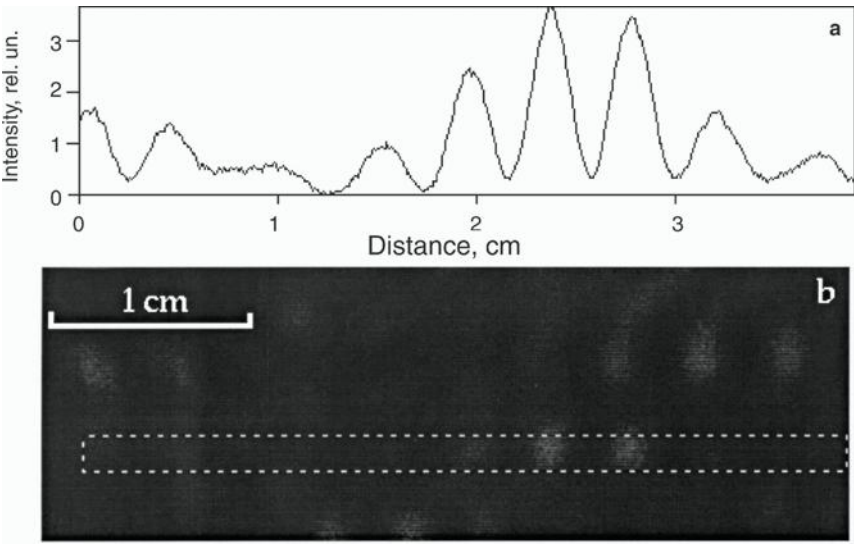

FIGURE 2.19. (a) Light intensity distribution and (b) corresponding fringe pattern recorded in the detector plane when the slits were illuminated with scattered 0.53 μm light imaged from the sample surface. The profile in (a) corresponds to the dashed box in (b). (*Source*: Ref. [18].)

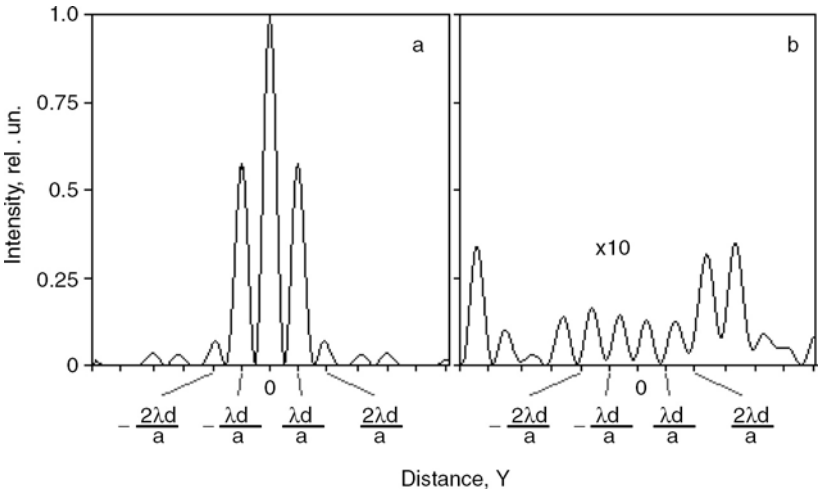

FIGURE 2.20. Calculated fringe pattern in the cases of (a) coherent and (b) "coherence scrambled" illumination of the slits. (The amplitude of light intensity distribution in (b) is magnified 10 times). (*Source*: Ref. [18].)

accounted for, the calculated distribution of light intensity was similar to the experimental one: the fringe pattern had a period $\lambda d/a$, it was widely spread, and randomly modulated (Figure 2.20b). Obviously, the scattering "scramble" was different at different vertical positions on the observation screen. This explains numerous phase shifts between different fringe layers observed experimentally (Figure 2.19b).

Because the CCD camera in Reference [18] was not sensitive in the infrared, a low-aperture Si detector (equipped with a horizontally oriented cylindrical lens to improve the efficiency of the light collection) was used to record the intensity distribution at both random laser wavelength 1.06 μm, and pumping wavelength 0.53 μm (Figure 2.18). The fringe pattern produced by scattered pumping light, recorded with the help of a Si detector, is shown in Figure 2.21a. Only a 4 mm-wide horizontal slit in the center of the cylindrical lens was open for light. However, this width already corresponded to more than two high-contrast fringe layers observed in the lens plane, reducing the contract of the interference pattern. Without doubt, the characteristic "scrambled" interference pattern, similar to that in Figure 2.19a, is seen in Figure 2.21a.

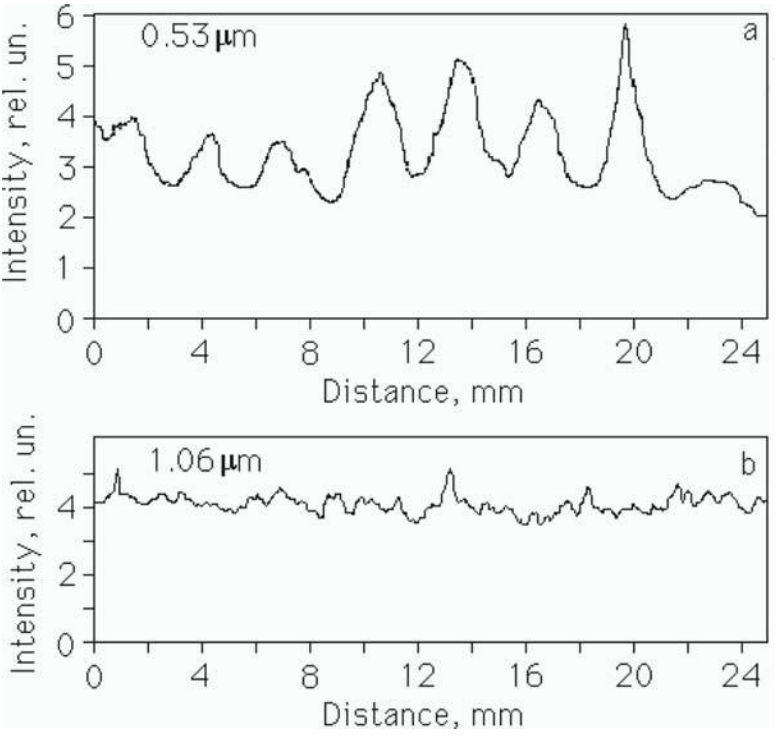

FIGURE 2.21. Far-field light intensity distribution recorded with the help of fast Si detector (and cylindrical lens) when the pumped spot was imaged to the slits: (a) $\lambda = 532$ nm; (b) $\lambda = 1.06$ μm. (*Source*: Ref. [18].)

In the next measurement, the same scan was repeated with the long-pass color filter placed in front of the detector. (The filter transmitted 1.06 μm random laser emission and cut off 0.53 μm pumping.) No interference fringes comparable to or exceeding the noise level could be seen in the intensity distribution pattern at 1.06 μm (Figure 2.21b). The recordings at 0.53 and 1.06 μm were repeated several times. The result was perfectly reproducible: the fringes were clearly seen at 0.53 μm and not at 1.06 μm. Similar results were also obtained when the distance between the two spots on the emitting surface, which were imaged onto the two slits, was larger than 86 μm.

The preceding experimental result can, in principle, have alternative explanations.

1. Coherent random laser emission occurs in small uncorrelated volumes (like bright spots in near-field emission pattern [29,53]) and the size of those volumes is smaller than 86 μm. However, localized bright spots of stimulated emission were never observed in $Nd_{0.5}La_{0.5}Al_3(BO_3)_4$ ceramic.

2. The spatial transversal coherence is diminished due to the existence of a very large number of strongly coupled modes in the stochastic resonator of a random laser [6]. Because of the exchange between modes, many uncorrelated coherent field distributions change each other in time, smearing out any speckle or interference fringe pattern. This explanation, similar to the one given in Reference [13], appears to be more plausible.

As proposed in [13], low-coherence laser sources can be advantageous in holography, laser inertial confinement fusion, transport of energy in fibers for medical applications, etc., where the coherent properties of conventional lasers present a severe drawback by degrading the luminescence uniformity. Beam-smoothing techniques used in laser fusion are based on incoherent superposition of uncorrelated speckle patterns [54,55]. Such superposition is naturally generated in neodymium random lasers with incoherent (nonresonant) feedback.

2.8 Dependence of the Stimulated Emission Threshold on the Diameter of the Pumped Spot

The dependence of the random laser threshold E_{th} on the diameter of the pumped spot d was studied in highly scattering sintered $Nd_{0.5}La_{0.5}Al_3(BO_3)_4$ ceramic in References [16,35,56]. The SEM image of the ceramic surface is shown in Figure 2.22. The coherent backscattering technique [57,58] was used to characterize the transport mean free path l_t in the sample. (The experimentally measured CBS cone is shown in the inset of Figure 2.22.) Calculated from the angular width W of the backscattering cone as $l_t \approx 0.7\lambda/2\pi W$ [24–26], l_t was estimated to be approximately equal to 4.5 μm. This value was much smaller than the thickness of the sample $L \sim 1$ cm and the smallest diameter of the pumped spot d (∼60 μm) used in the experiments.

Two different experimental setups were used in the studies of relatively large pumped volumes and small pumped volumes. In the first setup [35], the lens

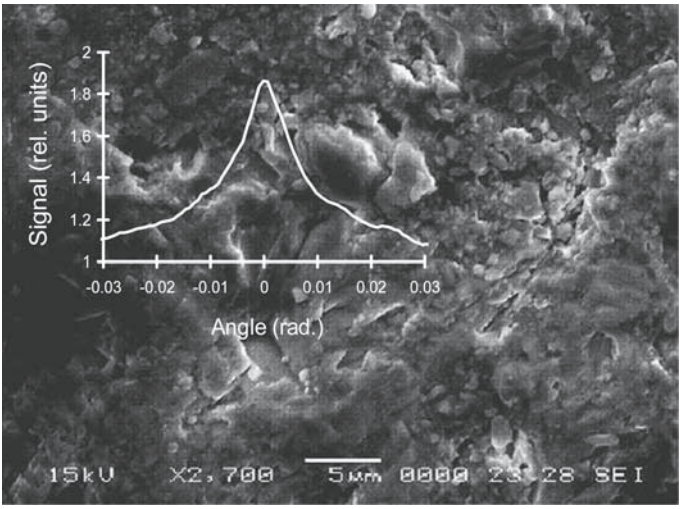

FIGURE 2.22. Scanning electron microscope image of the surface of the $Nd_{0.5}La_{0.5}Al_3(BO_3)_4$ ceramic sample. Inset: CBS cones measured at $\lambda = 514.5$ nm. (*Source*: Ref. [56].)

focusing the pumping beam (focal distance $f = 1$ m) was installed on the optical rail in front of the sample. By moving the lens along the beam, it was possible to vary the pumped spot diameter (measured at the level $1/e^2$) between 0.4 and 5 mm. A fast Si photodetector covered with an IR long-pass filter and positioned approximately 20 cm from the sample was used to detect random laser emission. In order to average the signal better over different local spots on the sample, the piece of ceramic, mounted on a motorized stage, was slowly rotated during the data collection. The diameter of the pumped spot d was measured with the help of a CCD camera placed in the position of the sample.

In the second setup, the lens with a shorter focal length ($f \approx 9$ cm) allowed one to vary beam spot diameters between $\sim$60 µm and $\sim$350 µm. The sample in this case was mounted in the object plane of an optical microscope equipped with a visible/IR CCD camera (Figure 2.23, see Color Plate 1). Depending on the spectral filter installed in the microscope, the CCD camera could monitor the near-field distribution of scattered pumping light ($\lambda = 0.53$ µm) or emitted light ($\lambda = 1.06$ µm) on the surface of the sample. A fraction of emitted and/or scattered light was collected with a bundle of optical fibers and delivered to a monochromator with a photomultiplier tube (PMT) attached to its exit slit. This setup allowed one to study simultaneously the spectral dynamics of emission and its near-field distribution.

At relatively large diameters of the pumped spot, $d \geq 130$ µm, the emission behavior was typical of a majority of known neodymium random lasers (see Section 2.2). No pronounced localized bright spots were found in the near-field

intensity pattern below or above the threshold. This was in contrast to References [29–31,53,59] where sharp bright spots were observed in the near-field emission of $NdAl_3(BO_3)_4$ and ZnO random lasers. The threshold pumping energy was measured at the first appearance of a short (nanosecond-scale) pulse of stimulated emission.

The experimentally measured threshold energy E_{th} and threshold energy density E_{th}/S are plotted versus the size of the pumped spot in Figures 2.24a and 2.24b. As follows from these figures, at $d > 130$–$150\,\mu m$, the threshold energy increases almost linearly with the increase of the diameter of the pumped spot. The experimental dependence $E_{th}(r)/S$ can be fitted with the formula [35]

$$\frac{E_{th}}{S}\left[\frac{mJ}{cm^2}\right] = C_1\left[\frac{1}{r[cm]} + C_2\right], \tag{2.2}$$

where $r = d/2$ is the radius of the pumped spot, $C_1 = 17.3$, and $C_2 = 2.02$. The nature of this functional dependence is discussed in Chapter 4.

The threshold pumping energy increased remarkably at small diameters of the pumped spot d ($\leq 110\,\mu m$) (Figure 2.24a). At the further reduction of d ($\leq 90\,\mu m$), a sharp bright spot appeared in the near-field emission pattern. The spectroscopic studies demonstrated that this bright spot was not related to neodymium emission and possibly was due to laser-induced plasma or continuum wave generation.

2.9 Dependence of the Stimulated Emission on the Powder Volume Density

The influence of the volume density of scattering material on the operation of random lasers has been studied in Reference [33]. The experimental samples in

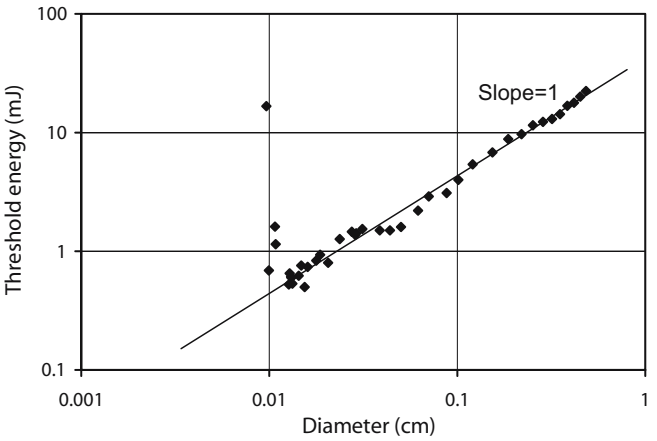

FIGURE 2.24a. Threshold pumping energy E_{th} in $Nd_{0.5}La_{0.5}Al_3(BO_3)_4$ ceramic as a function of the diameter of the pumped spot d. (After [16].)

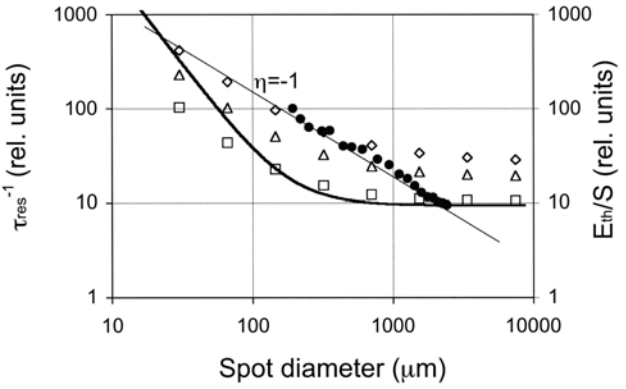

FIGURE 2.24b. Circles: experimental values E_{th}/S versus d in $Nd_{0.5}La_{0.5}Al_3(BO_3)_4$ ceramic; squares, triangles, and diamonds: Monte Carlo simulation of the dependence $(\tau_{res}^{p})^{-1}$ versus d calculated for different values of the scattering length (sizes of the cubic cell s); squares: $s = 1\,\mu$m, triangles: $s = 3\,\mu$m, and diamonds: $s = 9\,\mu$m. Solid curve: dependence calculated according to the Letokhov formula $g_{th} \propto 1/d^2 + const$ [6]. (*Source*: Ref. [56].)

that particular experiment were $Nd_{0.5}La_{0.5}Al_3(BO_3)_4$ powders of different volume density loaded in flat 1 mm thick optical cuvettes and a piece of scattering ceramic of the same material. All powder samples had the same mean particle size, $\approx 4\,\mu$m.

In the first particular experiment, the intensity of the 532 nm pumping light scattered off different samples studied has been measured. The scattered light was detected in a small solid angle, the same for all samples, which did not coincide with either the direction of exact backscattering or the direction of specular reflection off the cuvette wall. It was assumed that the angular distribution of scattered light, $\propto \cos(\Theta)$ (Figure 2.6), was the same for all samples studied. The forward scattering (transmission) in all samples was very small, $\ll 1\%$. Thus, the reflection signal was proportional to the amount of energy that was not absorbed by the material. The results of the reflection measurements are summarized in Table 2.4. All reflection intensities in Table 2.4 are normalized

TABLE 2.4. Volume density[a] and reflection[b] from different $Nd_{0.5}L_{a0.5}Al_3(BO_3)_4$ samples at 532 nm

Sample	Low Density Powder	Medium Density Powder	High Density Powder	Ceramic
Volume density	0.48	0.54	0.59	0.63
Reflection	0.66	0.52	0.53	0.40

[a]Ratio of powder or ceramic density to that of single crystal.
[b]Reflection normalized to that from Al_2O_3 powder [33].

to that of Al_2O_3 powder, the scattering material without absorption. As follows from Table 2.4, high-density samples absorb (utilize) more pumping energy than low-density samples.

The input–output curves of stimulated emission in $Nd_{0.5}La_{0.5}Al_3(BO_3)_4$ samples of different volume density are shown in Figure 2.25a. The same curves recalculated in terms of absorbed pumping energy are depicted in Figure 2.25b. In conventional lasers, a set of input–output curves characterized by similar slopes and

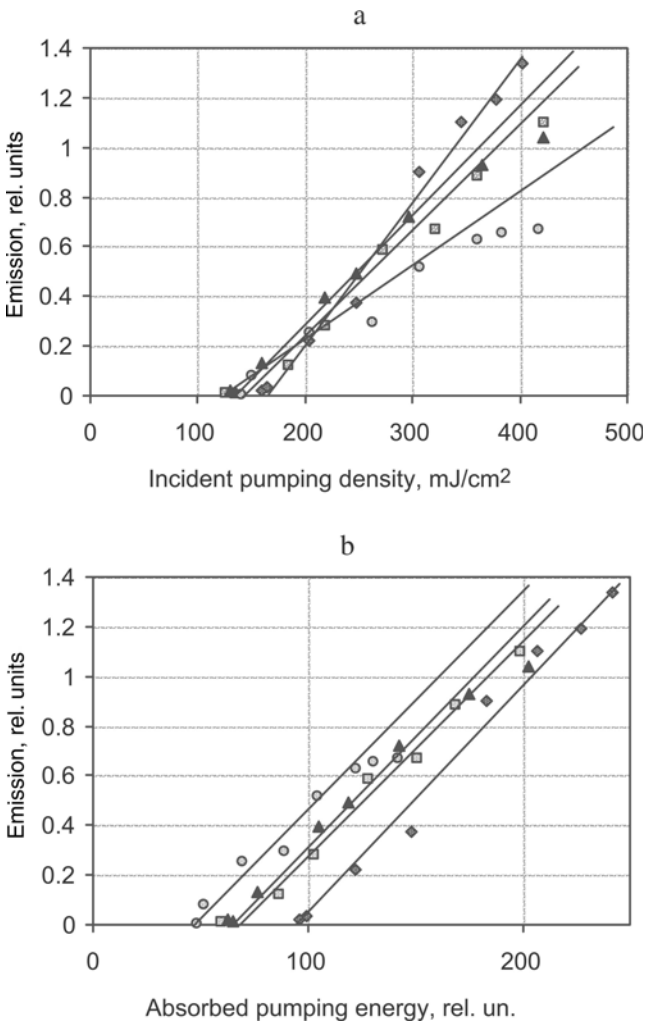

FIGURE 2.25. Stimulated emission intensity plotted as a function of (a) incident pumping energy and (b) absorbed pumping energy in $Nd_{0.5}La_{0.5}Al_3(BO_3)_4$ sample of volume density equal to 0.48 (circles), 0.54 (triangles), 0.59 (squares), and 0.63 (diamonds). (*Source*: Ref. [33].)

different thresholds, like that in Figure 2.25b, is typical for a series of measurements done with different output couplers, when the intracavity loss is negligibly small. The analogy with conventional lasers implies that the effective output coupling is higher (and the cavity Q-factor is lower) in high-density samples than in low-density samples. The theoretical model describing this experiment is presented in Chapter 4.

2.10 Dependence of the Stimulated Emission on the Powder Particle Size

The fact that the stimulated emission in random lasers depends on the powder density (see Section 2.9) suggests that it should also depend on the average size of the particles. The effect of the granule size on the properties of the $NdSc_3(BO_3)_4$ random (powder) laser was studied in Reference [48].

In the course of experiments, 13 powder samples of $NdSc_3(BO_3)_4$ were prepared by grinding (with mortar and pestle) single crystals. Samples were ground for different periods ranging between 1 and 50 min, which resulted in powders of different mean particle size. The finer powders were further suspended in acetone. Relatively large particles precipitated first and smaller ones stayed suspended for a longer time. This helped one to separate powders of different size and to fabricate samples with a mean particle size below 0.5 μm. Images of all powder samples, one of which is shown in Figure 2.7a, were acquired by a scanning electron microscope. As one can see from this figure, all the particles had irregular shapes. This was true for particles of all sizes. The sizes of the particles in each SEM image were measured and presented in the form of the histogram (Figure 2.7b). At the same time, the mean particle size was calculated.

The powder samples were placed in glass cylinders, each several millimeters long with inner diameter 1 mm and outer diameter 1.5 mm, and excited at 532 nm with a Q-switched, frequency-doubled Nd:YAG laser (pulse duration, 10 ns; repetition rate, 10 Hz). The diameter of the pumped spot, measured by a knife-edge technique, was varied in different experiments between ≈0.3 mm and ≈0.7 mm [48].

First, the luminescence kinetics were recorded in $NdSc_3(BO_3)_4$ powder samples at weak excitation. In the powder composed of large particles (190 μm—nearly bulk crystallines), a slightly nonexponential decay of luminescence was determined by the combination of spontaneous emission, multiphoton decay, and cross-relaxation [48]. With a decrease in particle size below 1 μm, the emission kinetic shortened. The characteristic decay times measured (i) at the initial stage of the decay kinetic, and (ii) when the luminescence intensity dropped below the level $1/e$ are plotted versus mean particle size in Figure 2.26. The shortening of the emission kinetics in smaller particles can possibly be explained by luminescence quenching on surface-related defects, or change of the phonon spectrum, or may be due to the increased rate of energy transfer cross-relaxation associated with the change of the phonon spectrum [60–62]. The shortening of the decay time with

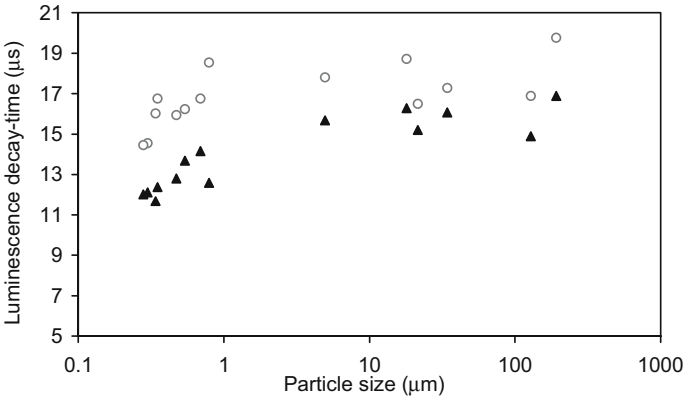

FIGURE 2.26. Luminescence decay times in $NdSc_3(BO_3)_4$ powder as a function of particle size. Triangles: measurements done at the initial stage of the decay kinetics; circles: measurements done when the luminescence signal has dropped to the level $1/e$. (*Source:* Ref. [48].)

reduction in particle size in the microsecond range was not larger than ≈25%. This could not seriously affect stimulated emission in the random laser, which develops at a nanosecond scale.

Different powder samples had different reflection coefficients at the pumping wavelength and, accordingly, absorbed different fractions of incident pumping energy. It was assumed that the amount of pumping energy absorbed by a sample was proportional to the intensity of neodymium spontaneous emission excited by short, 532 nm laser pulses. Absorption efficiency determined in this way is plotted against mean particle size in Figure 2.27.

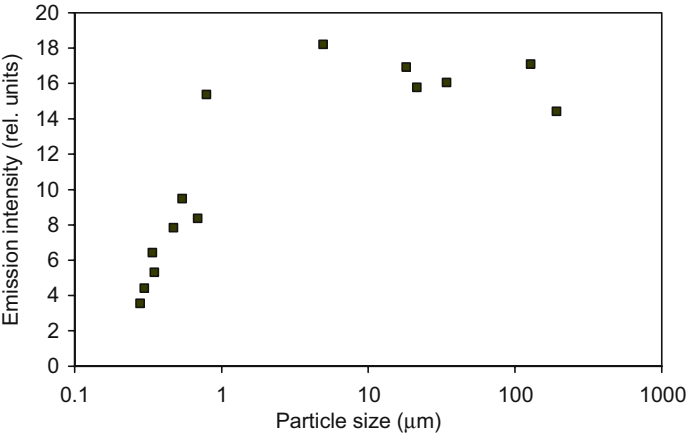

FIGURE 2.27. Emission intensity as a function of the particle size, measured at weak pumping. (*Source:* Ref. [48].)

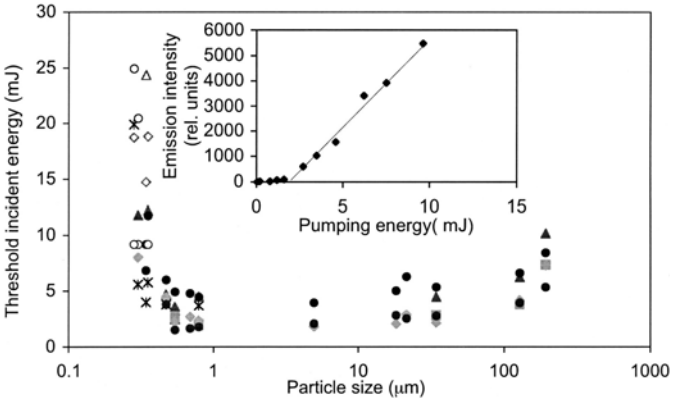

FIGURE 2.28. Threshold of stimulated emission in $NdSc_3(BO_3)_4$ random laser as a function of the particle size. Different characters correspond to measurements done at different pumped spot diameters. Open characters indicate the measurements where the threshold could not be reached at the maximum applied pumping energy. The vertical axis corresponds to incident pumping energy. Inset: typical input–output curve. (*Source*: Ref. [48].)

The input–output curves of stimulated emission were recorded in all 13 samples studied. The value of the random laser threshold was determined at the intersection of the slope line and the horizontal axis, as shown in the inset of Figure 2.28. The results of the incident energy threshold measurement in different powder samples are summarized in Figure 2.28. The values of the absorbed threshold

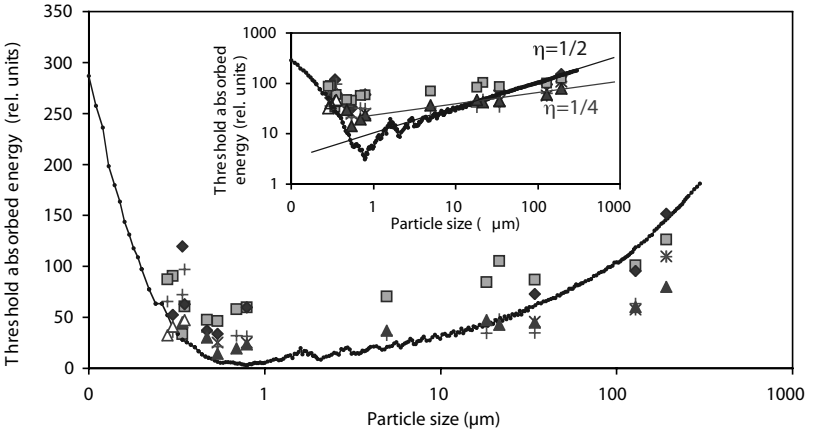

FIGURE 2.29. Threshold absorbed energy as a function of the particle size in $NdSc_3(BO_3)_4$ powder. Different characters correspond to measurements done at different pumped-spot diameters. Connected dots represent theoretical curve P_{th}/S calculated in diffusion approximation by using Eq. (4.26b). Inset: same data plotted in log–log scale. (The experimental data in Figure 2.29 correspond to those in Figure 2.28). (*Source*: Ref. [48].)

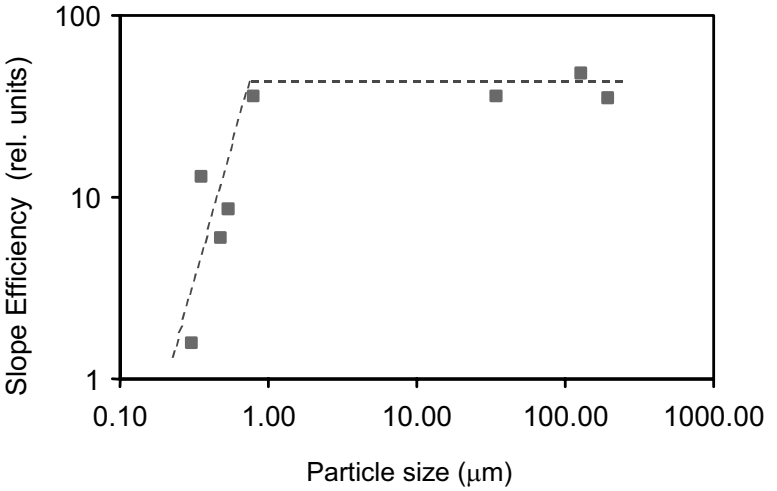

FIGURE 2.30. Slope efficiency of stimulated emission in $NdSc_3(BO_3)_4$ random laser (normalized to absorbed pumping energy) as the function of the particle size. (*Source*: Ref. [48].)

energies are plotted versus s in Figure 2.29. It is evident from this figure that in the $NdSc_3(BO_3)_4$ random laser, the threshold pumping density is nearly independent of particle size s in a wide range of values of s, $1\,\mu m < s < 50\,\mu m$. However, at $s < 1\,\mu m \approx \lambda_{em}$ and $s > 50\,\mu m$, the value of the threshold density increases dramatically. A qualitatively similar result was observed in neodymium random lasers in Reference [12].

The slope efficiency in the $NdSc_3(BO_3)_4$ random laser (defined as dE_{out}/dE_{input} above the threshold and normalized to the absorption efficiency) is plotted versus s in Figure 2.30. By comparing the data in Figures 2.28 through 2.30, one can see that at $s < 1\,\mu m$, the increase in the threshold pumping energy corresponds to the strong reduction of the slope efficiency of stimulated emission.

Note that the dependence of the threshold E_{th} on the particle size d in ZnO random lasers has been studied experimentally and theoretically in Reference [63]. (For the detailed discussion of ZnO random lasers read Chapter 7.) The dependence E_{th} *vs* d in Reference [62], measured when the particle size diameters varied from less than 100 nm to more than 600 nm, qualitatively resembles the reduction of the threshold with the increase of the particle size in the corresponding part of Figure 2.28.

The experimental results of this section are discussed in detail in Chapter 4.

References

1. V.M. Markushev, V.F. Zolin, and Ch.M. Briskina, Luminescence and stimulated emission of neodymium in sodium lanthanum molybdate powders, *Sov. J. Quantum Electron.*, **16**: 281–283 (1986).

2. V.M. Markushev, V.F. Zolin, and Ch.M. Briskina, Poroshkovyi Lazer (Powder Laser) *Zhurnal Prikladnoy Spektroskopii*, **45**: 847–850 (1986) Russian.
3. V.F. Zolin, private communication.
4. V.F. Zolin, The nature of plaser-powdered laser, *J. Alloys Compounds*, **300–301**: 214–217 (2000).
5. V.S. Letokhov, Stimulated emission of an ensemble of scattering particles with negative absorption [*ZhETF Pis'ma*, **5**: 262–265 Russian] *JETP Lett.*, **5**: 212–215 (1967).
6. V.S. Letokhov, Generation of light by a scattering medium with negative resonance absorption [*Zh. Exp. and Teor. Fiz.*, **53**: 1442–14452 Russian] *Sov. Phys. JETP*, **26**: 835–840 (1968).
7. V.S. Letokhov, Stimulated radio emission of the interstellar medium [*Pis'ma Zh. Eksp. i Teor. Fiz.*, **4**: 477–481 (1966) Russian] *JETP Lett.*, **4**: 321–323 (1966).
8. N.N. Lavrinovich and V.S. Letokhov, The possibility of the laser effect in stellar atmospheres [*Zh. Eksp. i Teor. Fiz.*, **67**: 1609–1620 (1974) Russian] *Sov. Phys. JETP*, **40**: 800–805 (1975).
9. V.S. Letokhov, Noncoherent feedback in space masers and stellar lasers. In *Amazing Light, A Volume Dedicated to Charles Hard Townes on His 80*th *Birthday*, R.Y. Chiao, ed., Springer-Verlag: New York (1996), p. 409.
10. V.M. Markushev, N.È. Ter-Gabriélyan, Ch.M. Briskina, V.R. Belan, and V.F. Zolin, Stimulated emission kinetics of neodymium powder lasers, *Sov. J. Quantum Electron.*, **20**: 772–777 (1990).
11. N.È. Ter-Gabriélyan, V.M. Markushev, V.R. Belan, Ch.M. Briskina, and V.F. Zolin, Stimulated emission spectra of powders of double sodium and lanthanum tetramolybdate, *Sov. J. Quantum Electron.*, **21**: 32–33 (1991).
12. N.È. Ter-Gabriélyan, V.M. Markushev, V.R. Belan, Ch.M. Briskina, O.V. Dimitrova, V.F. Zolin, and A.V. Lavrov, Stimulated radiation emitted by lithium neodymium tertaphosphate $LiNd(PO_3)_4$ and neodymium pentaphosphate NdP_5O_{14} powders, *Sov. J. Quantum Electron.*, **21**: 840–841 (1991).
13. C. Gouedard, D. Husson, C. Sauteret, F. Auzel, and A. Migus, Generation of spatially incoherent short pulses in laser-pumped neodymium stoichiometic crystals and powders, *J. Opt. Soc. Am. B*, **10**: 2358–2363 (1993).
14. M.A. Noginov, N.E. Noginova, H.J. Caulfield, P. Venkateswarlu, T. Thompson, M. Mahdi, and V. Ostroumov, Short-pulsed stimulated emission in the powders of $NdAl_3(BO_3)_4$, $NdSc_3(BO_3)_4$, and $Nd:Sr_5(PO_4)_3F$ laser crystals, *J. Opt. Soc. Am. B*, **13**: 2024–2033 (1996). M.A. Noginov, N.E. Noginova, H.J. Caulfield, P. Venkateswarlu, T. Thompson, M. Mahdi, and V. Ostroumov, Stimulated emission without cavity in powders and single crystals of Nd doped materials. In *OSA Trends in Optics and Photonics on Advanced Solid State Lasers*, Vol. 1, S.A. Payne and C.R. Pollock, eds. Optical Society of America: Washington, DC (1996), pp. 585–590.
15. R.C. Powell, *Physics of Solid-State Laser Materials*, Springer-Verlag: New York (1998).
16. M. Bahoura, N. Noginova, K.J. Morris, G. Zhu, S. Williams, J. Novak, I. Fowlkes, A. Frantz, and M.A. Noginov, Threshold conditions for a random laser mode. In *Proceedings of SPIE Laser Crystals, Glasses, and Nonlinear Materials Growth and Characterization*, Vol. 4970, Y.Y. Kalisky, ed. SPIE: Bellingham, WA, pp. 118–127.
17. A.A. Kaminskii, Cystalline Lasers: Physical Processes and Operating Schemes, CRC Press: Boca Raton, FL (1996).
18. M.A. Noginov, S.U. Egarievwe, N. Noginova, H.J. Caulfield, and J.C. Wang, Interferometric studies in a powder laser, *Opt. Mater.*, **12**: 127–134 (1999).

19. M.A. Noginov, N.E. Noginova, S.U. Egarievwe, H.J. Caulfield, P. Venkateswarlu, A. Williams, and S.B. Mirov, Color-center powder laser: The effect of pulverization on color-center characteristics, *J. Opt. Soc. Am. B*, **14**: 2153–2160 (1997).
20. H. Cao, Y.G. Zhao, H.C. Ong, S.T. Ho, J.Y. Dai, J.Y. Wu, and R.P.H. Chang, Ultraviolet lasing in resonators formed by scattering in semiconducor polycrystalline films, *Appl. Phys. Lett.*, **73**: 3656–3658 (1998).
21. H. Cao, J.Y. Xu, Y. Ling, S.-H. Chang, S.T. Ho, E.W. Seelig, X. Liu, and R.P.H. Chang, Random lasers with coherent feedback, *Photonic Crystals and Light Localization in the 21st Century*, C.M. Soukoulis, ed., NATO Science Series, Series C: Mathematical and Physical Sciences, Vol. 563, Kluwer Academic: Boston (2001).
22. H. Cao, Random lasers with coherent feedback. In *Optical Properties of Nanostructured Random Media*, V. M. Shalaev, ed., *Topics in Applied Physics*, Vol. 82, Springer-Verlag, New York (2002).
23. M. Shukri and R.L. Armstrong, Coherent, directional, laserlike emission from random gain media, *Appl. Opt.*, **39**: 4300–4305 (2000).
24. M.B. van der Mark, M.P. van Albada, and A. Lagendijk, Light scattering in strongly scattering media: Multiple scattering and weak localization, *Phys. Rev. B*, **37**: 3575–3592 (1988).
25. E. Akkermans, P.E. Wolf, and R. Maynard, Coherent backscattering of light by disordered media: Analysis of the peak line shape, *Phys. Rev. Lett.*, **56**: 1471–1474 (1986).
26. E. Akkermans, P.E. Wolf, R. Maynard, and G. Maret, Theoretical study of the coherent backscattering of light by disordered media, *J. Phys. France*, **49**: 77–98 (1988).
27. Ch.M. Briskina, V.M. Markushev, and N.È. Ter-Gabriélyan, Use of a model of coupled microcavities in the interpretation of experiments on powder lasers, *Quantum Electron.*, **26**: 923–927 (1996).
28. S.N. Vetkina, V.P. Sirotkin, V.M. Markushev, and N.È. Ter-Gabriélyan, Powder lasers based on lanthanum niobate and lanthanum tantalate, *Izvestiya Akademii Nauk SSSR, Seriya Fizicheskaya*, **56**: 86–89 (1992) Russian.
29. A.A. Lichmanov, Ch.M. Briskina, V.M. Markushev, V.N. Lichmanova, and N.P. Soshchin, Degree of coherence and dimensions of the generation region of powder lasers, *J. Appl. Spectroscopy*, **65**: 818–825 (1998).
30. A.A. Lichmanov, Ch.M. Briskina, N.P. Soshchin, and V.F. Zolin, Lasing in powders and its use for data processing, *Bull. Russian Acad. Sci. Phys. (Izvestiya Rossiiskoi Akademii Nauk. Seriya Fizicheskaya)*, **63**: 922–926 (1999).
31. A.A. Lichmanov, Ch.M. Brickina, V.N. Lichmanova, N.P. Soshchin, and V.F. Zolin, Experimental studies of the lanthanide doped lasing powders (plasers). In *Proceedings of the International Conference LASERS'98* (Tucson, AZ, December 7–11, 1998), pp. 725–731 (1999).
32. F. Auzel and P. Goldner, Coherent light sources with powder: Stimulated amplification versus super-radiance, *J. Alloys Compounds*, **300–301**: 11–17 (2000).
33. M.A. Noginov, N. Noginova, S.U. Egarievwe, H.J. Caulfield, C. Cochrane, J.C. Wang, M.R. Kokta, and J. Paitz, Study of the pumping regimes in Ti-sapphire and $Nd_{0.5}La_{0.5}Al_3(BO_3)_4$ powders, *Opt. Mater.*, **10**: 297–303 (1998).
34. M.A. Noginov, N. Noginova, S.U. Egarievwe, J.C. Wang, and H.J. Caulfield, New advances in solid-state powder lasers: The effects of external seeding and external mirror. In *ICONO'98: Nonlinear Optical Phenomena and Coherent Optics in information Technologies*, S.S. Chesnokov, V.P. Kandidov, and N.I. Koroteev, eds. *Proceedings of SPIE* **3733**: (1999).

35. M. Bahoura, K.J. Morris, and M.A. Noginov, Threshold and slope efficiency of $Nd_{0.5}La_{0.5}Al_3(BO_3)_4$ ceramic random laser: Effect of the pumped spot size, *Opt. Commun.*, **201**: 405–412 (2002).
36. M.A. Noginov, S.U. Egarievwe, N. Noginova, J.C. Wang, and H.J. Caulfield, Demonstration of a second harmonic powder laser, *JOSA B*, **15**: 2854–2860 (1998).
37. S.C. Rand, G. Williams, T. Hinklin, and R.M. Laine, Blue and infrared laser action in strongly scattering Nd:alumina nanopowders. In *Conference on Lasers and Electo-Optics*, OSA Technical Digest, Optical Socity of America: Washington, DC (1999), p. 483.
38. R.M. Laine, T. Hinklin, G. Williams, and S.C. Rand, Low-cost nanopowders for phosphor and laser applications by flame spray pyrolysis, *Materi. Sci. Forum.* **343**: 500–510 (2000).
39. B. Li, G. Williams, S.C. Rand, T. Hinklin, and R.M. Laine, Continuous-wave ultraviolet laser action in strongly scattering Nd-doped alumina, *Opt. Lett.*, **27**: 394–396 (2002).
40. G. Huber, Miniature neodymium lasers. In *Current Topics in Materials Science*, Vol. 4, E. Kaldis, ed., North-Holland: Amsterdam (1980), pp. 1–45.
41. G. Huber and H.G. Danielmeyer, NdP_5O_{14} and $NdAl_3(BO_3)_4$ lasers at 1.3 μm, *Appl. Phys.*, **18**: 77–80 (1979).
42. H.-D. Hattendorf, Dissertation zur Erlangung des Doktorgrades des Fachbereich Physik der Universität Hamburg, Hamburg, 1979.
43. J.-P. Mein, T. Jensen, and G. Huber, Spectroscopic properties and efficient diode-pumped laser operation of neodymium-doped lanthanum scandium borate, *IEEE J. Quant. Electron.*, **30**: 913–917 (1994).
44. V. Ostroumov, T. Jensen, J.-P. Meyn, G. Huber, and M.A. Noginov, Study of luminescence concentration quenching and energy transfer upconversion in Nd-doped $LaSc_3(BO_3)_4$ and $GdVO_4$ laser crystals, *J. Opt. Soc. Am. B*, **15**: 1052–1060 (1998).
45. J.-P. Meyn, Neodym-Lanthan-Scandium-Borat ein neus Material für miniaturisierte Festkörperlaser, Dissertation zur Erlangung des Doktorgrades des Fachbereich Physik der Universität Hamburg, Hamburg, 1994.
46. X.X. Zhang, P. Hong, G.B. Loutts, J. Lefaucheur, M. Bass, and B.H.T. Chai, Efficient laser performance of Nd^{3+}:$Sr_5(PO_4)_3F$ at 1.059 and 1.328 mm, *Appl. Phys. Lett.*, **64**: 3205–3207 (1994).
47. X.X. Zhang, M. Bass, and B.H.T. Chai, Flashlamp pumped neodymium doped strontium flurapatite lasers. In *OSA Proceedings on Advanced Solid State Lasers*, Vol. 24, B.H.T. Chai and S.A. Payne, eds., Optical Society of America: Washington, DC (1995), pp. 150–152.
48. M.A. Noginov, G. Zhu, A. Frantz, J. Novak, S. Williams, and I. Fowlkes, Dependence of the $NdSc_3(BO_3)_4$ random laser parameters on the particle size, *JOSA B*, **21**: 191–200 (2004). M.A. Noginov, M. Bahoura, N. Noginova, G. Zhu, K.J. Morris, S. Williams, J. Novak, A. Frantz, and I. Fowlkes, Stimulated emission in scattering and composite dielectric media (random lasers): Effect of particle size, in Proceedings of SPIE Vol. **5218**, Complex mediums IV: Beyond Linear Isotropic Dielectrics, Martin W. McCall and Graeme Dewar, eds. (SPIE, Bellingham, WA, 2003) pp. 124–139.
49. M.A. Noginov, G. Zhu, and I. Fowlkes, Fiber-coupled random laser, *International Quantum Electronics Conference, Paper #IFB14, CD ROM 2004 CLE/IQEC Technical Digest, ISBN# 1-55752-770-9* (2004).
50. M.V. Klein and T.E. Furtak, *OPTICS*, 2d ed., Wiley: New York (1986).
51. J.W. Goodman, *Statistical Optics*, Wiley: New York (2000).

52. H. Cao, Y. Ling, and C.Q. Cao, Photon statistics of random lasers with resonant feedback, *Phys. Rev. Lett.*, **86**: 4524–4527 (2001).
53. H. Cao, J.Y. Xu, E.W. Seeling, and R.P. Chang, Microlaser made of disordered media, *Appl. Phys., Lett.*, **76**, 2997–2999 (2000).
54. R.H. Lehmberg and S.P. Obenschain, Use of spatial incoherence for uniform illumination of random fusion targets, *Opt. Commun.*, **46**: 27–31 (1983).
55. D. Véron, H. Ayral, C. Gouédard, D. Husson, J. Lauriou, O. Martin, B. Meyer, M. Rostaing, and C. Sautert, Optical spatial smoothing of Nd-glass laser beam, *Opt. Commun.*, **65**: 42–46 (1988).
56. M. Bahoura, K.J. Morris, G. Zhu, and M.A. Noginov, Dependence of the neodymium random laser threshold on the diameter of the pumped spot, *IEEE Journal of Quantum Electronics*, **41**: 677–685 (2005).
57. M.P. van Albada and A. Lagendijk, Observation of weak localization of light in random medium, *Phys. Rev. Lett.*, **55**: 2693–2695 (1985).
58. P.E. Wolf and G. Maret, Weak localization and coherent backscattering of photons in disordered media, *Phys. Rev. Lett.* **55**: 2696–2699 (1985).
59. H. Cao, J.Y. Xu, D.Z. Zhang, S.-H. Chan, S.T. Ho, E.W. Seelig, X. Liu, and R.P.H. Chang, Spatial confinement of laser light in active random media, *Phys. Rev. Lett.*, **84**: 5584–5587 (2000).
60. B.M. Tissue, Synthesis and luminescence of lanthanide ions in nanoscale insulating hosts, *Chem. Mater.*, **10**: 2837–2845 (1998).
61. T. Hase, T. Kano, E. Nakazawa, and H. Yamamoto, Phosphor materials for cathode-ray tubes. In *Advances in Electronics and Electron Physics*, Vol. 79, Academic (1990).
62. D. Wolf, J. Wang, S.R. Phillpot, and H. Gleiter, Phonon-induced anomalous specific heat of a nanocrystalline model material by computer simulation, *Phys. Rev. Lett.*, **74**: 4686–4689 (1995).
63. X.H. Wu, A. Yamilov, H. Woh, and H. Cao, Random lasing in closely packed resonant scatterers, *J. Opt. Soc. Am. B*, **21**: 159–167 (2004).

3
Propagation of Light in Neodymium Random Lasers

Scattering of photons in random lasers governs propagation of both pumping light and stimulated emission. Scattering and light propagation in neodymium-doped and some other random laser materials are discussed in this chapter.

3.1 Propagation of Pumping Light

In powders of solid-state optical materials light propagates in a highly irregular manner, both inside and outside the granules. The boundaries of large particles, small particles, as well as small air gaps between particles play the role of scatterers.

In neodymium random lasers, the diameter of the pumped spot typically strongly exceeds the characteristic penetration depth of pumping light. In such geometry, the Kubelka–Munk two-flux model can be successfully used to describe propagation of light in scattering media with absorption [1]. The advantage of the method is that it needs no more than simple algebraic operations and has been found to give reasonably good agreement with experimental data. The drawback of the method is that it requires empirical determination of coefficients and the range of its validity and its theoretical basis are not well established [1].

In this section, the two-flux model is applied to describe the propagation of pumping light in random (powder) laser material. Experimentally, the transmission and reflection of light by $Nd_{0.5}La_{0.5}Al_3(BO_3)_4$ and Ti-sapphire powder samples, placed in cuvettes of different thickness, have been studied at several different wavelengths [2]. An adequate agreement between the theoretical predictions and the experimental results has been demonstrated, and the parameters characterizing light propagation in the examined random laser materials have been determined.

3.1.1 Model

The most general two-flux Kubelka–Munk model [1,3] can be used to describe incident plane wave propagation in a scattering medium. This theory does not require any additional assumptions on the nature of the scatterers, and is based

on the consideration of two diffuse light fluxes F_+ and F_- traveling in opposite (inbound, z, and outbound, $-z$) directions, with the energy exchange between the fluxes due to scattering.

Following Reference [1], the flux intensities in a scattering medium can be described with two coupled differential equations

$$\mathrm{dF}_+/\mathrm{dz} = -(K+S)F_+ + SF_-, \tag{3.1}$$

$$\mathrm{dF}_-/\mathrm{dz} = (K+S)F_- - SF_+, \tag{3.2}$$

where z is the distance from the plane boundary of the scattering medium, and K and S are the coefficients (in cm^{-1}) representing absorption and scattering. According to Reference [1], K is approximately equal to $2k^{\mathrm{plane}}$, where k^{plane} is the absorption coefficient for hypothetical nonscattering propagation of a plane wave in the medium. In the first approximation, k^{plane} can be defined as

$$k^{\mathrm{plane}} = k^{\mathrm{abs}}\rho, \tag{3.3}$$

where k^{abs} is the average over different polarizations' absorption coefficient in a single crystal material and ρ is the volume density of powder (defined as the ratio of the powder density and that of single crystal). Thus,

$$K \approx 2k^{\mathrm{abs}}\rho. \tag{3.4}$$

At $K = 0$[1], the solution to Eqs. (3.1) and (3.2) is given by [1]:

$$F_+(z)/F_0 = C_1 e^{\alpha z} + C_2 e^{-\alpha z}, \tag{3.5}$$

$$F_-(z)/F_0 = C_1 A^{-1} e^{\alpha z} + C_2 A e^{-\alpha z}, \tag{3.6}$$

where F_0 is the incident photon flux, α has a meaning of inverse effective penetration depth and is defined as $\alpha = (K(K+2S))^{1/2}$, A is defined as $A = S/(S+K+\alpha)$, and C_1 and C_2 are the coefficients determined by the boundary conditions. For a powder sample of thickness z_0, coefficients C_1 and C_2 are given by [1],

$$C_1 = (1-R_i)(A-R_2)\exp(-\alpha z_0)/\Delta, \tag{3.7}$$

$$C_2 = -(1-R_i)(A^{-1}-R_2)\exp(\alpha z_0)/\Delta, \tag{3.8}$$

and

$$\begin{aligned}\Delta = {} & (1-R_1A^{-1})(A-R_2)\exp(-\alpha z_0) \\ & -(1-R_1A)(A^{-1}-R_2)\exp(\alpha z_0),\end{aligned} \tag{3.9}$$

where R_i is the reflection coefficient for the incident wave at $z = 0$, R_1 is the reflection coefficient for F_- incident upon the front surface at $z = 0$, and R_2 is the reflection coefficient for F_+ incident upon the back surface at $z = z_0$.

[1] In practice, some nonzero absorption is present in all, even nominally not absorbing, materials.

Following Reference [1], one can define the reflectance at $z = 0$ as

$$R = R_i + (1 - R_1)F_-(0)/F_0 \tag{3.10}$$

and the transmittance at $z = z_0$ as

$$T = (1 - R_2)F_+(z_0)/F_0. \tag{3.11}$$

For a semi-infinite medium ($z_0 \to \infty$), the reflectance at $z = 0$ can be found as

$$R = R_i + (1 - R_1)(1 - R_i)/(1 - R_1 A). \tag{3.12}$$

The transmittance T and reflectance R are the system parameters, which can be measured experimentally. The comparison of the experimentally measured values $T(z)$ and $R(z_0 \to \infty)$ with the theoretically predicted ones allows one to conclude on the model applicability to a particular scattering medium and determine scattering and reflection coefficients entering the model.

3.1.2 Transmission and Reflection Measurements in Powders

Experimentally, the reflection and transmission have been studied in powders of $Nd_{0.5}La_{0.5}Al_3(BO_3)_4$ and Ti(0.1%,0.2%)-sapphire laser crystals and nominally not absorbing α-alumina (Al_2O_3) [2]. The average particle size was equal to $s \approx 3.5\,\mu m$ in neodymium-doped powder, $s \approx 3\,\mu m$ in Ti-sapphire powders, and $s \approx 1\,\mu m$ in Al_2O_3 powder. The powders of the volume density equal to ≈55% were filled into optical cuvettes with plane-parallel walls. The thickness of the cuvettes ranged from $z_0 = 0.4\,mm$ to $z_0 = 3\,mm$. The powders were illuminated with laser beams (at $\lambda = 514.5$, 532, 632.8 nm) incident nearly normally to the sample surface. The diameters of the laser beams were comparable to or larger than the thickness of the cuvettes. The transmission of the powder samples has been studied as a function of z_0. Several representative curves obtained in the transmission measurements are depicted in Figure 3.1.

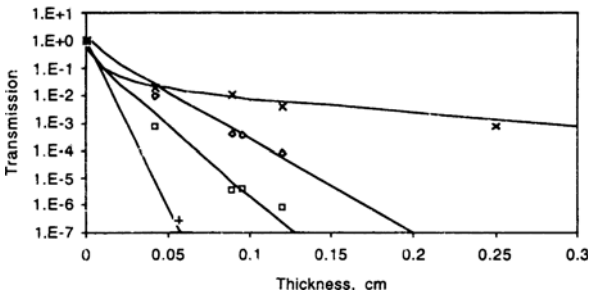

FIGURE 3.1. Experimental transmittance $T(z_0)$ as a function of thickness of cuvette z_0 for Al_2O_3 powder at 632.8 nm (×), $Nd_{0.5}La_{0.5}Al_3(BO_3)_4$ powder at 632.8 nm (◇), Ti-sapphire powder at 514.5 nm (□), and $Nd_{0.5}La_{0.5}Al_3(BO_3)_4$ powder at 532 nm (+). Solid lines are the theoretical curves calculated according to Eqs. (3.5) to (3.9). (After [2].)

The reflection of 532 nm laser light off several powder samples was experimentally studied using the setup described in Section 2.9. In the particular measurement discussed in this section, the powders were loaded into optically thick cuvettes. The powder volume density, ≈55%, approximately corresponded to the "medium" category in Table 2.4. The results of the transmission and the reflection measurements are summarized in Table 3.1.

3.1.3 Comparison of the Model Predictions with the Experimental Results

In the comparison of the theory with the experiment, the experimentally obtained data $T(z_0)$ and $R(z_0 \to \infty)$ were fitted with the theoretical curves calculated according to Eqs. (3.10) to (3.12). The fitting parameters were the scattering coefficient S and the reflection coefficients R_i, R_1, and R_2. The effective absorption coefficient K was calculated according to Eq. (3.4).

The function $T(z_0)$, calculated according to Eq. (3.11), is proportional to $\exp(-\alpha z_0)$ at large values of z_0 and characterized by a shorter-range decay component as $z_0 \to 0$ (Figure 3.1). Accordingly, in a strongly absorbing medium, such as $Nd_{0.5}La_{0.5}Al_3(BO_3)_4$ at $\lambda = 532$ nm, the dependence $T(z_0)$ is predominantly determined by the exponential decay $\propto \exp(-\alpha z_0)$. At the same time, the short-range component in the dependence $T(z_0)$ at $z_0 \to 0$, strongly dependent on the reflection coefficients, is more pronounced in media with low absorption or nominally nonabsorbing media (such as Al_2O_3).

This implies that the accuracy of determination of α is higher in *strongly* absorbing media, where the result is practically independent of the assumptions made on the values of the reflection coefficients R_i, R_1, R_2 varied in the fitting procedure in the range $0.1 < R_i, R_1, R_2 < 0.9$. On the other hand, the shape of the curve $T(z_0)$ in *weakly* absorbing media and the reflection coefficient R calculated according to Eq. (3.12) are strongly sensitive to the choice of R_i, R_1, and R_2. Correspondingly, the experimental values of R and $T(z_0)$ in samples with low absorption were predominantly used for the determination of the reflection coefficients R_i, R_1, and R_2. Because the front surface of the cuvette with powder was identical to the rear surface, it was assumed $R_1 = R_2 \equiv R_{1,2}$.

It was found that the experimental dependence $T(z_0)$ could be adequately fitted with the model, Eqs. (3.5) to (3.9) and (3.11), at the system parameters given in Table 3.1. The reflection coefficient $R_{1,2}$, obtained in the fitting procedure, was close to 0.7, the value determined in Al_2O_3 powder for the diffuse flux incident to the plane medium/air interface from the side of a scattering medium [4]. The reflection coefficient R_i was of the order of 0.1, the value close to that for a plane wave normally falling from the air to a nonscattering medium with the index of refraction equal to 1.8.[2] The agreement between the experimentally measured $R^{\exp}(z_0 \to \infty)$ and calculated $R^{\text{calc}}(z_0 \to \infty)$ reflection off the

[2] The index of refraction of $Nd_{0.5}La_{0.5}Al_3(BO_4)_3$ is equal to ≈1.84 [5] and that of sapphire (α-alumina) is equal to 1.76 [6].

TABLE 3.1. Experimental and calculated parameters in $Nd_{0.5}La_{0.5}Al_3(BO_3)_4$, Ti-sapphire, and Al_2O_3 scattering materials[a]

1 Material	2 λ [nm]	3 s [μm]	4 ρ	5 k_{abs} [cm^{-1}]	6 $R^{exp} z_0 \to \infty$	7 $R^{calc} z_0 \to \infty$	8 K [cm^{-1}]	9 S [cm^{-1}]	10 S^{-1} [cm]	11 R_i	12 $R_{1,2}$
$Nd_{0.5}La_{0.5}Al_3(BO_3)_4$	532	3.5	0.55	12.5	0.52	0.7	13.75[b]	2500	4.0×10^{-4}	0.1	0.75
$Nd_{0.5}La_{0.5}Al_3(BO_3)_4$	632.8	3.5	0.55	1		0.91	1.1[b]	2250	4.0×10^{-4}	0.1	0.7
0.2% Ti-sapphire	514.5	3	0.55	2.7		0.87	2.97[b]	2200	4.5×10^{-4}	0.1	0.65
0.2% Ti-sapphire	532	3	0.55	2.5	0.86	0.88	2.75[b]	2200	4.5×10^{-4}	0.1	0.7
0.1%Ti-sapphire	514.5	3	0.55	1.35		0.9	1.49[b]	2200	4.5×10^{-4}	0.1	0.7
0.1% Ti-sapphire	532	3	0.55	1.25	0.88	0.9	1.38[b]	2200	4.5×10^{-4}	0.1	0.7
Al_2O_3	632.8	1	0.55	Nominally not absorbing	1.0	0.99	0.011[c]	5000	2×10^{-4}	0.08	0.6

[a] 1: material; 2: wavelength; 3: mean particle size; 4: volume density of pulverized material (defined as the ratio of the density of the powder and that of single crystal); 5: absorption coefficient in single crystal material averaged over different polarizations; 6: experimentally measured (in a thick cuvette) reflection coefficient normalized to that of Al_2O_3 powder; 7: reflectance calculated according to Eq. (3.12); 8: effective absorption coefficient K; 9: effective scattering coefficient S; 10: inverse scattering coefficient S^{-1}; 11: reflection coefficient for the incident wave (at $z = 0$); 12: $R_{12} = R_1 = R_2$, where R_1 is the reflection coefficient for F_- incident upon the front surface at $z = 0$, and R_2 is the reflection coefficient for F_+ incident upon the back surface at $z = z_0$.

[b] Calculated from Eq. (3.3).

[c] Determined from the fitting.

Source: Reference [2].

powder sample was reasonably good but not always absolutely perfect, such as $R^{\exp}(z_0 \to \infty) = 0.52$ and $R^{\text{calc}}(z_0 \to \infty) = 0.7$ in $Nd_{0.5}La_{0.5}Al_3(BO_3)_4$ at 532 nm. This discrepancy limits the accuracy of the model, which nevertheless appears to be adequate for semi-quantitative evaluation of the propagation of light in random laser media.

The determined value of the scattering parameter S is larger in 1 μm Al_2O_3 powder ($S = 5000\,\text{cm}^{-1}$) than in 3 to 3.5 μm Ti-sapphire and $Nd_{0.5}La_{0.5}Al_3(BO_3)_4$ powders ($S = 2200\,\text{cm}^{-1}$ and $S = 2500\,\text{cm}^{-1}$, respectively). In $Nd_{0.5}La_{0.5}Al_3(BO_3)_4$ and Ti-sapphire powders, the value of S^{-1} varies between $1.1s$ to $1.5s$, whereas in undoped Al_2O_3 powder S^{-1} is equal to $2s$ (Table 3.1). The relationship between the scattering efficiency of the powder and the mean particle size is discussed in detail in Section 3.2.

The experimental dependence $T(z_0)$ in undoped Al_2O_3 can be fitted with high accuracy at $K = 0.011\,\text{cm}^{-1}$. This low value, which corresponds to ≈ 1 m absorption length in a single crystal, is reasonable for nominally nonabsorbing material. Some traces of absorption in Al_2O_3 could also originate from unintentional contamination of Al_2O_3 powder with foreign particles.

As follows from Eqs. (3.5) to (3.9), the function $F_+(z)$ describing the photon flux propagating in a thick cuvette ($z_0 \to \infty$) is single exponential, $\propto \exp(-\alpha z)$, over the whole length of the cuvette except the vicinity of the back wall. Thus, the penetration depth for pumping light in random laser media is simply given by $\alpha^{-1} = (K(K + 2S))^{-1/2}$. Substituting in this formula the coefficients K and S from Table 3.1, one can calculate the penetration depth of $\lambda = 532$ nm pumping light to be equal to 38 μm in $Nd_{0.5}La_{0.5}Al_3(BO_3)_4$ powder and 91 μm in (0.2%) Ti-sapphire powder.

3.2 Determination of the Transport Mean Free Path in Random Laser Material

Determination of the photon mean free path is a substantial fundamental problem in the physics of scattering media. It has a special practical significance in the case of solid-state random (powder) lasers. The knowledge of this parameter is important to understand the regime of operation of a random laser [7] and to model its behavior. The scattering process in $NdAl_3(BO_3)_4$ powder (random) laser material was studied in Reference [8]. This included experimental evaluation of the photon transport mean free path l_t and derivation of the relationship between l_t and the mean particle size s.

The transport mean free path l_t, is the average distance a wave travels before its direction of propagation is randomized. In Reference [8], it was experimentally determined in $NdAl_3(BO_3)_4$ powder using the coherent backscattering technique [9–11], a mature experimental method that was proved to yield adequate results in suspensions of scatterers in liquids [12,13]. In a number of publications, CBS was used to determine the parameter l_t in solid-state random laser materials; see,

for example, [14–16]. However, the applicability of this method to tightly packed solid-state powders has not been rigorously proven. In [8], the relationship between l_t and the mean particle size s was theoretically derived and compared with the experiment.

3.2.1 Experimental Samples and Absorption Spectra

A ground powder of $NdAl_3(BO_3)_4$ laser crystals was studied in the experiment. The SEM picture of a monolayer of powder was taken and the sizes of particles were measured. The average particle size, defined as an arithmetic mean, was equal to

$$s = \frac{\sum_i f(s_i)\, s_i}{\sum_i f(s_i)} = 3.55\,\mu\text{m}. \tag{3.13}$$

The porosity of the powder sample placed in a 1 mm thick cuvette was equal to 46% (the volume-filling factor of crystalline material was equal to 54%).

The absorption spectra of a $NdAl_3(BO_3)_4$ single crystal in polarizations $E\|c$ and $E\perp c$ were experimentally obtained in Reference [17]. Because the crystal is uniaxial, the isotropically average spectrum $\bar{k}_{abs}$ (averaged over $E\|c$ and $E\perp c$ polarizations) can, in the first approximation, be calculated as $\bar{k}_{abs} = (2k_{abs}^{E\perp c} + k_{abs}^{E\|c})/3$, where $k_{abs}^{E\perp c}$ and $k_{abs}^{E\|c}$ are the absorption spectra in polarizations $E\perp c$ and $E\|c$, respectively (Figure 3.2). To calculate the effective absorption spectrum in the porous samples, the absorption spectrum of a single crystal was multiplied by the volume-filling factor.

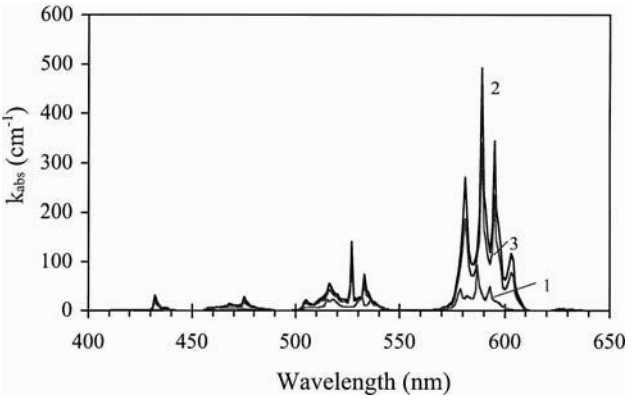

FIGURE 3.2. Absorption spectrum of $NdAl_3(BO_3)_4$ single crystal: (1) $E\perp c$, (2) $E\|c$, (3) averaged spectrum (digitized and recalculated from the transmission spectra published in [17]). (*Source*: Ref. [8].)

3.2.2 Idea of Coherent Backscattering

CBS was first experimentally demonstrated in pioneering studies [9–11], where enhanced scattering intensities (cones) were observed in the exact backscattering direction. Photons incident onto a scattering medium experience a smaller or larger number of (random) scattering events until they leave the medium through the front surface or are absorbed. However, light is a wave and the light diffusion process should be described by amplitudes rather than by probabilities [18]. Any random path of light inside a scattering medium can be time reversed and followed in the opposite direction. Two photons counterpropagating along the same optical path have equivalent phase delays. Thus if two partial waves entering the same optical path from the opposite ends are in phase, they will also be in phase when they leave the sample, causing constructive light interference in the exact backscattering direction. The theoretical model describing the shape of the CBS cones in diffusion approximation [13, 19–21] allows one to determine the parameters l_t and k_{abs} by fitting the experimental curve with the calculated one.

3.2.3 Experimental Setup

The measurements of the CBS cones were done in a standard setup depicted in Figure 3.3. A low divergence (<0.45 mrad) Ar laser was used as a light source. The linearly polarized laser beam ($1/e^2$ waist of 1.7 mm) was sent to the sample by a beamsplitter. The light power incident onto the sample did not exceed 10 mW. The direct beam transmitted through the beam splitter was carefully dumped. The CBS cones were recorded at four different wavelengths, 457.9 nm, 488 nm, 496.5 nm, and 514.5 nm.

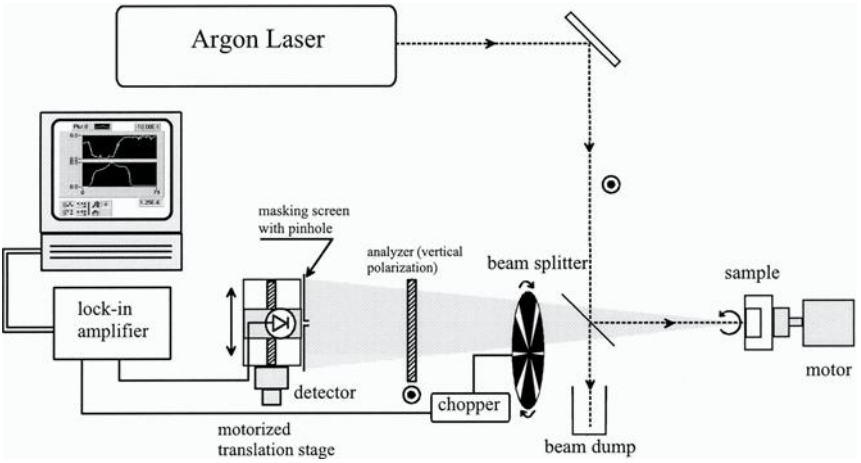

FIGURE 3.3. Setup for coherent backscattering measurements. (*Source*: Ref. [8].)

The angular distribution of the backscattered light intensity was recorded using a photodiode mounted on a motorized translation stage (Figure 3.3) [8]. The distance between a silicon photodetector and the sample was equal to ≈87.5 cm. A mask with small pinhole (0.5 mm diameter) was placed in front of the detector. The corresponding angular resolution in the experiment, predominantly determined by the finite size of the laser spot on the sample, was approximately equal to 2 mrad. The detection was performed in the polarization-conserving channel. The plane of the cuvette wall was slightly tilted from the normal to the incident beam in order to prevent the specular reflection from reaching the detector. The sample was mounted on a motorized spinning holder to provide for the averaging over speckle patterns (Figure 3.3). Stray light scattered off various surfaces and optical components was carefully eliminated.

3.2.4 Experimental Results

As an example, the CBS cone obtained at 488 nm is shown in Figure 3.4. The solid line in the figure is the theoretical fit to the experiment. The theoretical curve, as given in References [13,19–21], was fitted to the experimental data with the following adjustable coefficients: (1) the transport mean free path l_t, (2) the enhancement factor, and (3) a numerical factor that scales the y-axis, whereas the absorption coefficient (determined from the spectrum in Figure 3.2) was taken fixed. The transport mean free path determines the width of the backscattering cone, whereas the ratio between the top and the diffuse background is determined by the enhancement factor. The enhancement factors for the cones recorded at different wavelengths, defined as the ratio between the intensity scattered in

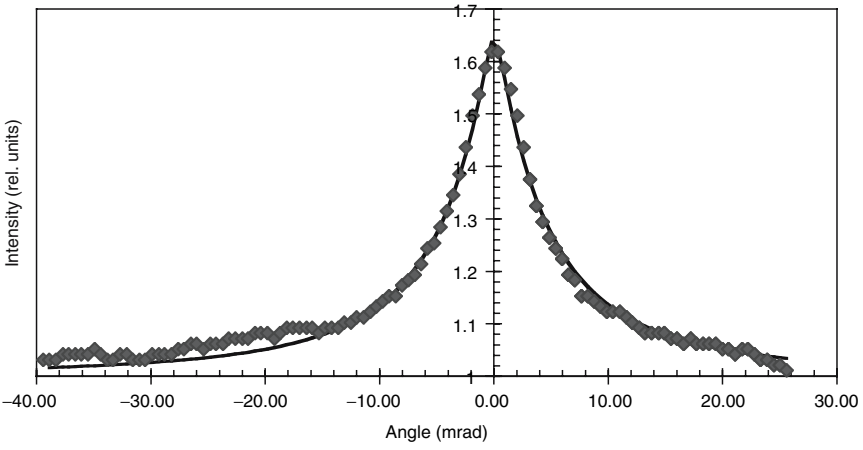

FIGURE 3.4. CBS cone in $NdAl_3(BO_3)_4$ powder at 488 nm. Diamonds: experiment; solid curve: theoretical fitting following Refs. [13, 19–21]. (*Source*: Ref. [8].)

TABLE 3.2. Absorption and transport mean free path length in the $NdAl_3(BO_3)_4$ powder[a]

Wavelength, nm	k_{abs},cm^{-1}	FWHM, mrad	l_t, μm (cone fitting)	l_t, μm (FWHM)
514.5	15.4	9.3	7.64	6.2
496.5	0.46	8	6.32	6.9
488	1.04	8.1	6.26	6.7
457.9	3.21	8.3	6.74	6.1

[a] The values l_t are obtained by two different methods, cone fitting and FWHM measurements. Absorption coefficients k_{abs} used in the fitting procedure are corrected for porosity. *Source*: Reference [8].

the exact backward direction and the diffuse background, range between 1.6 and 1.8. These numbers (common to polarization-conserving measurements in which single scattering cannot be eliminated) are smaller than the maximum theoretically possible value equal to 2. The results of the fitting are summarized in Table 3.2.

For wavelengths ranging from 457.9 nm to 514.5 nm, l_t is practically independent of λ. This is an expected result at $\lambda \ll s$. The average value of l_t calculated with this method and averaged over the four different wavelengths studied is equal to $l_t^{FIT} = 6.7\,\mu\text{m}$.

In $NdAl_3(BO_3)_4$ powder at the laser wavelengths used, the maximum product $(k_{abs}l_t)_{\max}$ was approximately equal to 10^{-2}. It was hypothesized [8] that at $(k_{abs}l_t)_{\max} \ll 1$, the absorption in the medium could be neglected and the transport mean free path l_t could be calculated from the full width at half maximum (FWHM) W of the CBS cones [13,19–21]:

$$l_t \approx 0.7\frac{\lambda}{2\pi W}. \tag{3.14}$$

The values of l_t determined using approximation (3.14) are given in Table 3.2, along with the data obtained from curve fitting. The average (over the four wavelengths studied) transport mean free path l_t^{FWHM} calculated from the FWHM is equal to 6.5 μm, which is close to l_t^{FIT} determined by the first method. This proves that at $(k_{abs}l_t)_{\max} \ll 10^{-2}$, l_t can be determined by use of the simple FWHM method instead of much more elaborative curve fitting.

3.2.5 Correlation Between Transport Mean Free Path l_t and Particle Size s: Comparison with Experiment

The concepts of the scattering mean free path l_s and the transport mean free path l_t were originally introduced in the literature to describe scattering in media where the average distance between particles is significantly larger than the particle size. This is not the case of tightly packed powders.

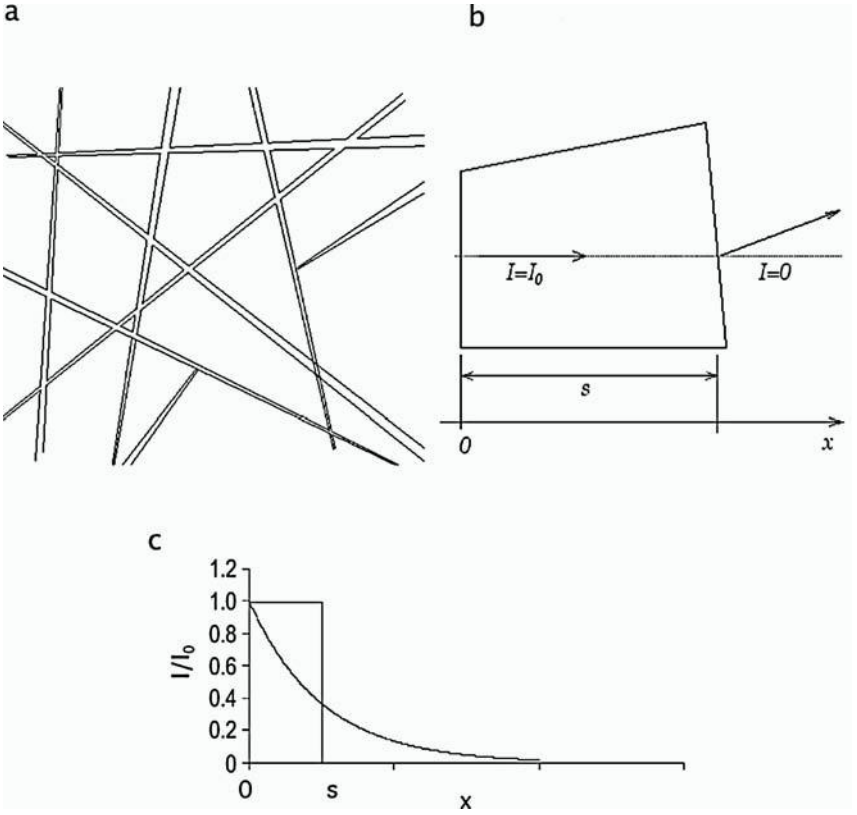

FIGURE 3.5. (a) Schematic drawing of tightly packed powder; (b) propagation of a photon flux inside a particle; (c) steplike distribution of the photon flux intensity $I(x)$ and its approximation with an exponential function. (*Source*: Ref. [8].)

In the first approximation, tightly packed powder (with a large filling factor) can be modeled as an almost monolithic solid with air gaps crossing it in all directions (Figure 3.5a). One can assume that the air gaps are not exactly plane-parallel, although they are not very far from being plane-parallel. By definition, the scattering mean free path l_s is the length at which the intensity of photon flux (plane wave) that falls onto the sample is reduced by a factor $1/e$. This definition assumes that (1) all photons, whose directions of propagation have been disturbed even slightly, are lost for the original photon flux; (2) the decay of the original photon flux is exponential, $\propto \exp(-x/l_s)$; and (3) all surface effects at the medium–air interface are neglected.

The flux of photons propagating along the direction x inside a particle is not disturbed until the flux reaches the particle wall at $x = s$ ($I(x) = I_0$ at $x \leq s$), and it is totally refracted at $x = s$ (correspondingly, at $x > s$ the intensity of the

original flux propagating in the direction x is equal to zero) (Figure 3.5b). The plot of the function $I(x)$ (a step function) is shown in Figure 3.5c. The most adequate fit of the step function $I(x)$ with the exponential function $\propto I_0 \exp(-x/l_s)$ is such that conserves the area under the $I(x)$ trace,

$$\int_0^\infty I_0 e^{-l_s x} dx = \int_0^\infty I(x) dx = \int_0^s I_0 dx, \tag{3.15}$$

yielding $l_s = s$. Thus in the first approximation, in tightly packed powder, the scattering mean free path l_s can be assumed to be equal to the average particle size s. The transport mean free path l_t, can be calculated from l_s using the formula

$$l_t = \frac{1}{1 - \langle \cos(\theta) \rangle} l_s, \tag{3.16}$$

where $\langle \cos(\theta) \rangle$ is the average cosine of the scattering angle. In Reference [8], $\langle \cos(\theta) \rangle$ was calculated assuming that scatterers are (plane-parallel) air gaps separating different particles in a powder. In the model, when the angle of incidence was smaller than the angle of total internal reflection φ_{crit}, the reflection coefficients of the material–air boundaries were calculated according to the known Fresnel formula

$$\rho_\perp = \left(\frac{n_1 \cos(\varphi) - n_2 \cos(\psi)}{n_1 \cos(\varphi) + n_2 \cos(\psi)} \right)^2 \tag{3.17a}$$

and

$$\rho_\parallel = \left(\frac{n_2 \cos(\varphi) - n_1 \cos(\psi)}{n_2 \cos(\varphi) + n_1 \cos(\psi)} \right)^2, \tag{3.17b}$$

where $\rho_\perp$ is the reflection coefficient for light polarized in the direction perpendicular to the plane of incidence, $\rho_\parallel$ is the reflection coefficient for light polarized in the plane of incidence, n_1 is the refraction index of the crystalline material, $n_2 = 1$ is the refraction index of air, φ is the angle of incidence in the crystalline medium, and ψ is the propagation angle of the refracted light inside of the air gap. The corresponding angles and light rays are shown in Figure 3.6.

Light was assumed to be randomly polarized [8]. Thus in the model, some effective reflection coefficient ρ was calculated as

$$\rho = \sqrt{\frac{\rho_\perp^2 + \rho_\parallel^2}{2}}. \tag{3.18}$$

To take into account the effect of two material–air boundaries associated with every gap, the effective reflection and transmission coefficients were calculated as

$$\rho_{eff} = 2\rho - \rho^2 \tag{3.19a}$$

and

$$\tau_{eff} = 1 - 2\rho + \rho^2. \tag{3.19b}$$

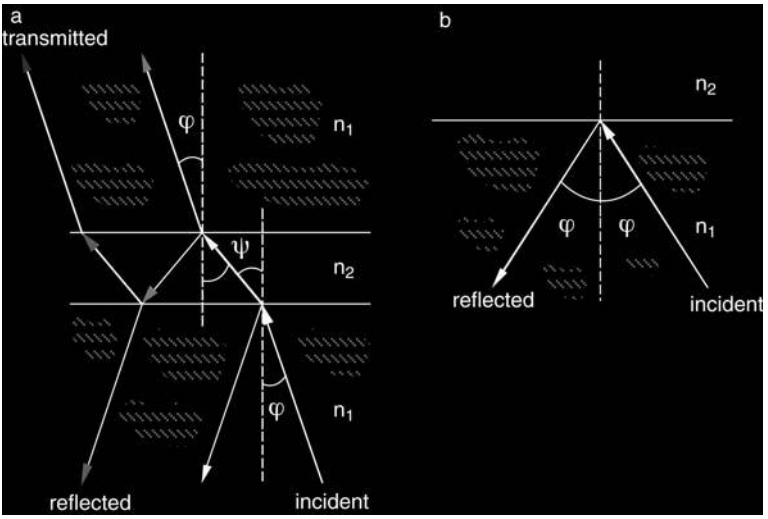

FIGURE 3.6. (a) Refraction of the light beam at the crystalline–air boundaries separating two particles of powder; (b) total internal reflection. (*Source*: Ref. [8].)

The critical angle of the total reflection φ_{crit} was calculated according to Snell's law

$$\sin(\varphi_{crit})n_1 = \sin(\pi/2)n_2. \tag{3.20}$$

At incidence angles larger than φ_{crit}, a scattering event manifests itself as total internal reflection. To calculate the average cosine of the scattering angle, $\langle\cos(\theta)\rangle$, the integral over all incidence angles $\varphi(0 < \varphi < \pi/2)$ was taken, at each angle accounting for the intensities and the directions of the reflected and transmitted beams (the integral was normalized by 2π). The calculated dependence of $l_t/l_s = 1/(1 - \langle\cos(\theta)\rangle)$ on the index of refraction n_1 is shown in Figure 3.7.

As follows from Figure 3.7, in a wide range of the practically important values of $n_1(1.6 < n_1 < 3.2)$, the ratio l_t/l_s is nearly constant, $l_t/l_s = 2.0 \pm 0.4$.

The index of refraction in $NdAl_3(BO_3)_4$ is close to $\approx$1.84 [5]. At this value of n_1, $l_t/l_s = 1/(1 - \langle\cos(\theta)\rangle) = 2.07$. If l_s is equal to the average particle size $s = 3.55\,\mu m$, then the calculated transport mean free path would be equal to $7.3\,\mu m$, which is reasonably close (within 10%) to the value $l_t = 6.7\,\mu m$ obtained from the CBS cone fitting.

Thus, the value of the transport mean free path l_t obtained in the CBS experiment appears to be reasonable (at the given index of refraction and particle size distribution). This validates the proposed model that allows one to determine l_t in tightly packed powders if the particle size and the index of refraction are known.

Note that the Fresnel formulas (3.17a) and (3.17b) are derived in the geometrical-optics approximation, which is valid at $s \gg \lambda$. As shown in Reference [8], adequate

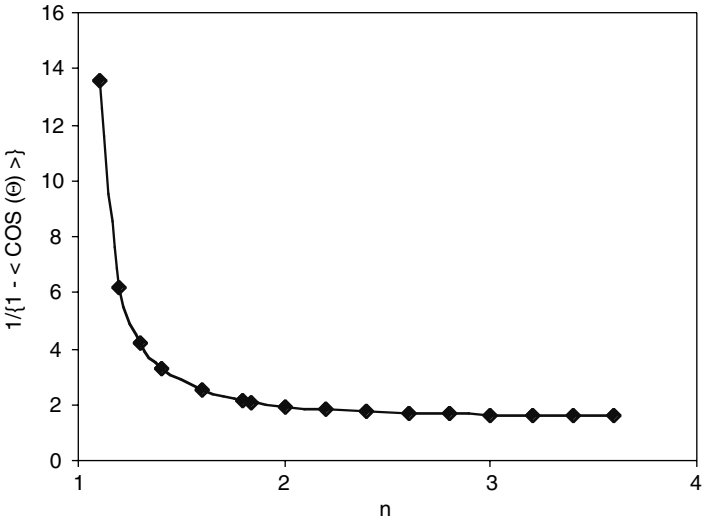

FIGURE 3.7. Calculated dependence $1/1 - \langle \cos\theta \rangle$ versus n_1. (*Source*: Ref. [8].)

results can be obtained at $s/\lambda \approx 7$. Experimental data available in the literature demonstrate that the model can predict the correct order of magnitude of l_t even at $s < \lambda$. In ZnO nanopowders, the ratios l_t/s were equal to ≈3.2 ($s = 100$ nm, $\lambda = 410$ nm) [22] and ≈4 ($s = 50$ nm, $\lambda = 410$ nm) [23]. The index of refraction in ZnO is equal to 2.008 and 2.029 for two different crystallographic directions [6,24]. Thus, according to the model [8] (Figure 3.7), the ratio l_t/s in ZnO powder with large particle sizes ($s \gg \lambda$) should be equal to 1.9, which is still not so far from the experimental data 3.2 and 4 obtained in fine-particle powders.

The increase of the ratio l_t/s in fine-particle ZnO powders (as discussed above) can be qualitatively explained in terms of Rayleigh theory (at $s \ll \lambda$) or Mie theory (at $s \leq \lambda$) [25], both of which predict the reduction of scattering efficiency when the size of the scatterer is smaller than the wavelength. The dependence of the normalized scattering cross-section Q^S on the particle size, calculated according to the Mie model [26] at $\lambda = 0.41\ \mu$m for particles with refraction index of $n = 2.02$, is shown in Figure 3.8. The transport mean free path, corrected for the function of Figure 3.8, can be calculated as

$$l_t^{corr} = l_t \left[Q^S(s \to \infty)/Q^S \right], \tag{3.21}$$

where $Q^S(s \to \infty)$ is the normalized scattering cross section at $s \to \infty$ and l_t is the transport mean free path calculated in the geometrical-optics approximation. This suggests an increase of l_t^{corr} and l_t^{corr}/s at $s \to 0$, which is in qualitative agreement with the results of References [22,23]. However, quantitatively, the function of Figure 3.8 predicts much greater values of l_t^{corr}/s than those in [22,23]. The possible reasons for this discrepancy are: large-scale inhomogeneities

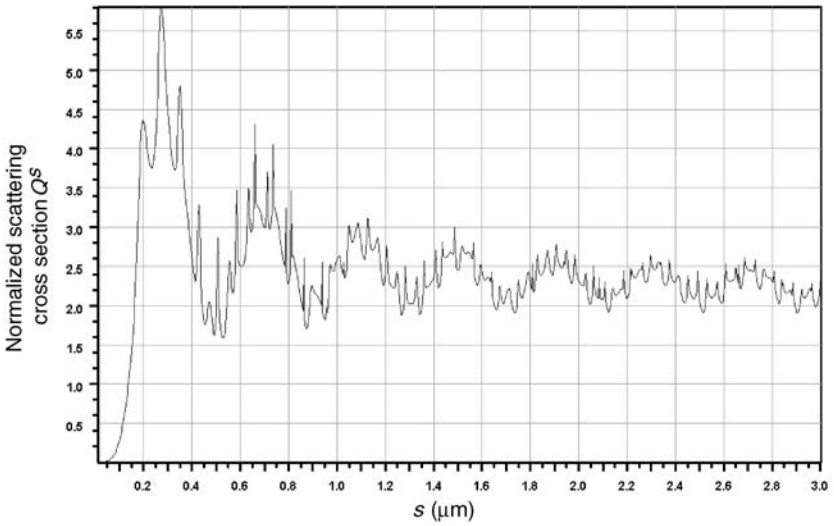

FIGURE 3.8. Normalized scattering cross-section Q^s of dielectric spheres with a refractive index of 2.02 as a function of the particle size s calculated for $\lambda = 0.41\,\mu$m with the help of the MIECALC program [26]. (*Source*: Ref. [8].)

on the powder density, failure of Mie theory to describe scattering in dense media, or possible localization of light [27].

References

1. A. Ishimaru, *Wave Propagation and Scattering in Random Media*, Vol. 1, Academic: San Diego (1978).
2. M.A. Noginov, N. Noginova, S. Egarievwe, J.C. Wang, M.R. Kokta, and J. Paitz, Study of light propagation in scattering powder laser materials, *Opt. Mater.*, **11**: 1–7 (1998).
3. G. Kortüm, *Reflectance Spectroscopy, Principles, Methods, Applications*, Springer: New York (1969).
4. A. Dogariu, J. Uozumi, and T. Acura, Particle size effect on transport through strong scattering media, *Part. Part. System Characterization*, **11**: 250–257 (1994).
5. S.T. Durmanov, O.V. Kuzmin, G.M. Kuzmicheva, S.A. Kutovoi, A.A Matrynov, E.K. Nesynov, V.L. Panyutin, Yu.P. Rudnitsky, G.V. Smirnov, V.L. Hait, and V.I. Chizhikov, Binary rare-earth scandium borates for diode-pumped lasers, *Opt. Mater.*, **18**: 243–284 (2001).
6. D.R. Lide, *Handbook of Chemistry and Physics*, 82d ed., CRC Press: Boca Raton, FL (2001).
7. D.S. Wiersma and A. Lagendijk, Light diffusion with gain and random lasers, *Phys. Rev. E*, **54**: 4256–4265 (1996).
8. M. Bahoura and M.A. Noginov, Determination of the transport mean free path in a solid-state random laser, *JOSA B*, **20**: 2389–2394 (2003).
9. Y. Kuga and A. Ishimaru, Retroreflectance from a dense distribution of spherical particles, *J. Opt. Soc. Am. A*, **1**: 831–836 (1984).

10. M.P. van Albada and A. Lagendijk, Observation of weak localization of light in random medium, *Phys. Rev. Lett.*, **55**: 2693–2695 (1985).
11. P.E. Wolf and G. Maret, Weak localization and coherent backscattering of photons in disordered media, *Phys. Rev. Lett.*, **55**: 2696–2699 (1985).
12. P.E. Wolf, G. Maret, E. Akkermans, and R. Maynard, Optical coherent backscattering by random media: An experimental study, *J. Phys. France*, **49**: 63–75 (1988).
13. M.B. van der Mark, M.P. van Albada, and A. Lagendijk, Light scattering in strongly scattering media: Multiple scattering and weak localization, *Phys. Rev. B*, **37**: 3575–3592 (1988).
14. H. Cao, J.Y. Xu, D.Z. Zhang, S.H-. Chang, S.T. Ho, E.W. Seelig, X. Liu, and R.P.H. Chang, Spatial confinement of laser light in active random media, *Phys. Rev. Lett.*, **84**: 5584–5587 (2000).
15. S.C. Rand, *Strong localization of light and photonic atoms*, *Can. J. Phys.*, **78**: 625–637 (2000).
16. R.C. Polson, J.D. Huang, and Z.V. Vardeny, Random lasers in π-conjugated polymer films, *Synth. Metals*, **119**: 7–12 (2001).
17. H.-D. Hattendorf, *Dissertation zur Erlangung des Doktorgrades des Fachbereich Physik*, Universität Hamburg, Hamburg, Germany 1994).
18. S. John, Localization of light, *Phys. Today*, 32–40 (1991).
19. M.B. van der Mark, M.P. van Albada, and A. Lagendijk, Light scattering in strongly scattering media: Multiple scattering and weak localization, *Phys. Rev. B*, **37**: 3575–3592 (1988).
20. E. Akkermans, P.E. Wolf, and R. Maynard, Coherent backscattering of light by disordered media: Analysis of the peak line shape, *Phys. Rev. Lett.*, **56**: 1471–1474 (1986).
21. E. Akkermans, P.E. Wolf, R. Maynard, and G. Maret, Theoretical study of the coherent backscattering of light by disordered media, *J. Phys. France*, **49**: 77–98 (1988).
22. H. Cao, Y.G. Zhao, S.T. Ho, E.W. Seelig, Q.H. Wang, and R.P.H. Chang, Random laser action in semiconductor powder, *Phys. Rev. Lett.*, **82**: 2278–2281 (1999).
23. H. Cao, J.Y. Xu, D.Z. Zhang, S.-H. Chang S.T. Ho, E.W. Seelig, X. Liu, and R.P.H. Chang, Spatial confinement of laser light in active random media, *Phys. Rev. Lett.*, **84**: 5584–5587 (2000).
24. V.A. Rabinovich and Z.Ya. Khavin, *Short Handbook on Chemistry*, (*Kratkii khimicheskii spravochnik*) Khimia: Leningrad (1977).
25. M. Born and E. Wolf, *Principles of Optics*, 6th (corrected) ed., Cambridge University Press: Cambridge, (1997).
26. B. Michel, MieCalc—Freely configurable program for light scattering Calculations (Mie theory) http://www.lightscattering.de/MieCalc/eindex.html.
27. J.G. Rivas, R. Sprik, A. Lagendijk, L.D. Noordam, and C.W. Rella, Static and dynamic transport of light close to the Anderson localization transition, *Phys. Rev. E*, **63**: 046613 (2001).

4
Theoretical Modeling of Neodymium Random Lasers

Understanding of the mechanisms of stimulated emission in powder (random) lasers is of great academic interest and practical importance. Neodymium powder lasers were the first random lasers studied systematically. A review of several theoretical models proposed to explain the behavior of neodymium random lasers is given in this chapter. After little modification, the same arguments are applicable to many other solid-state random lasers.

The diffusion model of random lasers proposed by Letokhov in the late 1960s is discussed in Section 4.1. Historically, this was the first model describing stimulated emission in scattering media with gain. The results of many experimental works on random lasers, including neodymium random lasers, are compared to the predictions of the diffusion model.

The results of the rate equation modeling of relaxation oscillations and the thresholds in the neodymium random laser, presented in Section 4.2, are in rather good qualitative and quantitative agreement with the experimental data. As shown in Section 4.3, the kinetics of random laser emission are strongly different at different widths of the pumping pulse. However, according to the laser model, the threshold energy does not depend on the pumping regime as long as the duration of the pumping pulse is shorter than the spontaneous lifetime. The extended rate equation model is used to calculate the spectral dynamics in $NdAl_3(BO_3)_4$ random laser in Section 4.4.

The importance of feedback in random lasers and the dramatic difference between the emission in a scattering medium with feedback and that in open amplification paths elongated by scattering is outlined in Section 4.5.

The penetration depth of the pumping energy, the photon residence time in a gain volume, and the threshold pumping power are calculated in the diffusion approximation in Section 4.6.

The effect of the mean particle size and the volume density (filling factor) of the random laser material are analyzed and compared with the experiment in Section 4.7.

In Section 4.8, a Monte Carlo simulation of the diffusion process is used to calculate the photon residence time that determines the threshold. It is shown that when the realistic geometry of the experiment and the boundary conditions are

taken into account, the diffusion model can predict the experimental dependence of the threshold on the diameter of the pumping spot d, $\propto 1/d + \text{const}$, which is different from that proposed by Letokhov [1–3], $\propto 1/d^2 + \text{const}$.

The model of coupled intraparticle resonators (oscillators), which enable random laser emission, is discussed in Section 4.9.

4.1 Diffusion Model

4.1.1 Prediction of Stimulated Emission

Assuming that photon migration in a scattering medium is diffusion, Letohkov has proposed the following equation describing the flux density $\Phi_\omega(r, t)$ of emitted photons in pumped volume with high concentration of scatterers [1–3]:

$$\frac{1}{c}\frac{\partial \Phi_\omega(r,t)}{\partial t} = D\Delta\Phi_\omega(r,t) + Q_\omega(r,t)n_0\Phi_\omega(r,t), \tag{4.1}$$

where D is the diffusion coefficient, n_0 is the concentration of particles with gain, Q_ω is the cross section of negative absorption of light (gain), c is the speed of light, r is the coordinate, ω is the frequency of light, and t is time. The general solution of Eq. (4.1) is given by

$$\Phi_\omega(r,t) = \sum_n a_n \psi_n(r) \exp\left[-\left(DB_n^2 - Q_\omega n_0\right)ct\right], \tag{4.2}$$

where $\psi_n(r)$ and B_n are the eigenfunctions and eigenvalues of the equation:

$$\Delta\psi_n(r) + B_n^2\psi_n(r) = 0. \tag{4.3}$$

The threshold condition (corresponding to the divergence of the flux density $\Phi_\omega(r, t)$) comes from the requirement

$$\left(DB^2 - Q_0 n_0\right)ct \le 0. \tag{4.4}$$

Hence, the threshold value of gain $g_{th} = n_0 Q_0$ is given by

$$n_0 Q_0 = DB^2, \tag{4.5}$$

where B is the smallest eigenfunction of Eq. (4.3). For a cylinder with radius r and height h (which is a typical geometry of a pumped volume in random laser experiments), the threshold gain g_{th} depends on h and r as

$$g_{th} \propto B = \left[\left(\frac{2.4}{r}\right)^2 + \left(\frac{\pi}{h}\right)^2\right]^{1/2}. \tag{4.6}$$

If the gain in the system is assumed to be constant in time, then Eqs. (4.1) to (4.5) predict an infinite increase of the emission flux density above the threshold. This is qualitatively similar to an "atomic bomblike" explosion behavior for multiple scattering of light in an amplifying medium at critical volume and gain. Following Letokhov, many researchers (see, e.g., Refs. [4–6]) have identified this divergence

of the emission flux with the random laser threshold in incoherent or coherent systems. However, gain (or the imaginary part of the particle's permittivity $\varepsilon''(r,t)$, which is a function of $\Phi_\omega(r,t)$), is not constant. According to [2,3], it is described by the equation

$$\frac{\partial\varepsilon''(r,t)}{\partial t}+\frac{1}{T_1}\partial\varepsilon''(r,t)=-2\sigma_a\partial\varepsilon''(r,t)\int a(\omega)\Phi_\omega(r,t)d\omega+\frac{1}{T_1}\tilde{\varepsilon}''(r), \quad (4.7)$$

where $\sigma_0=\sigma(\omega_0)$ is the emission cross section of active ions, T_1 is the spontaneous decay time of excitations, $a(\omega)$ is the spectral shape of the emission line normalized to unity in the maximum, and $\tilde{\varepsilon}''(r)$ is the term proportional to the pumping power. Thus, above the threshold, the exponential rise of the emission intensity continues until the decrease in gain $\varepsilon''(r,t)$, caused by the depopulation effect, is getting strong and drives $\varepsilon''(r,t)$ below the threshold. As a result, the emission intensity falls sharply, but then, because of pumping $\tilde{\varepsilon}''(r)$ the threshold is exceeded again and pulsations are repeated. Pulsations of this kind are known as *relaxation oscillations*; see, for example, [7–9]. The calculated dynamics of relaxation oscillations in a random laser is shown in Figure 1.2. Relaxation oscillations in random lasers with diffusion have been studied in the more recent Reference [10] and other works.

4.1.2 Spectrum Narrowing

As shown in References [2,3,11], in lasers with nonresonant feedback, and in random lasers in particular (in which the photon migration is assumed to be diffusion), the process of spectrum narrowing is much slower than the process of establishment of stationary intensity. Thus, the generation spectrum remains nonstationary even when the integral intensity stabilizes in time at its cw value. The asymptotic dynamics of the emission spectrum was calculated in [2,3,11] under the following assumptions.

1. The pumping pulse is a step function "turned on" at $t=0$.
2. Given sufficient time, the integral emission intensity $I(t)$ and the excited state concentration $n(t)$ are close to their stationary values and their damped pulsations (relaxation oscillations) are small.
3. The emission line-shape $a(\nu)$ is Lorentzian with the characteristic spectral width equal to $\Delta\nu_0$.
4. The width of the stimulated emission line $\Delta\nu$ is much smaller than $\Delta\nu_0$.

It was shown in [2,3,11] that the dynamics of spectral narrowing can be described as

$$\Phi(\nu,t)\approx\Phi'(\nu)\exp\left\{-Q_0n_0ct\left(2\frac{\nu-\nu_0}{\Delta\nu_0}\right)^2\right\}, \quad (4.8)$$

where $\Phi'(\nu)$ is the normalization factor and ν_0 is the central frequency of the amplification spectrum. The momentary width of the emission spectrum at

half-maximum, $\Delta\nu$, can be calculated from Eq. (4.8), at $\Delta\nu \ll \Delta\nu_0$, as

$$\Delta\nu = \Delta\nu_0 \left(\frac{Q_0 n_0 ct}{\ln 2} \right)^{-1/2}. \tag{4.9}$$

The authors of Reference [12], who did not rely in their calculations on the assumption $\Delta\nu \ll \Delta\nu_0$, obtained the following expression for the line-width dynamics:

$$\frac{(\Delta\nu/\Delta\nu_0)^2}{1+(\Delta\nu/\Delta\nu_0)^2} = \frac{1}{g_0 l} \ln \left[\frac{2}{1+(\Delta\nu/\Delta\nu_0)^2} \right], \tag{4.10}$$

where $g_0 = Q_0 n_0$ is the gain and $l = ct$ is the photon propagation path in the amplifying medium over time t. [At $\Delta\nu \ll \Delta\nu_0$, Eq. (4.10) is identical to Eq. (4.9)].

In [12,13], Eqs. (4.9) and (4.10) were used to calculate the effective photon path-length l in neodymium random lasers from the known narrowing of emission linewidth $\Delta\nu/\Delta\nu_0$ and gain g_0. The value of l calculated this way in the Nd:$Na_5La(MoO_4)_4$ powder laser was equal to $\approx$2 cm [12]. The calculation done in [13] for the random laser experiment described in [14] yielded $l = 1.63$ cm. Both values appeared to be too large for photon paths in submillimeter pumped volumes. However, one should note that assumptions 1 to 3 above were not strictly satisfied in the experiments of References [12–14]. In fact, (a) the pumping pulse was short and had a bell-shape form, (b) short-pulse stimulated emission, which was very far from the cw limit, was studied experimentally, and (c) the neodymium emission spectrum, consisting of a large number of partially overlapped Stark-split lines, which suffer (to a smaller or larger extent) from inhomogeneous broadening, cannot be accurately approximated with a Lorentzian line shape. Thus, the estimations of photon pathlength l done in [12,14] could be not accurate enough.

4.1.3 Application of the Diffusion Model to Stimulated Emission in a Mixture of Powders

Stimulated emission in mixtures of $Na_5La_{1-x}Nd_x(MoO_4)_4$ powders with different concentrations of neodymium ions (x) has been studied experimentally and theoretically in [15,16]. The wavelength of stimulated emission in a mixture of two powders depended both on the proportion between the powder components and the excitation wavelength. The relative value of the shift x of the laser wavelength λ was defined as

$$x = \frac{\lambda_{hc} - \lambda}{\lambda_{hc} - \lambda_{lc}}, \tag{4.11}$$

where λ_{hc} and λ_{lc} were the emission wavelengths in the high and low neodymium-doped components, correspondingly.

Under the assumption of the diffusion mechanism of stimulated emission and Lorentzian shape of the gain spectrum, the value of x was shown to be determined by the equation:

$$\frac{x(n_1/n_2)}{1+x^2\,(\lambda_{hc}-\lambda_{lc}/\Delta)^2} = \frac{(1-x)M_2/M_1}{1+(1-x)^2\,(\lambda_{hc}-\lambda_{lc}/\Delta)^2}, \tag{4.12}$$

where M_1 and M_2 were the volume fractions of the high and low neodymium-doped components, n_1 and n_2 were the corresponding excited state concentrations, and Δ was the full width at half maximum of the gain spectral band. Assuming further that the ratio n_1/n_2 was governed by the ratio of the fractions A_1 and A_2 of incident radiation absorbed by the two components, and using the theory developed by Melamed in [17], the ratio n_1/n_2 was determined to be equal to

$$\frac{n_1}{n_2} = \frac{A_1}{A_2} = \frac{\left[1 - \exp(-2k_1 d/3)\right]\left[1 - m_i \exp(-2k_2 d/3)\right]}{\left[1 - m_i \exp(-2k_1 d/3)\right]\left[1 - \exp(-2k_2 d/3)\right]}, \tag{4.13}$$

where k_1 and k_2 were the absorption coefficients of the two components. By substituting Eq. (4.13) into Eq. (4.12), the relative wavelength shift x was theoretically calculated and compared with the experiment [16].

In particular, it was shown that when the ratio of concentrations of $Na_5La_{0.05}Nd_{0.95}(MoO_4)_4$ and $Na_5La_{0.85}Nd_{0.15}(MoO_4)_4$ powders in the mixture was equal to 1:7 (by volume), the calculated value of x was equal to $\approx$0.8 in the center of the excitation line and $\approx$0.5 at the wings of the line. At the same time, the experimental values of x measured in the center of the line and at its wings were equal to $\approx$0.7 to 0.8 and $\approx$0.1, respectively. Thus, it has been concluded [16] that the diffusion model does not adequately describe the behavior of a powder (random) laser and some alternative concept or theory is needed. (The model of coupled intraparticle resonators developed in Reference [16] is presented in Section 4.9.)

4.2 Modeling of Stimulated Emission Dynamics

In regular lasers, the solution of rate equations for the population inversion and the density of emitted photons predicts damped oscillations of the emission intensity known as *relaxation oscillations* [7–9]. A similar system of rate equations was used to model the dynamics of stimulated emission in neodymium random lasers in Reference [18]:

$$\frac{dn}{dt} = \frac{P(t)}{Sl_p h\nu_{pump}} - \frac{n}{\tau} - \frac{E}{h\nu_{em}} c\sigma_{em} n,$$

$$\frac{dE}{dt} = -\frac{E}{\tau_{res}} + \zeta \frac{n}{\tau} h\nu_{em} + Ec\sigma_{em} n. \tag{4.14}$$

Here n is the concentration of excited neodymium ions (in state $^4F_{3/2}$); $P(t)/S$ is the pumping power density; l_p is the penetration depth of pumping light (in the absence of scattering, $l_p = N\sigma_{abs}$, where N is the neodymium ground state concentration and σ_{abs} is the absorption cross section at the pumping wavelength); E is the emission energy density; σ_{em} is the emission cross section; $h\nu_{pump}(h\nu_{em})$ is the photon energy at the pumping (emission) wavelength; τ is the lifetime of the upper laser level $^4F_{3/2}$, which is determined by spontaneous emission decay, multiphonon decay, and (cross relaxation) self-quenching; ζ is the quantum yield of excitation of the metastable level $^4F_{3/2}$ spontaneously emitted to the random laser

mode(s); τ_{res} is the effective residence time of the photon in a pumped volume (in conventional lasers, a similar term represents the lifetime of a photon in a cavity); and c is the speed of light. In Reference [18], the spatial nonuniformity of pumping, emission, and population inversion, as well as the spectral dependence of the emission intensity, have been neglected for simplicity. Equations (4.14) are written in the most general form and are suitable for almost any feedback mechanism. In approximation of the diffusion model, the parameters τ_{res} and l_p are calculated in Section 4.6.

The calculated dynamics of the emission energy density and the $^4F_{3/2}$ excited state concentration (population inversion) is shown in Figure 4.1. Calculations predict that one short ($\approx$1 ns) high-intensity pulse appears in the emission kinetics at the lasing threshold. With the increase of the pumping energy, the intensity of this pulse increases; it gets shorter and shifts toward the beginning of the pumping pulse. At even stronger pumping, the second short pulse appears in the emission kinetics. At further increase of the pumping energy, the number of short emission pulses (which resemble relaxation oscillations in a highly nonlinear regime) increases and the time intervals between pulses shorten. It is important to note a remarkable similarity between the calculated emission kinetics (Figure 4.1) and the experimental one observed in the $NdAl_3(BO_3)_4$ random laser (Figure 2.3).

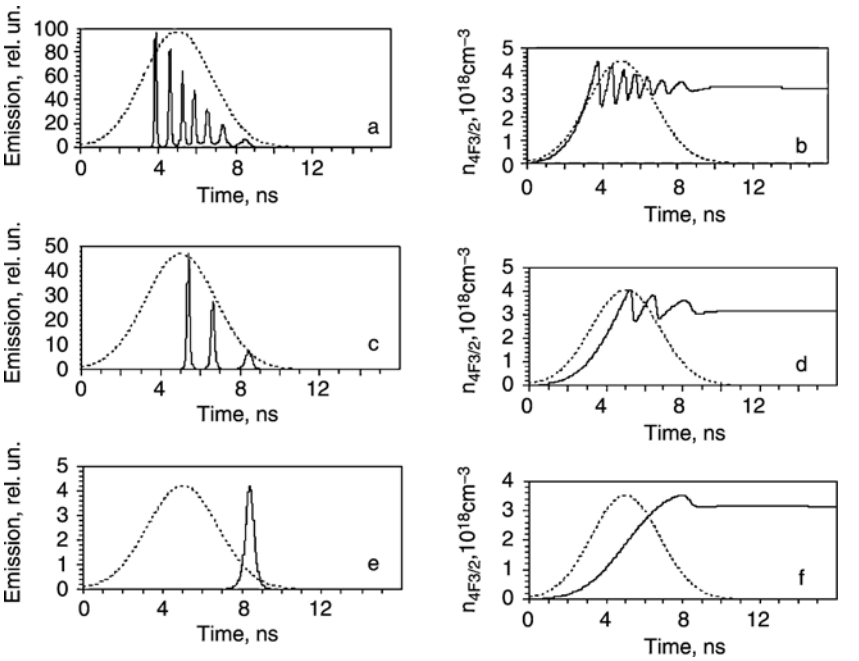

FIGURE 4.1. Calculated [according to Eqs. (4.14)] dynamics of stimulated emission (a, c, f) and $^4F_{3/2}$ excited state concentration (b, d, e) in $NdAl_3(BO_3)_4$ powder. Pumping density: 1000 mJ/cm^2 in a,b; 400 mJ/cm^2 in c,d, and 200 mJ/cm^2 (the threshold) in f,e. Dashed line: pumping pulse (not plotted to scale). (*Source*: Ref. [18].)

In Reference [18], the following set of spectroscopic parameters, approximating those in $NdAl_3(BO_3)_4$ powder (Table 2.2), was used in the numerical solution of Eq. (4.14): $\sigma_{em} = 1 \times 10^{-18}\,\mathrm{cm}^2$, $l_p \approx [N\sigma_{abs}]^{-1} = [(5 \times 10^{21}\,\mathrm{cm}^{-3}) \times (3 \times 10^{-21}\,\mathrm{cm}^2)]^{-1} \approx 0.67\,\mathrm{mm}$, $h\nu_{abs} = 4 \times 10^{-19}\,\mathrm{J}$, $h\nu_{em} = 2 \times 10^{-19}\,\mathrm{J}$, $\tau = 20\,\mu\mathrm{s}$, $\zeta \approx 0.9$. The pumping pulse was assumed to have Gaussian form with the full width at half of maximum equal to 4.1 ns (close to that used in the experiment). The only unknown parameter in Eq. (4.14) was the effective photon residence time in the pumped volume τ_{res}. Its value was used as an adjustable parameter to fit the experimental energy threshold, $\int (P(t)/S)\,dt = 200\,\mathrm{mJ/cm}^2$ (Table 2.2). The best fit was obtained at $\tau_{res} = 10\,\mathrm{ps}$. At the index of refraction equal to $n \approx 1.8$, which is typical of the crystals of this family [19], the value of τ_{res} obtained from the threshold fitting corresponds to the effective photon path length in the pumped medium equal to $l = 1.7\,\mathrm{mm}$. The estimated value of l appears to be reasonable for the experiment, where the characteristic pumped volume was of the order of $\approx 1\,\mathrm{mm}^3$ [18]. The resemblance of the calculated and the experimental emission kinetics as well as a fairly accurate fit of the lasing threshold suggest that rate Equations (4.14) can describe (with reasonable accuracy) stimulated emission in neodymium random lasers both qualitatively and quantitatively.

As follows from Figure 4.1, the amplitude of oscillations of population inversion n is much smaller than that of emission energy density E. The steady-state value of n, realized when the relaxation oscillations are damped, practically does not depend on the pumping energy. This behavior is typical of lasers operating according to a four-level scheme. Figure 4.2 depicts the input–output curve of stimulated emission and the dependence of steady-state population inversion on the pumping density calculated for the system parameters listed above. Both calculated curves are typical of lasers; compare, for example, Figures 4.2 and 2.5a.

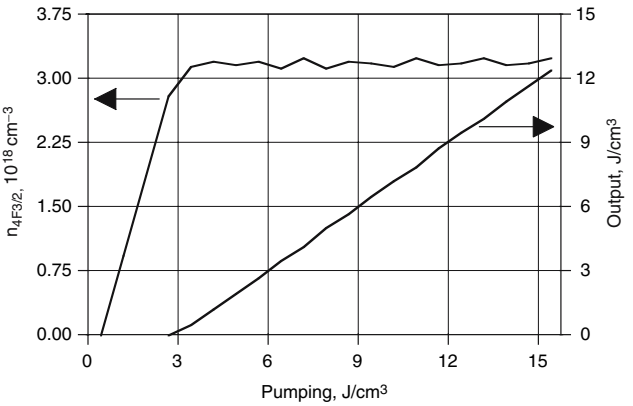

FIGURE 4.2. Calculated input–output curve (right vertical axis) and dependence of the $^4F_{3/2}$ excited state concentration (left vertical axis) on pumping density in $NdAl_3(BO_3)_4$ powder laser. (*Source*: Ref. [18].)

Calculations have shown that the emission decay time τ and the quantum yield of luminescence ζ slightly affect the phase of relaxation oscillations but practically do not influence the input–output curve. The calculated threshold pumping energy density (registered at the appearance of the first emission spike) was found to be proportional to the thickness of the pumped layer l_p and inversely proportional to the emission cross-section σ_{em} and the photon residence time τ_{res}.

The calculated stimulated emission pulses in Figure 4.1 are always delayed in respect to the beginning of the pumping pulse. This delay is partly because of the finite time needed to reach the critical population inversion and partly because the emission photon density inside the amplifying volume needs some time to build up. In References [12,20], the experimentally observed delay between the pumping pulse and the short stimulated emission pulse ($\Delta t = 10$ to 30 ns) was explained by slow relaxation of excitation from the directly pumped upper excited state ($^4G_{5/2}$) to the metastable state $^4F_{3/2}$ [this delay is not taken into account in Eq. (4.14)]. Apparently, in real experimental situations, all three factors contribute to the delay of the stimulated emission with respect to the pumping pulse.

Relaxation oscillation kinetics similar to that depicted in Figure 4.1 can be predicted at different mechanisms of the stimulated emission feedback. For example, compare Figure 4.1 with the emission kinetics calculated in a random laser when (i) the diffusion term was explicitly taken into account in the rate equations (Figure 1.2 [2]); (ii) Maxwell equations describing phase-dependent electromagnetic fields were used in the model instead of the rate equation for light intensity (Figure 4.3a [21]); or (iii) the laser action was assumed to be supported by resonances within individual powder particles or an ensemble of coupled intraparticle resonators (Figure 4.3b [12]).

The resemblance above presents a difficulty for random laser analysis, because it makes it impossible to distinguish between different mechanisms of stimulated emission based solely on the shape of the emission kinetics. On the other hand, this similarity allows one to evaluate certain important random laser parameters without detailed knowledge of underlying physical mechanisms of the random laser emission.

4.3 Invariance of the Threshold Pumping Energy in Different Pumping Regimes

The analysis of the system of Eqs. (4.14) shows that the behavior of the stimulated emission kinetics depends strongly on the duration of the pumping pulse. The series of emission kinetics calculated at fixed pumping energy and different pulse widths is shown in Figure 4.4. As follows from this figure, by merely changing the duration of the pumping pulse, one can predict (i) single-spike emission, (ii) multiple-spike emission, or (iii) smooth emission kinetics without any sharp spikes, the shape of which closely resembles that of the pumping pulse.

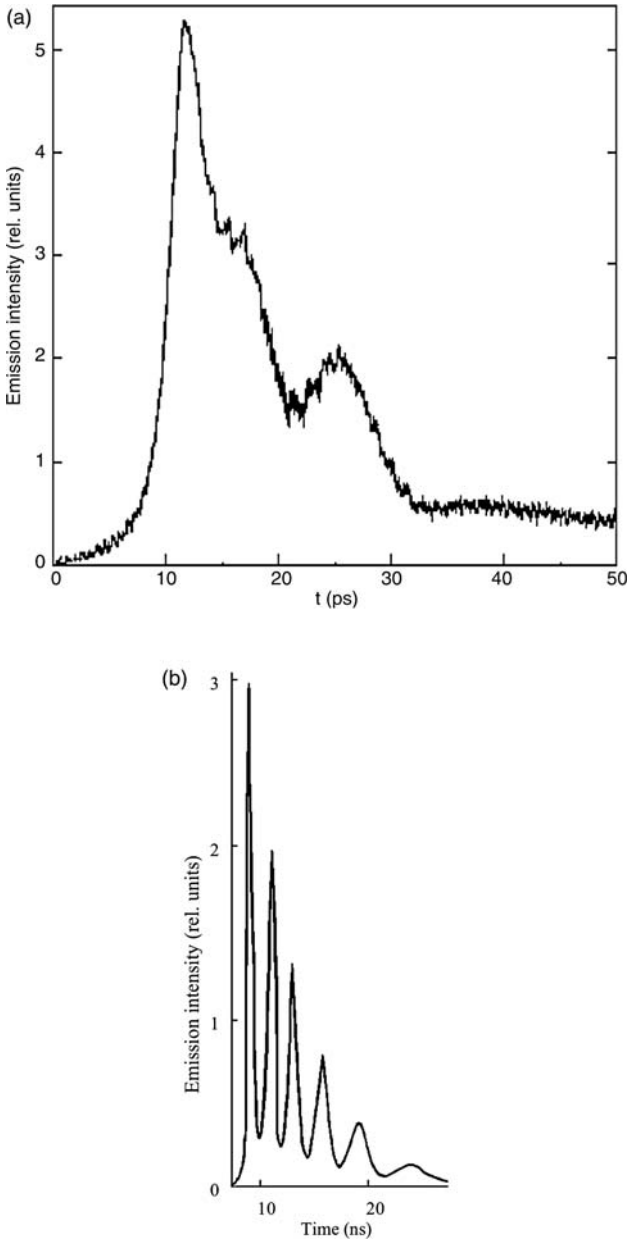

FIGURE 4.3. Emission kinetics with relaxation oscillations calculated in random laser when (a) the model is based on Maxwell equations and phase-dependent electromagnetic fields instead of the rate equation for light intensity (after [21]) and (b) the laser action is assumed to be supported by three coupled intraparticle resonators (after [12]).

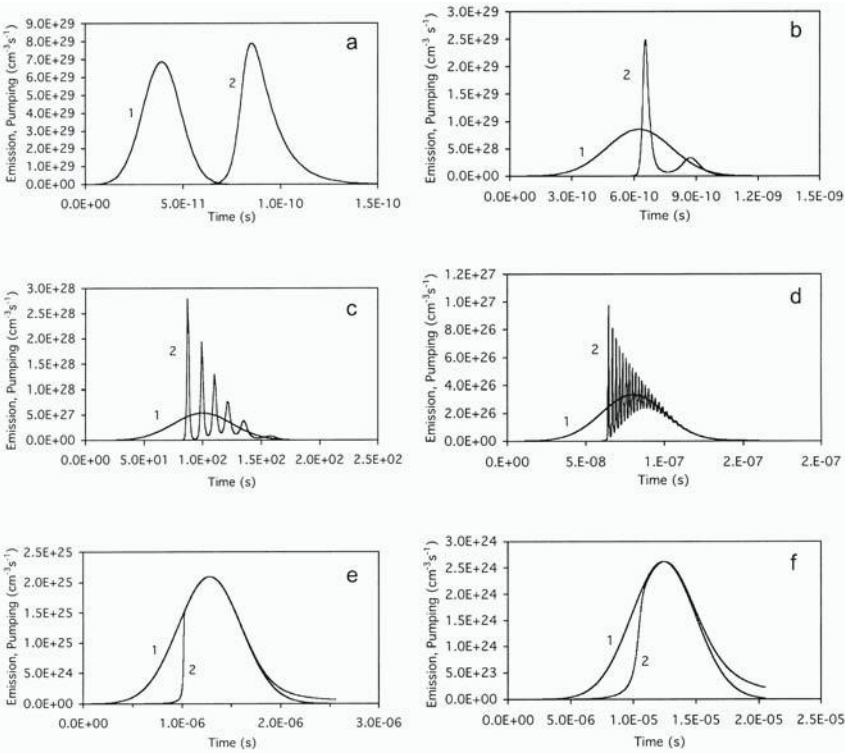

FIGURE 4.4. Pumping pulses (1) and corresponding stimulated emission pulses (2) calculated in random laser at constant pumping energy density $E/S = 0.5\,\mathrm{J/cm^2}$ and varying pumping pulse durations, t_{pump}. (a) $t_{pump} = 19.6\,\mathrm{ps}$; (b) $t_{pump} = 313\,\mathrm{ps}$; (c) $t_{pump} = 2.5\,\mathrm{ns}$; (d) $t_{pump} = 40\,\mathrm{ns}$; (e) $t_{pump} = 640\,\mathrm{ns}$; and (f) $t_{pump} = 5.12\,\mu\mathrm{s}$. Absorbed pumping rate and emission rate are given in terms of quanta/cm^3 s. Parameters of the system approximately correspond to $NdAl_3(BO_3)_4$ random laser: $\tau = 20\,\mu\mathrm{s}$, $\lambda_{em} = 1.06\,\mu\mathrm{m}$, $\sigma_{em} = 1 \times 10^{-18}\,\mathrm{cm^2}$, $\tau_{res} = 10\,\mathrm{ps}$, $k_{abs,532} = 12.5\,\mathrm{cm^{-1}}$. (*Source*: Ref. [22].)

In regular lasers, when the duration of a pumping pulse t_{pump} is shorter than the spontaneous emission lifetime τ, the threshold energy E_{th} is nearly independent of t_{pump} and equal to

$$E_{th} \approx P_{th}^{\mathrm{cw}} \tau. \tag{4.15}$$

In random lasers characterized by a very strong dependence of the emission kinetics on t_{pump} (Figure 4.4), the invariance of the threshold pumping energy is not obvious a priori. The question arises whether dramatic threshold changes of the emission behavior in a pulsed regime can be described in terms of the same simple balance between gain and loss, which determines the threshold in a cw regime. In order to answer this question, the solution of Eqs. (4.14) was studied in Reference [23] in a wide range of shapes and widths of the pumping pulse.

4.3.1 Random Laser Threshold in cw Regime

In cw approximation, the system of rate equations (4.14) has a solution

$$n = \frac{E}{\tau_{res}\left(\dfrac{\zeta h\nu_e}{\tau} + c\sigma_{em}E\right)}, \tag{4.16}$$

$$E = \frac{\tau_{res}\nu_e}{2Sl_p\nu_p}\left[\left(P - P^*\right) \pm \sqrt{(P - P^*)^2 + 4\zeta 4PP^*}\right], \tag{4.17}$$

where

$$P^* = \frac{h\nu_p Sl_p}{\tau\tau_{res}\sigma_{em}c}. \tag{4.18}$$

[In Eq. (4.17), only the "+" sign has a physical meaning.] At $P \to \infty$, the asymptotic behavior of E is

$$E = \frac{\tau_{res}\nu_e}{Sl_p\nu_p}\left[P - P^*(1-\zeta)\right], \tag{4.19}$$

and at $P \to 0$,

$$E = \frac{\tau_{res}\nu_e}{Sl_p\nu_p}P\zeta. \tag{4.20}$$

According to Eq. (4.19), the slope efficiency above the threshold is independent of ζ and equal to

$$\eta \equiv \frac{E}{P} = \frac{\tau_{res}\nu_e}{Sl_p\nu_p}.$$

(The slope efficiency defined this way has units [s/cm^3]. It always can be easily renormalized to become unitless.)

At $\zeta \to 0$, the threshold pumping power is equal to $P_{th}^{\mathrm{cw}} = P^*$ [Eq. (4.19)] and the slope efficiency below the threshold approaches zero [Eq. (4.20)]. This is the case of regular lasers, in which $\zeta \to 0$.

In random lasers, especially in random lasers with incoherent feedback, where the emission is omnidirectional and the density of spectrally overlapped modes is very high, the value of ζ is determined by the quantum yield of luminescence (in a spectral band of laser emission) and cannot be neglected. The nonzero value of ζ lowers the value of the threshold to $P^*(1-\zeta)$ [Eq. (4.19)] and provides for nonzero slope below the threshold [Eq. (4.20)].

The input–output curves and the functions $n(P)$ calculated at different values of ζ and the spectroscopic parameters, which are typical of neodymium random lasers ($\sigma_e = 1 \times 10^{-18}\,\mathrm{cm}^2$, $\tau = 2 \times 10^{-4}\,\mathrm{s}$, $\tau_{res} = 1 \times 10^{-11}\,\mathrm{s}$, $l_p = 0.8\,\mathrm{mm}$, and $\lambda_p = c/\nu_p = 532\,\mathrm{nm}$), are depicted in Figure 4.5. The calculated value of P_{th}^{cw}/S is equal to $5 \times 10^2\,\mathrm{W/cm}^2$, expectantly, much lower than those experimentally determined in short-pulsed neodymium random lasers, $2 \times 10^5 - 10^9\,\mathrm{W/cm}^2$ [13] (the experimental pumping pulse durations are typically much shorter than the life-time of the metastable laser level). The curves calculated at $\zeta \to 0$,

which exhibit sharp thresholds and locking of the population inversion above the threshold, are typical of regular lasers. As ζ increases, the input–output curves become smoother and the value of population inversion determined at the threshold differs from that as $P \to \infty$. The predicted smoothness of cw thresholds in random lasers is in agreement with that observed experimentally [24] (inset of Figure 4.5).

At $\zeta = 1$, the input–output curve does not have a threshold at all. This result is easy to understand because the laser process cannot improve the quantum yield of emission (which is already equal to unity), and the output is linearly proportional to the input. The pumping-dependent contributions from the spontaneous emission and the stimulated emission to the total emission are also shown in Figure 4.5. Note that at $P \to \infty$, the asymptotic behavior of *stimulated* emission is given by Eq. (4.19) at $\zeta = 0$. (The same asymptotic behavior of stimulated emission contribution holds for all values of ζ.)

Note the thickness of the pumped layer l_p and the residence time τ_{res}, which enter Eqs. (4.14 to 4.20), can be calculated using the diffusion model; see Section 4.6.

4.3.2 Random Laser Threshold in Pulsed Regime

In Reference [23], the study of random laser dynamics started with examining the case of an infinitely long steplike pumping pulse turned on at $t = 0$. The kinetics of emission $E(t)$ and population inversion $n(t)$ have been calculated numerically at different pumping intensities.

At low pumping power, $P < P_{th}^{\mathrm{cw}}$, the emission is predominantly spontaneous. In this regime, the characteristic time constant of the buildup of $E(t)$ and $n(t)$ $[\infty(1 - e^{-t/\tau})]$ is close to the lifetime τ. With an increase of the pumping power to P_{th}^{cw}, gain balances loss and the system reaches the lasing threshold. However at ζ of the order of 1 (the condition which is approximately satisfied in many random lasers), this does not cause any significant change of the stimulated emission dynamics (Figure 4.6a). Likewise, the character of stimulated emission remains the same in some range of power exceeding P_{th}^{cw}. In the latter case, the only predicted change is the shortening of the characteristic buildup times for $E(t)$ and $n(t)$.

At much higher pumping power, the character of stimulated emission changes significantly: after a certain duration of the pumping pulse, the emission intensity increases in almost steplike manner (Figure 4.6b). A sharp increase of the emission density is associated with the threshold of the random laser. At even stronger pumping power, characteristic relaxation oscillations are predicted in the stimulated emission kinetics (Figure 4.6c).

Note that at $\zeta \to 0$ (the case of regular lasers), the shape of the stimulated emission kinetic calculated at $P = P_{th}^{\mathrm{cw}}$ approximately resembles the one in Figure 4.6b, but not that in Figure 4.6a. At the same time, kinetics computed at much higher pumping intensities do not strongly depend on the value of ζ.

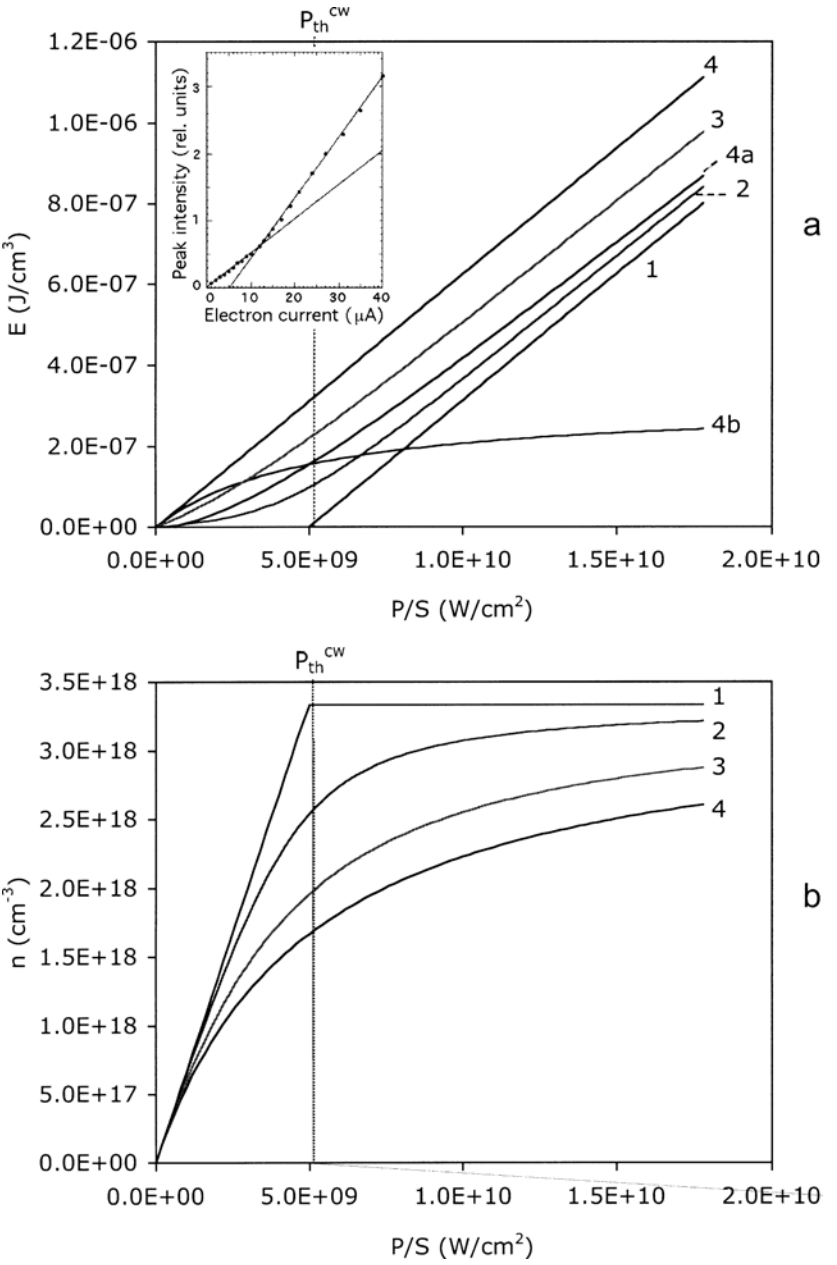

FIGURE 4.5. (a) Calculated input–output curves of random laser emission. Curve 4, calculated at $\zeta = 10^{-6}$, is typical of regular lasers. Curves 2, 3, and 4 are calculated at $\zeta = 0.1$, 0.5, and 1, correspondingly. Curves 4a and 4b, calculated at $\zeta = 1$, correspond to the *stimulated* emission contribution and *spontaneous* emission contribution to the total emission. (b) Functions $n(P)$ corresponding to the emission curves in Figure a. (*Source*: Ref. [23].) Inset of (a): peak emission intensity (at $\lambda_{em} = 362\,\text{nm}$) of Ce:$\delta$-$Al_2O_3$ random laser pumped with dc electron beam as a function of current. (After [24].)

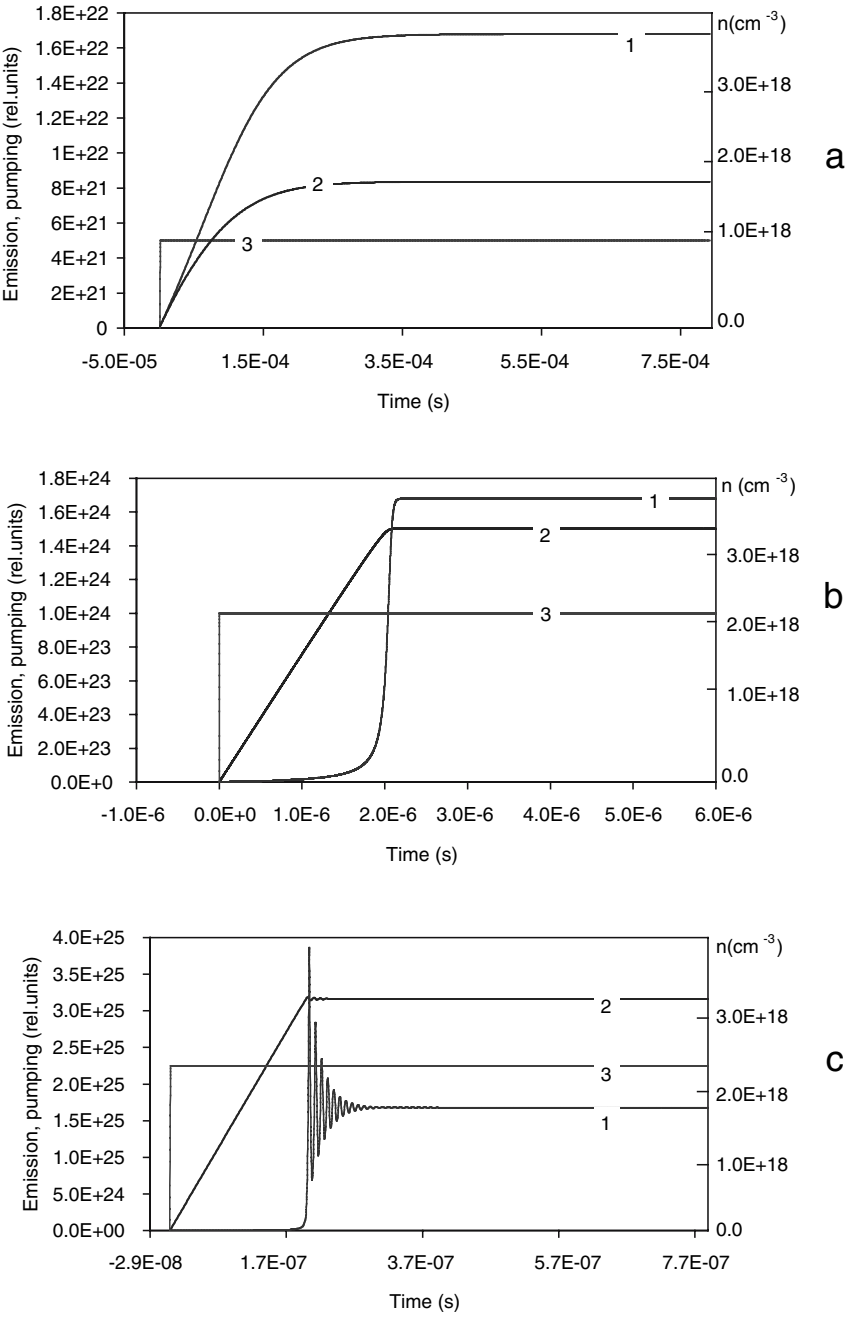

FIGURE 4.6. Kinetics of emission energy density $E(t)$ (trace 1) and population inversion $n(t)$ (trace 2) calculated at $\zeta \to 1$ at steplike pumping (trace 3): (a) $P/S = 5 \times 10^2\,\mathrm{W/cm^2} = P_{th}^{\mathrm{cw}}/S$; (b) $P/S = 5 \times 10^4\,\mathrm{W/cm^2} = 100 P_{th}^{\mathrm{cw}}/S$; and (c) $P/S = 5 \times 10^5\,\mathrm{W/cm^2} = 1000 P_{th}^{\mathrm{cw}}/S$. (*Source*: Ref. [23].)

TABLE 4.1. Invariance of pumping energy in random laser excited with pulses of different duration. (*Source*: Ref. [23].)

Type of pumping	P/S (W/cm^2)	t_{pump} (ns)	E/S (J/cm^2)
cw	5×10^2		
Infinitely long rectangular step	5×10^4	2000[a]	0.1
Infinitely long rectangular step	5×10^5	200[a]	0.1
Rectangular pulse	2×10^5	500	0.1
Rectangular pulse	2×10^6	50	0.1
Rectangular pulse	2×10^7	5	0.1
Gaussian pulse		50	0.1
Gaussian pulse		10	0.1
Gaussian pulse		2.5	0.1

[a]Time of the steplike increase of the emission intensity.

The dynamics of stimulated emission and the lasing thresholds were further investigated under pumping of the system with short rectangular and Gaussian pulses, the duration of which ranged between 5 and 500 ns [22]. In this regime, which closely resembles the one realized in many random laser experiments, the threshold is associated with the appearance of the first short pulse in the stimulated emission kinetics; see also Section 4.2.

In several different pumping regimes discussed above the behavior of stimulated emission was strongly different. However, as follows from Table 4.1, summarizing pumping powers and pulse durations at different excitation conditions, the threshold energy is an invariant value given by Eq. (4.15) if $t_{pump} \ll \tau$. Thus, knowing the threshold pumping power of a random laser at one pulse duration, it is possible to predict its value at a different pulse duration or cw excitation.

The result above has another important consequence. Despite the fact that the majority of random lasers operate in pulsed regime, many theoretical studies of random laser emission are carried out in cw approximation; see, for example, References [25–27]. At the same time, few studies were done to justify the use of a cw approximation for the analysis of pulsed random lasers. The result above suggests that it is possible to study the dependence of the random laser threshold or slope efficiency on some of the system parameters (transport mean free path, diameter of the pumped spot, etc.) in a cw regime and expect to have the same dependence in a pulsed regime.

4.4 Spectral Dynamics of Neodymium Random Lasers

To calculate the spectral dynamics of random laser, one can divide the spectrum of spontaneous emission $I(\nu)$ into N frequency channels $(\nu_1, \nu_2, \ldots, \nu_i, \ldots, \nu_N)$ and then expand the system (4.14) to $N + 1$ equations, where the first equation accounts for the population inversion n and other N equations describe the

stimulated emission dynamics $E(\nu_i)$ in each of N spectral channels:

$$\frac{dn}{dt} = \frac{P(t)}{Sl_p h\nu_{pump}} - \frac{n}{\tau} - \sum_{i=1,\ldots,N} \frac{E(\nu_i)}{h\nu_i} c\sigma_{em}(\nu_i)n,$$

$$\frac{dE(\nu_1)}{dt} = -\frac{E(\nu_1)}{\tau_{res}} + \frac{I(\nu_1)}{\sum_{i=1,\ldots,N} I(\nu_i)} \zeta \frac{n}{\tau} h\nu_1 + E(\nu_1) c\sigma_{em}(\nu_1)n,$$

$$\frac{dE(\nu_i)}{dt} = -\frac{E(\nu_i)}{\tau_{res}} + \frac{I(\nu_i)}{\sum_{i=1,\ldots,N} I(\nu_i)} \zeta \frac{n}{\tau} h\nu_i + E(\nu_i) c\sigma_{em}(\nu_i)n,$$

$$\frac{dE(\nu_N)}{dt} = -\frac{E(\nu_N)}{\tau_{res}} + \frac{I(\nu_N)}{\sum_{i=1,\ldots,N} I(\nu_i)} \zeta \frac{n}{\tau} h\nu_N + E(\nu_N) c\sigma_{em}(\nu_N)n. \quad (4.21)$$

Here $E(\nu_i)$ is the emission energy density and $\left(I(\nu_i)\big/\sum_{i=1,\ldots,N} I(\nu_i)\right)$ is the fraction of total spontaneous emission intensity in the spectral channel i. The photon residence time τ_{res} was assumed to be frequency-independent. The calculated spectral dynamics in the very beginning of the development of the emission pulse is shown in Figure 4.7a. As follows from this figure, different spectral components attain significant stimulated emission intensities at different times, depending on their emission cross sections. With the increase of time, the spectral component characterized by the highest emission cross section predominates in the spectrum. Simultaneously, the intensities of other (weaker) spectral components become saturated (compare, for example, the emission dynamics at 1.061 and 1.042 μm, Figure 4.7a). When the strongest spectral component predominates over all others, it behaves as predicted by Eqs. (4.14), which neglect any spectral dependence of the emission intensity. This is confirmed by Figure 4.8b showing the further evolution of the spectral dynamics depicted in Figure 4.7a. Note that the intensity scale in Figure 4.7b is 10,000 times larger than that in Figure 4.7a. The dramatic increase of the peak emission intensity above the threshold is in agreement with the experimental results (Ref. [20]).

Note that in Reference [28] a spectral dynamics of a liquid dye random laser emission, qualitatively similar to that discussed in this section, was modeled using a Monte Carlo simulation of a random photon walk (diffusion photon motion) in a scattering medium with gain.

4.5 Stimulated Emission in One-Dimensional Array of Coupled Lasing Volumes

The dynamics of stimulated emission in a one-dimensional strip of amplifying volumes separated by partially reflective walls (granules composing random laser

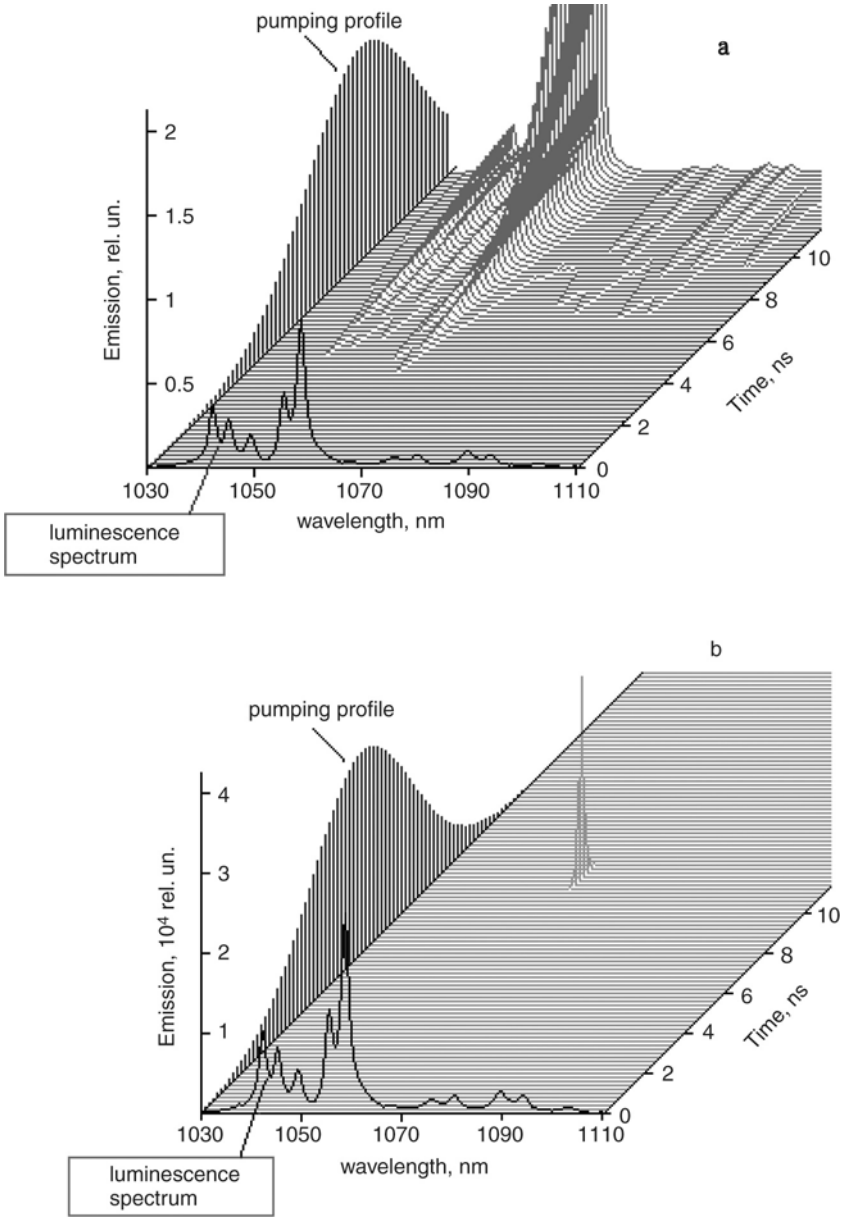

FIGURE 4.7. Spectral dynamics of stimulated emission in $Nd_{0.5}La_{0.5}Al_3(BO_3)_4$ powder under 532 nm Q-switched pumping: (a) initial stage of the pulse development; (b) developed laser pulse. Pumping pulsewidth (at $1/e^2$ level): 5 ns; absorption coefficient at the pumping wavelength: $25\,cm^{-1}$; photon residence time $\tau_{res} = 10$ ps; Nd luminescence lifetime: 20 μs, maximum Nd emission cross section: 1×10^{-18} cm^2. The intensities of the pumping pulse and the Nd luminescence spectrum are not shown in scale. (*Source*: Ref. [22].)

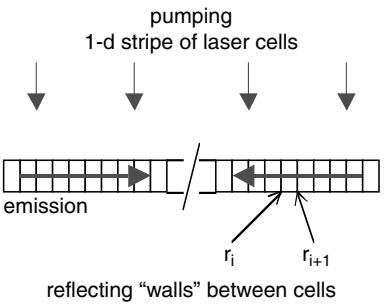

FIGURE 4.8. Schematic diagram of one-dimensional strip of lasing volumes. (*Source*: Ref. [29].)

material) was studied in References [29,30], Figure 4.8. In the numerical calculations, the cell size was equal to 1 μm, which corresponded to a typical particle size in neodymium random lasers. All cells were assumed to be pumped uniformly. In the model, emission could propagate only along the strip, one photon flux going to the right and one to the left. Reflection coefficients of the cell walls r were calculated with the help of a random function generator and were randomly distributed between $r = 0$ and $r = 2r_{aver}$, where r_{aver} was the average reflection coefficient. In a similar way, the photon loss l (caused, for example, by absorption) was calculated for each cell, with the value of l randomly distributed between $l = 0$ and $l = 2l_{aver}$, where l_{aver} was the mean value of the loss.

The model aimed to describe neodymium random lasers, which are characterized by low coherence (Section 2.7), and was based on the system of rate Eqs. (4.14) that inherently neglected any coherence effects. In the computation procedure, instead of direct introduction of the residence time τ_{res} to the system, two neighboring cells were allowed to "communicate" with each other, exchanging photons, in accordance with the reflection and transmission coefficients assigned to each intercell boundary. The bouncing of reflected photons back and forth determined the photon residence time in a strip. The other random laser parameters were assumed to be similar to those used in the calculations in Sections 4.2 and 4.3.

The typical calculated two-dimensional (time/cell number) kinetics of emission characterized by relaxation oscillations is shown in Figure 4.9a (see Color Plate 2). In this particular calculation, the strip consisted of 100 cells, r_{aver} was equal to 8% and the mean residence time of the photon in the system was equal to $\tau_{res} = 0.43$ ps. As follows from Figure 4.9a, in the system with feedback the emission becomes localized (confined) in the central part of the pumped volume.

In the presence of loss, multiple spatially confined locations of stimulated emission can be predicted in a strip of lasing cells (Figure 4.10, see Color Plate 3). (At the threshold, the stimulated emission in the strip occurs only in one localized spot. However, with the increase of the pumping energy, the number of locations of confined stimulated emission increases.)

In a number of theoretical and experimental works (see, for example, Refs. [21,31–34]), the localization of random laser modes to volumes with characteristic sizes ranging from a fraction of wavelength to hundreds of wavelengths has been reported. According to [32], the number of localized lasing modes first increases

with the increase of the pumping intensity (in agreement with the results presented in this section) and then saturates at stronger pumping power. It is important to note that the localization in References [21,31–34] was treated as a property directly relevant to the coherence of a light wave. In contrast, as shown in [30], spatial localization of random laser intensity can also take place in the case of incoherent (nonresonant) feedback.

Figure 4.9b shows the dynamic of stimulated emission in a strip consisting of a larger number of cells, 400, and without loss or reflection at the cell boundaries, $l_{aver} = 0$, $r_{aver} = 0$. Because of the larger size of the strip, the mean photon residence time τ_{res} was equal to 0.67 ps, longer than that in the strip of Figure 4.9a. The amount of pumping energy per cell in Figure 4.9b was the same as that in Figure 4.9a. However, despite longer residence time, no short high-intensity pulses of stimulated emission have been predicted in the long strip. Furthermore, no spatial confinement of emission to the central part of the pumped volume is seen in Figure 4.9b. Instead, the emission has its maximum values at the ends of the strip, which is an expected behavior in the case of amplification in open paths. Although this has not been proved rigorously [30], it appears likely that relaxation oscillations and the spatial confinement accompany each other and can serve as evidence of feedback in the system.

The majority of known solid-state random lasers, including optically pumped neodymium random lasers [12,14,18], ZnO random lasers [21], and random lasers based on scattering polymers [35], operate in pulsed regime with relaxation oscillations. Based on the calculated result above, it has been concluded that all types of random lasers listed above do have feedback, which is necessary for the realization of relaxation oscillations and confinement of a lasing mode. Simple ASE in photon open paths, which are elongated by scattering, is not enough to cause the stimulated emission dynamics similar to that observed experimentally.

The major results of Reference [30] can be summarized as follows. (i) The feedback in random lasers is essential for the regime of relaxation oscillations. Elongation of open photon paths by scattering is not enough for producing a train of short stimulated emission pulses (relaxation oscillations) in response to one longer pumping pulse. (ii) Relaxation oscillations and the spatial localization of the stimulated emission accompany each other and apparently serve as evidence of feedback in the system.

4.6 Calculation of Random Laser Threshold in Diffusion Approximation

The threshold conditions for the appearance of short-pulsed stimulated emission in a medium with gain and scattering have been derived by Letokhov in the diffusion approximation in References [1–3]. The isolated gain volume in [1–3] was assumed to be uniformly pumped; however, the means of such pumping were not specified.

Most of the known solid-state random lasers are excited through the front surface and only a thin layer of the material is pumped efficiently.

In Section 4.3, the threshold population inversion n (Eq. 4.16) and the threshold absorbed pumping power $P_{th}^{cw}(1-\zeta) \equiv P^*(1-\zeta)$ [Eqs. (4.18) and (4.19)] were derived as functions of the thickness of the pumped layer l_p and the photon residence time τ_{res}. In Reference [29], the diffusion model was employed to derive the expressions for l_p and τ_{res} in a surface-pumped random laser in terms of the transport mean free path l_t and the absorption length l_a and then, after substituting the calculated values into Eq. (4.18), determining the threshold absorbed pumping density. In [29], the value ζ was assumed to be negligibly small. (Note that the pumping of a scattering gain medium from the front surface has also been considered in Refs. [10,36,37] and other publications.)

If the diameter of the pumped spot d is much greater than l_p, the propagation of incident light in scattering absorbing media can be adequately described in terms of the Kubelka–Munk model [38]. According to this model, the distribution of light intensity $I(z)$ in the depth of the medium is given by

$$I(z) \propto \exp(-\alpha z) \equiv \exp(-z/l_p), \tag{4.22}$$

where z is the coordinate perpendicular to the sample surface and $l_p \equiv \alpha^{-1}$ is the characteristic penetration depth given by

$$l_p = [K(K+2S)]^{-1/2}. \tag{4.23}$$

Here $K \approx 2\rho k_{abs}$ is the effective absorption coefficient of the material corrected for the porosity ρ, and S is the effective scattering coefficient [38]. One can rewrite Eq. (4.23) in terms of the absorption length $l_{abs} \equiv 1/k_{abs}$ and the transport mean free path at the pumping wavelength l_t^a as

$$l_p = \left[\frac{1}{l_{abs}}\left(\frac{1}{l_{abs}} + 2\frac{p}{l_t^a}\right)\right]^{-1/2}, \tag{4.24}$$

where p is the numerical factor of the order of unity. Note that Eq. (4.24) is almost equivalent to that known in diffusion theory

$$l_p = \sqrt{l_{abs} l_t/3} \tag{4.25}$$

at $l_t^a \ll l_{abs}$, and is more accurate than Eq. (4.25) at $l_t^a \geq l_{abs}$.

If the photon motion in scattering media is diffusion, the residence time of the emission photon in a pumped layer of thickness l_p is given in a first approximation by

$$\tau_{res} = \frac{q l_p^2}{D}, \tag{4.26}$$

where D is the diffusion coefficient and q is the form factor of the order of unity. To a first approximation, the layer of thickness l_p can be assumed to be pumped uniformly. The diffusion coefficient for photons in scattering media is given by [39]

$$D = \frac{c l_t^e}{3}. \tag{4.27}$$

Here l_t^e is the transport mean free path at the emission wavelength and l_a is the absorption length.

Combining Eqs. (4.24), (4.26), and (4.27) one gets the following expression for the photon residence time τ_{res}:

$$\tau_{res} = q\frac{3l_{abs}^2 l_t^a}{cl_t^e(2pl_{abs} + l_t^a)}. \tag{4.28a}$$

In many practically important situations in random lasers, $l_t^a \ll l_{abs}$. In this case Eq. (4.28a) can be simplified and rewritten as

$$\tau_{res} = \frac{3q}{2p}\frac{l_{abs}l_t^a}{cl_t^e}. \tag{4.28b}$$

If the transport mean free path at the pumping wavelength l_t^a is equal to that at the emission wavelength l_t^e, which is the case in powder composed of large particles ($s > \lambda$), then the photon residence time τ_{res} is determined solely by the absorption length l_{abs} and is independent of scattering,

$$\tau_{res} = \frac{3q}{2p}\frac{l_{abs}}{c} \approx \frac{3}{2}\frac{l_{abs}}{c}. \tag{4.28c}$$

(The index of refraction n is neglected in the consideration above. To account for the index of refraction, c should be replaced with c/n.)

Substituting Eqs. (4.24) and (4.28a) into Eq. (4.18), one obtains the following expression for the threshold absorbed pumping density in a random laser in the cw regime $P_{th}^{\mathrm{cw}} \equiv P^*$:

$$\frac{P_{th}}{S} = \frac{h\nu_{pump}\left[\frac{1}{l_{abs}}\left(\frac{1}{l_{abs}} + 2\frac{p}{l_t^a}\right)\right]^{-1/2} l_t^e}{3q\sigma_{em}\tau}. \tag{4.29a}$$

At $l_t^a \ll l_{abs}$, Eq. (4.29a) can be rewritten as

$$\frac{P_{th}}{S} = \left(\frac{\sqrt{2}}{3}\right)\left(\frac{\sqrt{p}}{q}\right)\frac{h\nu_{pump}}{\sigma_{em}\tau\sqrt{l_{abs}}}\frac{l_t^e}{\sqrt{l_t^a}}. \tag{4.29b}$$

If one assumes further that $l_t^a = l_t^e = l_t$, then Eq. (4.29b) can be simplified and rewritten as

$$\frac{P_{th}}{S} = \left(\frac{\sqrt{2}}{3}\right)\left(\frac{\sqrt{p}}{q}\right)\frac{h\nu_{pump}}{\sigma_{em}\tau}\sqrt{\frac{l_t}{l_{abs}}}. \tag{4.29c}$$

Note that a similar dependence of the threshold absorbed pumping density on l_t and l_{abs} has been derived in Reference [25] from a different physical requirement: that the frequency spacing between localized modes should be larger than the mode line width.

In diffusion approximation, the fraction of incident pumping power, which is absorbed in scattering medium, is proportional to $\sqrt{l_t^a/l_{abs}}$ [40,41]. Thus, under the assumptions used in Eq. (4.29b), the threshold incident pumping density is independent of absorption length l_{abs} and proportional to l_t^e/l_t^a. (A similar result was obtained in Ref. [42].) Correspondingly, under the additional assumption

$l_t^e = l_t^a$, the threshold incident pumping density is independent of both absorption length and photon mean free path.

4.7 Application of the Diffusion Model: Comparison with Experiment

In this section, the predictions of the diffusion model developed in Section 4.6 are compared with the experimental results of Section 2.10 (dependence of the random laser emission on the mean particle size) and Section 2.9 (dependence of the random laser emission on the powder density).

In both experiments, relaxation oscillations (which serve as an evidence of feedback in a system, Section 4.5) have been observed in the stimulated emission kinetics. The lack of coherence in neodymium random lasers indicates that the feedback mechanism is not resonant. Large mean scattering paths (longer than the wavelength) typical for the majority of the samples studied exclude the mechanism of Anderson localization [43–46]. Because crystalline granules composing the experimental samples were small and irregularly shaped (similar to those in Figure 2.7a), it was concluded that the feedback in laser powders occurred in *ensembles* of scatterers; see Sections 2.4 and 2.5.

According to Reference [39], the diffusion character of photon motion realizes at

$$\lambda < l_t \ll L, \tag{4.30}$$

where λ is the emission wavelength and L is the smallest linear size of the random laser medium (in the geometry of random experiments in Sections 2.9 and 2.10, L is equal to the penetration depth of pumping l_p).

In Section 3.2, the relationship between the transport mean free path l_t and the scattering mean free path l_s, which in tightly packed powders is approximately equal to the mean particle size s, has been studied in the geometrical optics approximation and at $s < \lambda$. The dependences l_t versus s calculated in a $NdSc_3(BO_3)_4$ random laser at the pumping and the emission wavelengths are shown in Figure 4.11 [29]. [This calculation is based on Eqs. (3.16) and (3.21), the value $1/(1 - \langle \cos \Theta \rangle)$ determined at the index of the refraction of the material $n = 1.84$ (Figure 3.7), and the normalized Mie scattering cross-section $Q^S(s)$, computed using the application program [47].]

The dependences depicted in Figure 4.11 are qualitatively similar to those experimentally measured and theoretically calculated in Reference [48] for ensembles of closely packed ZnO particles.

It has been shown in [29] that the condition (4.30) is satisfied in $NdSc_3(BO_3)_4$ powder at $s < 115$ (almost the whole range of the granule sizes used in Section 2.10). This justifies the application of the model developed in Section 4.6 to the neodymium random lasers of Section 2.10. (The same arguments are applicable to the samples of Section 2.9.)

In neodymium random lasers studied in Chapter 2, the values of the transport mean free path at the pumping and the emission wavelengths are much smaller

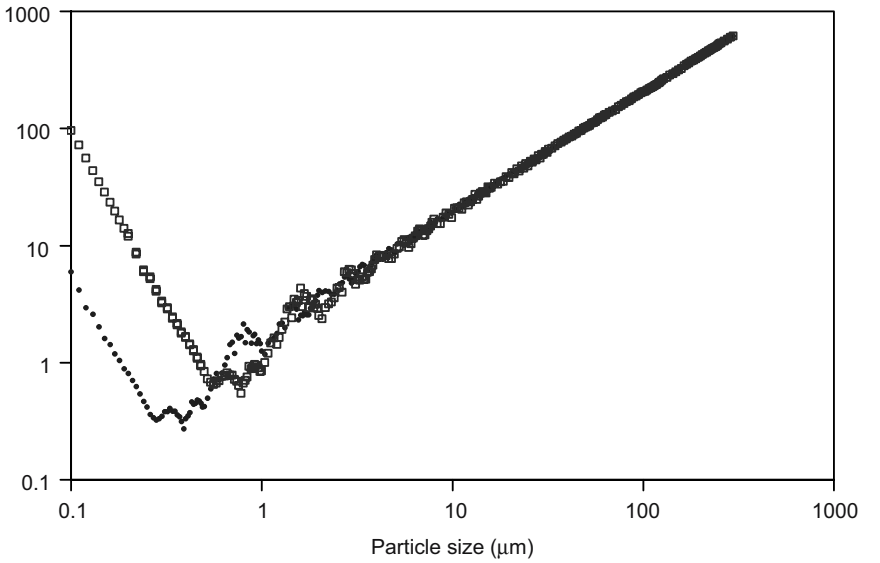

FIGURE 4.11. Transport mean free path l_t in $NdSc_3(BO_3)_4$ powder calculated according to Eqs. (3.16) and (3.21) as a function of mean particle size $s (s = l_s)$: trace 1 (open squares), $\lambda = 1.06\,\mu m$; trace 2 (filled circles), $\lambda = 0.53\,\mu m$; dashed line, wavelength-independent value of l_t calculated according to Eq. (3.16). (*Source*: Ref. [29].)

than the absorption length l_{abs} or the gain length l_g. Thus, Eq. (4.29b) can be used for the calculation of the threshold absorbed pumping density.

By substituting $l_t^a(s)$ and $l_t^e(s)$ plotted in Figure 4.11 into Eq. (4.29b) and assuming that the powder volume density and, correspondingly, l_{abs} do not change with the change of s, one can calculate the dependence of the threshold absorbed pumping energy in the $NdSc_3(BO_3)_4$ random laser on the particle size s (Figure 2.29). According to Figure 2.29, the dependence of the threshold absorbed pumping density on s, as calculated in the diffusion approximation, is in good qualitative agreement with the analogous experimental curves. Indeed, both calculated and experimental curves demonstrate strong increase of the threshold pumping density at very small and very large particle sizes and reduction of the threshold at intermediate particle sizes. However, a more careful analysis of the data plotted in log–log coordinates shows that the calculated and the experimental curves have significantly different slopes at $s > 1\,\mu m$ (1/2 and $<1/4$, respectively); see Figure 2.29 inset.

The input–output curves plotted in Figure 2.25b (Section 2.9) versus absorbed pumping energy correspond to four $Nd_{0.5}la_{0.5}Al_3(BO_3)_4$ random lasers characterized by different volume densities (filling factors) of laser material. In regular lasers, such a series of parallel input–output curves would be expected if the only difference among the four lasers (characterized by low intracavity loss) is the cavity Q-factor, higher Q-factor corresponding to lower threshold.

In random lasers, it is reasonable to relate the Q-factor to the photon residence time τ_{res}, which is inversely proportional to the absorption coefficient k_{abs}; see Eq. (4.28c). [Note that in powders of Section 2.9, $s > \lambda$ and $l_t^a \approx l_t^e$. This justifies the use of Eqs. (4.28c) and (4.29c).] Following this argument, the input–output curve characterized by the lowest threshold (circles) should correspond to the smallest absorption coefficient k_{abs} and the input–output curve characterized by the highest threshold (diamonds) should correspond to the largest absorption coefficient. This is exactly the case for the data of Figure 2.25b, because the curve with the lowest threshold corresponds to the material with the smallest volume density and the curve with the highest threshold corresponds to the material with the largest volume density.

Alternatively, according to Eq. (4.29c) the value of the threshold should be proportional to $\sqrt{l_t k_{abs}}$. If l_t is constant, then the monotonic dependence of the threshold on k_{abs} is qualitatively similar to that discussed above. The dependence of l_t on the material volume density is not known exactly. One can speculate that in strongly compressed powders or sintered ceramics, the air gaps between particles become smaller than the wavelength, which leads to the reduction of the scattering efficiency and increase of l_t. Thus, the experimental dependence of the random laser threshold on the volume density (filling factor) of the laser material can be qualitatively explained in terms of the diffusion model developed in Section 4.6.

4.8 Dependence of the Random Laser Threshold on the Diameter of the Pumped Spot

As shown in Section 2.8, the threshold energy density E_{th}/S in a $Nd_{0.5}La_{0.5}Al_3(BO_3)_4$ random laser depends on the diameter of the pumped spot d as $E_{th}/S \propto 1/d + const$ at $d \geq 130$ (Figure 2.24b, circles). Reasonably similar functional relationships have been observed in ZnO thin films, $E_{th}/S \propto 1/d^{1.04}$, and the PMMA film doped with rhodamine 640 dye and TiO_2 nanoparticles ($l_t = 0.9\,\mu m$), $E_{th}/S \propto 1/d^{1.2}$ [25].

The threshold dependence above is strongly different from that predicted by Letokhov in the diffusion approximation for a uniformly pumped cylinder with height h and diameter d, $\propto (4.8/d)^2 + (\pi/h)^2$ [1–3] (Figure 2.24b, solid line). A seeming discrepancy between the experimental results and the predictions of the diffusion model initiated a number of theoretical studies where the experimental threshold dependence was explained in terms of low dimensionality of a thin-film random laser [25] or strong dispersion of the loss factors of lasing modes [25,49]. As shown in this section, the experimental dependence E_{th}/S versus d can be predicted in terms of the diffusion model if the realistic geometry of experiment and boundary conditions are taken into account [50]. In the numerical simulation [50], emitted photons were allowed to walk both in a pumped volume and surrounding it scattering medium without gain. On the other hand, Letokhov

considered a 'free-standing' cylindrical pumped volume with no reflections at the boundaries [1–3]. This was the principal difference between the assumptions made in References [1–3] and in this section.

4.8.1 Model and Monte Carlo Simulation of the Residence Time

The developed theoretical model, explaining the experimental results of Section 2.8, is based on the following assumptions:

1. Stimulated emission in a random laser occurs in a system with feedback. In fact, according to Section 4.5, relaxation oscillations observed in the kinetics of a random laser emission serve as evidence of feedback in the system.
2. Because crystalline granules composing the experimental sample are small and irregularly shaped, it has been concluded that the feedback in the random laser studied occurs in an *ensemble* of scatterers (Sections 2.4 and 2.5).
3. Stimulated emission in neodymium random lasers can be adequately described with the system of Eqs. (4.14).
4. The residence time τ_{res} is assumed to be proportional to the average photon pathlength inside the pumped volume. The pathlengths of random photon walks are assumed to be unaffected by gain or absorption. An escape of photons to the air is assumed to be the only loss mechanism for the photon density in the scattering medium.
5. Because the transport mean free path of photons in the experiment was much greater than the light wavelength and much smaller than the characteristic linear size of the pumped volume, the character of the photon motion in the random laser medium (following the criterion of Ref. [39]) was assumed to be diffusion.

In the $Nd_{0.5}La_{0.5}Al_3(BO_3)_4$ ceramic sample studied in Section 2.8, irregularly shaped and randomly positioned granules of laser material are separated by air gaps. Reflection and refraction of light at crystalline–air boundaries determine the scattering of photons in the medium. In the computer simulation, for the sake of simplicity, the photon walks were examined in a periodic three-dimensional matrix composed of cubic cells (Figure 4.12a). Because no wave coherence effects have been taken into account, the diffusion character of photon motion in a regular matrix should not be much different from that in an ensemble of randomly positioned scatterers. The size of a cubic cell was associated with the average size of granules forming the ceramic. Each cell was assumed to contain five partially reflecting planes (thin plane-parallel slides) with the index of refraction equal to that of $Nd_{0.5}La_{0.5}Al_3(BO_3)_4$ (Figure 4.12b). Photons in the system were allowed to propagate through the centers of the cubic cells along the axes of a matrix [1,0,0], [0,1,0], and [0,0,1]. The probability of a photon to be reflected by one of the planes (or to propagate through the cell without reflection) was proportional to the corresponding Fresnel coefficients. Light was assumed to be depolarized. The

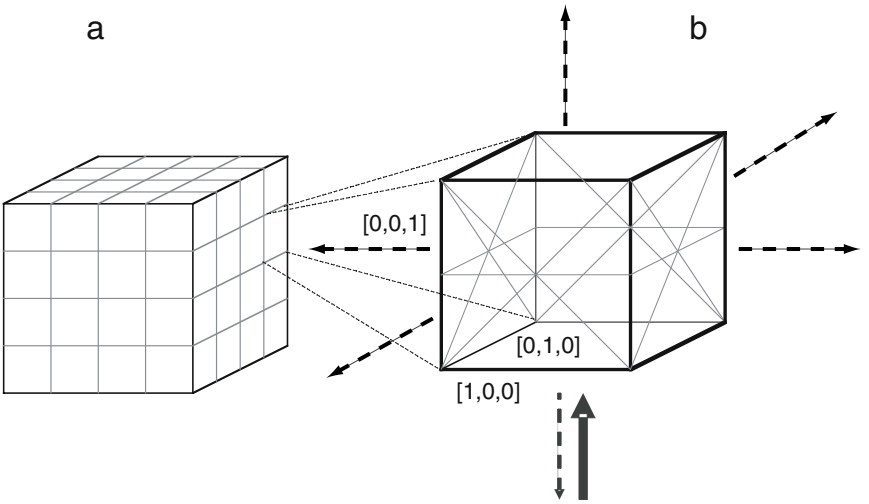

FIGURE 4.12. (a) Matrix of scattering cubic unit cells; and (b) a single cubic unit cell with scattering planes, where a bold arrow indicates the incoming light and dashed arrows indicate possible directions of the reflected light. (*Source*: Ref. [50].)

pumped volume in the model was a cylinder (disk), with diameter d and height h, adjacent to the medium–air boundary. The cylinder was assumed to be uniformly pumped.

In the computer model, the spontaneous emission of photons inside a pumped volume, as well as the further photon motion through the scattering medium, was governed by a random function generator, which output, when appropriate, was weighed with the Fresnel reflection coefficients. The photon walks were calculated until photons left the scattering medium to the air. (Otherwise, the calculation was aborted after 10^5 steps. Only very small percentage of photons did not leave the system over this time.) For each photon walk, the number of steps inside the pumped volume was counted. A large number of photon walks were simulated and the average was taken over different realizations. As with any simplified model, this calculation neglected certain effects that can take place in real ceramic, such as occasional multiple reflections of light inside crystalline granules. However, as shown below, the model adequately describes the diffusion character of photon motion and, thus, serves the purpose.

4.8.2 Calculation Results

To confirm that the photon motion calculated according to the procedure described in Section 4.8.1 was, indeed, diffusion, the average square deviation of the photon position from the point of the photon's origin was calculated as the function of

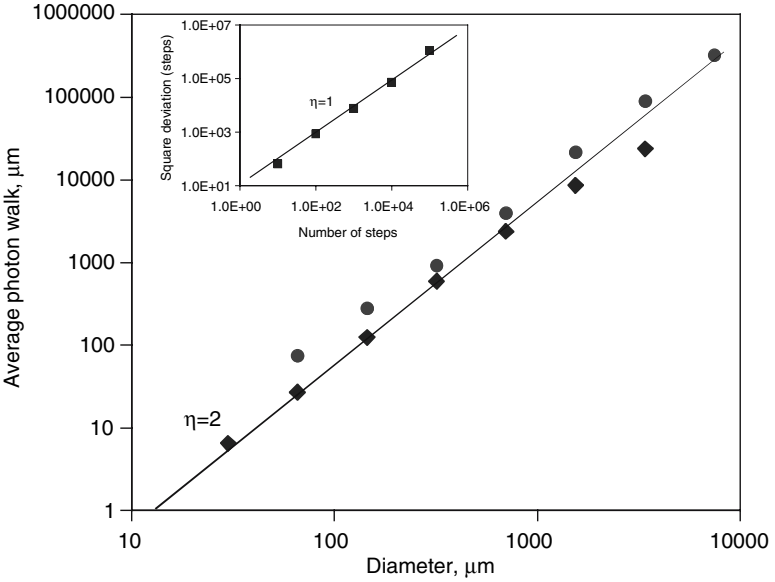

FIGURE 4.13. Dependence of the average photon walk versus d, calculated for different sizes of the cubic unit cell. Circles: cylinder with height $h = 60\,\mu$m, and diamonds: sphere. Inset: computed average square deviation of the photon from the point of its origin as the function of the step number. (*Source*: Ref. [50].)

the step number (which is proportional to time in a real experiment). The linear dependence depicted in the inset of Figure 4.13 confirms the diffusion character of the modeled photon motion.

As the next step, the dependence of the residence time τ_{res}^{p} and, accordingly, of the threshold gain g_{th} on the size of the pumped volume was calculated in two configurations studied by Letokhov in [1–3]. (In the used model of a random laser, which is outlined in Sections 4.2 and 4.8.1, τ_{res} is proportional to the number of steps, g_{th} is proportional to the threshold pumping energy E_{th}, and E_{th} is inversely proportional to τ_{res}.) In particular, the dependence of g_{th} on d was examined in spherical and cylindrical uniformly pumped scattering volumes. The boundary conditions (similarly to Refs. [1–3]) neglected any reflection at the medium–air interface or the return of escaped photons back to the gain volume. The calculation yielded the dependence $g_{th} \propto (\tau_{res}^{p})^{-1} \propto d^{-2}$ for the sphere and the dependence $g_{th} \propto (\tau_{res}^{p})^{-1} \propto d^{-2} + const$ for the cylinder, both relationships predicted by Letokhov [1–3]. This agreement can be used as reasonable evidence of the validity of the proposed model and the assumptions made.

Finally, the dependence of the photon residence time τ_{res}^{p} on d for the flat-disk geometry of the pumped volume realized in the experiment of Section 2.8 was calculated. The series of the $(\tau_{res}^{p})^{-1}$ versus d curves, calculated for different sizes of the cubic unit cell, is shown in Figure 2.24b. In this calculation, the depth of the pumped layer was assumed to be $60\,\mu$m, which is a reasonable value for

neodymium random lasers [51]. As follows from this figure, the inverse photon residence time $(\tau_{res}^{p})^{-1}$, which is proportional to the threshold pumping density E_{th}/S, depends on d as $(\tau_{res}^{p})^{-1} \propto 1/d + const$, which means that the experimental and the calculated curves in Figure 2.24b have the same functional dependence on d. This functional dependence is distinctly different from that predicted by Letokhov [1–3] (Figure 2.24b, solid curve) and the one calculated when no escaped photons were allowed to return back to the pumped volume (Figure 4.13). The agreement between the theory and the experiment in the power dependence E_{th}/S versus d obtained above justifies the proposed theoretical model and the assumptions made in the beginning of Section 4.8.1.

The numerical discrepancy between the experimental and the calculated values of the constant C_2 in formula (2.2) ($1\,\mathrm{cm}^{-1}$ and $\approx 1\,\mathrm{mm}^{-1}$, respectively) can probably be explained by underestimated values of h or l_t or by nonuniform spatial distribution of excitation in the pumped volume.

By varying parameters h, l_t, s, and the distance between the pumped volume and the medium–air boundary, one can obtain a broad variety of the functional relationships $(\tau_{res}^{p})^{-1} \propto 1/d^{x} + const$, with the parameter x varying between 1 and 2. Thus, various functional dependences E_{th}/S versus d obtained in the experiments of different research groups may not be in disagreement with the predictions of the diffusion model.

4.9 Model of Coupled Intraparticle Resonators

In order to characterize the effective cavity (cavities) supporting stimulated emission in a neodymium random laser, the authors of Reference [12] analyzed its linewidth $\Delta\nu$. Assuming that $\Delta\nu$ is determined by the loss in a resonator cavity, they have used a standard formula for a resonator Q-factor

$$Q = \frac{\nu_0}{\Delta\nu} = \frac{2\pi l \nu_0}{\frac{c}{n}(1-r)} \tag{4.31}$$

to estimate the value of the output coupling $(1 - r)$. (Here ν_0 is the central frequency of emission, l is the effective distance between reflectors, n is the index of refraction, and c is the speed of light.) Further presuming that the effective cavity length l was equal to the particle size, $s \approx 10^{-3}$ cm, they have determined from the experimental value $\nu_0/\Delta\nu$ the parameters $Q = 10^4$ and $r = 0.99$. The closeness of the effective reflection coefficient to unity suggested that the total internal reflections played a significant role in the lasing process.

In a typical laser material with the index of refraction $n = 1.8$–2.0, the angle of total internal reflection is equal to $\varphi = 33.7$–30 degrees. Assuming that the angles of incidence of emission light-generated inside particles are random, the average probability of total internal reflection is given by $F = \cos\varphi$. Correspondingly, the

average number of reflections, which the photon makes inside a particle before it leaves it, is equal to $k = (1 - F)\sum_m mF^{m-1}$ [12]. At $n = 1.9$, $F = 0.85$ and $k \approx 7$. It was further calculated [12] that for a photon, which makes $k = 7$ reflections within one particle before moving to another particle (experiencing 20% reflection loss at the two medium–air boundaries), the average reflection coefficient is equal to $r \approx 0.97$. This value is much smaller than $r = 0.99$ estimated above from the linewidth $\Delta\nu$. Thus, it has been concluded [12] that ring laser modes supported by total internal reflections within individual particles, rather than collective modes in which photons freely walk from one particle to another, support stimulated emission in neodymium powder (random) lasers.

The emission supported by intraparticle ring resonators was further modeled in Reference [12] with the rate equations, which accounted for the population inversion and the emission photon density in a cavity and, similar to Eqs. (4.14), predicted relaxation oscillations in random lasers. Different powder particles have different shapes and sizes. In addition, the pumping intensity varies with the depth of the powder. The dispersion of individual parameters of independent granules should smear out any short spikes in the emission kinetics of an ensemble of particles, thus making the calculated kinetics different from those observed experimentally.

In order to describe the (not smeared) relaxation oscillations observed in experiments, it was further assumed that emission in individual particles was synchronized due to a weak coupling between them [12]. The calculated dynamics of stimulated emission in two and three coupled resonators (see, for example, Figure 4.3b) looked similar to the experimental ones. Thus, it was concluded [12] that stimulated emission in a random laser was supported by weakly coupled intraparticle resonators.

(The arguable point in the analysis above is the unjustified assumption that the characteristic cavity size l is equal to the particle size $s \approx 10^{-3}$ cm. Instead, one can hypothesize that l is larger than s; for example, $l = 10s$. In this case, the effective reflection coefficient will be equal not to $r = 0.99$, but to $r = 0.9$, Correspondingly, no assumption of high-quality intraparticle ring resonators would be needed to explain the relatively low value of the reflection coefficient $r = 0.9$.)

The idea of coupled intraparticle resonators has been further developed in Reference [16]. As shown in Section 4.1, the diffusion model cannot adequately describe the wavelength shifts in the mixture of $Na_5La_{0.05}Nd_{0.95}(MoO_4)_4$ and $Na_5La_{0.85}Nd_{0.15}(MoO_4)_4$ powders. In search for a better theory explaining the experimental results, the authors of [16] employed the model of coupled intraparticle resonators. The active material was described in terms of the Liouville equation for the density matrix and the field was described by the reduced Maxwell equation taking into account the polarization of the medium determined by the off-diagonal elements of the density matrix. It was further assumed that there were only two types of particles in the mixture (highly doped and low doped) and that the transition frequency was the only difference between them. By introducing the normalized values of the density matrix elements $R = \rho\mu^2/2\varepsilon_0\hbar\omega$, complex field amplitude $E = E\mu/\hbar\omega$, pumping intensity $P = p\mu^2/2\varepsilon_0\hbar\omega$, decay rate $\Gamma = \gamma/\omega$, and time

$t_1 = t\omega$, the following system of equations was obtained [16].

$$\begin{aligned}
\frac{dR_{ja}}{dt_1} &= -\Gamma_a R_{ja} - \frac{i}{2}\left(R_j E_j^* - R_j^* E_j\right) + P_j,\\
\frac{dR_{jb}}{dt_1} &= -\Gamma_b R_{jb} + \frac{i}{2}\left(R_j E_j^* - R_j^* E_j\right),\\
\frac{dR_j}{dt_1} &= -\Gamma R_j - \frac{iR_j}{\omega}\left(\omega_j - \nu\right) - i\left(R_{ja} - R_{jb}\right)E_j,\\
\frac{dE_j}{dt_1} &+ \frac{iE_j}{\omega}\left(\Omega_j - \nu\right) + \frac{E_j}{Q_j} - M_{jl}E_l = iR_j. \qquad (4.32)
\end{aligned}$$

Here indexes $j, l = 1, 2$ apply to high and low neodymium-doped components, respectively; R_a and R_b are the diagonal elements of the density matrix and R_j are the off-diagonal elements of the density matrix; Ω_j and Q_j are, respectively, the eigenfrequency and the quality factor of the cavity of the j_{th} type; and ν is the steady-state frequency. The coupling coefficient M_{jl} is given by $M_{jl} = k_{jl}\tau_l$, where k_{lj} is the number of particles of type l located near the particle of type j and $\tau_l = \tau\exp(i\zeta)$ is the complex coupling coefficient.

Solving Eqs. (4.32) and substituting to the solution the known values of the spectroscopic parameters, the authors of [16] obtained better agreement between the calculation and the experiment than in the case where they used a diffusion model. This agreement was used as a proof of the validity of the coupled resonator model.

One should note that the model developed in Reference [16] used many simplifying assumptions. Thus, only two types of particles were considered, the only difference between high- and low-concentration particles was the transition frequency, etc. This makes the justification of the model of coupled resonators not very rigorous.

Apparently, an intraparticle feedback scenario is realized in certain random laser materials, but not in all of them. As shown in [52], stimulated emission supported by intraparticle resonances is observed in powders composed by large ($\geq$50 μm) regularly shaped particles. At the same time in fine powders, the particles of which have irregular shapes, stimulated emission is supported by scattering occurring in an ensemble of particles [52,18].

Note that the concept of coupled resonators is similar to the idea of coupled dipole oscillators (like those in the Mie theory), which was recently proposed in Reference [49] in order to describe the stimulated emission in ZnO powder and random lasers based on polymers mixed with TiO_2 particles.

References

1. V.S. Letokhov, Stimulated emission of an ensemble of scattering particles with negative absorption [*ZhETF Pis'ma*, **5**: 262–265 Russian], *JETP Lett.*, **5**: 212–215 (1967).

2. V.S. Letokhov, Generation of light by a scattering medium with negative resonance absorption [*Zh. Exp. and Teor. Fiz.*, **53**: 1442–14452 Russian], *Sov. Phys. JETP*, **26**: 835–840 (1968).
3. R.V. Ambartsumyan, N.G. Basov, P.G. Kryukov, and V.S. Letokhov, Non-resonant feedback in lasers. In *Progress in Quantum Electronic*, Vol. **1**, J.H. Sanders and K.W.H. Stevens, eds., Pergamon: New York (1970), p. 107.
4. C.W. Beenakker, J.C.J. Paasschens, and P.W. Brouwer, Probability of reflection by a random laser, *Phys. Rev. Lett.*, **76**: 1368–1371 (1996).
5. X. Jiang, Q. Li, and C.M. Soukoulis, Symmetry between absorption and amplification in disordered media, *Phys. Rev. B*, **59**: R9007–R9010 (1999).
6. M. Patra and C.W.J. Beenakker, Excess noise for coherent radiation propagating through amplifying random media, *Phys. Rev. A*, **60**: 4059–4066 (1999).
7. O. Svelto, *Principles of Lasers*, 4th ed., D.C. Hanna, trans. and ed. Plenum: New York (1998).
8. A. Yariv, *Quantum Electronics*, 3rd ed., Wiley: New York (1989).
9. W. Koechner, *Solid-State Laser Engineering*, 5th revised and updated ed., Springer-Verlag: New York (1999).
10. G. van Soest, F.J. Poelwijk, R. Sprik, and A. Lagendijk, Dynamics of a random laser above threshold, *Phys. Rev. Lett.*, **86**: 1522–1525 (2001).
11. R.V. Ambartsumyan, P.G. Kryukov, and V.S. Letokhov, Dynamics of emission line narrowing for a laser with nonresonant feedback, [*Zh. Eksp. i Teor. Fiz.*, **51**: 1669–1675 (1966) Russian] *Sov. Phys. JETP*, **24**: 1129–1134 (1967).
12. V.M. Markushev, N.È. Ter-Gabriélyan, Ch.M. Briskina, V.R. Belan, and V.F. Zolin, Stimulated emission kinetics of neodymium powder lasers, *Sov. J. Quantum Electron.*, **20**: 772–777 (1990).
13. F. Auzel and P. Goldner, Coherent light sources with powder: Stimulated amplification versus super-radiance, *J. Alloys Compounds*, **300–301**: 11–17 (2000).
14. C. Gouedard, D. Husson, C. Sauteret, F. Auzel, and A. Migus, Generation of spatially incoherent short pulses in laser-pumped neodymium stoichiometic crystals and powders, *J. Opt. Soc. Am. B*, **10**: 2358–2363 (1993).
15. N.È. Ter-Gabriélyan, V.M. Markushev, V.R. Belan, Ch.M. Briskina, and V.F. Zolin, Stimulated emission spectra of powders of double sodium and lanthanum tetramlybdate, *Sov. J. Quantum Electron.*, **21**: 32–33 (1991).
16. Ch.M. Briskina, V.M. Markushev, and N.È. Ter-Gabriélyan, Use of a model of coupled microcavities in the interpretation of experiments on powder lasers, *Quantum Electron.*, **26**: 923–927 (1996).
17. N.T. Melamed, Optical properties of powders. Part I. Optical absorption coefficients and the absolute value of the diffuse reflectance. Part II. Properties of luminescent powders. *J. Appl. Phys.*, **34**: 560–570 (1963).
18. M.A. Noginov, N.E. Noginova, H.J. Caulfield, P. Venkateswarlu, T. Thompson, M. Mahdi, and V. Ostroumov, Short-pulsed stimulated emission in the powders of $NdAl_3(BO_3)_4$, $NdSc_3(BO_3)_4$, and $Nd:Sr_5(PO_4)_3F$ laser crystals, *J. Opt. Soc. Am. B*, **13**: 2024–2033 (1996). M.A. Noginov, N.E. Noginova, H.J. Caulfield, P. Venkateswarlu, T. Thompson, M. Mahdi, and V. Ostroumov, Stimulated emission without cavity in powders and single crystals of Nd doped materials. In *OSA Trends in Optics and Photonics on Advanced Solid State Lasers*, Vol. 1 S.A. Payne and C.R. Pollock, eds., Optical Society of America: Washington, DC (1996), pp. 585–590.

19. S.T. Durmanov, O.V. Kuzmin, G.M. Kuzmiheva, S.A. Kutovoi, A.A. Martynov, E.K. Nesynov, V.L. Panyutin, Yu.P. Rudnitsky, G.V. Smirnov, and V.I. Chizhikov, Binary rare-earth scandium borates for diode-pumped lasers, *Opt. Mater.*, **18**: 243–284 (2001).
20. V.M. Markushev, V.F. Zolin, and Ch.M. Briskina, Luminescence and stimulated emission of neodymium in sodium lanthanum molybdate powders, *Sov. J. Quantum Electron.*, **16**: 281–283 (1986).
21. C.M. Soukoulis, X. Jiang, J.Y. Xu, and H. Cao, Dynamic response and relaxation oscillations in random lasers, *Phys. Rev. B*, **65**: 041103 (2002).
22. M.A. Noginov, I. Fowlkes, G. Zhu, and J. Novak, Neodymium random lasers operating in different pumping regimes, *J. Modern Optics*, **51**: 2543–2553 (2004).
23. M.A. Noginov, I.N. Fowlkes, G. Zhu, and J. Novak, Random laser thresholds in cw and pulsed regimes, *Phys. Rev. A*, **70**: 043811/1–5 (2004).
24. G. Williams, B. Bayram, S.C. Rand, T. Hinklin, and R.M. Laine, Laser action in strongly scattering rare-earth-doped dielecric nanophosphors, *Phys. Rev. A*, **65**: 013807 (2001).
25. Y. Ling, H. Cao, A.L. Burin, M.A. Ratner, X. Liu, and R.P.H. Chang, Investigation of random lasers with resonant feedback, *Phys. Rev. A*, **64**: 063808 (2001).
26. X. Jiang and C.M. Soukoulis, Transmission and reflection studies of periodic and random systems with gain, *Phys. Rev. B*, **59**: 6159–6166 (1999).
27. Q. Li, K.M. Ho, and C.M. Soukoulis, Mode distribution in coherently amplifying laser medium, *Physica B*, **296**: 78–84 (2001).
28. G.A. Berger, M. Kempe, and A.Z. Genack, Dynamics of stimulated emission from random media, *Phys. Rev. E*, **56**: 6118–6122 (1997).
29. M.A. Noginov, G. Zhu, A.A. Frantz, J. Novak, S.N. Williams, and I. Fowlkes, Dependence of $NdSc_3(BO_3)_4$ random laser parameters on particle size, *JOSA B*, **21**: 191–200 (2004).
30. M.A. Noginov, J. Novak, and S. Williams, Modeling of photon density dynamics in random lasers, *Phys. Rev. A*, **70**: 063810/1–5 (2004).
31. X. Jiang and C.M. Soukoulis, Theory and simulations of random lasers. In *Photonic Crystals and Light Localization in the 21st Century*, C.M. Soukoulis, ed., NATO Science Series, Series C: Mathematical and Physical Sciences, Vol. 563, Kluwer Academic: Boston (2001), pp. 417–433.
32. X. Jiang and C.M. Soukoulis, Time-dependent theory for random lasers, *Phys. Rev. Lett.*, **85**: 70–73 (2000).
33. S.C. Rand, Strong localization if light and photonic atoms, *Can. J. Phys.*, **78**: 625–637 (2000).
34. H. Cao, Y. Ling, J.Y. Xu, and A.L. Burin, Probing localized states with spectrally resolved speckle techniques, *Phys. Rev. E*, **66**: 025601(R) (2002).
35. C.W. Lee, K.S. Wong, J.D. Huang, S.V. Frolov, and Z.V. Vardeny, Femtosecond time-resolved laser action in poly (*p*-phenylene vinylene) films: Stimulated emission in an inhomogeneously broadened exciton distribution, *Chem. Phys. Lett.*, **314**: 564–569 (1999).
36. G. van Soest, M. Tomita, and A. Lagendijk, Amplifying volume in scattering media, *Opt. Lett.*, **24**: 306–308 (1999).
37. K. Totsuka, G. van Soest, T. Ito, A. Lagendijk, and M. Tomita, Amplification and diffusion of spontaneous emission in strongly scattering medium, *J Appl. Phys.*, **87**: 7623–7628 (2000).
38. A. Ishimaru, *Wave Propagation and Scattering in Random Media*, Vol. 1, Academic: New York (1978), p. 250.

39. D.S. Wiersma and A. Lagendijk, Light diffusion with gain and random lasers, *Phys. Rev. E*, **54**: 4256–4265 (1996).
40. M.A. Noginov, M. Bahoura, N. Noginova, and V.P. Drachev, Study of absorption and reflection in solid-state random laser, *Applied Optics*, **43**: 4237–4243 (2004).
41. B.A.L. Burin, private communication.
42. C.A.L. Burin, H. Cao, and M.A. Ratner, Two-photon pumping of a random laser, *IEEE J. Selected Topics Quantum Electron.*, **9**: 124–127 (2003).
43. P.W. Anderson, Absence of diffusion in certain random lattices, *Phys. Rev.*, **109**: 1492–1505 (1958).
44. P.W. Anderson, The question of classical localization: A theory of white paint, *Philos. Mag. B*, **52**: 505–509 (1985).
45. S. John, Electromagnetic absorption in a disordered medium near a photon mobility edge, *Phys. Rev. Lett.*, **53**: 2169–2172 (1984).
46. S. John, Localization of light, *Phys. Today*, 32–40 (May 1991).
47. B. Michel, MieCalc—freely configurable program for light scattering calculations (Mie theory) http://www.lightscattering.de/MieCalc/eindex.html.
48. X.H. Wu, A. Yamilov, H. Noh, and H. Cao, Random lasing in closely packed resonant scatterers, *J. Opt. Soc. Am.*, **21**: 159–167 (2004).
49. A.L. Burin, M.A. Ratner, H. Cao, and R.P.H. Chang, Model for a random laser, *Phys. Rev. Lett.*, **87**: 215503 (2001).
50. M. Bahoura, K.J. Morris, G. Zhu, and M.A. Noginov, Dependence of the neodymium random laser threshold on the diameter of the pumped spot, *IEEE Journal of Quantum Electronics*, **41**: 677–685 (2005).
51. M.A. Noginov, N. Noginova, S. Egarievwe, J.C. Wang, M.R. Kokta, and J. Paitz, Study of light propagation in scattering powder laser materials, *Opt. Mater.*, **11**: 1–7 (1998).
52. N.È. Ter-Gabriélyan, V.M. Markushev, V.R. Belan, Ch.M. Briskina, O.V. Dimitrova, V.F. Zolin, and A.V. Lavrov, Stimulated radiation emitted by lithium neodymium tertaphosphate $LiNd(PO_3)_4$ and neodymium pentaphosphate NdP_5O_{14} powders, *Sov. J. Quantum Electron.*, **21**: 840–841 (1991).

5
Engineering Aspects of Neodymium Random Lasers: External Seeding, Design, and Second Harmonic Generation

5.1 Control of Neodymium Random Laser Emission with External Seeding Light

As shown in Sections 2.4, 4.1, and 4.9, two laser powders characterized by slightly different emission wavelengths, when mixed together, can influence stimulated emission in each other. Similarly, random laser emission can be affected by intense external laser light (control light or seeding light), the wavelength of which is reasonably close to that of the random laser emission.

In Reference [1], a $Nd_{0.5}La_{0.5}Al_3(BO_3)_4$ powder sample was illuminated with short ($\approx$10 ns) pulses of 532 nm pumping light and 1064 nm control light. The wavelength of the control light was 0.9 nm longer than the wavelength of the strongest emission line in $Nd_{0.5}La_{0.5}Al_3(BO_3)_4$ powder, 1063.1 nm. The two light spots with diameters equal to $\approx$2.5 mm, ideally overlapped each other. The dynamics of the $Nd_{0.5}La_{0.5}Al_3(BO_3)_4$ random laser emission and the seeding light were monitored with a streak camera connected to a widely open output slit of a monochromator.

The characteristic two-dimensional streak camera patterns recorded with and without seeding light are depicted in Figure 5.1. Varying the intensity of the seeding light, it was possible to control both the intensity (Figure 5.2) and the wavelength (Figure 5.3) of the random laser emission. As shown in Figure 5.1, when 532 nm pumping energy is close to the threshold, external seeding light can totally suppress the random laser emission. Thus, using the control laser light, one can switch the random laser emission on and off.

5.2 Effect of External Mirror on Stimulated Emission

The fact that stimulated emission in neodymium random lasers is sensitive to external seeding light (Section 5.1) suggests that it also should be sensitive to the presence of external mirrors. As shown in Section 4.2, the threshold of stimulated emission in a random laser is inversely proportional to the photon residence time

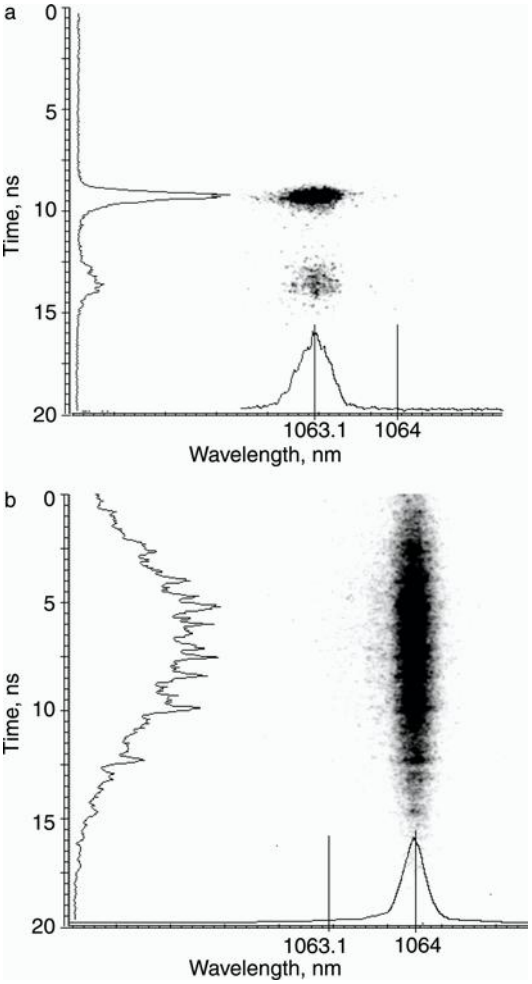

FIGURE 5.1. (a) Streak camera image of the stimulated emission in $Nd_{0.5}La_{0.5}Al_3(BO_3)_4$ random laser at the excitation of the powder with 532 nm pumping light only. (b) The absence of the random laser emission (at 1063.1 nm) at the simultaneous excitation of the powder with 532 nm pumping light [of the same intensity as in Figure (a)] and 1064 nm seeding light. (*Source*: Ref. [1].)

τ_{res} in the pumped volume. Thus, it is logical to assume that external mirrors, which elongate the residence time τ_{res}, should be advantageous for stimulated emission in random lasers.

The results obtained in laser dyes mixed with scattering particles (liquid random lasers), which were operated with external reflectors, seem to be controversial. Thus, the authors of Reference [2] claim that external reflectors broaden the stimulated emission line and, hence, are disadvantageous for the random laser. On the

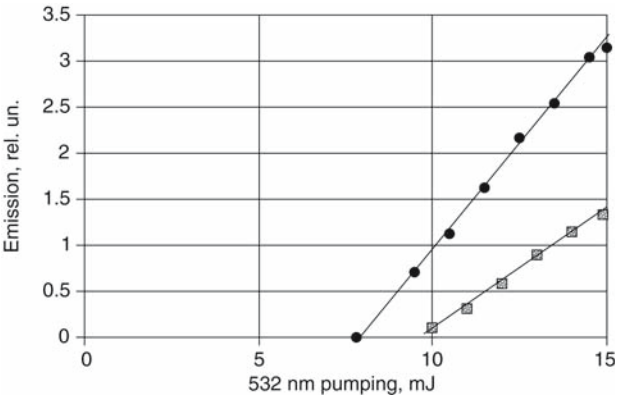

FIGURE 5.2. Input–output curves of 1063.1 nm stimulated emission in $Nd_{0.5}La_{0.5}Al_3(BO_3)_4$ powder. Solid circles: 532 nm pumping only; shaded squares: 532 nm pumping and 1064 nm seeding. (*Source*: Ref. [1].)

other hand, according to [3], external mirrors lead to three- to fivefold reduction of the emission linewidth and, thus, are highly beneficial for the stimulated emission of random lasers. Apparently, so large a difference between the conclusions above is due to the difference in the experimental parameters, such as the diameter of the pumped spot, the thickness of the gain volume, the concentration and the size of the scatterers, the value of the gain, etc.

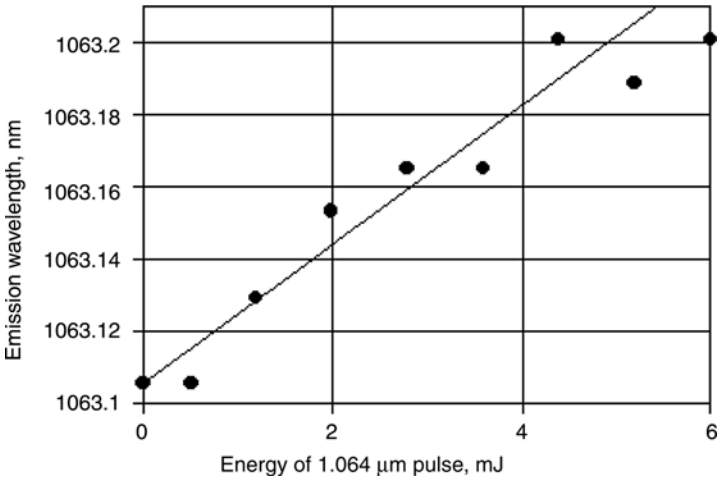

FIGURE 5.3. Wavelength of the $Nd_{0.5}La_{0.5}Al_3(BO_3)_4$ random laser emission as a function of the 1064 nm seeding pulse energy. (*Source*: Ref. [1].)

In ZnO random lasers, the presence of an external reflector strongly influences the laser modes, the output intensity, and the threshold of stimulated emission. An almost tenfold increase of the output energy was obtained in ZnO film consisting of 20 to 150 nm nanoparticles in Reference [4]; see Section 7 for more details.

In order to investigate the effect of external mirrors on stimulated emission in the neodymium random laser, the experiment was carried out in [1]. In the setup shown in Figure 5.4, the mirror, which had high reflection at 1.06 μm and high transmission at 0.53 μm, was positioned close to the front wall of the 1 mm thick cuvette containing $Nd_{0.5}La_{0.5}Al_3(BO_3)_4$ powder. The powder was pumped (with the radiation of a frequency-doubled Q-switched Nd:YAG laser) through the mirror and the emission was collected from the rear side of the cuvette (Figure 5.4). In the reference measurement, the mirror was removed from the setup. The input–output curves obtained with and without the external mirror are shown in Figure 5.5. As follows from this figure, the external mirror helps to reduce the threshold and increase the slope efficiency of random laser emission.

The relative smallness of the effect (≈20%) can be explained by a considerably large distance between the powder and the mirror (≈1 mm) determined by the thickness of the cuvette wall and the air gap between the cuvette and the mirror. In Reference [5], where the layer of $NdSc_3(BO_3)_4$ powder was placed between the dichroic dielectric mirror and the gold mirror (without gaps between the mirrors and the powder), the reduction of the threshold was fourfold. These experiments suggest that a significant improvement of random laser efficiency can be expected if laser powder is enclosed in a black-body like cavity with highly reflective walls and a small opening for pumping and delivery of stimulated emission (Figure 5.1b).

A dramatic reduction of the threshold in the setup of Figure 5.4 (much larger than that in Figure 5.5) has been predicted theoretically in Reference [6]. The calculated decrease of the threshold was due to a better overlap between the pumped region and the lasing modes, as well as different eigenmode structures of the systems with and without the mirror. An analysis of the decay rate distributions in one-dimensional systems open at one end and both ends showed an enhancement of localization in the former case.

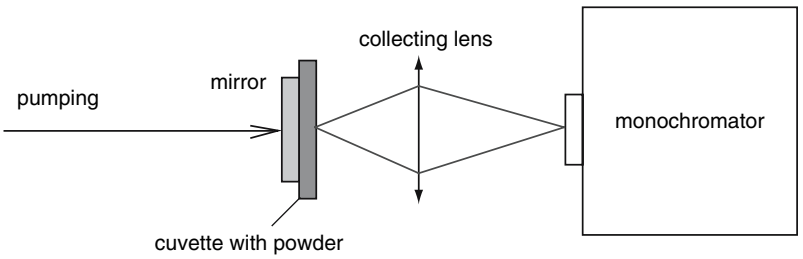

FIGURE 5.4. Schematic diagram of the $Nd_{0.5}La_{0.5}Al_3(BO_3)_4$ powder laser with external mirror. The mirror has high transmission at the pumping wavelength, 532 nm, and high reflection at the random laser wavelength, 1063.1 nm (after [1]).

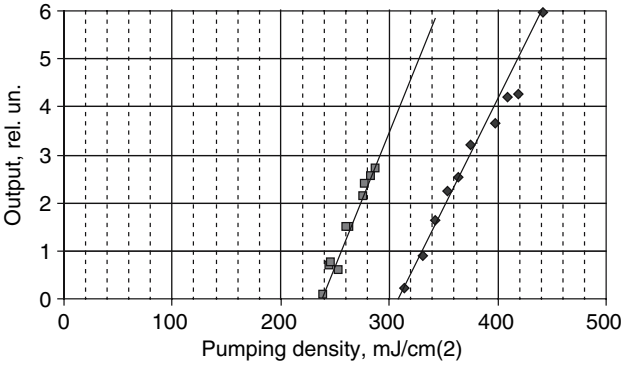

FIGURE 5.5. Stimulated emission in $Nd_{0.5}La_{0.5}Al_3(BO_3)_4$ powder with external mirror (squares) and without external mirror (diamonds). (*Source*: Ref. [1].)

The threshold reduction in the one-mirror random laser scheme allowed the authors of Reference [7] to demonstrate a quasi-cw Nd:YAG random laser pumped with 100 to 200 μs rectangular pulses of semiconductor laser ($\lambda_{pump} \approx 805$ nm). The random laser consisted of a 4%-doped Nd^{3+}:YAG powder tablet with a dimension of Ø $16 \times 3\,mm^3$ and a mirror with high-reflective coating at 1064 nm (measured to be ~99.5%). The coated mirror face was at the powder side. A scanning electron microscope image showed that the powder particles had an average size of about 250 nm. The volume fraction of powder was approximately equal to 50%.

Experimentally, the threshold behavior and a substantial spectral narrowing of the spectral line ($\delta\nu \leq 0.1$ nm) were observed at the increase of the pumping power [7]. In addition, spiking behavior was observed when the pumping power exceeded the second critical threshold. When the pumping power increased further, the spiking behavior, explained in terms of relaxation oscillations, became more pronounced (larger amplitude and higher repetition rate).

5.3 Fiber-Coupled Random Laser

Random lasers pumped through the surface of a scattering medium have two obvious disadvantages: a fraction of the pumping energy, sometimes very large, is reflected by the sample and, thus, wasted; and the gain volume in the medium is, as a rule, located very close to the surface of the sample, which reduces Q-factors of effective cavities formed by scatterers. These two factors increase the threshold energy and reduce the slope efficiency of stimulated emission.

Both the threshold energy and the slope efficiency can be improved if a random laser is excited through an optical fiber that delivers pumping energy deep inside the scattering medium. For example, such pumping was realized in [8], where a

relatively high quantum yield of stimulated emission, $\eta \sim 0.2$ to 0.25 (measured with respect to the stored population inversion), was reported.

In Reference [9], the threshold and the slope efficiency of stimulated emission in the $NdSc_3(BO_3)_4$ random laser were studied when the powder was pumped through (I) the 400 μm fiber that was inserted deep inside (∼5 mm) the volume of the powder and (II) the same fiber separated from the surface of the powder by ∼0.35 mm glass wall. Similar to many other neodymium random lasers (see, for example, Refs. [8,10,11]), the peak emission intensity of $NdSc_3(BO_3)_4$ powder increased dramatically above the threshold, its emission spectrum narrowed to a single line, and the emission kinetics changed from ∼16 μs nearly exponential decay to one or several pulses of nanosecond scale (relaxation oscillations).

The input–output curves recorded in configurations I and II are shown in Figure 5.6, where the energy of short-pulsed stimulated emission delivered through the fiber is plotted along the vertical axis.

One can see that in setup #I the threshold energy is half as large and the slope efficiency is fivefold larger than in the surface-pumped configuration of setup #II. The observed reduction of the threshold was, most likely, caused by the higher fraction of absorbed pumping energy and the longer photon residence time in setup #I. The relatively high slope efficiency in setup #I originated partially from the enhanced fraction of absorbed pumping energy and partially from the larger fraction of stimulated emission coupled to the fiber.

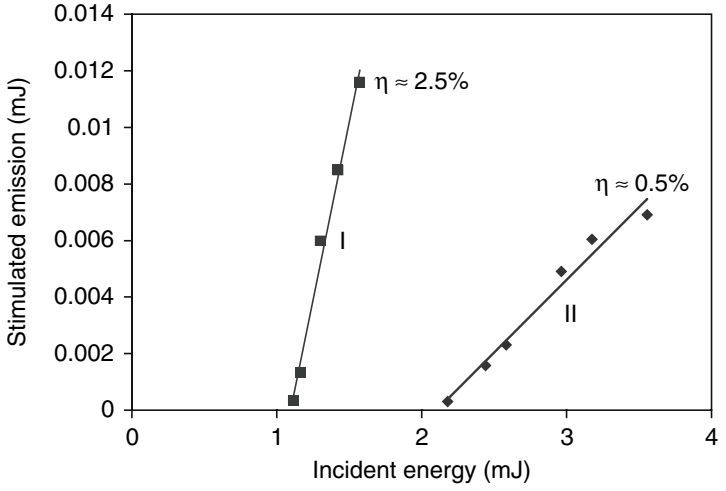

FIGURE 5.6. Input–output curves of $NdSc_3(BO_3)_4$ random laser emission recorded in fiber-pumping configurations I and II. In all experiments, the samples were pumped with ∼10 ns laser pulses at 532 nm. (*Source*: Ref. [9].)

The time interval Δt_{12} between the first and the second relaxation oscillation pulses in the emission kinetics, in the first approximation, can be associated with the inverse frequency of relaxation oscillations $\Delta t_{12} \sim \nu^{-1}$. As shown in Reference [12], with the increase of the pumping energy Δt_{12} decreases first and then saturates at large pumping energies. The saturated value Δt_{12} monotonically increases with the increase of the photon residence time and, correspondingly, the Q-factor of a random laser [12]. (Note that in the literature [13–15] the dependence $\nu \sim \tau_{res}^{-1/2}$ takes place only in the case of *damped* relaxation oscillations.)

The experimentally measured (saturated) time interval Δt_{12} is larger by ~20% in configuration I than in configuration II [9]. This suggests that the photon residence time and the Q-factor of an effective cavity get larger when the fiber is inserted deep inside the scattering medium. (Due to the nonlinear dependence of Δt_{12} on Q, the ratio of the Q-factors in configurations I and II should be larger than 20%.)

To investigate the efficiency of stimulated emission that is unaffected by the fraction of emitted light collected to the detector, the total number of stimulated emission photons was normalized by the total number of neodymium ions excited to the upper laser state $^4F_{3/2}$. (The latter is proportional to the time-integrated spontaneous emission signal below the threshold.) It has been found that the slope efficiency normalized this way is as high as 80–90% in configuration I [9].

Note that in addition to the demonstrated significant improvement of the operation parameters, fiber-coupled random lasers may be advantageous for photonics applications because of easy-to-handle stimulated emission delivered through a fiber.

5.4 Demonstration of a Second-Harmonic Powder Laser

In Reference [16], a second-harmonic generation in a mixture of powders of laser $Nd_{0.5}La_{0.5}Al_3(BO_3)_4$ and frequency-doubling 2-methyl-4-nitroaniline (MNA) materials has been demonstrated. The short-spike 1.06 μm stimulated emission and its second harmonic have been described with the model accounting for the population inversion and the energy density of 1.06 μm and 0.53 μm radiation in the pumped volume. The experimental results are in good agreement with the model predictions. The optimum MNA concentration was shown to be dependent on the pumping energy. The theoretically predicted optimal nonlinear coefficient in (pulverized) nonlinear material was 10^2 to 10^3 times larger than that in MNA.

5.4.1 Experimental Samples

As an active medium for the second-harmonic random (powder) laser, a mixture of $Nd_{0.5}La_{0.5}Al_3(BO_3)_4$ and 2-methyl-4-nitroaniline was used in [16]. The average size of $Nd_{0.5}La_{0.5}Al_3(BO_3)_4$ powder particles was approximately equal to 3.5 μm.

MNA was obtained from Aldrich Chemical and then was purified by the physical transport method using argon gas as the carrier at 150 to 160°C.

The spectroscopic and frequency-doubling properties of MNA, one of the most efficient second-harmonic materials, are described in [17] and [18]. The $\chi^{(2)}$ nonlinear coefficients reported in MNA ($d_{12} = 38$ and $d_{11} = 250\,\text{pm/V}$ [17]) are many times larger than those of conventional inorganic nonlinear materials such as potassium dihydrogen phosphate and lithium niobate. Other nonlinear optical coefficients in MNA (d_{33}, d_{13}, etc.) are at most only a few percent of d_{11} [17]. The comparison of several powders of frequency-doubling materials, which included MNA, methyl-(2,4-dinitrophenyl)-aminopropanoate (MAP), MAP:MNA mixed crystal [19], $LiNbO_3$, and Nd:$YAl_3(BO_3)_4$] has shown that MNA gives the most efficient $1.06 \rightarrow 0.53\,\mu\text{m}$ frequency conversion. This determined the choice of MNA as the nonlinear material in the random laser experiment.

Three mixed $Nd_{0.5}La_{0.5}Al_3(BO_3)_4$/MNA samples studied in Reference [16] contained 4, 16, and 29% of MNA (by weight). A pure $Nd_{0.5}La_{0.5}Al_3(BO_3)_4$ powder was also used in some of the measurements for comparison.

5.4.2 Experimental Results

Experimentally, the powders were excited with yellow light ($\lambda = 580\,\text{nm}$) of a pulsed dye laser pumped by a frequency-doubled Q-switched Nd:YAG laser. The duration of 580 nm pulses was close to 10 ns. The pumping beam was focused to $0.02\,\text{cm}^2$ spot. The measurements of the emission intensity were carried out with a small-aperture detector that was set up at 20 cm from the illuminated sample.

Under intense pumping, one or several short (~1 ns) stimulated emission pulses were observed in all powder samples studied. Simultaneously, a second-harmonic radiation was found in the mixed samples. The spectra of ≈1063.1 nm random laser emission and its ≈531.6 nm second harmonic are shown in Figure 5.7.

The 531.6 nm light intensity ($I_{0.53}$) is plotted against 1063.1 nm light intensity ($I_{1.06}$) in Figure 5.8. As follows from this figure, the slope of the dependence $\log(I_{0.53})$ versus $\log(I_{1.06})$ is equal to 2, which is an expected signature of a second harmonic generation.

The input–output curves of stimulated emission in the four samples studied are shown in Figure 5.9. As follows from this figure, the threshold of stimulated emission increases and the slope efficiency decreases with the increase of MNA concentration in the mixture. Two possible reasons for this, the reduction of the absorbed pumping energy in $Nd_{0.5}La_{0.5}Al_3(BO_3)_4$ powder mixed with MNA powder and the effect of $1.06 \rightarrow 0.53\,\mu\text{m}$ frequency conversion, are discussed in Section 5.4.3.

The dependence of the second-harmonic output on MNA concentration, which has the maximum close to a MNA concentration equal to 16%, is shown in

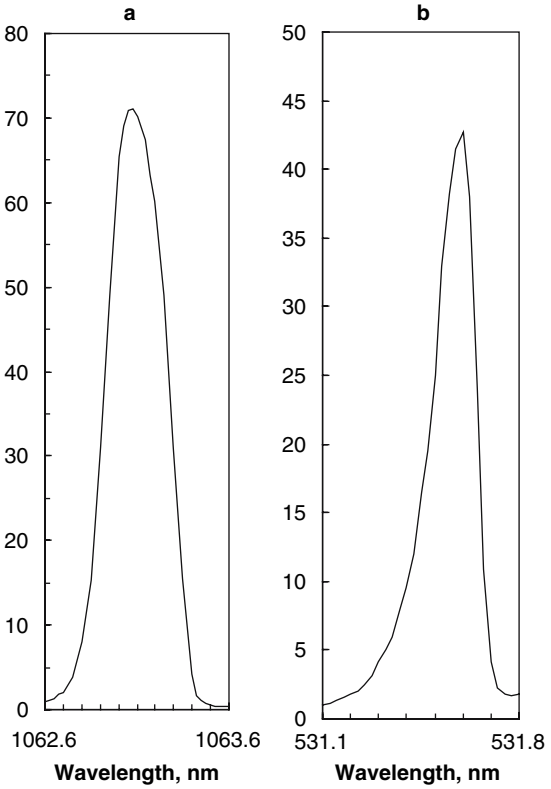

FIGURE 5.7. The spectra of (a) ≈1063.1 nm emission and (b) ≈531.6 nm emission in a mixture of $Nd_{0.5}La_{0.5}Al_3(BO_3)_4$ and MNA powders. The linewidth is limited by the spectral resolution of a monochromator. (*Source*: Ref. [16].)

Figure 5.10. This experimental dependence is compared with the theoretical modeling in Section 5.4.3.

At 580 nm pumping, the efficiency of 1063.1 nm stimulated emission in the $Nd_{0.5}La_{0.5}Al_3(BO_3)_4$ powder laser was of the order of ≈1%. This measurement was done by comparison of the random laser emission intensity (at the pumping energy approximately two times the threshold energy) and the intensity of light scattered from nonabsorbing Al_2O_3 powder. The intensity of 531.6 nm second-harmonic radiation was approximately three orders of magnitude smaller than that of 1063.1 nm stimulated emission.

5.4.3 Modeling: Comparison of Theory and Experiment

As shown in Section 4.2, the rate equation model similar to that describing relaxation oscillations in regular lasers, which accounts for population inversion

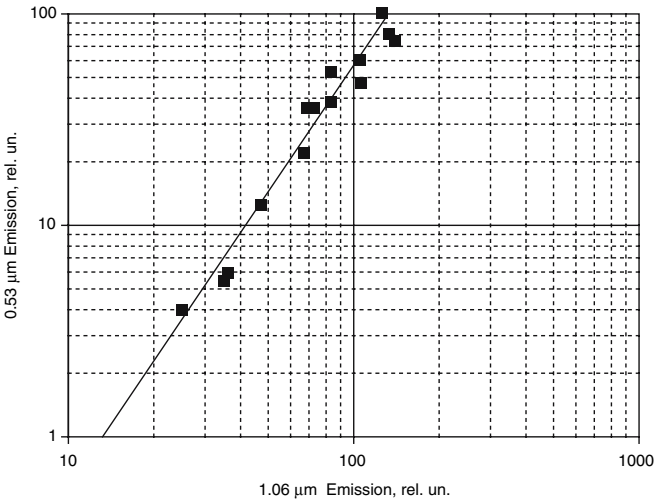

FIGURE 5.8. Dependence of the 531.6 nm light intensity versus 1063.1 μm light intensity. (*Source*: Ref. [16].)

and density of stimulated emission energy in the pumped volume, in the first approximation adequately describes the dynamics of stimulated emission pulses and the threshold in neodymium random lasers. To account for second-harmonic generation in the mixture of laser and frequency-doubling powders, the system of

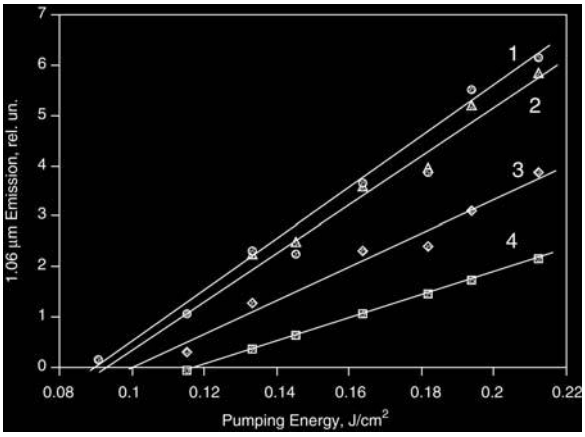

FIGURE 5.9. Input–output curves in pure $Nd_{0.5}La_{0.5}Al_3(BO_3)_4$ powder and mixtures of $Nd_{0.5}La_{0.5}Al_3(BO_3)_4$ and MNA powders. 1 (circles): $x = 0$; 2 (triangles): $x = 0.04$; 3 (diamonds): $x = 0.16$; 4 (squares): $x = 0.29$. (*Source*: Ref. [16].)

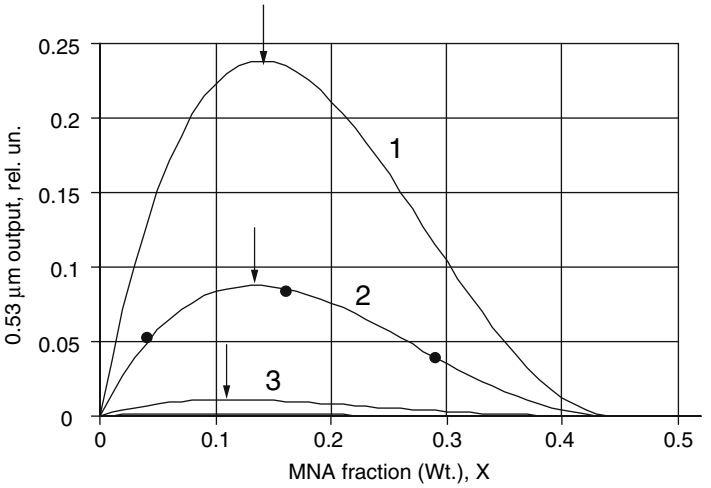

FIGURE 5.10. Solid curves indicate calculated dependencies E_{SH} versus X. (1) $E_{in} = 5.5$ mJ; (2) $E_{in} = 4$ mJ; (3) $E_{in} = 2.5$ mJ. Arrows indicate the optimum MNA concentrations. Circles indicate experimental data obtained at $E_{in} = 4$ mJ. The effective area of the pumped spot is equal to $\approx 0.02\,\text{cm}^2$. (*Source*: Ref. [16].)

Eqs. (4.14) was modified to the form [16],

$$\begin{aligned}
\frac{dn}{dt} &= \frac{P(t)}{Sl_p h\nu_{pump}} - \frac{n}{\tau} - \frac{E_{1.06}}{h\nu_{em}} c\sigma_{em} n, \\
\frac{dE_{1.06}}{dt} &= -\frac{E_{1.06}}{\tau_{res}} + \zeta \frac{n}{\tau} h\nu_{em} + E_{1.06} c\sigma_{em} n - xAE_{1.06}^2, \\
\frac{dE_{0.53}}{dt} &= xAE_{1.06}^2 - \frac{E_{0.53}}{\tau_{res}}.
\end{aligned} \tag{5.1}$$

Here $E_{1.06}$ is the energy density of random laser emission, $E_{0.53}$ is the energy density of second-harmonic radiation, and A is the factor accounting for the second-harmonic conversion efficiency. In Reference [16], the penetration depth of pumping l_p has been assumed to be equal to $[(1-x)k_{abs}^0]^{-1}$, where x is the relative concentration of MNA powder in the mixture and k_{abs}^0 is the absorption coefficient in pure laser powder. For simplicity, the photon residence time τ_{res} was assumed to be the same for 1063.1 nm stimulated emission and 531.6 nm second-harmonic radiation. The numerical values of spectroscopic parameters in Eq. (5.1) were taken to be the same as in Section 4.2.

According to [17], when 1.06 μm pumping flux exciting $l = 50$ μm thick plate of (not specially oriented) MNA is of the order of $P_{1.06}/S = 10^8\,\text{W/cm}^2$, the approximate second-harmonic converting efficiency is equal to $\varsigma = 10^{-3}$. The refraction index in MNA, averaged over different polarizations and propagation directions, is approximately equal to $n^* = 2$. Equating second-harmonic

energy density generated during the time that a photon needs to propagate through the sample ($AE_{1.06}^2 n^* l/c$) and the product of $E_{1.06}$ and ς, one gets $(n^* l/c)AE_{1.06}^2 = \varsigma E_{1.06}$, where $E_{1.06} = (P_{1.06}/S)n^*/c$. Combining these two equations, one can roughly estimate the value of A in MNA powder to be equal to $A = \varsigma c^2/[(P_{1.06}/S)n^{*2} l] \approx 4.5 \times 10^{11}\,\mathrm{cm^3\,s^{-1}\,J^{-1}}$.

Solving the system of rate equations (5.1) at $x = 0.1$ and A ranging from $10\,\mathrm{cm^{10}\,s^{-1}\,J^{-1}}$ to $10^{17}\,\mathrm{cm^3\,s^{-1}\,J^{-1}}$, one can show that at $A < 10^{13}\,\mathrm{cm^3\,s^{-1}\,J^{-1}}$, the dynamics of 1063.1 nm stimulated emission pulses, Figure 5.11, is similar to that obtained experimentally and calculated theoretically in the system without second-harmonic generation (Figures 2.3 and 4.1).

The set of input–output curves of 1063.1 nm stimulated emission, $I_{1.06}$, and 531.6 nm second-harmonic radiation, $I_{0.53}$, calculated at $A = 4.5 \times 10^{11}\,\mathrm{cm^3\,s^{-1}\,J^{-1}}$ and x equal to 0, 0.04, 0.16, and 0.29 is shown in Figure 5.12. Comparing Figures 5.12a and 5.9, one can see that the model predictions for 1063.1 nm emission are in good qualitative agreement with the experimental results. The data from Figures 5.12a and 5.12b are plotted according to the basis $\ln(I_{0.53})$ versus $\ln(I_{1.06})$ in Figure 5.13. As follows from Figure 5.13, the slope of the $\ln(I_{0.53})$ versus $\ln(I_{1.06})$ dependence is close to 2. More careful consideration shows that this slope is slightly larger than 2 before the threshold, the slope increases to an even higher value after the threshold (at small emission energies), and finally, it decreases to a value slightly less than 2 at large pumping (and emission) energies. The increase of the slope to a value larger than 2 can be explained by reduction of the 1063.1 nm pulse duration and corresponding increase of the 1063.1 nm peak emission power, which occur at the increase of the pumping energy (Sections 2.2.1 and 4.2, Ref. [11]). The reduction of the slope at high pumping energy is due to the increase of the number of pulses in the series, which reduces the 1063.1 nm peak emission power. In the fairly wide range of the emission intensities (above the threshold) the slope of the dependence $\ln(I_{0.53})$ versus $\ln(I_{1.06})$ is very close to 2. The experimental curve shown in Figure 5.8 corresponds to this energy range. The good agreement between the calculations above [dynamics of stimulated-emission pulses, input–output dependences, and $\ln(I_{0.53})$ versus $\ln(I_{1.06})$ dependence] and the experimental results proves that, in a first approximation, the system of rate equations (5.1) adequately describes stimulated-emission and second-harmonic generation in a mixture of laser and frequency-doubling powders.

According to Figure 5.12, the maximum $1.06 \rightarrow 0.53\,\mu\mathrm{m}$ conversion efficiency is of the order of 3.2×10^{-3}. This result is in reasonable agreement with the experimental observation. To determine optimum frequency-conversion efficiency for second-harmonic generation in a random laser, one can calculate the series of input–output curves for $x = 0.1$ and $A = 10^8\,\mathrm{cm^3\,s^{-1}\,J^{-1}}, 10^9\,\mathrm{cm^3\,s^{-1}\,J^{-1}}, \ldots, 10^{17}\,\mathrm{cm^3\,s^{-1}\,J^{-1}}$ (Figure 5.14). As follows from Figure 5.14a, the effect of second-harmonic generation in the mixture of powders in practice does not affect the threshold and the slope efficiency of $1.06\,\mu\mathrm{m}$ stimulated emission if $A \leq 10^{12}\,\mathrm{cm^3\,s^{-1}\,J^{-1}}$. This implies that the change in the threshold and the slope efficiency observed experimentally (Figure 5.9) and

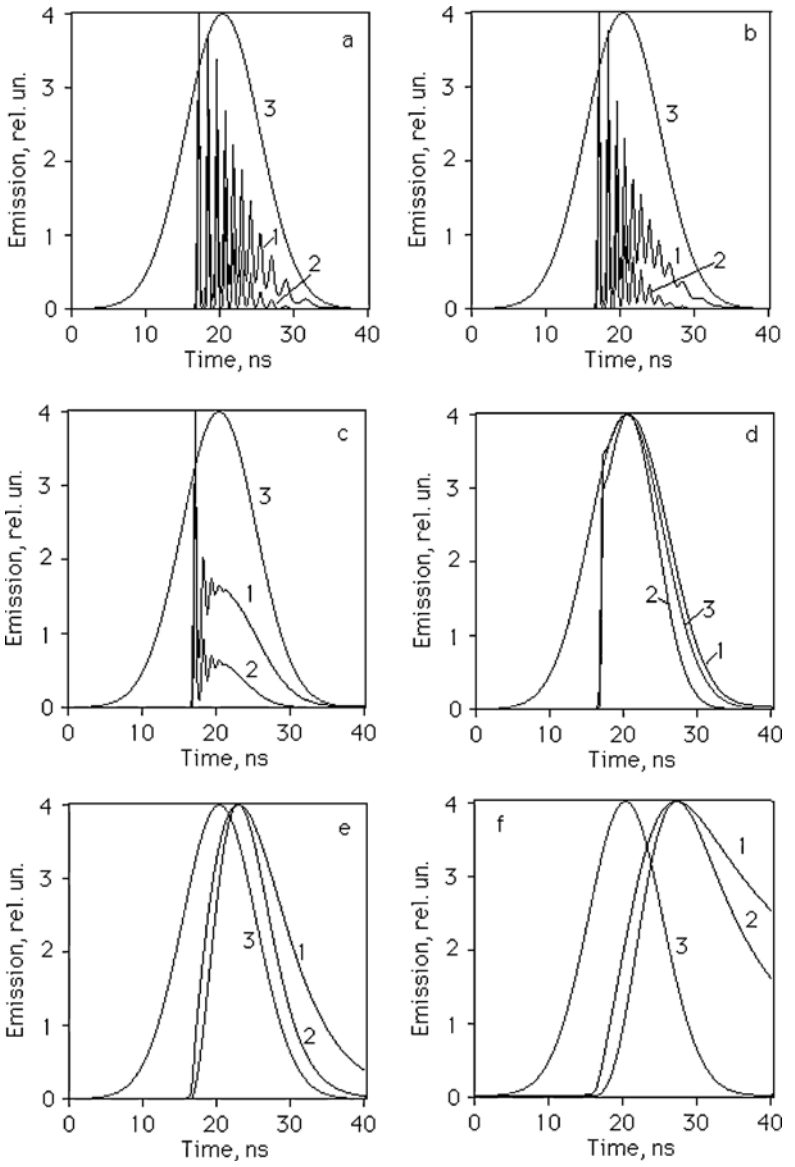

FIGURE 5.11. Calculated dynamics of (1) 1063.1 nm stimulated-emission pulses and (2) 531.6 nm second-harmonic radiation in the mixture of powders of laser and frequency-doubling materials; (3) pumping pulse shape. The stimulated-emission kinetics are calculated for pumping energy equal to $500\,\mathrm{mJ/cm^2}$, $x = 0.1$, and (a) $A = 10^{11}\,\mathrm{cm^3\,s^{-1}\,J^{-1}}$, (b) $A = 10^{12}\,\mathrm{cm^3\,s^{-1}\,J^{-1}}$, (c) $A = 10^{13}\,\mathrm{cm^3\,s^{-1}\,J^{-1}}$, (d) $A = 10^{14}\,\mathrm{cm^3\,s^{-1}\,J^{-1}}$, (e) $A = 10^{15}\,\mathrm{cm^3\,s^{-1}\,J^{-1}}$, and (f) $A = 10^{16}\,\mathrm{cm^3\,s^{-1}\,J^{-1}}$. (*Source*: Ref. [16].)

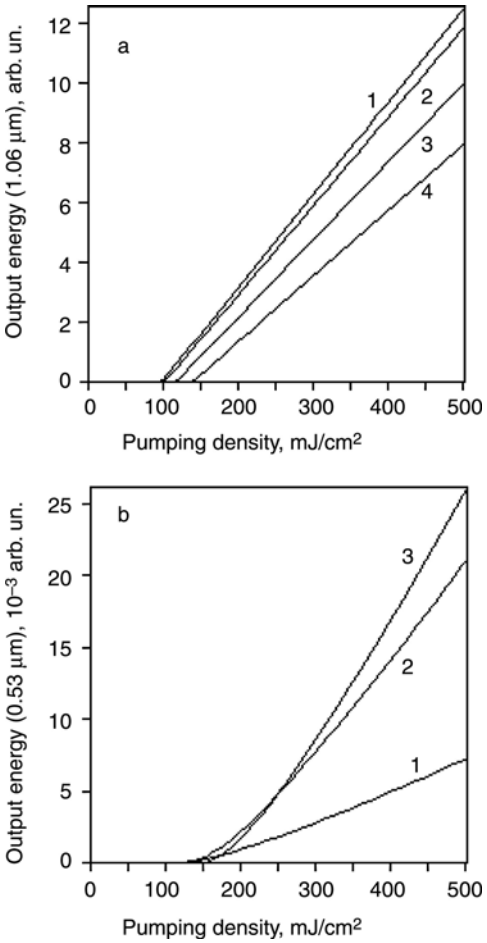

FIGURE 5.12. (a) Calculated input–output curves of 1063.1 nm μm stimulated emission. The calculation is done for $A = 4.5 \times 10^{11}\,\mathrm{cm^3\,s^{-1}\,J^{-1}}$ and (1) $x = 0$, (2) $x = 0.04$, (3) $x = 0.16$, and (4) $x = 0.29$. (b) Calculated input–output curves for 531.6 μm second-harmonic radiation. The calculation is done for $A = 4.5 \times 10^{11}\,\mathrm{cm^3\,s^{-1}\,J^{-1}}$ and (1) $x = 0.04$, (2) $x = 0.16$, and (3) $x = 0.29$. The vertical scale in Figure (a) is compatible with that in Figure (b). (*Source*: Ref. [16].)

calculated at $A = 4.5 \times 10^{11}\,\mathrm{cm^3\,s^{-1}\,J^{-1}}$ (Figure 5.12a) is due to the reduction of pumping-absorption efficiency in $Nd_{0.5}La_{0.5}Al_3(BO_3)_4$ powder diluted with MNA powder but not to second-harmonic generation. The relevant dependence of the stimulated-emission intensity on powder volume density (filling factor) is discussed in Reference [20]. The efficiency of second-harmonic conversion at $A \leq 10^{12}\,\mathrm{cm^3\,s^{-1}\,J^{-1}}$ is also fairly small. (The value of A in MNA is equal to

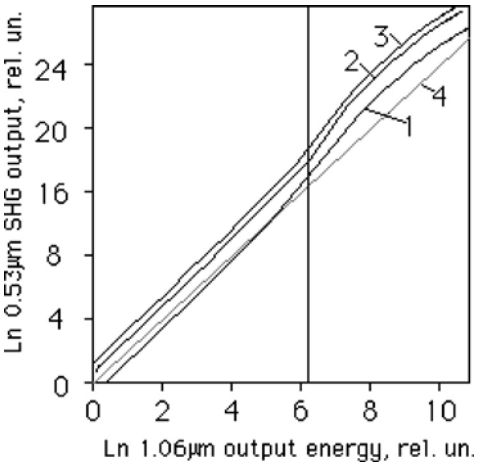

FIGURE 5.13. Calculated $\ln(I_{0.53})$ versus $\ln(I_{1.06})$ dependence corresponding to the input–output curves shown in Figure 5.12. The curves are calculated for $A = 4.5 \times 10^{11}\ \mathrm{cm^3\ s^{-1}\ J^{-1}}$ and (1) $x = 0.04$, (2) $x = 0.16$, and (3) $x = 0.29$. Trace 4 corresponds to the slope equal to 2. The vertical line corresponds to 1% of the maximum 1.06 μm emission signal in Figure 5.12a. (*Source*: Ref. [16].)

$4.5 \times 10^{11}\ \mathrm{cm^3\ s^{-1}\ J^{-1}}$.) The efficiency of 1063.1 nm stimulated emission significantly decreases with the increase of A at $A \geq 10^{13}\ \mathrm{cm^3 s^{-1} J^{-1}}$. This effect is understandable, because efficient frequency conversion reduces 1063.1 nm emission energy density, which is essential for stimulated emission. The decrease of peak 1063.1 nm emission power with the increase of A as well as the behavior of peak second-harmonic radiation power with the change of A are shown in Figure 5.15. As follows from Figure 5.11, sharp emission spikes disappear and the emission kinetics becomes smoother with the increase of A. This behavior is reasonable because the efficiency of second-harmonic generation is proportional to $E^2_{1.06}$, and thus the frequency conversion is damping primarily sharp high-power 1063.1 nm emission spikes. The efficiency of second-harmonic generation increases with the increase of A until $A = 10^{15}\ \mathrm{cm^3\ s^{-1}\ J^{-1}}$ and then rapidly decreases with a further increase of A. The roll-off of second-harmonic energy at large values of A can be explained with a significant decrease of the peak 1063.1 nm emission power and net emission energy.

As follows from Figure 5.12b, close to the threshold, the energy of 531.6 nm radiation is larger in the mixture of powders with MNA concentration equal to $x = 0.04$, at larger pumping energy the second-harmonic output is larger in the mixture with $x = 0.16$, and at maximum pumping energy it is larger at $x = 0.29$. To optimize MNA concentration, the input–output dependence in the mixed $Nd_{0.5}La_{0.5}Al_3(BO_3)_4$/MNA samples (Figure 5.9) was described in the first approximation with the formula

$$E^{out}_{1.06} = (E^{in} - E^{th}(1 + \chi x))\eta(1 - \xi x), \tag{5.2}$$

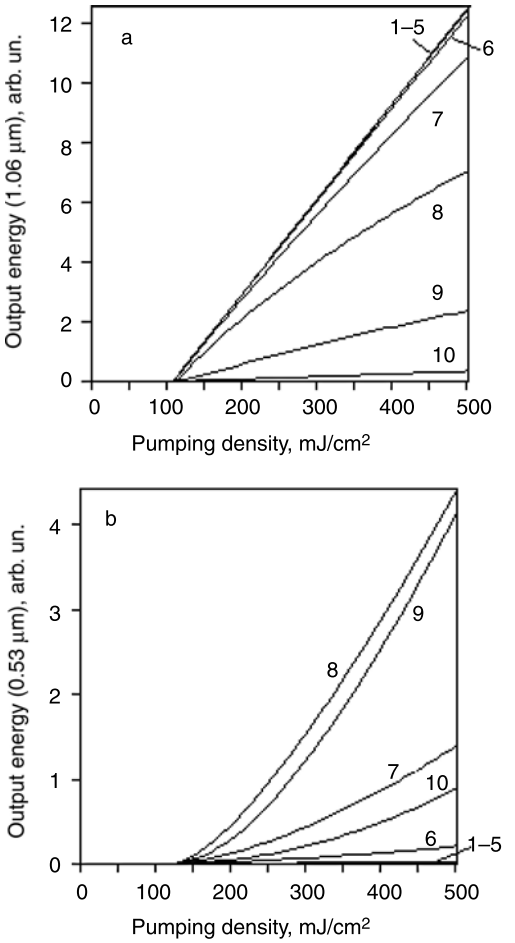

FIGURE 5.14. Calculated input–output curves (a) of 1063.1 nm stimulated emission and (b) of 531.6 nm second-harmonic radiation. The calculation is done for $x = 0.1$ and $A = 10^8\,\mathrm{cm^3\,s^{-1}\,J^{-1}}$, (2) $A = 10^9\,\mathrm{cm^3\,s^{-1}\,J^{-1}}, \ldots$, (10) $A = 10^{17}\,\mathrm{cm^3\,s^{-1}\,J^{-1}}$. The vertical scale in (a) is compatible with that in (b). (*Source*: Ref. [16].)

where $E_{1.06}^{out}$ is the output energy (at 1063.1 nm), E_{in} is the pumping energy, E_{th} is the threshold pumping energy in pure $Nd_{0.5}La_{0.5}Al_3(BO_3)_4$ powder, η is the slope efficiency in pure $Nd_{0.5}La_{0.5}Al_3(BO_3)_4$, x is the percentage of MNA powder in the mixture (by weight), and χ and ξ are the coefficients accounting for the increase of the threshold and reduction of the slope in the mixed samples. The experimental data of Figure 5.9 can be reasonably accurately fitted with Eq. (5.2) at $\chi = 0.8$ and $\xi = 2.25$. The dependences E_{out} versus x calculated according to Eq. (5.2) for different pumping energies are shown in Figure 5.16.

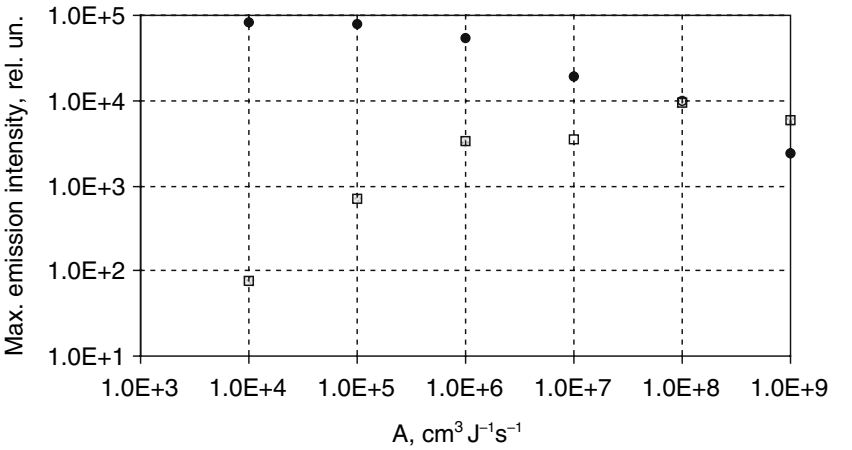

FIGURE 5.15. Dependence of the peak 1063.1 nm emission intensity (closed circles) and 531.6 nm second-harmonic radiation intensity (open squares) on A. The calculation is done for MNA concentration equal to $x = 0.1$ and pumping density equal to 500 mJ/cm^2. (*Source*: Ref. [16].)

Because the energy of second-harmonic generation E_{SHG} is proportional to $(E_{1.06}^{out})^2$ and x [see Figures 5.8 and 5.13 and Eq. (5.1)], one can write

$$E^{SHG} = \{[E^{in} - E_{th}(1 + \chi x)]\eta(1 - \xi x)\}^2 x. \tag{5.3}$$

The dependences of E_{SHG} on x calculated according to Eq. (5.3) for several different pumping energies are shown in Figure 5.10. Good agreement between calculated and experimental results (Figure 5.10) validates this simple model. As follows from Figure 5.16, the MNA concentration at which the second-harmonic output reaches its maximum value is different at different pumping energies. This gives one a tool for optimizing second-harmonic generation in powder lasers.

The model considered in Reference [16] [Eq. (5.1)] accounts only for spatially averaged population inversion and energy density of 1063.1 nm emission and its second harmonic in the pumped volume, and does not account for any specific features of light propagation in the pumped volume. The effect of scattering comes to the model only through the photon residence time τ_{res}, which is determined by the diffusion of photons in a scattering medium.

Second-harmonic generation in scattering materials has been studied in detail in theoretical work [21]. According to [21], the size of the particles, elastic scattering lengths at fundamental and second-harmonic frequencies, the sign of the frequency dispersion of the refractive index (it should be negative for the best result), and many other parameters (in addition to second-harmonic nonlinear coefficients) are very important for optimization of the second-harmonic output. Apparently, these factors, as well as the pumped volume, penetration depth for pumping, volume density (filling factor) of the powder particles, and so on, determine the efficiency of second-harmonic generation in a powder laser. This suggests many

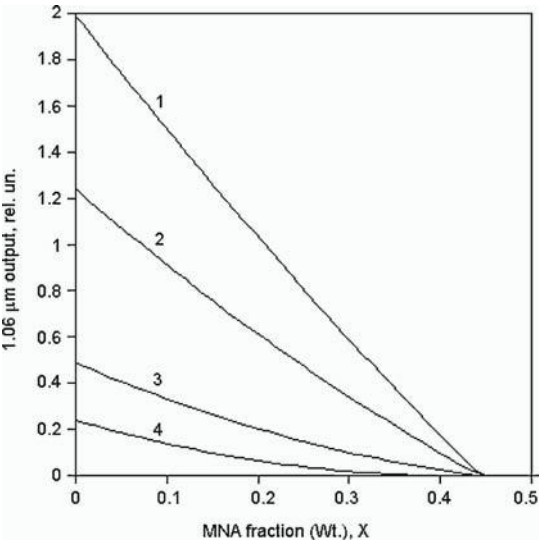

FIGURE 5.16. Calculated dependences $E_{1.06}^{out}$ versus x. (1) $E^{in} = 5.5$ mJ, (2) $E^{in} = 4$ mJ, (3) $E^{in} = 2.5$ mJ, (4) $E^{in} = 2$ mJ. The effective area of the pumped spot is equal to $\approx 0.02\,\text{cm}^2$. (*Source*: Ref. [16].)

opportunities for the further study and optimization of second-harmonic intensity in random (powder) lasers. The possibility of frequency conversion in powder lasers strongly increases their spectral range and can lead to new and interesting applications.

References

1. M.A. Noginov, N. Noginova, S.U. Egarievwe, J.C. Wang, and H.J. Caulfield, New advances in solid-state powder lasers: The effects of external seeding and external mirror. In *ICONO'98*: *Nonlinear Optical Phenomena and Coherent Optics in information Technologies*, S.S. Chesnokov, V.P. Kandidov, and N.I. Koroteev, eds., *Proceedings of SPIE*, **3733**: 223–227 (1999).
2. R.M. Balachandran and N.M. Lawandy, Interface reflection effects in photonic paint, *Opt. Lett.*, **20**: 1271–1273.
3. P.C. Oliveria, J.A. McGreevy, and N.M. Lawandy, External feedback effects in high gain scattering media, *Opt. Lett.*, **22**: 895–897 (1997).
4. H. Cao, Y.G. Zhao, X. Liu, E.W. Seelig, and R.P.H. Chang, Effect of external feedback on lasing in random media, *Appl. Phys. Lett.*, **75**: 1213–1215 (1999).
5. M.A. Noginov, G. Zhu, C. Small, and J. Novak, Neodymium random laser with external mirrors, Quantum Electronics and Laser Science (QELS) Conference, Presentation # JThE108, Baltimore, MD, May 22–27, 2005.
6. Y. Feng and K. Ueda, One-mirror random laser, *Phys. Rev. A*, **68**: 025803 (2003).

7. Y. Feng, J.-F. Bisson, J. Lu, S. Huang, K. Takaichi, A. Shirakawa, M. Musha, and K. Ueda, Thermal effects in quasi-continuous-wave Nd^{3+}:$Y_3Al_5O_{12}$ nanocrystalline-powder random laser, *Appl. Phys. Lett.*, **84**: 1040–1042 (2004).
8. V.M. Markushev, N.È. Ter-Gabriélyan, Ch.M. Briskina, V.R. Belan, and V.F. Zolin, Stimulated emission kinetics of neodymium powder lasers, *Sov. J. Quantum Electron.*, **20**: 772–777 (1990).
9. M.A. Noginov, I.N. Fowlkes, and G. Zhu, Fiber-coupled random laser, *Appl. Phys. Lett.*, **86**: 161105/1–3 (2005).
10. C. Gouedard, D. Husson, C. Sauteret, F. Auzel, and A. Migus, Generation of spatially incoherent short pulses in laser-pumped neodymium stoichiometic crystals and powders, *J. Opt. Soc. Am. B*, **10**: 2358–2363 (1993).
11. M.A. Noginov, N.E. Noginova, H.J. Caulfield, P. Venkateswarlu, T. Thompson, M. Mahdi, and V. Ostroumov, Short-pulsed stimulated emission in the powders of $NdAl_3(BO_3)_4$, $NdSc_3(BO_3)_4$, and Nd:$Sr_5(PO_4)_3F$ laser crystals, *J. Opt. Soc. Am. B*, **13**: 2024–2033 (1996). M.A. Noginov, N.E. Noginova, H.J. Caulfield, P. Venkateswarlu, T. Thompson, M. Mahdi, and V. Ostroumov, Stimulated emission without cavity in powders and single crystals of Nd doped materials. In *OSA Trends in Optics and Photonics on Advanced Solid State Lasers*, Vol. 1, S.A. Payne and C.R. Pollock, eds., Optical Society of America: Washington, DC (1996), pp. 585–590.
12. M.A. Noginov, G. Zhu, A.A. Frantz, J. Novak, S.N. Williams, and I. Fowlkes, Dependence of $NdSc_3(BO_3)_4$ random laser parameters on particle size, *JOSA B*, **21**: 191–200 (2004).
13. O. Svelto, *Principles of Lasers*, 4th ed., D.C. Hanna, trans. and ed., Plenum: New York (1998).
14. A. Yariv, *Quantum Electronics*, 3rd ed., Wiley: New York (1989).
15. W. Koechner, *Solid-State Laser Engineering*, 5th revised and updated ed., Springer-Verlag: New York (1999).
16. M.A. Noginov, S.U. Egarievwe, N. Noginova, J.C. Wang, and H.J. Caulfield, Demonstration of a second harmonic powder laser, *JOSA B*, **15**: 2854–2860 (1998).
17. B.F. Levine, C.G. Bethea, C.D. Thurmond, R.T. Lynch, and J.L. Bernstein, An organic crystal with an exceptionally large optical second-harmonic coefficient: 2-Methyl-4-nitroaniline, *J. Appl. Phys.*, **50**: 2523–2527 (1979).
18. G.F. Lipscomb, A.F. Garito, and R.S. Narang, An exceptionally large linear electro-optic effect in the organic solid MNA, *J. Chem. Phys.*, **75**: 1509–1516 (1981).
19. S.M. Rao, A.K. Batra, R.R. Lal, R.A. Evans, B.H. Loo, R.M. Metzger, and W.J. Lee, Mixed methyl-(2,4-dinitrophenyl)-aminopropanoate: 2-methyl-4-nitroaniline crystal—a new nonlinear optical material, *J. Appl. Phys.*, **70**: 6674–6678 (1991).
20. M.A. Noginov, N. Noginova, S.U. Egarievwe, H.J. Caulfield, C. Cochrane, J.C. Wang, M.R. Kokta, and J. Paitz, Study of the pumping regimes in Ti-sapphire and $Nd_{0.5}La_{0.5}Al_3(BO_3)_4$ powders, *Opt. Mater.*, **10**: 297–303 (1998).
21. V.E. Kravtsov, V.M. Agranovich, and K.I. Grigorovoch, Theory of second-harmonic generation in strongly scattering media, *Phys. Rev. B*, **44**: 4931–4942 (1991).

6
Random Lasers Pumped with Electron Beam

6.1 Rare-Earth Random Lasers Directly Pumped with Electron Beam

The majority of random lasers are pumped optically, in most cases via the sample surface. In such pumping geometry, scattering, which is essential for providing a stimulated emission feedback, also plays a negative role, reflecting pumping light and reducing the pumping efficiency. One of the ways to increase the pumping efficiency is to deliver excitation light deep inside a scattering volume through an optical fiber [1,2] or a narrow channel "drilled" in a powder by focused laser light [3]. Alternatively, the thickness of a pumped layer and, correspondingly, the quality factor of an effective resonator formed by scatterers, can be increased if electron beam pumping is used instead of optical pumping [4–7]. In the latter case, the penetration depth can be controlled by the energy of an electron beam [5,6] (Figure 6.1).

Rare-earth random lasers pumped with a *dc* electron beam have been studied in References [4–10]. The nanopowders of δ-alumina doped with Ce^{3+}, Pr^{3+}, and Nd^{3+} ions have been synthesized using a flame spray pyrolysis technique [8]. In different samples, the doping level varied between 100 and 1000 ppm and the size of individual particles varied between 10 and 40 nm. The typical transmission electron microscope image of doped δ-alumina nanoparticles is shown in Figure 6.2.

Loose powders were lightly compressed and mounted in several-millimeter-wide shallow recesses of oxygen-free copper platen in an ultra-high vacuum ($6 \times 10^{-10} - 9 \times 10^{-10}\,T$) and irradiated with an electron beam. In different experiments, the diameter of the electron beam varied between 1 and 7 mm, and the electron energy varied between 1 and 10 keV. The spectra of cathodoluminescence at different electron beam currents and energies were recorded using a 1 m grating spectrometer.

6.1.1 Ce:δ-Alumina Random Laser

Stimulated emission in Ce^{3+} doped δ-alumina (δ-Al_2O_3) has been studied in References [4,5,8,9]. In the experiment described in [6], the mean particle size

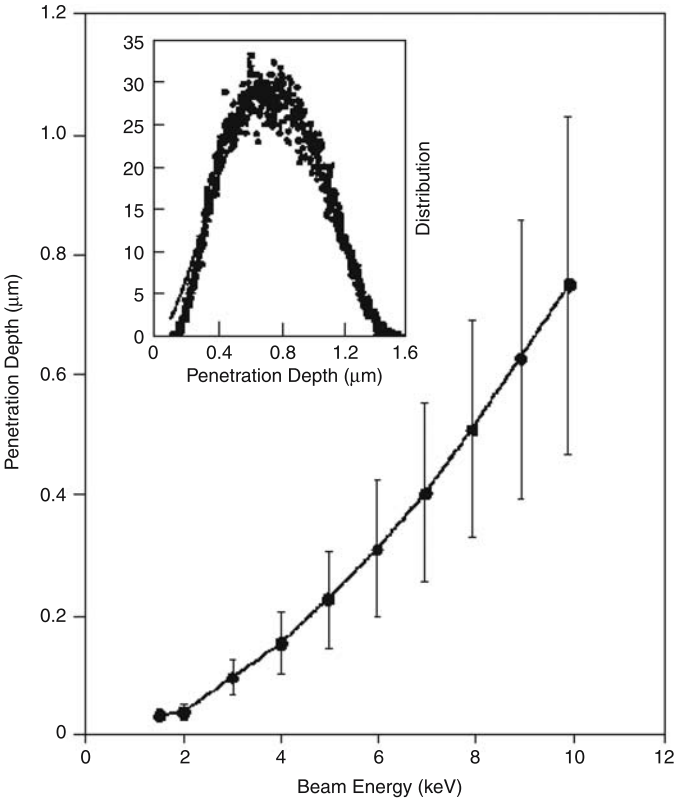

FIGURE 6.1. Monte Carlo simulation of mean electron penetration in alumina versus incident energy. The mean value of the Gaussian distribution in the inset is plotted versus energy in the main frame. (*Source*: Ref. [5].)

was equal to 20 nm and the doping level was equal to 1000 ppm. The transport mean free path, determined in the coherent backscattering (CBS) experiment, was equal to $l_t = 114\,\text{nm}$ at the wavelength $\lambda = 363.8\,\text{nm}$.

The spectrum of cathodoluminescence consisted of two almost unresolved bands, corresponding to the transitions $5d{-}4f^2\text{F}_{5/2}$ (higher energy) and $5d{-}4f^2\text{F}_{7/2}$ (lower energy) Figure 6.3. (A Dieke diagram for the energy levels of trivalent cerium, praseodymium, and neodymium ions discussed in this chapter is shown in Figure 6.4.) The physical mechanism of the excitation of cathodoluminescence, supposedly similar to that in scintillators [12,13], was not discussed in detail in References [4,5,8,9].

At small pumping current, the combined emission band had a peak at approximately $2.6 \times 10^4\,\text{cm}^{-1}$ ($\approx$0.385 μm) and a full width at half maximum equal to $6.6 \times 10^3\,\text{cm}^{-1}$. With the increase of the pumping current above a certain critical threshold value, the emission band narrowed to $4.8 \times 10^3\,\text{cm}^{-1}$ and its maximum shifted to approximately $2.8 \times 10^4\,\text{cm}^{-1}$ ($\approx$0.36 μm). The dependence of the

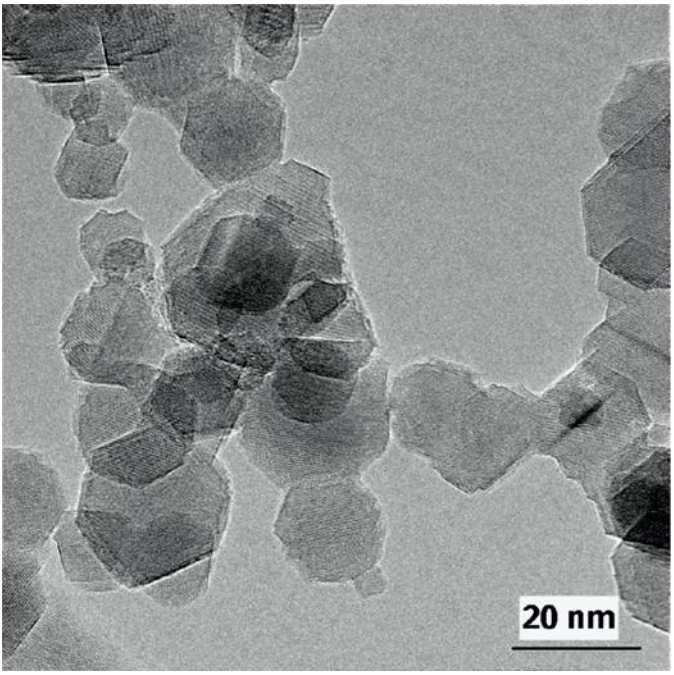

FIGURE 6.2. Transmission electron microscope picture of δ-alumina nanoparticles. (*Source*: Ref. [9].)

emission intensity at $\lambda = 362\,\text{nm}$ versus pumping current can be described with a combination of two straight lines with different slopes (inset of Figure 4.5a). The change of the slope occurs at exactly the same threshold at which the narrowing of the emission band is observed.

The experimental results above were explained by an onset of cw stimulated emission at the Ce^{3+} $5d-4f^2F_{5/2}$ transition. In fact, in the case of lasing, only the emission intensity at the laser transition continues to grow above the threshold, and the emission intensity at the other transition originating from the same upper laser level ($5d-4f^2F_{7/2}$) saturates at its threshold value. This explains the experimentally observed spectral changes. The fact that the input–output curve consisted of straight lines (as opposed to an exponential function) was used as reasonable evidence that the observed phenomenon was a stimulated emission with feedback rather than an amplified spontaneous emission (ASE) in open paths.

Note that the threshold behavior lacking a strong change of the slope (inset of Figure 4.5a) is in line with the results of the theoretical modeling of a cw random laser emission discussed in Section 4.3. The fact that the stimulated emission threshold is first achieved at the transition terminating at the ground state $4f^2F_{5/2}$ (three-level laser scheme) rather than at the empty excited state $4f^2F_{7/2}$ (four-level laser scheme) can be explained if one assumes that the transition $5d-4f^2F_{5/2}$ has a higher cross section than the transition

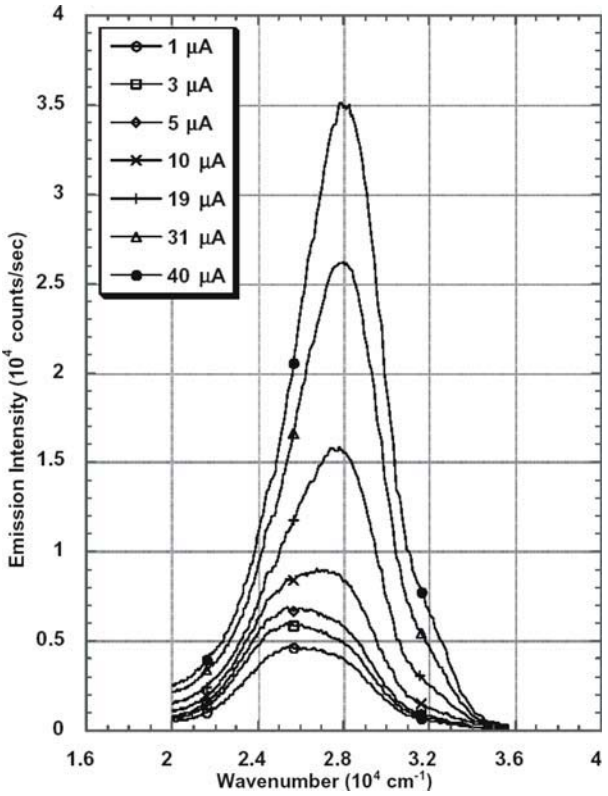

FIGURE 6.3. Cathodoluminescence spectra of Ce:δ-Al_2O_3 nanoparticles excited by various electron beam current levels (4 keV, 2 mm beam diameter). (*Source*: Ref. [9].)

$5d-4f^2F_{7/2}$ and that the ground state $4f^2F_{5/2}$ is strongly depopulated by strong pumping [14].

The spectrum of Ce:δ-Al_2O_3 stimulated emission depicted in Figure 6.3 was lacking any sharp lines, which could be attributed to coherent laser modes supported by morphological intraparticle or interparticle resonators. In addition, no speckle pattern was seen in cerium random laser emission [9]. These two observations served as evidence of low coherence of the Ce:δ-Al_2O_3 random laser. The low degree of coherence has been explained by a very short (shorter than half of wavelength) photon mean free path, which causes strong (Anderson [15–18]) localization of light in a scattering material.

It has been argued [7,9] that if emitted electromagnetic energy is significantly attenuated (by scattering) at a distance shorter than a wavelength, the emitted light does not propagate or diffuse at all. Instead, it assumes a distribution similar to that of a three-dimensional evanescent field as a result of lossless reflection between particles. Accordingly, if closed paths providing for feedback are shorter than half

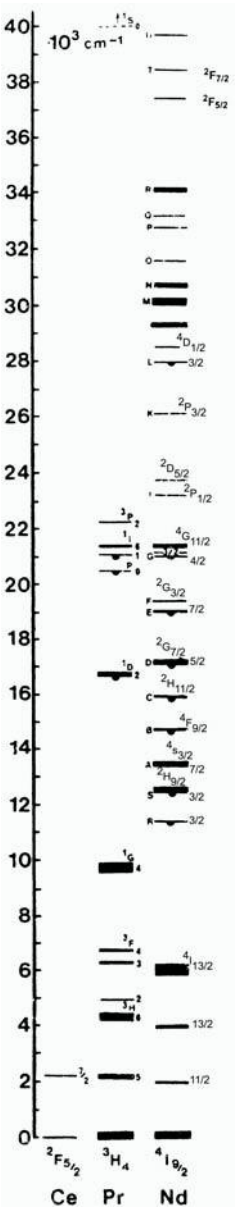

FIGURE 6.4. Dieke diagram for the energy levels of trivalent cerium, praseodymium, and neodymium ions (after [11]).

wavelength, interference of light required to produce frequency selectivity cannot occur [9].

The proposed applications of electron-beam-pumped Ce:δ-alumina lasers included nanolithography, sources for airborne and space communication devices, and novel materials for displays [4].

6.1.2 Pr:δ-Alumina Random Laser

Stimulated emission in Pr^{3+} doped δ-alumina has been studied in References [5,8,9] (in [5] the same material was identified as β"-alumina). The mean particle size was equal to 40 nm and the level of praseodymium doping was equal to 1000 ppm [9]. The transport mean free path, determined in a CBS experiment, was equal to $l_t = 311$ nm at $\lambda = 632.8$ nm, less than half a wavelength.

The change in the spectrum of electron-beam-pumped praseodymium emission with the increase of current is shown in the inset in Figure 6.5. As follows from this inset, the two sharp emission lines at 15,810 cm^{-1} and 16,000 cm^{-1} ($\lambda \approx 0.63\,\mu m$), which are almost nonexistent at small current, become predominant in the spectrum at stronger pumping. These spectral lines were assigned to the Pr^{3+} transition $^3P_0 - {}^3H_6$ (Figure 6.4) [9]. These stimulated emission wavelengths and the transition were different from those in the optically pumped praseodymium random laser, 0.76 to 0.77 μm and $^3P_0 - {}^3F_4$ [19,20].

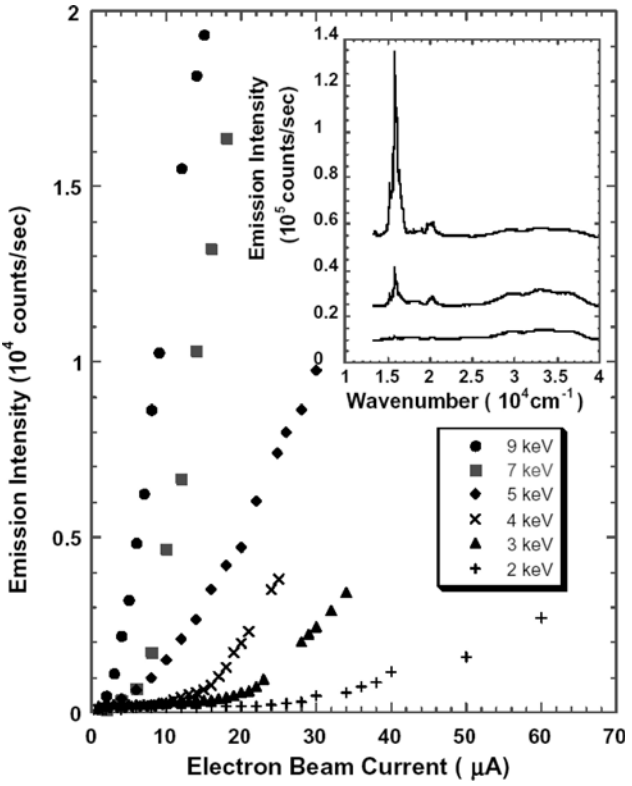

FIGURE 6.5. Emission intensity versus current at $\lambda_{em} = 633$ nm in Pr:δ-Al_2O_3 nanoparticles, and electron energy (1 to 10 keV). Inset: Emission spectra of Pr:δ-Al_2O_3 illustrating growth of the red transition with increasing current at 7 keV. (*Source*: Ref. [9].)

The series of input–output curves (emission versus current) measured at different electron beam energies is shown in the main frame of Figure 6.5. Based on the combination of the threshold behavior of input–output curves, which was more pronounced at small energies of an electron beam, and the evolution of the spectra, the observed emission was concluded to be a stimulated emission of Pr:δ-alumina random laser.

With the increase of electron beam energy, the input–output curves became steeper, developed more curvature, and the threshold current lowered [5,9] (Figure 6.5). This threshold behavior was not surprising, since with the increase of the electron energy, the penetration depth of pumping and, correspondingly, the Q-factors of effective cavities increased too [5,9,14]. The input–output curves characterized by not very dramatic changes of the slope are in good qualitative agreement with those calculated in cw approximation in Section 4.3 (Figure 4.5). The curvature of input–output dependences became highly pronounced at the electron energy exceeding ≈4 keV (Figure 6.5), at which the penetration depth of an electron pumping was of the order of the transport mean free path. This effect was explained by stimulated emission generated in the depth of powder and amplification of spontaneous emission occurring in the layers of powder, which were relatively close to the surface [5,9,14].

The stimulated emission of Pr:δ-alumina, similar to that of Ce:δ-alumina, was characterized by the absence of speckle pattern, absence of directionality, and absence of narrow emission lines (coherent modes) in the spectrum [5]. The observed properties of the praseodymium random laser emission were explained (analogous to the case of Ce:δ-Al_2O_3 random laser) by strong localization of light in subvolumes much smaller than the emission wavelength. When $l_t \ll \lambda$, the coherence length l_c is also shorter than λ, and light becomes evanescent and nonpropagating, oscillating in time but not in space. In this regime, a low-coherence omnidirectional laser emission without any speckle or mode structure is expected [5].

Studies of emission in a praseodymium random laser pumped with electron beam were also mentioned in References [19,20]; however, no experimental details were given.

6.1.3 Nd:δ-Alumina Random Laser

Stimulated emission in Nd:δ-Al_2O_3 nanopowders pumped with an electron beam has been observed at several different wavelengths in References [6] and [10]. In [6], δ-alumina particles had log-normal distribution of their sizes, mean diameter equal to 27 nm, and 1000 ppm concentration of Nd^{3+} ions (≈240 neodymium ions per granule). The diameter of the focused electron beam was equal to 1 to 2 mm. By varying the energy of an electron beam between 2 and 10 keV, one could control the penetration depth of electrons (Figure 6.1) and, correspondingly, the position of the pumped volume with respect to the surface of the sample.

It has been found [6] that at the energy of electron beam equal to 8 keV and relatively small current, 3.3 μA, the largest emission peaks in the vicinity of 400 nm

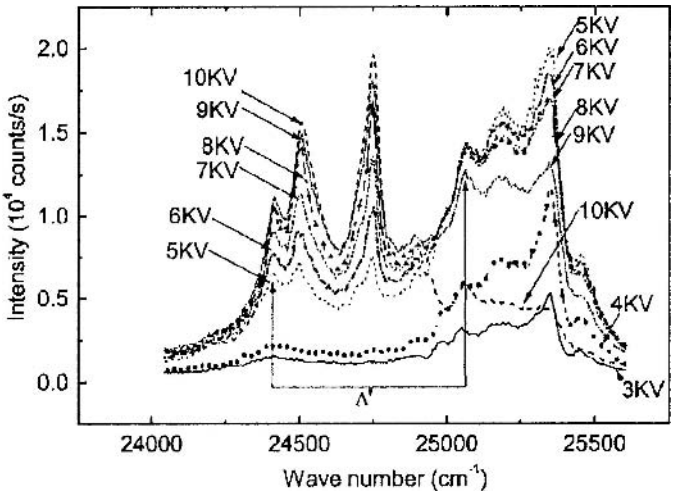

FIGURE 6.6. Voltage dependence of cathodoluminescence spectral peaks in the 25,000 cm^{-1} region. Features above 25,000 cm^{-1} (attributed to the transitions originating from the state $^2F_{7/2}$) grow rapidly up to 5 kV and then quench. Features below 25,000 cm^{-1} (attributed to the transitions originating from the state $^2F_{5/2}$) are absent until 5 kV. (*Source*: Ref. [6].)

are located above 25,000 cm^{-1}. At the same time, at stronger current, 16.9 μA, the largest peaks appear below 25,000 cm^{-1} and the original intense lines vanish. A similar pattern is observed with the increase of the electron energy as shown in Figure 6.6. Spectroscopic studies allowed one to assign most of the observed emission lines to corresponding electronic transitions [6]. Thus, spectral features above 25,000 cm^{-1} were assigned to transitions originating at the state $^2F_{7/2}$ and those below 25,000 cm^{-1} were attributed to transitions originating at the state $^2F_{5/2}$ (Figure 6.4).

Emission intensities observed at several UV and visible transitions starting at the levels $^2F_{5/2}$ and $^2F_{7/2}$ are plotted versus electron beam current in Figure 6.7a [6]. According to this figure, emission at all transitions, except $^2F_{5/2} - {}^4F_{9/2}$, quenches rapidly above $\approx$3 μA. (The population of the state $^2F_{7/2}$ follows that of $^2F_{5/2}$ because the two states have a relatively small energy gap, $\Delta \sim 650\,cm^{-1}$ and are strongly thermally coupled.) At the same time, the emission at the transition $^2F_{5/2} - {}^4F_{9/2}$ demonstrates a typical laser input–output curve, with a sharp threshold and linear growth above the threshold. Note that in lasers, the population inversion above the threshold should be locked at its threshold value. Thus, the reduction of intensities of spontaneous emission transitions originating from the upper laser level with an increase of the pumping power above the threshold (Figure 6.7a) is rather unusual. However, as shown in Figure 6.7b, a simple rate equation model, which takes into account ASE transitions originating from the upper laser level, gives semiquantitative agreement with experimentally observed

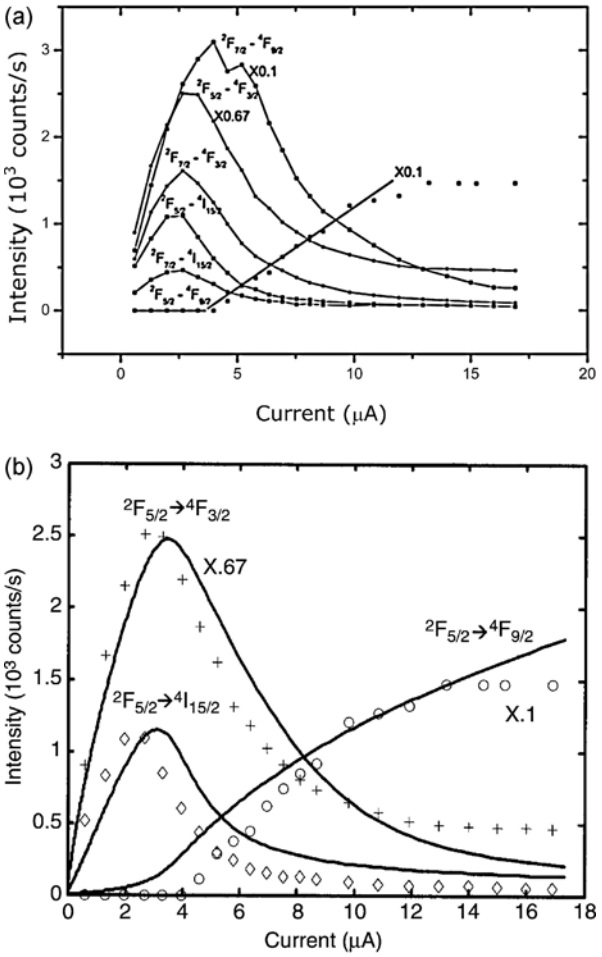

FIGURE 6.7. (a) Current dependence of ultraviolet and visible cathodoluminescence intensities of the $^2F_{5/2}$ and $^2F_{7/2}$ states at 8 kV. All curves (but one) quench rapidly above 3 μA, where intensity of the $^2F_{5/2} - {}^4F_{9/2}$ transition undergoes an abrupt change in slope. (*Source*: Ref. [6], modified in accordance with [14].) (b) Intensities of stimulated emission originating at the same upper level $^4F_{3/2}$ and terminating at different lower levels in Nd^{3+}:d-Al_2O_3 nanopowder pumped with electron beam. Data points: experiment; solid lines: calculation [14]. [The rate equation model comprised only the ground state ($|1> {}^4I_{9/2}$), the metastable excited state ($|2> = {}^2F_{5/2}$), and three intermediate states ($|3> = {}^4F_{9/2}$; $|4> = {}^4F_{3/2}$; $|5> = {}^4I_{15/2}$). Fixed decay rates γ_{ij} from level i to level j were taken to be $\gamma_{23} = 2.1 \times 10^5\, s^{-1}$, $\gamma_{24} = 2 \times 10^6\, s^{-1}$, $\gamma_{25} = 4.25 \times 10^5\, s^{-1}$, $\gamma_{34} = 6 \times 10^8\, s^{-1}$, $\gamma_{35} = 6 \times 10^8\, s^{-1}$. The diameter of the cavity was assumed to be $\lambda = 400$ nm and cavity decay time was determined to be $\tau_c = 100 \pm 50$ ps [14].

quenching dynamics [14,21]. The three emissions depicted in Figure 6.7b share a common upper level $^2F_{5/2}$ in a 5-level model. Three terminal levels of three stimulated emission transitions, $^4F_{9/2}$, $^4F_{3/2}$, and $^4I_{15/2}$, are coupled via the excitation relaxation $^4F_{9/2} \rightarrow {}^4F_{3/2} \rightarrow {}^4I_{15/2}$, which suppresses the stimulated emission at the transitions $^2F_{5/2} \rightarrow {}^4F_{3/2}$, and $^2F_{5/2} \rightarrow {}^4I_{15/2}$ and increases the relative intensity of the stimulated emission at the transition $F_{5/2} \rightarrow {}^4F_{9/2}$. In calculations, the cavity size was taken to be equal to the wavelength, and the best agreement with the experiment was obtained at the cavity decay time equal to $\tau_c = 100$ ps.

Based on the spectral evolution (Figure 6.6) and the input–output behavior (Figure 6.7), the authors of Reference [6] concluded that the observed phenomenon was a laser emission with highly efficient feedback. When the energy of an electron beam and, accordingly, the distance between the pumped volume and the surface of the sample increased, the intensity of the stimulated emission increased (Figure 6.6) and the threshold decreased. The observed stimulated emission was speckle-free; its spectrum did not depend on the detection angle, and it lacked any narrow lines (similar to those found in ZnO or polymer films [22–26] and associated with frequency resonances).

It has been concluded [6] that the obtained laser action (similar to the case of Ce:δ-Al_2O_3 and Pr:δ-Al_2O_3 random lasers discussed in Sections 6.1.1 and 6.1.2) resulted from strong localization of light. In fact, according to the coherent backscattering measurements, the transport mean free path was equal to $l_t \approx 174 \pm 31$ nm, shorter than half the emission wavelength. Given that the coherence length l_c is limited to a subwavelength value, $l_c < l_t < \lambda$, light generated by impurity ions necessarily acquires a spatial distribution resembling that of a three-dimensional evanescent wave [27]. This property in combination with spatial randomization on length scales smaller than $\lambda/2$ precludes directionality, mode selectivity, and coherence of random emission.

In Reference [10], a Nd^{3+}:δ-alumina sample synthesized from a different metallorganic precursor than the sample of [6] (and possibly having different absorption loss and porosity [14]) was studied in an experimental setup almost similar to that of [6]. A series of emission spectra recorded at different electron beam currents reveals many lines characteristic of Nd^{3+} (Figure 6.8). At low current, 1 μA, the most prominent line, assigned to the transition $^2F_{5/2} - {}^4F_{7/2}$ [10], was observed at 25,000 cm^{-1} (Figure 6.4). At intermediate current values (20 to 40 μA) the intensities of transitions at 25,000 and 24,500 cm^{-1} reverse [14], just as in [6]. At much stronger current, >50 μA, three emission lines originating from the state $^2F_{5/2}$ (at 25,000 cm^{-1}, 32,500 cm^{-1}, and 34,500 cm^{-1}) were completely quenched and the intensity of the fourth transition originating from the same level ($^2F_{5/2} - {}^4F_{3/2}$ at 27,000 cm^{-1}) grew up strongly. In the same strong current range (>50 μA), the spectral line at 23,000 cm^{-1}, corresponding to the transition $^2P_{1/2} - {}^4I_{9/2}$, was quenched, whereas the intensity of another emission line originating from the same state ($^2P_{1/2} - {}^4I_{11/2}$ at 21,000 cm^{-1}) increased significantly. This spectral redistribution, along with the threshold behavior of the input–output curves (Figure 6.9), served as evidence of stimulated emission at 367 nm, 469 nm, and 870 nm (not shown in Figure 6.8) [10].

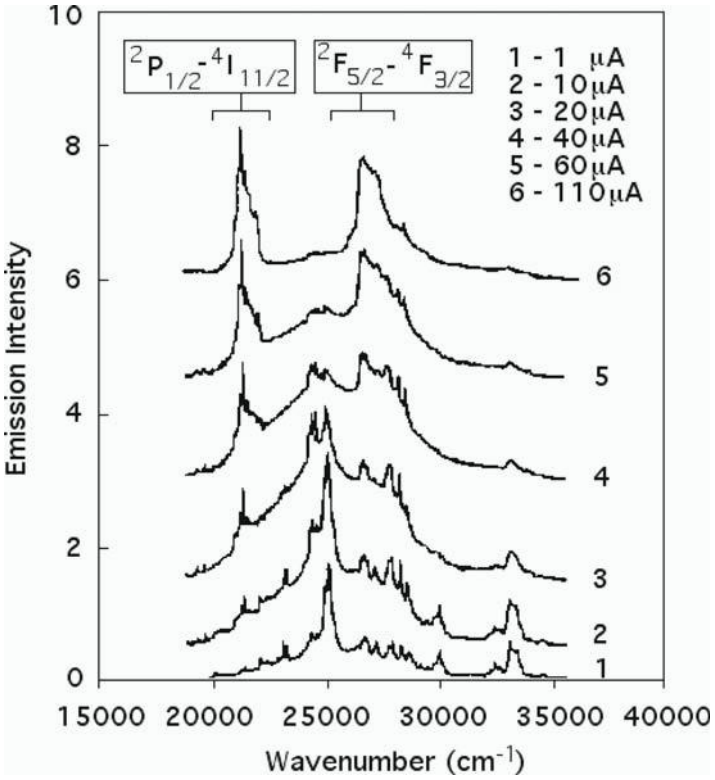

FIGURE 6.8. Spectra of cathodoluminescence of Nd:δ-Al_2O_3 powder excited by various electron beam currents at 10 keV ($T = 295$ K). (*Source*: Ref. [10].)

6.1.4 Discussion of Experiments with Electron Beam-Pumped δ-Alumina Powders

In References [4–10], low-coherence, speckle-free, resonance-free, omnidirectional random laser emission, observed in scattering media characterized by the transport mean free path shorter than $\lambda/2$, was explained in terms of strong (Anderson) localization of light in volumes of subwavelength size. It has been assumed that strong localization provides for high-quality effective cavities capable of supporting cw laser emission at low gain [9]. The open questions relevant to understanding of experiments discussed in this section are:

1. If the stimulated emission is supported by localization of light in small isolated volumes, then what is the fraction of those small volumes in the total pumped volume, and what, accordingly, is the efficiency of stimulated emission?
2. How do evanescent modes radiate light? What is the coupling mechanism between localized modes and propagating modes?

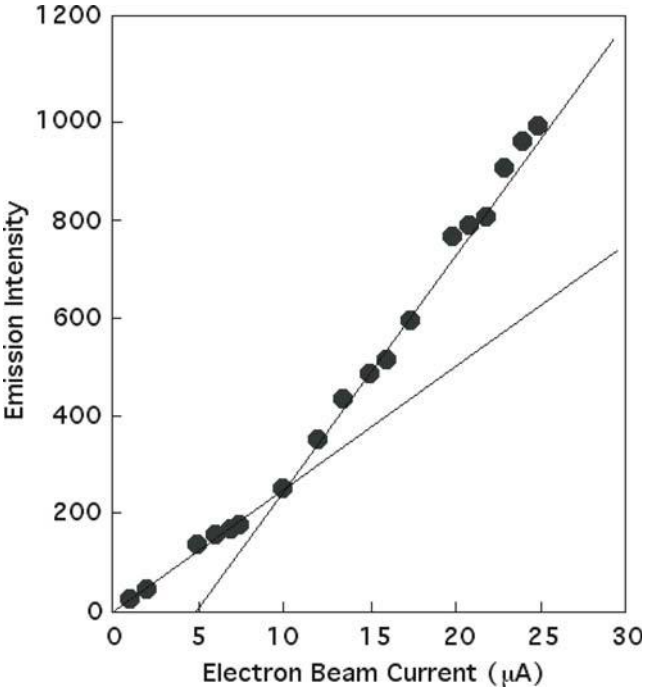

FIGURE 6.9. Peak emission intensity at $\lambda = 469$ nm in Nd:δ-Al_2O_3 powder pumped with electron beam at 5 keV, plotted versus electron current ($T = 295$ K). (*Source*: Ref. [10].)

Note that low-coherence omnidirectional random laser emission cannot be used as sufficient proof of localization of laser modes to subwavelength volumes. Incoherent emission is also expected in diffusion-dominated random lasers with incoherent feedback [28,29]. However, direct evidence has recently been provided that the experiment in [6] involved cavity feedback on the scale of an optical wavelength. As the electron penetration depth was increased from 0.25 to 1.2λ, laser emission intensity has been shown to increase [30]. Because this result is the opposite of what would be expected if the sample surface acted as a mirror, and occurred on the distance scale of the optical wavelength, it furnishes evidence both of the laser mechanism being independent of surface reflections and the cavity size being of the order of a wavelength.

6.2 Nd:YAG Pumped with an Electron Beam via Scintillator

The pumping of Nd:YAG with electron beam via scintillator has been demonstrated in References [31,32]. A special electron-beam tube was designed, which allowed one to cool samples down to 77 K. The layer of Nd:YAG and the layer of scintillator

(cathodoluminophore) were deposited onto the surface of the target and coated from the top with the reflecting layer of aluminum. (The parameters of powders were not specified in References [31,32].) The scintillator was pumped by an electron beam and produced an optical emission, the spectrum of which matched the absorption spectrum of Nd:YAG. The aluminum film served as a mirror helping to increase the efficiency of pumping and provide a confinement for Nd:YAG emission.

The electron beam pulses were 0.7 μs long. When the pumping energy was increased from 18 to 20 keV, the ratio of the intensities of the 1063 and 1081 nm spectral lines (at the transition $^4F_{3/2} - {}^4I_{11/2}$) increased sharply in a threshold-like manner, from 2 to 3. Although the behavior of the Nd:YAG emission closely resembled that of Ce:δ-alumina random lasers and Nd:δ-alumina random lasers described in Sections 6.1.1 and 6.1.3, the authors of References [31,32] described the observed emission as superfluorescence, meaning by it a stimulated emission process below the threshold. It was further estimated that it is unlikely that a short-pulsed random laser emission (similar to that excited with Q-switched laser light) can be obtained under electron beam pumping of reasonable intensity. However, a combined pumping by an electron beam and a laser light is possible and can potentially find application in information processing [31,32].

References

1. V.M. Markushev, N.È. Ter-Gabriélyan, Ch.M. Briskina, V.R. Belan, and V.F. Zolin, Stimulated emission kinetics of neodymium powder lasers, *Sov. J. Quantum Electron.*, **20**: 772–777 (1990).
2. M.A. Noginov, G. Zhu, and I. Fowlkes, Fiber-coupled random laser, to be presented at International Conference on Quantum Electronics (IQEC), paper #IFB1, 2004 CD ROM CLEO/QELS Technical Digest, ISBN # 1-55752-770-9, 2004.
3. M.A. Noginov, N. Noginova, S.U. Egarievwe, H.J. Caulfield, C. Cochrane, J.C. Wang, M.R. Kokta, and J. Paitz, Study of the pumping regimes in Ti-sapphire and $Nd_{0.5}La_{0.5}Al_3(BO_3)_4$ powders, *Opt. Mater.*, **10**: 297–303 (1998).
4. G. Williams, S.C. Rand, T. Hinklin, and R.M. Laine, Ultraviolet laser action in strongly scattering Ce:alumina nanoparticles. In *Conference on Lasers and Electro-Optics*, OSA Technical Digest, Optical Society of America: Washington, DC (1999), p. 90.
5. S.C. Rand, Strong localization of light and photonic atoms, *Can. J. Phys.*, **78**: 625–637 (2000).
6. B. Li, G. Williams, S.C. Rand, T. Hinklin, and R.M. Laine, Continuous-wave ultraviolet laser action in strongly scattering Nd-doped alumina, *Opt Lett.*, **27**: 394–396 (2002).
7. S.C. Rand, Bright storage of light, *Opt. Photon. News*, 32–37 (May 2004).
8. R.M. Laine, T. Hinklin, G. Williams, and S.C. Rand, Low-cost nanopowders for phosphor and laser applications by flame spray pyrolysis, *Mater. Sci. Forum*, **343**: 500–510 (2000).
9. G. Williams, B. Bayram, S.C. Rand, T. Hinklin, and R.M. Laine, Laser action in strongly scattering rare-earth-doped dielecric nanophosphors, *Phys. Rev. A*, **65**: 013807 (2001).

10. G. Williams, S.C. Rand, T. Hinklin, and R.M. Laine, Blue and infrared laser action in strongly scattering Nd:alumina nanopowders. In *Conference on Lasers and Electo-Optics*, OSA Technical Digest, Optical Society of America: Washington, DC (1999), p. 483.
11. G.H. Dieke and H.M. Crosswhite, The spectra of doubly and triply ionized rare earths, *Appl. Opt.*, **2**: 675–686 (1963).
12. A. Lempicki, A.J. Wojtowicz, and E. Berman, Fundamental limits of scintillator performance, *Nucl. Instrum. Methods Phys. Res. A*, **333**: 304–311 (1993).
13. J. Anderson, P. Dorenbos, and C.W.E. van Eijk, Calculation of energy levels of cerium in inorganic scintillator crystals, *Mater. Res. Soc. Symp. Proc.*, **348**: 355–365 (1994).
14. S.C. Rand, private communication.
15. P.W. Anderson, Absence of diffusion in certain random lattices, *Phys. Rev.*, **109**: 1492–1505 (1958).
16. P.W. Anderson, The question of classical localization: A theory of white paint, *Philos. Mag. B*, **52**: 505–509 (1985).
17. S. John, Electromagnetic absorption in a disordered medium near a photon mobility edge, *Phys. Rev. Lett.*, **53**: 2169–2172 (1984).
18. S. John, Localization of light, *Phys. Today*, 32–40 (May 1991).
19. V.F. Zolin, A.A. Lichmanov, and N.P. Soshchin, *Abstracts of Reports to the First International Conference on Chemistry and Technology of Luminophores*, Institute of Luminophores Press: Stavropol, 1988.
20. V.F. Zolin, The nature of plaser-powdered laser, *J. Alloys Compounds*, **300–301**: 214–217 (2000).
21. B. Li and S.C. Rand, Nonlinear spectral quenching in random lasers. OSA Conference on Nonlinear Optics, Hawaii, August 2–6 (2004).
22. H. Cao, Y.G. Zhao, H.C. Ong, S.T. Ho, J.Y. Dai, J.Y. Wu, and R.P.H. Chang, Ultraviolet lasing in resonators formed by scattering in semiconductor polycrystalline films, *Appl. Phys. Lett.*, **73**: 3656–3658 (1998).
23. H. Cao, Y.G. Zhao, S.T. Ho, E.W. Seelig, Q.H. Wang, and R.P.H. Chang, Random laser action in semiconductor powder, *Phys. Rev. Lett.*, **82**: 2278–2281 (1999).
24. H. Cao, J.Y. Xu, Y. Ling, S.-H. Chang, S.T. Ho, E.W. Seelig, X. Liu, and R.P.H. Chang, Random lasers with coherent feedback. In *Photonic Crystals and Light Localization in the 21st Century*, C.M. Soukoulis, ed., Kluwer: Dordrecht, The Netherlands (2001).
25. H. Cao, Random lasers with coherent feedback. In *Optical properties of nanostructured random media*, V.M. Shalaev, ed., Springer: New York (2002).
26. R.C. Polson, A. Chipouline, and Z.V. Vardeny, Random lasing in p-conjugated films and infiltrated opals, *Advan. Mater.*, **13**: 760–764 (2001).
27. J.W. Goodman, *Statistical Optics*, Wiley: New York (1985), p. 206.
28. V.S. Letokhov, Generation of light by a scattering medium with negative resonance absorption [*Zh. Exp. and Teor. Fiz.*, **53**: 1442–14452, (Russian)], *Sov. Phys. JETP*, **26**: 835–840 (1968).
29. R.V. Ambartsumyan, N.G. Basov, P.G. Kryukov, and V.S. Letokhov, Non-Resonant Feedback in Lasers. In *Progress in Quantum Electronics*, Vol. 1, J.H. Sanders and K.W.H. Stevens, ed., Pergamon: New York 107 (1970).
30. S.M. Redmond, G.L. Armstrong, H.-Y. Chan, E. Mattson, A. Mock, B. Li, J.R. Potts, M. Gui, S.C. Rand, S.L. Oliveira, J. Marchal, T. Hinklin, and R.M. Laine, Electrical generation of stationary light in random scattering media, *JOSA B*, **21**: 214–222.

31. A.A. Lichmanov, Ch.M. Briskina, N.P. Soshchin, and V.F. Zolin, Lasing in powders and its use for data processing, *Bulletin of the Russian Academy of Sciences. Physics. Izvestiya Rossiiskoi Akademii Nauk. Seriya Fizicheskaya*, **63**: 922–926 (1999).
32. A.A. Lichmanov, Ch.M. Brickina, V.N. Lichmanova, N.P. Soshchin, and V.F. Zolin, Experimental studies of the lanthanide doped lasing powders (plasers). In *Proceedings of the International Conference LASERS'98* (Tucson, AZ, December 7–11, 1998), (1999), pp. 725–731.

7
Semiconductor Random Lasers

Stimulated emission in ZnO powder was first reported in 1981 in Reference [1]. Unfortunately, Reference [1] was lacking any details which could make it possible to conclude whether the stimulated emission in ZnO occurred in individual granules or was supported by an ensemble of particles, what the character of feedback was or the degree of coherence, and so on. The detailed study of ultraviolet stimulated emission in ZnO powders is primarily due to Cao et al. (see, for example, Refs. [2–5]). Near-infrared emission of semiconductor random lasers has been demonstrated in $GaAs_{0.972}N_{0.028}$ film [6] and GaAs powder [7]. Eye-safe mid-infrared random laser emission from Cr^{2+} doped semiconductor materials ZnSe and ZnS [8,9] is discussed in Chapter 9. Random lasers based on semiconducting polymers are described in Chapter 8.

7.1 ZnO Random Laser: Phenomenological Description and Intuitive Model

In Reference [2], Cao et al. investigated 300 to 350 nm thick ZnO films composed of 50 to 150 nm particles deposited (grown) on amorphous fused silica substrates by ablation. A cross-sectional transmission electron microscopy (TEM) image demonstrated a columnar growth of granules in the film. X-ray diffraction measurements indicated that the particles in the film were textured with the *c*-axis oriented perpendicularly to the substrate plate. The in-plane pattern of deposited polycrystalline particles was highly disordered, resulting in strong optical scattering of the film. The coherent backscattering measurements showed that the scattering mean free path was of the order of $0.4\,\mu m$.

The samples were optically pumped with 15 ps pulses of a frequency-tripled Nd:YAG laser at 355 nm. (The same type of pumping was used in the majority of ZnO experiments performed by Cao's group, which are discussed in this chapter.)

At low pumping intensity, a single spontaneous emission band, ascribed to the transition from the conduction band to the valence band of ZnO, with the maximum at $\approx$387 nm and the full width at half maximum equal to $\approx$10 nm has

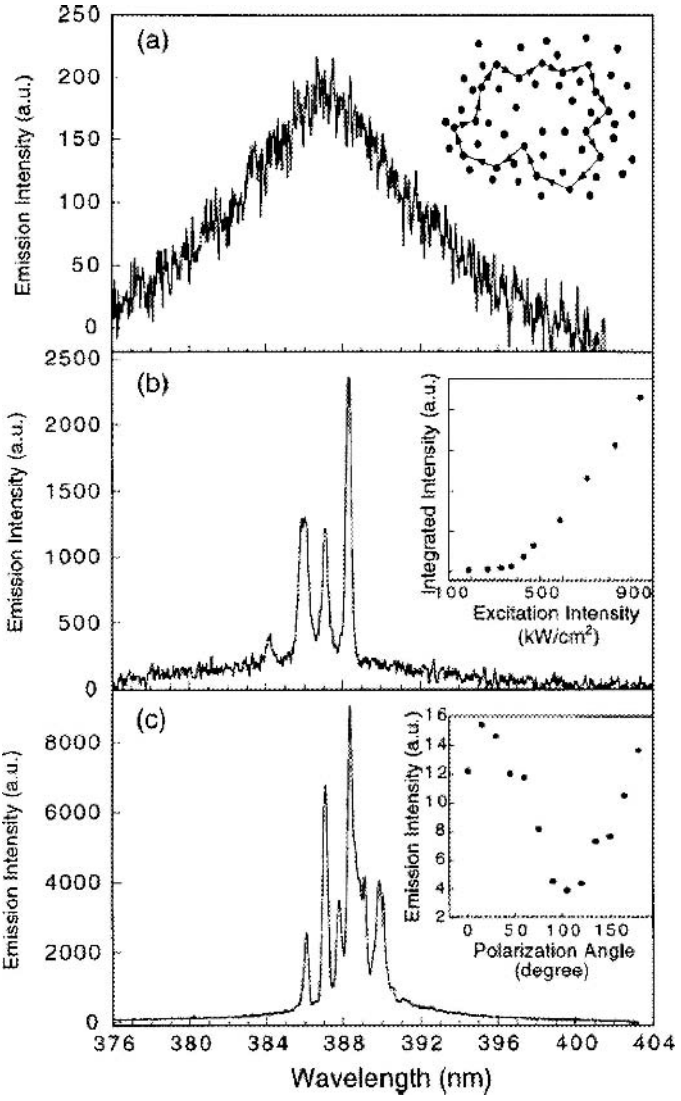

FIGURE 7.1. Emission spectra of ZnO film when the excitation intensities are (a) 330 kW/cm^2, (b) 380 kW/cm^2, and (c) 600 kW/cm^2. The excited area is a strip $100 \times 40\,\mu$m. The emission is collected from the edge of the film. (Pumping intensities are given in terms of absorbed power. Only ~1% of incident pumping power was absorbed and ~99% reflected [10]). The inset of (a) is a schematic diagram showing the formation of a closed-loop path for light through multiple optical scattering in a random medium. The inset of (b) shows the integrated emission intensity as a function of excitation intensity. The inset of (c) shows the intensity of the laser emission from the edge of the ZnO film as a function of polarization angle when the excitation intensity is 400 kW/cm^2. The intensity maximum corresponds to the polarization direction parallel to the film. (*Source*: Ref. [2].)

been observed (Figure 7.1a). As the pumping power increased, the emission band became narrower, due to amplification of spontaneous emission in the vicinity of the maximum of the gain band. When the pumping energy exceeded some threshold level, narrow emission lines, with the FWHM smaller than 0.4 nm, appeared in the spectrum (Figure 7.1b). The number of narrow lines in the emission spectrum increased with the further increase of the pumping energy (Figure 7.1c). The dependence of the integrated emission intensity on the pumping energy resembled the typical input–output curve known in regular lasers (inset of Figure 7.1b). The emission above the threshold was strongly polarized (inset of Figure 7.1c). The emission spectrum varied with the observation angle or when the pumped spot was moved along the sample. It was found that the threshold pumping energy density increased with the reduction of the pumped spot [2]. The threshold pumping densities measured in different semiconductor random laser experiments are summarized in Table 7.1. Similar laser effects have been observed in GaN powder with an average particle size of 100 nm [2].

To explain the observed phenomenon, it has been proposed [2] that due to strong scattering, emitted photons may return to the same positions where they were born, thereby forming closed-loop paths (see inset of Figure 7.1a). Such loops can serve as ring resonators for laser light, determining the frequencies of narrow stimulated emission lines. Because different resonators have different losses and support different oscillation frequencies, different stimulated emission lines appear in the spectrum at different thresholds.

It has been further suggested that multiple ring cavities can have outputs at different preferential directions. This explains the change of the emission spectrum with the change of the observation angle. With increase of the size of a pumped spot, the number of ring cavities increases, determining an increase of the number of narrow emission lines in the spectrum. Correspondingly, when the area of the pumped spot gets so small that it does not contain any low-loss modes, the threshold of the stimulated emission increases and, eventually, the lasing stops [2].

The intuitive model above [2], later regarded by its authors as "naive," qualitatively explains the majority of experimental features observed in ZnO random lasers. More accurate and elaborate models of stimulated emission in scattering ZnO powders and films are discussed below in this chapter.

7.2 Study of Angular Distribution of Stimulated Emission in ZnO Random Laser

In Reference [11], the angular distribution of random laser stimulated emission has been studied in 300 nm thick film of (0001) ZnO deposited on (0001) sapphire substrates. It has been shown that the emission collected from the edge of the film, both in the plane of the film and at the angles inclining to the surface of the film (Figure 7.2a) is much more sensitive to the observation angle than the emission collected from the film surface (Figure 7.2b).

TABLE 7.1. Parameters of different semiconductor random lasers[a]

Material	Pumping Wavelength/ Pulse Duration	Particle Size (nm)	Scattering Mean Free Path (μm)	Sample Thickness (μm)	Pumped Area	Threshold Energy (nJ)	Threshold Energy Density (mJ/cm^2)	Threshold Power Density (MW/cm^2)	Emission Lifetime (ps)	Remark	Ref.
ZnO	355 nm/15 ps	50–150	~0.39	0.3–0.35	$40 \times 100\,\mu m^2$			<0.38[b]		Gain = $100\,cm^{-1}$	[2]
ZnO	355 nm/15 ps			0.3	$40 \times 155\,\mu m^2$			<0.383[b]			[11]
ZnO	355 nm/15 ps	20–150		0.3–0.35	$40 \times 100\,\mu m$		<0.0145[b]	<1[b,c]			[12]
ZnO	355 nm/15 ps	100	0.33	6–15	$1600\,\mu m^2$			<0.763[b]		Change of slope at the threshold ~3.6 times	[13]
ZnO	355 nm/15 ps	70	0.38	1000	$d \approx 20\,\mu m$	<12.5 nJ	<4[c]	<265[c]	200		[5]
ZnO	355 nm/15 ps			1.7 (microsphere)	$2.3\,\mu m^2$[c]	<0.3 nJ	<13[c]	<880[c]		Absorption efficiency 1%	[5]
ZnO	355 nm	30–130		0.35	$d \approx 20\,\mu m$			≈450			[14]
ZnO	266 nm/20 ps	≈50	≈0.2	30	$d \approx 20\,\mu m$	<12.5 nJ	<4[c]	<265[c]	200		[15]
ZnO	266 nm/15 ps			1.7 (microsphere)	$2.3\,\mu m^2$[c]	<0.35 nJ	<15[c]	<1000[c]		Change of slope at the threshold ~14.5 times; absorption efficiency 1%	[16]
ZnO	355 nm/20 ps	100		10–30	$d \approx 20\,\mu m$			80	167		[17]
ZnO	355 nm/5 ns	20	0.238	8000	$d \approx 2\,cm$			1.5		Gain = $7.5\,cm^{-1}$	[18]
$GaAs_{0.972}N_{0.028}$	532 nm/1 μs	No intentional scatterers		>0.2				1×10^{-4}	355	$T < 100\,K$	[6]
$(GaAs)_{0.01}$: $(Al_2O_3)_{0.99}$	532 nm/ ~10 ns	1.7×10^3[d]	4.5	1000	$d \approx 0.8\,mm$		2	0.18		Absorption efficiency 13%	[7]
Cr^{2+}:ZnSe	1780 nm/10 ns	0.68×10^3[d]		~1000	0.6–1.2 mm	1.25×10^5	34		6×10^6		[8]

[a]When several threshold values were reported in the same publication for different experimental conditions, the smallest of the reported values was used in this table.
[b]The value corresponds to absorbed pumping. The fraction of incident pumping energy that is absorbed in a sample is equal to ~1% [10].
[c]The value is calculated by the author [M.N.] from the data reported in the paper. (In calculations, the threshold pumping energy and the threshold pumping power are related via the width of the pumping pulse, but not the spontaneous emission lifetime.)
[d]The mean particle size was calculated as $\bar{s} = \left(\left(\sum_i (1/s_i) s_i^2\right) / \sum_i s_i^2\right)^{-1}$, where s_i were the sizes of individual granules. In this method of calculation, the individual particles' contributions were taken with the weight factors proportional to the particles' cross sections.

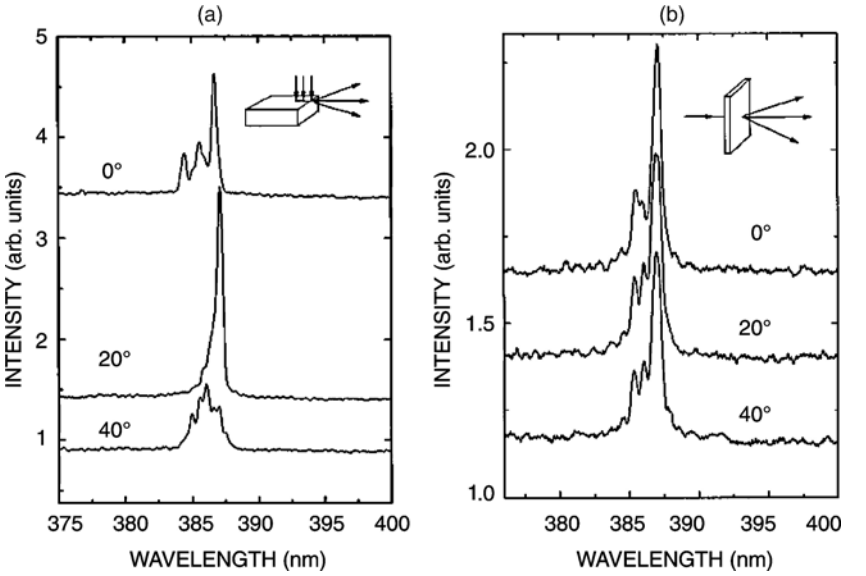

FIGURE 7.2. (a) Side emission spectra observed from different angles (0°, 20°, and 40°) in the plane of the film. The excitation intensity is 383 kW/cm^2. The excitation stripe length is 155 μm. The inset shows the experimental configuration. (b) Surface emission spectra observed at different observation angles (0°, 20°, and 40°) in the plane normal to the film. The excitation intensity is 382 kW/cm^2. (*Source*: Ref. [11].)

In the experiment, the central emission wavelength was equal to $\lambda \approx 385$ nm, the scattering mean free path (measured using the CBS technique) was equal to 2.6λ (≈ 1 μm), and the thickness of the film was equal to $\approx 0.8\lambda$. The linear size of the pumped spot varied in different measurements between 40 μm and 1 mm.

It has been argued [11] that because of a thin-film geometry of the samples and the fact that the thickness of the film does not exceed the photon mean free path, the effective lasing cavities (modes) lie and preferentially emit in the plane of the film. It has been also assumed that different effective laser cavities or modes, which oscillate at different resonant frequencies, can have one or several highly directional outputs at different angles. Correspondingly, light signals from different cavities (or ensembles of cavities) are detected at different angles, which results in a strong angular dependence of the stimulated emission spectrum collected from the edge of the film (Figure 7.2a).

It has been further speculated [11] that cavities (modes) have no highly directional outputs emerging from the surface of the film. Instead, each effective cavity has numerous (and presumably relatively weak) nearly omnidirectional surface losses. Thus, each cavity contributes to the surface emission at practically any angle, which explains relatively moderate angular dependence of the stimulated emission collected from the surface (Figure 7.2b).

7.3 Effect of External Feedback in ZnO Random Laser

The effect of an external feedback on stimulated emission of a ZnO random laser was studied in [12]. The experimental samples were 300 to 350 nm ZnO films consisting of grains, the sizes of which varied from 20 to 150 nm. The samples were pumped through the front surface. The width of the excitation stripe was equal to 40 μm and its length was varied in different measurements.

In two particular sets of experiments, an external mirror was placed (a) in front of the edge of the sample (perpendicular to the film and the excitation stripe, Setup #1) and (b) underneath the sample (parallel to the film, Setup #2). In both cases, the presence of the mirror helped to increase the efficiency of laser emission and the number of lasing modes.

It was inferred that in Setup #2, the primarily role of the mirror was to redirect the pumping energy transmitted by the ZnO film back to the sample and, thus, increase the pumping efficiency.

Because effective lasing cavities are preferentially oriented in the plane of the film [11,12], the mirror in Setup #1 can effectively couple stimulated emission back to lasing modes and, thus, increase their quality factors and reduce the threshold energies. This was the most important role of the mirror in Setup #1. (The results of this random laser experiment were consistent with the results of the ASE studies carried in the same setup below the threshold [12].) The secondary function of the mirror in Setup #1 was to increase the pumping efficiency via redirecting escaping pumping photons back to the pumped volume. However, the relative enhancement of stimulated emission caused by this latter mechanism was smaller in Setup #1 than in Setup #2.

7.4 ZnO Microlaser and Strong Spatial Confinement of Stimulated Emission

In References [15,16], ZnO powders with the average particle size equal to 50 nm (much finer than those used in Refs. [2,11–13]), were synthesized using the precipitation reaction [19]. These powders we used to fabricate ≈1 μm isolated clusters [15,16]; see inset of Figure 7.3. The samples were excited with a fourth harmonic of the Nd:YAG laser ($\lambda = 266$ nm, $t_{pulse} = 15$ ps). Experimentally, a near-field distribution of stimulated emission was monitored simultaneously with the emission spectra.

The evolution of the emission spectra and the input–output curves in [15,16] (Figure 7.3) were similar to those in [2,13] and other related works. It has been argued that the dramatic increase of the output efficiency above the threshold in the ZnO random laser is due to the increase of the emission quantum yield resulting from the competition between the radiative and nonradiative mechanisms of emission decay.

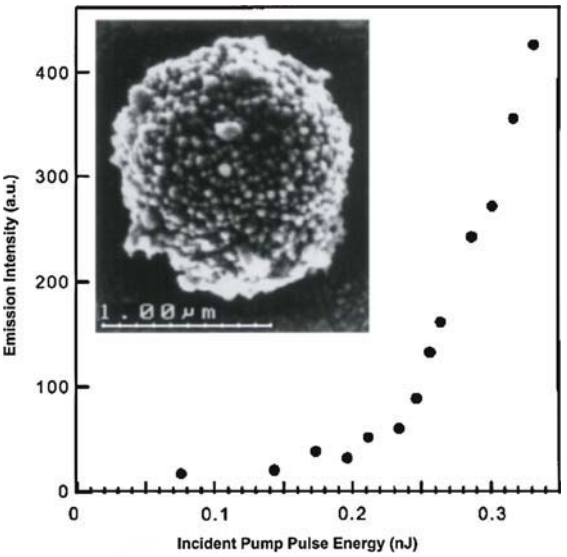

FIGURE 7.3. Spectrally integrated intensity of emission from the ZnO cluster as a function of the incident pump pulse energy. The inset is the SEM image of the cluster. (*Source*: Ref. [15].)

Below the threshold, the spatial distribution of emission intensity in a pumped spot was nearly uniform, resembling that of pumping [15,16]. At the lasing threshold, when the first narrow line appeared in the emission spectrum, two or several bright spots appeared in the near-field emission pattern (Figure 7.4). With further increase of the pumping energy, the number of bright spots in the near-field emission increased along with the increase of the number of narrow emission spectral lines. Because no spatial nonuniformity was detected in near-field spontaneous emission, it was concluded that bright spots observed in stimulated emission correspond not to the local areas where emission, hypothetically broadly distributed in the interior of the sample, leaks out, but to the areas of spatial confinement of stimulated emission.

It has been argued [15,16] that localization of emission observed in a near-field pattern can be evidence of Anderson localization of light in micrometer-scale random media [20–23].[1] To support this statement, the Thouless criterion, $\delta\nu/\Delta\nu < 1$ [26–29], was used, where $\delta\nu = 1.8 \times 10^{11}$ Hz (the mode linewidth in the ZnO microlaser) was narrower than the mode spacing $\Delta\nu = 2.4 \times 10^{11}$ Hz. Another argument supporting the existence of Anderson localization in the ZnO random laser was a nearly satisfied Ioffe–Regel criterion, $kl^* \leq 1$, where k was

[1]Anderson localization in combination with coherent amplification was shown to be the key factor determining an enhancement of reflection in random laser media [24]. Random laser thresholds in the regime of Anderson localization were studied theoretically in [25] and other works.

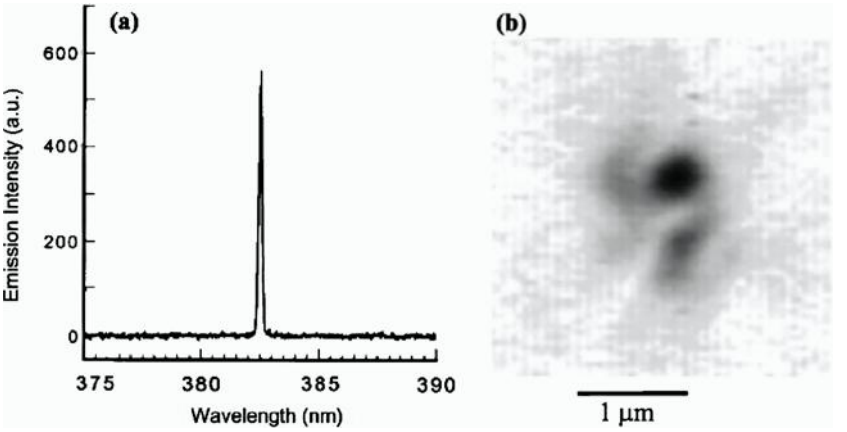

FIGURE 7.4. (a) The measured spectra of emission from the ZnO cluster. (b) The measured spatial distribution of emission intensity in the cluster. The incident pump pulse energy is 0.25 nJ. (*Source*: Ref. [15].)

the wave number of emission light and l^* was the scattering mean free path [30]. In References [15,16], $l^* \approx \lambda/2$ and, hence, $kl^* \approx 3$. A possible argument against Anderson localization in the ZnO random laser relies on a striking similarity of the emission spectra in [15,16] and those, for example, in [11], where $l^* \approx 2.6\lambda$, $kl^* \approx 16$, and the Ioffe–Regel criterion is not satisfied by far.

To model the near-field emission pattern and the spectrum of stimulated emission in the ZnO random laser, the electromagnetic field distribution in a random medium was calculated in [15] by solving Maxwell equations using a finite-difference time-domain (FDTD) method. The gain was introduced to the system via negative conductance σ and the randomness via the dielectric constant ε, which was varied spatially to model the random distribution of ZnO particles. The calculations have shown that when the optical gain exceeds its threshold value, the electromagnetic field oscillation starts building up in the time domain. Using the Fourier transform of the time domain data, the emission spectrum was calculated [15]. It has been theoretically predicted that just above the threshold, one narrow spectral line appears in the emission spectrum and several bright emission spots emerge in the near-field emission pattern, close to the center of the pumped area (Figure 7.5). Thus, the results of the model calculation resembled, in the first approximation, the experimental results (compare Figures 7.4 and 7.5). The independence of the near-field emission distribution and the emission spectrum of the boundary conditions indicated that the lasing mode was formed by multiple scattering and interference deep inside the disordered medium. In some sense, such a mode can be viewed as a localized mode.

The theoretical study above was in line with those of [31,32], where by combining the FDTD method with semiclassical laser theory [33,34], the authors were able to analyze the interplay of localization and amplification. They predicted the near-field pattern and the spectral peaks of localized laser modes in the system (similar to those observed experimentally), explained nonisotropic properties in

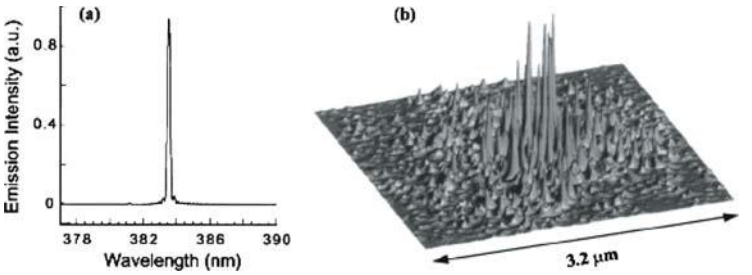

FIGURE 7.5. (a) The calculated emission spectrum. (b) The calculated spatial distribution of emission intensity in the random medium. (*Source*: Ref. [15].)

the emission spectra, and predicted a mode repulsion, which is responsible for the saturation of the number of lasing modes in a given laser system [31,32]. The mode distribution in random lasers with coherent feedback was studied in [35].

7.5 Photon Statistics in ZnO Random Laser

Photon statistics is among the most important characteristics of laser radiation. It was studied in lasers with nonresonant feedback and random lasers in References [36–38]. The photon statistics of the ZnO random emission laser was studied in [39]. The experimental sample in this particular measurement was a cold-pressed pellet composed of 80 nm ZnO particles. The diameter of the pellet and its thickness were equal to 1 cm and 2 mm, respectively. The diameter of the focused laser spot on the sample was equal to $\approx 15\,\mu$m, and the photon mean scattering path was equal to $\approx 2.3\lambda$ ($0.9\,\mu$m).

The random laser emission was experimentally studied using a streak camera, with 2 ps time resolution, attached to the output port of a spectrometer. This setup allowed one to monitor the emission dynamics in several laser modes (narrow spectral lines) simultaneously. A typical two-dimensional (time–wavelength) streak camera image of ZnO random laser emission is shown in Figure 7.6 [17]. The photon statistics was measured in rectangular area $\Delta t\,\Delta\nu$ of a streak camera image, in the maximum of an emission pulse in one of the strongest lasing modes. The sampling time Δt was chosen to be shorter than the coherence time of the radiation field $1/\Delta\nu$. Thus, the area $\Delta t\,\Delta\nu < 1$ corresponded to a single electromagnetic mode.

For single-mode coherent light, the photon number distribution $P(n)$ is Poissonian,

$$P(n) = \frac{\langle n\rangle^n e^{-n}}{n!}, \tag{7.1}$$

where $\langle n\rangle$ is the average photon number [40,41]. At the same time, for a single-mode chaotic light, $P(n)$ corresponds to the Bose–Einstein distribution,

$$P(n) = \frac{\langle n\rangle^n}{(1+\langle n\rangle)^{n+1}}. \tag{7.2}$$

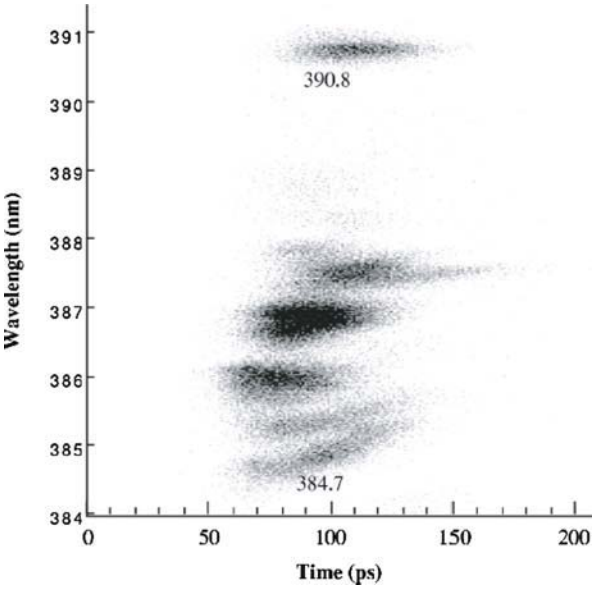

FIGURE 7.6. Typical two-dimensional streak camera image of ZnO random laser emission. (*Source*: Ref. [17].)

The character of distribution $P(n)$ determines the value of a second-order correlation coefficient

$$G_2 = 1 + \frac{\left(\langle(\Delta n)^2\rangle - \langle n\rangle\right)}{n^2}. \tag{7.3}$$

For a Poisson distribution $G_2 = 1$ and for a Bose–Einstein distribution $G_2 = 2$. Thus, by analyzing the experimentally measured photon number distribution $P(n)$, one can conclude the degree of coherence of laser emission [39].

The photon number distributions $P(n)$ measured in the ZnO random laser at different values of pumping energy are shown in Figure 7.7. The experimentally determined values G_2 are plotted against the pumping energy in Figure 7.8. As one can see from these two figures, at the threshold, when the narrow emission spectral lines just appeared, the photon statistics was very close to the Bose–Einstein statistics, and the corresponding G_2 number was equal to 1.94. With the increase of the pumping energy, the photon statistics got closer and closer to a Poissonian statistics and the second-order correlation coefficient gradually reduced to one (when the pumping energy was 5.6 times the threshold energy, the value G_2 was equal to 1.06).

Thus the photon statistics of light emitted by the ZnO pellet changed continuously from the Bose–Einstein statistics at the threshold to the Poisson statistics well above the threshold. The Poissonian photon statistics (typical for lasers) observed in this experiment is evidence of the coherent character of stimulated

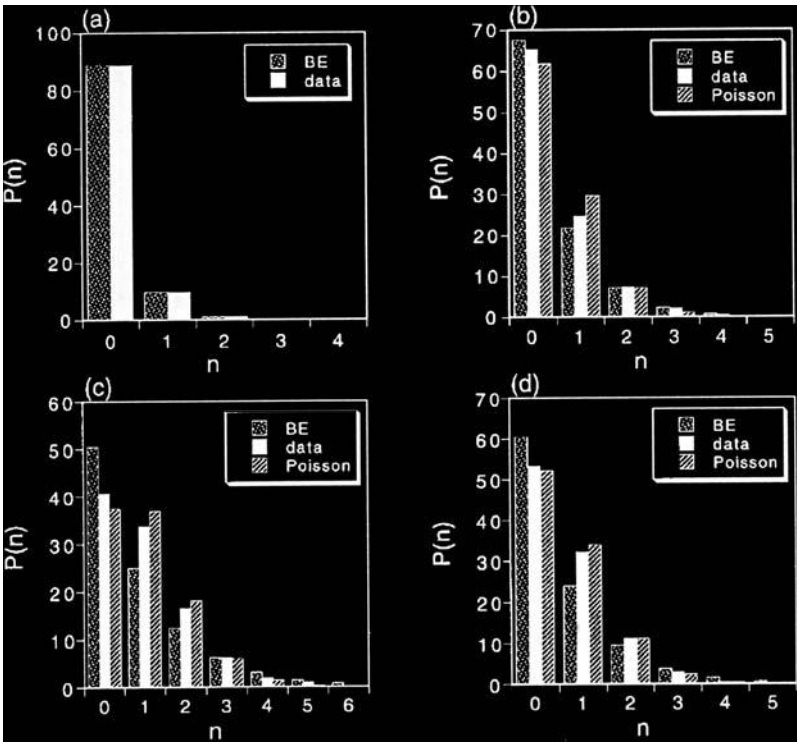

FIGURE 7.7. The solid columns are the measured photon count distribution of emission from a ZnO pellet. The dotted (dashed) columns are the Bose–Einstein (Poisson) distribution of the same count mean. The incident pump intensity is (a) 1, (b) 1.5, (c) 3.0, and (d) 5.6 times the threshold intensity where discrete spectral peaks appear. (*Source*: Ref. [39].)

emission in the ZnO random laser. It can be observed only at strong enough pumping, where the effect of gain saturation quenches the photon number fluctuations in (isolated) laser modes.

Note that in References [42,43] Poissonian photon statistics have been predicted in random lasers without direct use of wave equations or arguments of resonant feedback.

7.6 Effect of the Pumped Area on the Operation of ZnO Random Laser

In Reference [2], the threshold pumping energy density increased with the reduction of the size of the pumped spot. A qualitatively similar result was observed in [13,14]. In [13], ZnO powder with average particle size 100 nm was deposited onto ITO-coated glass substrates. The thickness of the films in [13] varied from

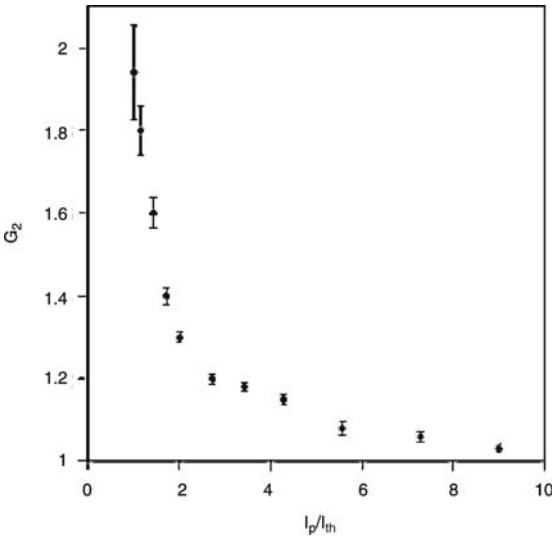

FIGURE 7.8. The second-order correlation coefficient G_2 as a function of the ratio of the incident pump intensity I_p to the threshold intensity I_{th}. (*Source*: Ref. [39].)

6 to 15 μm and the scattering mean free path, measured using the CBS technique, was equal to $l_t \approx 0.8\lambda$ at $\lambda = 410$ nm. When the area of the pumped spot was varied at constant pumping density, the number of narrow spectral lines representing laser modes increased with the increase of the size of the pumped spot. When the area of the pumped spot decreased below some critical value, the laser oscillation stopped. Correspondingly, at fixed pumping energy density, the intensity of stimulated emission increased with the increase of the pumped area.

The dependence of the threshold in the ZnO random laser on the pumped area was studied in detail in [14], where 350 nm thick film composed of ZnO particles (30 to 130 nm particle size) was etched to make disks with diameters ranging between 2 and 40 μm. The pumped spot in each particular measurement covered the whole individual disk. The dependence of the threshold pumping density I_{th} on the disk area A is depicted in Figure 7.9. It can be fitted with the formula $I_{th} \propto A^{-0.52} \propto d^{-1.04}$, where d is the disk diameter.

This experimental result is in seeming contradiction to the known prediction of the diffusion model, $I_{th} \propto a_1/d^2 + a_2/h^2$ [44,45], where h is the height of the pumped cylinder and a_1 and a_2 are the constants. In Reference [14], the experimentally obtained dependence I_{th} versus d has been explained under the following assumptions.

1. The ZnO random laser is a two-dimensional (2D) system, with the characteristic to 2D systems dependence of the mode density on the linear size, $\sim d^2$;
2. Individual modes in a random laser have a very broad distribution of quality factors;

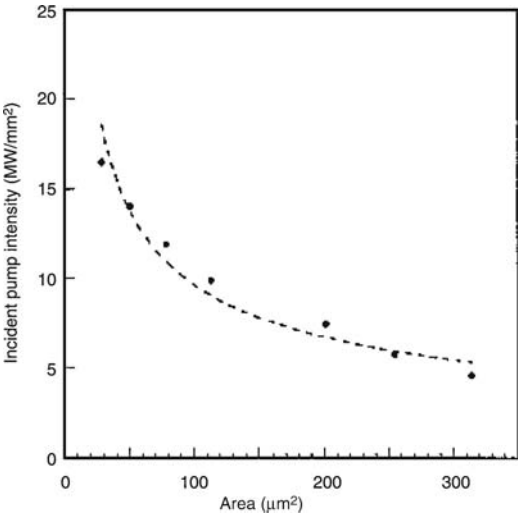

FIGURE 7.9. Threshold pumping intensity I_{th} as a function of ZnO disk area A. The dashed line is a fitting curve $I_{th} \propto A^{-0.52}$. (*Source*: Ref. [14].)

3. The random laser threshold is determined by the mode with the lowest loss γ; and
4. The distribution of the mode decay rates $P(\gamma)$ is assumed to be proportional to γ [14] [the latter assumption is consistent with the known distribution of delay times τ, $P(\tau) \propto 1/\tau^3$, when light passes through a random medium [46,47]].

Once the distribution function of the decay rates is known, the distribution of lasing thresholds, the mean value of the lasing threshold, and the average value of lasing modes can be derived [14,48]. It has been calculated [14] that the number of low-loss modes in the ZnO random laser increases with the increase of the diameter d, and the threshold pumping density I_{th} depends on d as $I_{th} \propto d^{-1}$, in good agreement with the experiment.

A similar theoretical result was obtained in Reference [49], where a 2D model of coupled dipole oscillators, representing pumped powder particles, has been studied. It has been argued that the dependence of I_{th} on the total number of particles, which is proportional to the area of the pumped disk, is strongly related to the fluctuations of quasistate decay rates. (Note that according to Ref. [50], statistically rare high-efficiency scattering events can cause random laser emission even in the media, the characteristic linear size of which is smaller than the photon transport mean free path.)

In [51], the experimental dependence $I_{th} \propto d^{-1}$ was predicted in approximation of the 3D diffusion model under the additional assumption of saturation of absorption transition by intense pumping light. As shown in Reference [52], the same dependence I_{th} versus d can be predicted in the 3D diffusion model without any saturation of absorption, if a realistic geometry of the pumped volume

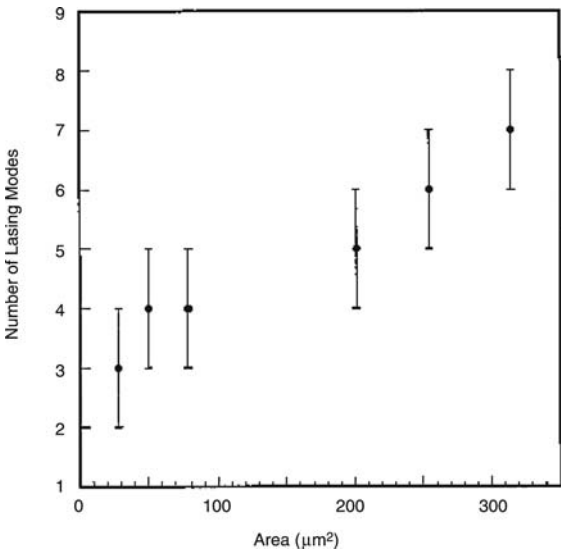

FIGURE 7.10. Saturated value of the number of lasing modes as a function of ZnO disk area. (*Source*: Ref. [14].)

and a photon exchange between the pumped volume and the rest of the scattering medium are taken into account (Chapter 4).

It has been experimentally shown in [14] that with an increase of the pumping energy above the threshold, the number of emission modes increases first and then saturates at higher pumping energy. Furthermore, the number of saturated laser modes increases with the increase of the disk diameter (Figure 7.10). According to [14], at high pumping power spatially overlapped laser modes strongly compete for gain and population inversion and, as a result, only one strongest mode survives at the expense of weaker overlapped modes. That is why only spatially separated modes can operate simultaneously. Comparing the sizes of ZnO disks with the maximum numbers of lasing modes, it has been concluded that one mode occupies between 10 and 40 μm^2. The mode repulsion leading to the saturation in the number of lasing modes was predicted in [31,32], where Maxwell equations for a system with scattering and gain were solved using a finite-difference time-domain (FDTD) method.

7.7 Study of the Dynamics of ZnO Random Laser Emission

The dynamics of stimulated emission in the ZnO random laser was studied in [17]. In this work, the average size of ZnO particles was equal to $\approx$100 nm and the thickness of different ZnO powder films studied varied between 10 and 30 μm.

The diameter of the pumped spot was equal to $\approx 20\,\mu$m. The kinetics of random laser emission at different wavelengths was recorded using a streak camera attached to the output of a spectrometer.

It was shown that the characteristic emission decay time in ZnO powder changes from 167 ps below the lasing threshold to 27 ps above the threshold [17]. The stimulated emission pulses observed at different wavelengths (lasing modes) started at different moments of time and had different widths. Close to the threshold, the relaxation oscillations (first predicted in a random laser by Letokhov in 1968 [45]) have been observed in stimulated emission of ZnO powder. In certain cases, stimulated emission started at one mode and then hopped to another one, or the lasing mode experienced a frequency shift during the pulse. (All these dynamics effects are well known in neodymium random lasers, see, e.g., Refs. [53,54].)

In Figure 7.6, some modes of the ZnO random laser experience a blue shift with time and other modes remain unchanged or even experience a slight red shift (such as those at $\sim$388 and $\sim$399 nm), with the tendency of the "mode attraction" toward some central frequency [17,55]. In [55], the spectral shifts in the ZnO random laser lines were explained by the third-order nonlinear optical effect.

The theoretical simulations based on the semi-classical laser model and the finite-difference time-domain (FDTD) computation method reproduced most of the experimental observations and additionally predicted a spatial motion of localized modes during the pumping pulse [17]. Note that relaxation oscillations in lasers can be predicted at many different feedback mechanisms, both resonant and nonresonant.

7.8 Spectrally Resolved Speckle Studies in ZnO Random Laser

In Reference [56], a speckle pattern of ZnO random laser emission was used to study localized states of light. It has been assumed [56] that some isolated localized states can exist in random lasers even when the scattering is not strong enough, and the system as a whole is far from the localization threshold. It has been further hypothesized that (i) in random laser emission the localized states strongly predominate over the extended states, and (ii) the localized states can be conveniently characterized based on their speckle patterns.

In the ZnO powders studied in [56], the product of the wave vector k and the mean scattering path l^* was smaller than 10 and larger than 1. Thus, the Ioffe–Regel criterion of Anderson localization, $kl^* \leq 1$ [30], was not exactly satisfied.

The schematic of the experimental setup used in [56] is shown in Figure 7.11. The samples placed in a focal plane of the objective lens ($f = 8.3$ mm) were pumped with a third harmonic of a Nd:YAG laser. A CCD array detector was attached to the output port of a spectrometer. In a CCD image obtained this way, the horizontal axis corresponded to the wavelength and the vertical axis corresponded to the angular direction (in a vertical plane) of the emitted light.

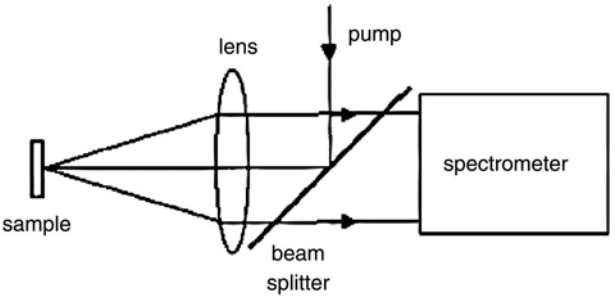

FIGURE 7.11. Schematic of spectrally resolved speckle measurement. (*Source*: Ref. [56].)

Above the threshold, when discrete narrow peaks emerged in the emission spectrum, a CCD image consisted of vertical dotted lines, each line manifesting a speckle pattern in individual lasing mode. At each wavelength, emission intensity fluctuated randomly with the angle. The emergence of the speckle pattern was direct evidence of coherent emission from a random laser. (Qualitatively similar dotted lines in the emission of a *polymer random laser* are shown in Figure 8.17.)

The experimentally measured (in one spectral line) angular distribution of the emission intensity $I(q)$ and the spatial field correlation function at the sample surface, $C(x) \equiv \int E^*(x')E(x+x')dx'$, form a Fourier transform pair [56],

$$C(x) = \int I(q)e^{-2\pi xq}dq. \tag{7.4}$$

Thus, a speckle pattern of a lasing state gives its spatial field correlation function. When plotted against x, the absolute value $|C(x)|$ looks like a noisy function decaying with the increase of x. The integration of $|C(x)|$ gives

$$S(x) = \int_x^\infty |C(x')|dx'. \tag{7.5}$$

Function $S(x)$ is much smoother than $|C(x)|$. (As an example, distributions $|C(x)|$ and $S(x)$ corresponding to one of the wavelengths in the pattern of Figure 8.17 are shown in Figure 8.18.) Well above the threshold, $S(x)$ and, accordingly, the envelope of the spatial field correlation function can be described with good accuracy by an exponent, $S(x) \propto |C(x)| \propto \exp(-x/l_d)$. The exponential decay manifests the localized emission state. The decay length l_d represents the characteristic size of this state.

The value l_d, which is relatively large at the threshold, decreases and then saturates at high pumping intensities. In the vicinity of the threshold, the shape of the function $S(x)$ somewhat deviates from the exponential. These two effects have been explained by the (discussed in Ref. [39]) increase of the degree of coherence of a laser state with the increase of the pumping power above the threshold.

In the ZnO random laser, the values l_d, different for different lasing modes, varied from 1.5 to 4 μm [56]. (This estimate of the spatial size of a localized mode in the ZnO random laser is close to that in Ref. [14].) According to [57,58], the

size of the localized mode in random laser emission is the same as that in a passive scattering medium. Hence, the experiment of [56] suggests that individual localized states of light, indeed, exist in scattering media far from the localization threshold for the whole volume.

7.9 Stimulated Emission from 3D Photonic Crystals Made of Self-Assembled ZnO Colloidal Spheres

The technique for producing monodisperse ZnO colloidal spheres composed of 10 to 20 nm crystallines has been reported in References [5,59]. The synthesis of nearly spherical particles ranging in size between ~100 and ~600 nm, with 6 to 8% variation of sphere diameter in each sample has been demonstrated. Periodic arrays of colloidal spheres were self-assembled by dropping the reaction solution onto substrates and evaporating the solvent. The fabricated arrays exhibited photonic gaps in the *fcc* (111) direction at approximately $2.2d$, where d was the particle diameter.

For random laser measurements, ZnO spheres of eight different diameters were used to prepare 16 samples [59]. Particles of each particular size were used to fabricate 2 samples, 1 random and 1 self-assembled periodic. The domain size of islands of ordered spheres exceeded 10 μm [5].

All 16 samples exhibited stimulated emission evidenced by an appearance of narrow spectral lines above a threshold. In all cases, periodic samples demonstrated lower lasing thresholds than corresponding random samples composed of spheres of the same size. The "periodic-to-random" threshold ratio factors varied between ~1.5 and 4 [59]. In a series of ordered arrays of monodispersed spheres, the lasing threshold reached its minimum when the photonic band gap (PBG) in the (111) direction overlapped with the ZnO emission band [5]. [Note that random laser emission in periodic (PBG-type) structures has been discussed and realized in [60–62].] According to [63], the maximum reduction of the threshold should be obtained at partial ordering of an ensemble of scatterers. Alternatively, the threshold reduction in ordered structures can be explained, at least in part, by higher sphere-packing densities in periodic structures [59].

7.10 Quasi cw Stimulated Emission in ZnO Pellet

In the ZnO random laser experiment discussed in Reference [18], a large pellet (cold-pressed under a pressure of 6 tonne for 20 min and then sintered at 1000°C for 5 h) with the diameter 20 mm and the thickness 8 mm has been studied. The pellet was composed of 20 nm ZnO particles. The photon transport mean free path in the sample, measured using a CBS technique, was equal to ~0.24 μm. Thus, because of small scattering length and small absorption length ($\leq$1 μm at 355 nm [10]), the thickness of the pumped volume was very small.

The sample was pumped with 5 ns pulses of a third harmonic of a Nd:YAG laser. Taking into account the fact that the lifetime of spontaneous emission in ZnO is equal to ∼0.17 ns [17], this was effectively a quasi cw pumping regime. The diameter of the pumped spot was considerably large, between 5 mm and 2 cm. Large sizes of the sample and the pumped spot, long durations of pumping pulses, and fairly short transport mean free path made this particular experiment different from other ZnO experiments discussed in this chapter.

The input–output curve and the evolution of the emission spectra in [18] were qualitatively similar to those in many other ZnO random lasers. The linewidths of individual modes in [18] decreased with an increase of the pumping energy, the emission spectrum depended on the observation angle, and the threshold pumping density decreased with the increase of the diameter of the pumped spot. All these effects have been discussed in the preceding sections of this chapter. At the same time, narrow lasing modes in [18] were distributed in a nearly regular manner (Figure 7.12), whereas in ZnO lasers based on scattering thin films such distribution appeared to be random (Figure 7.1). The regularity of emission modes is the most

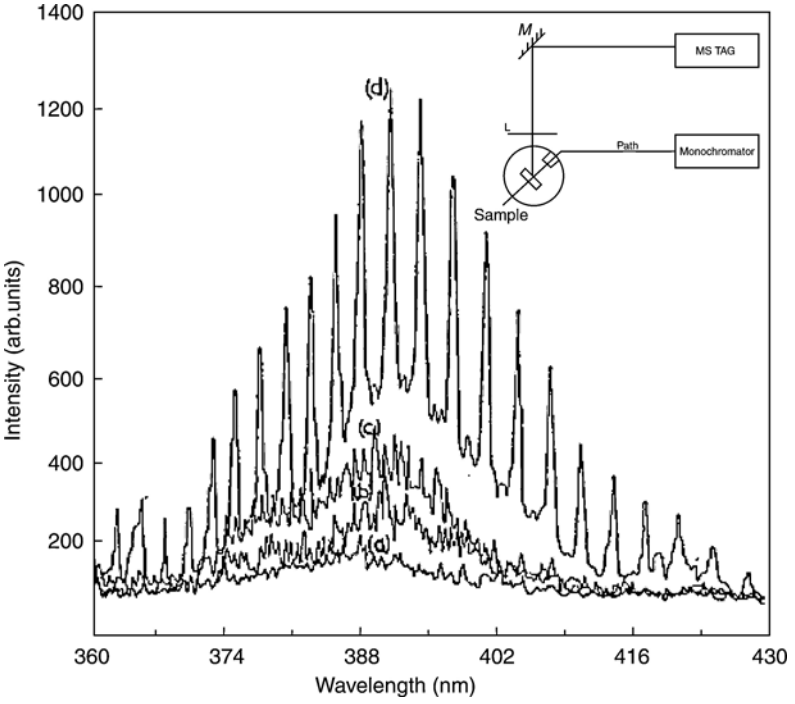

FIGURE 7.12. Emission spectra of the ZnO pellet taken at different excitation intensities, (a) 1527 kW/cm^2, (b) 2860 kW/cm^2, (c) 3310 kW/cm^2, (d) 7890 kW/cm^2. Inset: schematic diagram of the experimental setup, M: mirror, L: lens. (*Source*: Ref. [18].)

intriguing (and not well understood) feature of the bulk pellet ZnO random laser of [18].

Based on a simplistic model of ring cavities formed in an ensemble of scatterers [2] and using in calculations the experimentally measured mode spacing, the authors of [18] estimated the length of the perimeter of the ring cavity to be equal to 7 μm. This is close to the estimated size of localized modes in thin-film ZnO random lasers [14,56]. It has also been argued in [18] that in the ZnO random laser one cannot neglect absorption at the stimulated emission wavelength and that the ZnO random laser operates according to a three-level scheme rather than a four-level scheme.

7.11 New Technological Realizations of ZnO Random Lasers

A recent effort of several research groups has been focused on new technological realizations of ZnO random lasers.

Thus, random laser action with coherent feedback was achieved in composite films consisting of ZnO clusters embedded in SiO_2 dielectric matrix prepared by sol-gel technique [64]. The proper control of light confinement inside the random cavities led to coherent random lasing. In Reference [65], room-temperature ultraviolet lasing was demonstrated in ZnO thin-film waveguides on (100) silicon substrate. Laser cavities, which were due to optical scattering from the lateral facets of the irregular zinc oxide grains, were generated through the post-growth annealing of high-crystal-quality zinc oxide thin films obtained from the filtered cathodic vacuum arc technique.

A random laser action with coherent feedback was observed in ZnO nanorod arrays embedded in ZnO epilayers in Reference [66]. The sample was fabricated by depositing a MgO buffer layer and followed by a layer of ZnO thin film onto a vertically well-aligned ZnO nanorod arrays grown on sapphire substrate. The possibility of realization of a high-power single-mode emission in ZnO random laser, by the use of a proper coupled-cavity design, was investigated in Reference [67].

In Reference [68], ZnO thin film random laser has been fabricated by an electrochemical deposition performed in a chemical cell with three electrodes, using an aqueous solution of $Zn(NO_3)_2$ as electro-deposition solution. The observed emission wavelength, 403.9 nm, was slightly longer than that in the majority of known ZnO random lasers, 380–390 nm.

In Reference [69], random laser action was demonstrated in organic-inorganic, disordered hybrid materials consisting of ZnO semiconductor nanoparticles dispersed in an optically inert polymer matrix. Short-pulsed laser pumping of the nanohybrids led to a dramatic increase in the emitted light intensity accompanied by a significant spectral and temporal narrowing above a certain threshold of the excitation energy density.

7.12 Random Lasing in Epitaxially Grown GaAsN

In Reference [6], samples of GaAsN alloys containing 0.6, 1.77, and 2.8% nitrogen were grown on semi-insulating GaAs (100) substrates by low-pressure metalorganic chemical vapor deposition (MOCVD). The thickness of GaAsN layers varied between 200 and 800 nm. In spectroscopic and laser studies, experimental samples, $4 \times 4\,mm^2$ platelets, were excited with a cw Ar laser (at $\lambda = 514.5$ nm) or a pulsed frequency-doubled Nd:YAG laser ($\lambda = 532$ nm, $t_{pulse} = 1\,\mu s$). A femtosecond Ti-sapphire laser tunable between 750 and 900 nm was used in time-resolved photoluminescence (PL) measurements based on the known PL upconversion technique [70,71]. The samples were mounted in He cryostat, the temperature of which could be varied between 10 K and room temperature.

Strong reduction of a band gap even at a small concentration of nitrogen is one of the most interesting properties of Ga(In)AsN alloys [6]. The emission spectrum of a $GaAs_{0.972}N_{0.028}$ sample recorded at low temperature and low pumping intensity is shown in Figure 7.13a. A slightly asymmetric luminescence band has a maximum at ≈1095 nm and an exponential low-energy tail. At strong Nd:YAG pulsed pumping, the emission spectrum changed radically in the samples, which contained 2.8% nitrogen and which had the thickness of the GaAsN layer larger than ∼200 nm (Figure 7.13b,c). In such samples, several narrow lines (modes), similar to those in ZnO random lasers (Figure 7.1b,c), appeared in the emission spectrum above a certain pumping energy threshold.

The threshold behavior of several emission modes is shown in Figure 7.14. The lasing thresholds, varying for different modes between 0.1 and 10 kW/cm^2, depended on the position of the excitation spot on the sample. Correspondingly, the emission spectra measured in different excitation spots looked dissimilar to each other (Figure 7.13b,c). Thus, it was concluded that different laser modes were related to different effective cavities formed by scatterers. The narrow-line emission spectra of the $GaAs_{0.972}N_{0.028}$ samples were angle-dependent [6], and the threshold pumping density decreased with the increase of the diameter of the pumped spot. Narrow-line laser like emission in $GaAs_{0.972}N_{0.028}$ disappeared above ≈100 K.

Below the threshold, the emission kinetics in $GaAs_{0.972}N_{0.028}$ was characterized by the time constant ≈355 ps (Figure 7.15a). Above the threshold, the decay-time shortened to 20–80 ps, depending on the sample position and the excitation intensity. Moreover, the emission kinetics often exhibited two different time constants (Figure 7.15a). At some positions of the pumped spot on the sample, relaxation oscillations were observed (Figure 7.15b). Such temporal behavior is consistent with the nature of (stimulated) emission in the $GaAs_{0.972}N_{0.028}$ and similar to that in ZnO random lasers [17].

The emission properties of $GaAs_{0.972}N_{0.028}$ films discussed above were qualitatively similar to those of ZnO and other random lasers. Correspondingly, one can expect a similarity of physical mechanisms governing the stimulated emission in these systems. Scatterers were not intentionally introduced to the grown epitaxial GaAsN layers. However, this group of materials has inherent structural inhomogeneities, and the films have had dislocation defects and cracks [6]. Another

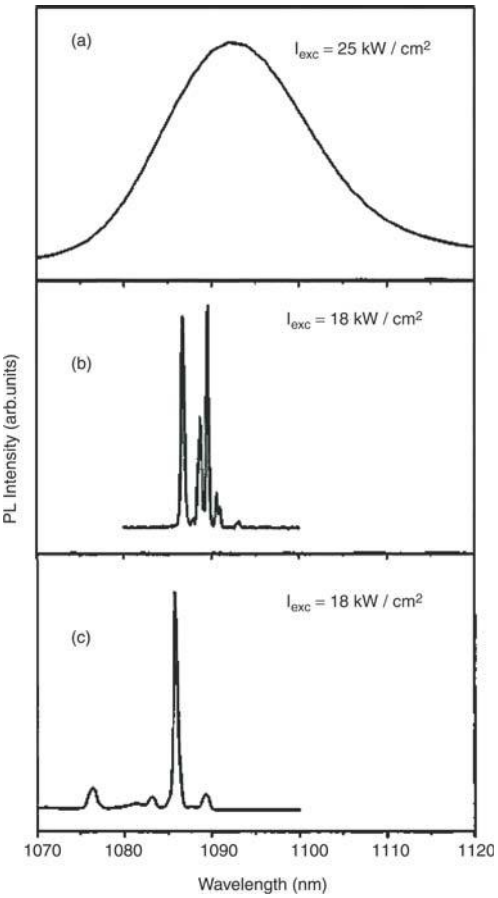

FIGURE 7.13. (a) Low temperature ($T = 10$ K) photoluminescence spectrum of $GaAs_{0.972}N_{0.028}$ layers grown on GaAs below threshold excitation. (b), (c) The emission spectra at two different points on the sample above the threshold. (*Source*: Ref. [6].)

source of scattering providing for the stimulated emission feedback in the system could be GaN nanocrystals embedded at the interface between the GaAsN film and GaAs substrate [6]. Note that the existence of critical thickness of the $GaAs_{0.972}N_{0.028}$ film, below which a random laser effect cannot be observed, may be an indication of a waveguide character of random laser modes, similar to that discussed in polymer films in [72].

7.13 GaAs Random Laser

In Reference [7], random laser emission in the most popular and commercially available semiconductor laser material, GaAs, has been reported. GaAs has

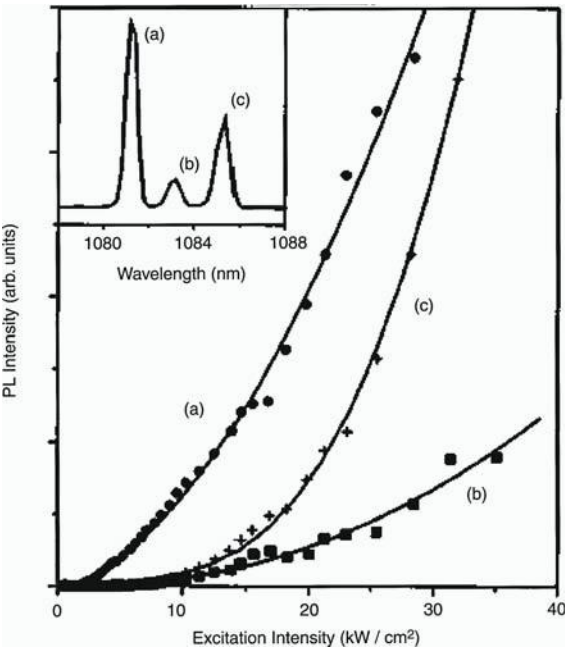

FIGURE 7.14. Low-temperature photoluminescence of a $GaAs_{0.972}N_{0.028}$ layer as a function of the excitation intensity for three laser modes, as shown in the insert, indicating the different threshold behavior for each of the emission modes. (*Source*: Ref. [6].)

the highest index of refraction (3.48) among all known random laser materials. Anderson localization of light in a powder of GaAs has been reported in [73].

Experimentally, a wafer of undoped GaAs was mechanically pulverized to a micron-sized powder. Loose powder samples were loaded in glass cuvettes and pumped with ~10 ns laser pulses at 532 nm. Because of very strong absorption of GaAs at 532 nm, all pumping energy is absorbed by a first layer of particles. Thus, in pure GaAs powder, scatterers provide rather poor feedback for emitted photons. To improve the situation, GaAs powder (x) was mixed with Al_2O_3 powder ($1 - x$), $x = 1$, 0.1, 0.01, and 0.001 (x indicates a weight fraction). In mixed samples, the penetration depth of pumping was larger than that in pure GaAs, and, correspondingly, the Q-factors of effective laser cavities were higher. In some measurements a free-standing cold-pressed tablet (thickness ~2.7 mm, diameter ~2.5 cm) of the composition $\{GaAs\}_{0.01}$:$\{Al_2O_3\}_{0.99}$ was used instead of powder.

The input–output curves of GaAs emission recorded in the four powder samples studied are shown in Figures 7.16a,b. A typical input–output curve has three characteristic regions:

I. A very weak spontaneous emission is observed at small pumping energy. In this regime, there is no population inversion in the material and the absorption at the stimulated emission wavelength is larger than the gain.

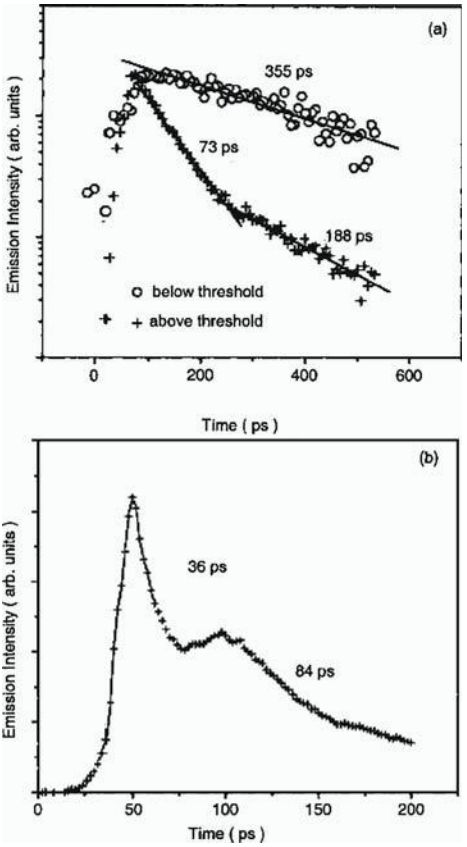

FIGURE 7.15. (a) Low-temperature emission decay as a function of time, demonstrating the reduction of the effective decay-time constant above the threshold. (b) Relaxation oscillations observed in emission of $GaAs_{0.972}N_{0.028}$ random laser. (*Source*: Ref. [6].)

II. Above a well-defined threshold, the emission intensity grows significantly and the emission band centered at ∼880 nm slightly narrows with the increase of the pumping energy (Figure 7.17). The spectral range of emission corresponds to the edge of a strong absorption band in GaAs.
III. Above the second energy threshold, the slope of the input–output curve increases considerably. The emission band (recorded using averaging over many pulses) narrows, and its maximum shifts to ∼886 nm. In the vicinity of the maximum of the emission band, 886 ± 10 nm, the output intensity becomes highly unstable, fluctuating strongly from pulse to pulse. The emission intensity in the wings of the spectral band is much more stable.

A seemingly similar two-threshold behavior, where the second threshold manifested the transition from the incoherent regime of operation to the coherent one, was observed in a polymer random laser in [74].

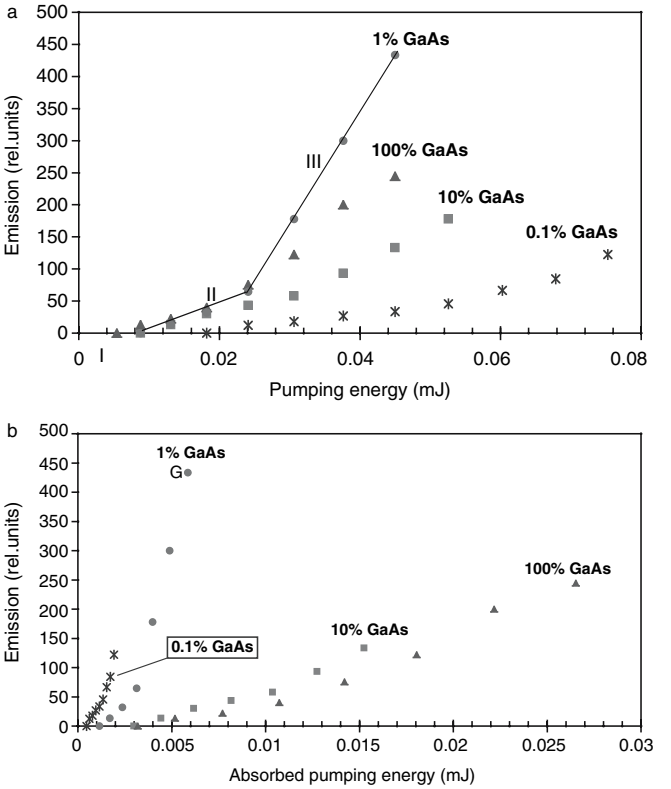

FIGURE 7.16. (a) Input–output curves in $(GaAs)_x$:$(Al_2O_3)_{1-x}$ random (powder) lasers. Triangles: $x = 1$, squares: $x = 0.1$, circles: $x = 0.01$, and crosses: $x = 0.001$. Regions I, II, and III, discussed in the text, are shown for the laser with $x = 0.01$. (b) The same curves as in (a) plotted versus absorbed pumping energy. The diameter of the pumped spot ~0.8 mm. (*Source*: Ref. [7].)

Single-pulse measurements of emission spectra were not done in [7]. So, it was not clear whether narrow lines in the stimulated emission spectra of $(GaAs)_x(Al_2O_3)_{1-x}$ existed. It was shown that pulse-to-pulse fluctuations of the integral emission intensity recorded in a wide spectral window, $\Delta\lambda = 20$ nm, centered at the emission maximum, $\lambda_0 = 885$ nm was very strong. However, this did not exclude the possibility of the existence of narrow spectral lines, the positions of which randomly changed pulse after pulse, similar to those in liquid dyes with scatterers [4,75].

According to Figure 7.16b, the absorbed energy thresholds are reduced and the slope efficiency, calculated relative to the absorbed pumping energy, is increased with the reduction of GaAs concentration in the mixture. This threshold behavior is in line with [14,68] predicting that the absorbed threshold energy E_{th} depends on the absorption length l_a as $E_{th} \propto l_a^{-1/2}$. The improvement of the laser performance

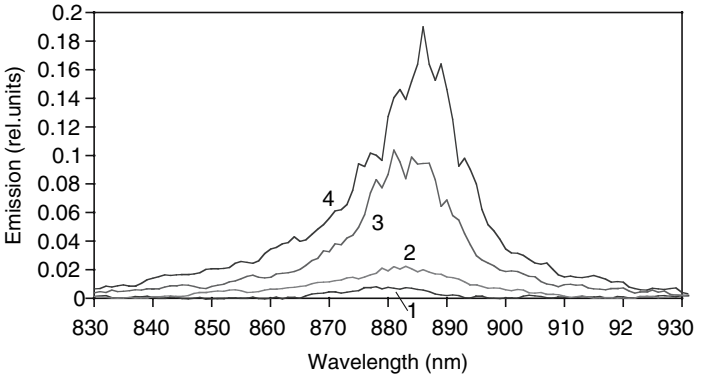

FIGURE 7.17. Typical emission spectra of $(GaAs)_x:(Al_2O_3)_{1-x}$ random lasers. Pumping energy: 1: 0.024 mJ, 2: 0.030 mJ, 3: 0.043 mJ, and 4: 0.085 mJ. The diameter of the pumped spot ~0.8 mm. (*Source*: Ref. [7].)

due to the dilution of GaAS powder was so high, that the highest slope efficiency calculated in respect to the incident pumping energy was obtained in different measurements[2] in the samples with $x = 0.1$ or $x = 0.01$, where the fraction of absorbed pumping energy was equal to 33% or 13%, respectively. The incident pumping density corresponding to the first threshold was approximately equal to $2\,mJ/cm^2$ or $0.2\,MW/cm^2$. These threshold values are lower than those reported in ZnO random lasers (Table 7.1). The second threshold, approximately three times larger than the first one, was also low.

Recently, the first anti-Stokes solid-state laser, in which only one pumping photon is required to produce one higher-energy emission photon, has been demonstrated in GaAs powder [77]. The maximum pumping wavelength in Reference [77] was equal to 1.3 μm, while the emission wavelength was equal to ≈885 nm. The difference of energy was drawn from phonons. The demonstrated results may lead to a breakthrough in solid-state laser cooling and heat management of solid-state lasers.

References

1. V.A. Nikitenko, A.I. Tereschenko, I.P. Kuz'mina, and A.N. Lobachev, Stimulated emission of ZnO at high level of single photon excitation, *Optika i Spektroskopiya.*, **50**: 605–607, Russian (1981).
2. H. Cao, Y.G. Zhao, H.C. Ong, S.T. Ho, J.Y. Dai, J.Y. Wu, and R.P.H. Chang, Ultraviolet lasing in resonators formed by scattering in semiconductor polycrystalline films, *Appl. Phys. Lett.*, **73**: 3656–3658, (1998).

[2]The results of the measurements depended on the diameter of the pumped spot, duration of the pumping pulse, etc.

3. H. Cao, J.Y. Xu, Y. Ling, S.-H. Chang, S.T. Ho, E.W. Seelig, X. Liu, and R.P.H. Chang, Random lasers with coherent feedback. In *Photonic Crystals and Light Localization in the 21st Century*, C.M. Soukoulis, ed., Kluwer: Dordrecht, The Netherlands (2001).
4. H. Cao, Random lasers with coherent feedback. In *Optical Properties of Nanostructured Random Media*, V.M. Shalaev, ed., Springer: New York (2002).
5. H. Cao, Y. Xu, Y. Ling, A.L. Burin, E.W. Seeling, X. Liu, and R.H.P. Chang, Random lasers with coherent feedback, *IEEE J. Quantum Electron.*, **9**: 111–119 (2003).
6. B.Q. Sun, M. Gal, Q. Gao, H.H. Tan, C. Jagadish, T. Puzzer, L. Ouyang, and J. Zou, Epitaxially grown GaAsN random laser, *J. Appl. Phys.*, 93: 5855–5858 (2003).
7. M.A. Noginov, G. Zhu, I. Fowlkes, and M. Bahoura, GaAs random laser, *Laser Phys. Lett.*, **1**: 291–293 (2004).
8. I.T. Sorokina, E. Sorokin, V.G. Shcherbitsky, N.V. Kuleshov, G. Zhu, A. Frantz, and M.A. Noginov, Room-temperature lasing in nanocrystalline Cr^{2+}:ZnSe random laser. In *Technical Digest: Advanced Solid-State Photonics, Nineteenth Topical Meeting and Tabletop Exhibit.*, (2004), ISBN # 1-55752-764-4.
9. I.T. Sorokina, E. Sorokin, V. Shcherbitsky, N.V. Kuleshov, G. Zhu, A. Frantz, and M.A. Noginov, First mid-infrared eye-safe random lasers based on Cr^{2+}:ZnS and Cr^{2+}:ZnSe. In *International Quantum Electronics Conference, paper #IThG22, CD ROM 2004 CLEO/IQEC Technical Digest* (2004), ISBN # 1-55752-770-9.
10. H. Cao, private communication.
11. H. Cao, Y.G. Zhao, H.C. Ong, and R.P.H. Chang, Far-field characteristics of random lasers, *Phys. Rev. B*, **59**: 15107–15111 (1999).
12. H. Cao, Y.G. Zhao, X. Liu, E.W. Seelig, and R.P.H. Chang, Effect of external feedback on lasing in random media, *Appl. Phys. Lett.*, **75**: 1213–1215 (1999).
13. H. Cao, Y.G. Zhao, S.T. Ho, E.W. Seelig, Q.H. Wang, and R.P.H. Chang, Random laser action in semiconductor powder, *Phys. Rev. Lett.*, **82**: 2278–2281 (1999).
14. Y. Ling, H. Cao, A.L. Burin, M.A. Ratner, X. Liu, and R.P.H. Chang, Investigation of random lasers with resonant feedback, *Phys. Rev. A.*, **64**: 063808 (2001).
15. H. Cao, J.Y. Xu, D.Z. Zhang, S.-H. Chan, S.T. Ho, E.W. Seelig, X. Liu, and R.P.H. Chang, Spatial confinement of laser light in active random media, *Phys. Rev. Lett.*, **84**: 5584–5587 (2000).
16. H. Cao, J.Y. Xu, E.W. Seeling, and R.P. Chang, Microlaser made of disordered media, *Appl. Phys., Lett.*, **76**: 2997–2999 (2000).
17. C.M. Soukoulis, X. Jiang, J.Y. Xu, and H. Cao, Dynamic response and relaxation oscillations in random lasers, *Phys. Rev. B*, **65**: 041103 (2002).
18. R.K. Thareja and A. Mitra, Random laser action in ZnO, *Appl. Phys. B*, **71**: 181–184 (2000).
19. D. Jezequel, J. Guenot, N. Jouini, and F. Fievet, Submicrometer zinc oxide particles: Elaboration in polyol medium and morphological characteristics, *J. Mater. Res.*, **10**: 77–83 (1995).
20. P.W. Anderson, Absence of diffusion in certain random lattices, *Phys. Rev.*, **109**: 1492–1505 (1958).
21. P.W. Anderson, The question of classical localization: A theory of white paint, *Philos. Mag. B*, **52**: 505–509 (1985).
22. S. John, Electromagnetic absorption in a disordered medium near a photon mobility edge, *Phys. Rev. Lett.*, **53**: 2169–2172 (1984).
23. S. John, Localization of light, *Phys. Today*, 32–40 (May 1991).

24. P. Pradhan and N. Kumar, Localization of light in coherently amplifying random media, *Phys. Rev. B*, **50**: 9644–9647 (1994).
25. A.L. Burin, M.A. Rathner, H. Cao, and S.H. Chang, Random laser in one dimension, *Phys. Rev. Lett.*, **88**: 093904 (2002).
26. D.J. Thouless, Electrons in disordered systems and the theory of localization, *Phys. Rep.*, **13**: 93–142 (1974).
27. D.J. Thouless, Maximum metallic resistence in thin wires, *Phys. Rev. Lett.*, **39**: 1167–1169 (1973).
28. A.Z. Genack, Universality of wave propagation in random media, *Europhys. Lett.*, **11**: 733–738 (1990).
29. A.Z. Genack, Fluctuations, correlation and average transport of electromagnetic radiation in random media. In *The Scattering and Localization of Classical Waves*, P. Sheng, ed., World Scientific: Singapore (1990).
30. A.F. Ioffe and A.R. Regel, Non-crystalline, amorphous, and liquid electronic semiconductors. In *Progress in Semiconductors*, Vol. 4, A.F. Gibbson, gen. ed., R.E. Burgess and F.A. Kröger, eds., Heywood: London (1960), pp. 237–291.
31. X. Jiang and C.M. Soukoulis, Time-dependent theory for random lasers, *Phys. Rev. Lett.*, **85**: 70–73 (2000).
32. X. Jiang and C.M. Soukoulis, Theory and simulations of random lasers. In *Photonic Crystals and Light Localization in the 21st Century*, C.M. Soukoulis, ed., NATO Science Series, Series C: Mathematical and Physical Sciences, Vol. 563, Kluwer Academic: Boston (2001).
33. A.E. Siegman, *Lasers*, University Science Books: Mill Valley, CA (1986), Chapters 2,3,6,13.
34. A. Maitland and H.M. Dunn, *Laser Physics*, North-Holland: Amsterdam (1969), Chapter 9.
35. Q. Li, K.M. Ho, and C.M. Soukoulis, Mode distribution in coherently amplifying laser medium, *Physica B*, **296**: 78–84 (2001).
36. R.V. Ambartsumyan, P.G. Kryukov, V.S. Letokhov, and Yu.A. Matveets, Emission statistics of a laser with nonresonant feedback [*Pis'ma Zh. Eksp. i Teor. Fiz.*, **5**: 378–382 (1967) Russian] *JETP Lett.*, **5**: 312–314 (1967).
37. R.V. Ambartsumyan, P.G. Kryukov, V.S. Letokhov, and Yu.A. Matveets, Statistical emission properties of a nonresonant feedback laser, [*Zh. Eksp. i Teor. Fiz.*, **53**: 1955–1966 (1967) Russian] *Sov. Phys. JETP*, **26**: 1109–1114 (1968).
38. R.V. Ambartsumyan, N.G. Basov, P.G. Kryukov, and V.S. Letokhov. In *Progress in Quantum Electronics*, J.H. Sanders and K.W.H. Stevens, eds., Pergamon: New York (1970), pp. 109–185.
39. H. Cao, Y. Ling, and C.Q. Cao, Photon statistics of random lasers with resonant feedback, *Phys. Rev. Lett.*, **86**: 4524– 4527 (2001).
40. J.W. Goodman, *Statistical Optics*, J. Wiley: New York (2000).
41. R. Loudon, The Quantum Theory of Light, 2nd ed., Oxford University Press: Oxford (1983).
42. L. Florescu and S. John, Photon statistics and coherence in light emission from a random laser, *Phys. Rev. Lett.*, **93**: 013602/1–4 (2004).
43. L. Florescu and S. John, Theory of photon statistics and optical coherence in a multiple-scattering random-laser medium, *Phys. Rev. E*, **69**: 46603/1–16 (2004).
44. V.S. Letokhov, Stimulated emission of an ensemble of scattering particles with negative absorption, *JETP Lett.*, **5**: 212–215 (1967). [*ZhETP Pis'ma* **5**: 262–265 (1967) Russian.]

45. V.S. Letokhov, Generation of light by a scattering medium with negative resonance absorption, [*Zh. Eksp. i Teor. Fiz.*, **53**: 1442–14452 (1967) Russian] *Sov. Phys. JETP*, **26**: 835–840 (1968).
46. A.Z. Genack, P. Sebbah, M. Stoichev, and B.A. van Tiggelen, Statistics of wave dynamics in random media, *Phys. Rev. Lett.*, **82**: 715–718 (1999).
47. B.A. van Tiggelen, P. Sebbah, M. Stoichev, and A.Z. Genack, Delay-time statistics for diffuse waves, *Phys. Rev. E*, **59**: 7166–7172 (1999).
48. T.Sh. Misirpashaev and C.W. Beenakker, Lasing threshold and mode competition in chaotic cavities, *Phys. Rev. A.*, **57**: 2041–2045 (1998).
49. A.L. Burin, M.A. Ratner, H. Cao, and R.P.H. Chang, Model for a random laser, *Phys. Rev. Lett.*, **87**: 215503 (2001).
50. N. Kumar, Life before mean free path, *Curr Sci.*, **76**: 1330–1333 (1999).
51. A.L. Burin, H. Cao, and M.A. Ratner, Understanding and control of random lasing, *Physica B: Condensed Matter*, **338**: 212–214 (2003).
52. M.A. Noginov, G. Zhu, A.A. Frantz, J. Novak, S.N. Williams, and I. Fowlkes, Dependence of $NdSc_3(BO_3)_4$ random laser parameters on particle size, *JOSA B*, **21**: 191–200 (2004).
53. N.È. Ter-Gabriélyan, V.M. Markushev, V.R. Belan, Ch.M. Briskina, O.V. Dimitrova, V.F. Zolin, and A.V. Lavrov, Stimulated radiation emitted by lithium neodymium tertaphosphate $LiNd(PO_3)_4$ and neodymium pentaphosphate NdP_5O_{14} powders, *Sov. J. Quantum Electron.*, **21**: 840–841 (1991).
54. M.A. Noginov, N.E. Noginova, H.J. Caulfield, P. Venkateswarlu, T. Thompson, M. Mahdi, and V. Ostroumov, Short-pulsed stimulated emission in the powders of $NdAl_3(BO_3)_4$, $NdSc_3(BO_3)_4$, and Nd:$Sr_5(PO_4)_3F$ laser crystals, *J. Opt. Soc. Am. B*, **13**: 2024–2033 (1996).
55. H. Cao, B. Liu, A. Yamilov, Y. Ling, and J. Xu, Dynamic nonlinear effect on lasing in random media. In *Quantum Electronics and Laser Science Conference*, paper #QThG3, CD ROM Technical Digest (2003).
56. H. Cao, Y. Ling, J.Y. Xu, and A.L. Burin, Probing localized states with spectrally resolved speckle techniques, *Phys. Rev. E*, **66**: 025601 (2002).
57. X. Jiang and C. Soukoulis, Localized random laser modes and a path for observing localization, *Phys. Rev. E*, **65**: 025601 (2002).
58. C. Vanneste and P. Sebbah, Selective excitation of localized modes in active random media, *Phys. Rev. Lett.*, 87: 183903 (2001).
59. E.W. Seelig, B. Tang, A. Yamilov, H. Cao, and R.P.H. Chang, Self-assembled 3D photonic crystals from ZnO colloidal spheres, *Mater. Chem. Phys.*, **80**: 257–263 (2003).
60. V.F. Zolin, The nature of plaser-powdered laser, *J. Alloys Compounds*, **300–301**: 214–217 (2000).
61. S.V. Frolov, Z.V. Vardeny, A.A. Zakhidov, and R.H. Baughman, Laser-like emission in opal photonic crystals, *Opt. Communi.*, **162**: 241–246 (1999).
62. R.C. Polson, A. Chipoline, and Z.V. Vardeny, Random lasing in π-conjugated films and infiltrated opals, *Adv. Mater.*, **13**: 760–764 (2001).
63. A. Yamilov and H. Cao, Highest-quality modes in disordered photonic crystals, *Phys. Rev. A*, **69**: 31803/1–4 (2004).
64. E.S.P. Leong, M.K. Chong, S.F. Yu, and K. Pita, Sol-gel ZnO-SiO_2 composite waveguide ultraviolet lasers, *IEEE Photonics Technology Letters*, **16**: 2418–2420 (2004).
65. S.F. Yu, C. Yuen, S.P. Lau, and H.W. Lee, Zinc oxide thin-film random lasers on silicon substrate, *Applied Physics Letters*, **84**: 3244–3246 (2004).

66. S.F. Yu, C. Yuen, S.P. Lau, W.I. Park, and Y. Gyu-Chul, Random laser action in ZnO nanorod arrays embedded in ZnO epilayers, *Applied Physics Letters*, **84**: 3241–3243 (2004).
67. S.F. Yu and E.S.P. Leong, High-power single-mode ZnO thin-film random lasers, *IEEE Journal of Quantum Electronics*, **40**: 1186–1194 (2004).
68. Z. Yu, W. Gang, C. Yi-Ping, W. Jian, M. Yi, X. Ling, X. Jun, C. Kun-Ji, Z. Hai-Qian, and G. Ning, Electrochemical deposition and stimulated emission of zinc oxide thin films, *Chinese Journal of Lasers*, **A31**: 97–100 (2004).
69. D. Anglos, A. Stassinopoulos, R.N. Das, G. Zacharakis, M. Psyllaki, R. Jakubiak, R.A. Vaia, E.P. Giannelis, and S.H. Anastasiadis, Random laser action in organic-inorganic nanocomposites, *J. Opt. Soc. Am. B*, **21**: 208–213 (2004).
70. K.S. Wong, H. Wang, and G. Lanzani, Ultrafast excited-state planarization of the hexamethylsexithiophene oligomer studied by femtosecond time-resolved photoluminescence, *Chem. Phys. Lett.*, **288**: 59–64 (1998).
71. C.W. Lee, K.S. Wong, J.D. Huang, S.V. Frolov, and Z.V. Vardeny, Femtosecond time-resolved laser action in poly(*p*-phenylene vinylene) films: Stimulated emission in an inhomogeneously broadened exciton distribution, *Chem. Phys. Lett.*, **314**: 564–569 (1999).
72. F. Hide, B.J. Schwartz, M.A. Días-García, and A.J. Heeger, Conjugated polymers as solid-state laser materials, *Synth. Metals*, **91**: 35–40 (1997).
73. D.S. Wiersma, P. Bartolini, A. Lagendijk, and R. Righini, Localization of light in a disordered medium, *Nature*, **390**: 671–673 (1997).
74. R.C. Polson, A. Chipouline, and Z.V. Vardeny, Random lasing in π-conjugated films and infiltrated opals, *Adv. Mater.* **13**: 760–764 (2001).
75. R.C. Polson, M.E. Raikh, and Z.V. Vardeny, Universal properties of random lasers, *IEEE J. Select. Topics Quantum Electron.*, **9**: 120–123 (2003).
76. M.A. Noginov, G. Zhu, A. Frantz, J. Novak, S. Williams, and I. Fowlkes, Dependence of the $NdSc_3(BO_3)_4$ random laser parameters on the particle size, *JOSA B*, **21**: 191–200 (2004).
77. M.A. Noginov, G. Zhu, and C. Small, Anti-stokes GaAs random laser, *Quantum Electronics and Laser Science (QELS)* Conference, paper QThE2, Baltimore, MD, May 22–May 27, 2005.

8
Dye and Polymer Random Lasers

Although the focus of this book is on solid-state random lasers, this chapter starts with a brief discussion of liquid dye random lasers because of their close relevance to the ones realized in polymer films.

8.1 Liquid Dye Random Lasers

8.1.1 Liquid Dye Random Lasers with Nonresonant Feedback

In 1993 and 1994, Lawandy et al. have shown that when the density of pumping of a mixture of liquid rhodamine 640 dye with TiO_2 nanoparticles exceeds some critical threshold value, (1) the emission band narrows dramatically, from ≈80 nm to ≈5 nm, (2) the emission decay time shortens from 4 ns to smaller than 300 ps, and (3) the peak emission intensity increases superlinearly, resembling the input–output intensity dependence in regular lasers (Figures 8.1 and 8.2) [1,2]. These phenomena, which appeared to be relevant to those earlier observed in neodymium-doped powders [3–5], tended to be explained in terms of model [6,7] of photon diffusion in a medium with gain and scattering. The major problem with invoking light diffusion as an origin of feedback in the system was that the scattering length in the experiments of Reference [2] did not exceed the thickness of the samples. In [8], Wiersma et al. attempted to explain the phenomena experimentally observed in [2] by the amplification of spontaneous emission in open paths.

However, according to [9–11], stimulated emission *with feedback* provided by scatterers can also take place in the case opposite the diffusion, when the photon mean free path is larger than the dimension of the pumped medium L. In this case, the threshold of stimulated emission is determined by the inequality

$$e^{\alpha L} > \alpha/\chi, \tag{8.1}$$

where α is amplification per unit length and χ is the backscattering coefficient ($\chi \ll \alpha, 1/L$) [9–11]. This regime of stimulated emission with feedback, arguably

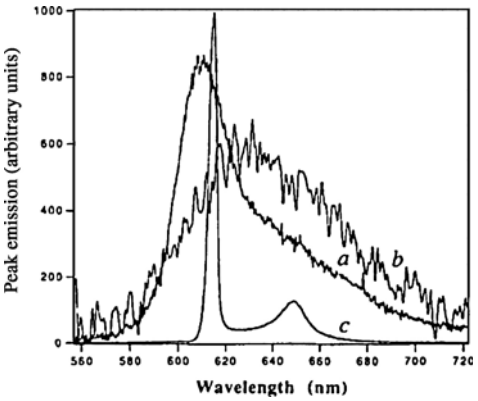

FIGURE 8.1. Trace a: emission spectrum of a 2.5×10^{-3} M solution of a rhodamine 640 perchlorate in methanol pumped by 3 mJ (7 ns) pulses at 532 nm. Traces b and c: emission spectrum of the TiO_2 nanoparticle ($2.8 \times 10^{10}\,cm^{-3}$) colloidal dye solution pumped by 2.2 μJ and 3 mJ pulses, respectively. The amplitude of the spectrum in b has been scaled up by a factor of 10, whereas that in c has been scaled down by a factor of 20. (*Source*: Ref. [2].)

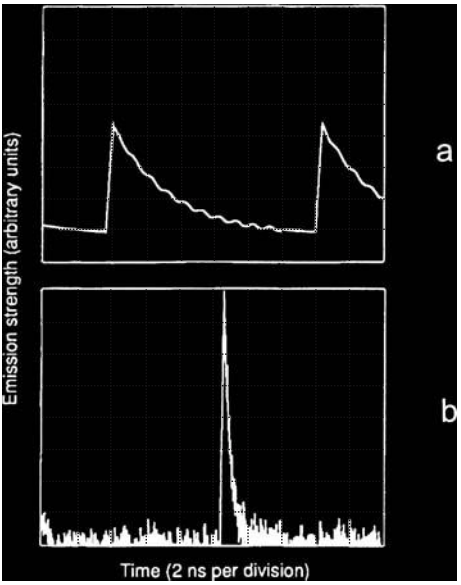

FIGURE 8.2. Emission kinetics of the dye and TiO_2 nanoparticle colloidal dye solution at (a) low, 1.2×10^{-2} mJ, and (b) high, 1.2×10^{-2} mJ pumping energies. The dye concentration is 2.5×10^{-3} M and the nanoparticle density is $2.8 \times 10^{19}\,cm^{-3}$. (*Source*: Ref. [2].)

different from the amplification of spontaneous emission in open paths without feedback, is predicted to occur in galaxy masers [9,11].

In [12], the dependence of the threshold of stimulated emission on the concentration of scatterers did not follow a simple pattern. Thus, scatterers strongly reduced the threshold of laserlike emission in highly concentrated rhodamine 640 solution, 2.5×10^{-2} M, and increased it in a dilute dye solution, 5×10^{-4} M. In the dye solution of medium concentration, 10^{-3} M, the addition of small concentrations of scatterers first increased the threshold and then decreased it, when the concentration of scatterers got higher.

In [13], where similar laserlike effects were observed in mixtures of rhodamine 6G dye and Al_2O_3 scatterers, the effect of scattering on the critical (threshold) pumping density, which corresponded to the line narrowing, was explained as follows. In a neat dye solution, ASE is strongest in the direction of the largest dimension of the pumped volume (Figure 8.3a). An addition of a small concentration of scatterers to such a sample disturbs and shortens long photon paths (Figure 8.3b) thus causing an increase of the threshold. Further increase of the concentration of scatterers causes a diffusionlike motion of photons, which elongates the residence time of emission photons in the pumped volume (Figure 8.3c) and reduces the threshold of stimulated emission again.

The effect of the diameter of the pumped spot d (or the ratio of d and the photon free path l^*) on the threshold pumping density in rhodamine B dye with TiO_2 scatterers was studied in [14]. It was shown that at constant value of l^*, the threshold increased ~70 times when the diameter of the pumped spot d was changed from $d \gg l^*$ (diffusion regime) to $d \approx l^*$ (low scattering regime, apparently similar to that

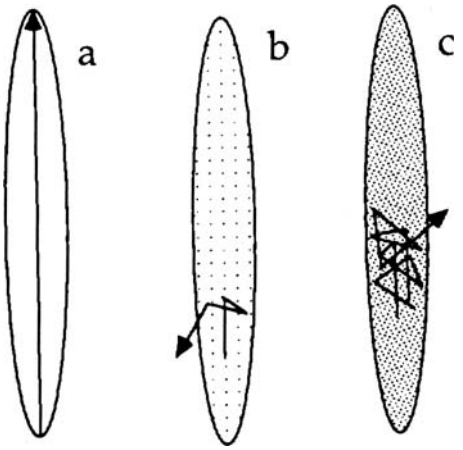

FIGURE 8.3. Propagation of stimulated emission in a pumped volume (a) without scatterers, (b) at small concentration of scatterers, and (c) at high concentration of scatterers. (*Source*: Ref. [13].)

in References [9–11]). This result is in qualitative agreement with those obtained in ZnO random lasers [15–17] and neodymium random lasers [18,19].

A blue shift of the stimulated emission line in comparison with the maximum of the spontaneous emission band (Figure 8.4) has been observed in solutions of dye and scatterers in [13,2] and several other works. In many laser dyes, the short-wavelength wing of the emission band overlaps the long-wavelength wing of the absorption band. This causes reabsorption of spontaneous emission and its red shift, which is especially strong when photon paths in the medium are long. Scatterers elongate photon paths in luminescent materials and, thus, cause an even stronger red shift of spontaneous emission.

On the other hand, stimulated emission first occurs at the wavelength at which gain exceeds loss or at the wavelength of maximum gain, if loss is wavelength-independent. With an increase of the population inversion (and partial bleaching of the ground-state absorption), the spectral band of gain experiences a blue shift, more closely resembling the emission cross-section band. Thus, it is well possible that at a high value of the population inversion, the wavelength of stimulated emission is shorter than that of (reabsorbed and re-emitted) spontaneous emission

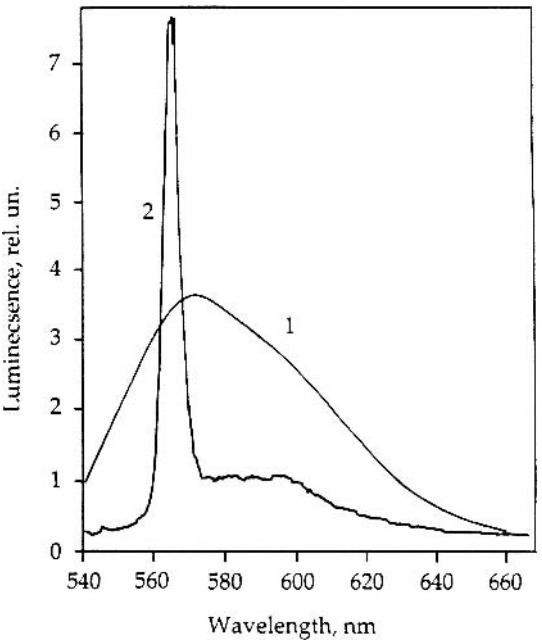

FIGURE 8.4. Emission of a highly concentrated rhodamine 6G dye with Al_2O_3 particles precipitated at the bottom of the cuvette at low pumping density $0.5\,J/cm^2$ (trace 1) and high pumping density $40\,J/cm^2$ (trace 2). (*Source*: Ref. [13].)

observed in dyes with or even without scatterers. Note that in [20], the wavelength of stimulated emission in rhodamine 640 dye with TiO_2 particles increased with the increase of dye concentration (at fixed concentration of particles equal to $\rho = 10^{11}\,\mathrm{cm}^{-3}$) and reached its maximum at $\rho = \approx 5 \times 10^{11}\,\mathrm{cm}^{-3}$ (at fixed concentration of dye equal to $c = 2.5 \times 10^{-3}\,\mathrm{M}$).

The details of temporal and spectral behavior of stimulated emission in liquid dye random lasers have been studied in [21–31]. A blue shift of a stimulated emission line, apparently similar to that discussed above [13], was predicted in Monte Carlo simulation of random walks of photons [26]. The computation procedure in [26] took into account a nonlinear relationship between the position-dependent values of population inversion and photon density within the spectral band of spontaneous emission. Many authors, describing the behavior of liquid random lasers, further developed or modified the diffusion model [28–31] proposed by Letokhov in [6,7,10].

The model of a random laser, which relies on nonresonant feedback provided by unexcited scattering volume positioned beneath the pumped volume, has been proposed in [23]. Alternatively, the model of a coherent stimulated emission feedback in random lasers (the idea of which is relevant to lasers with distributed feedback, although in an periodic media) has been discussed in [32].

Note that basic physical mechanisms of random laser operation, such as amplification of light by stimulated emission radiation and feedback due to scattering, are principally the same in the systems where gain is located inside or outside scattering particles. This makes the difference between liquid random lasers and solid-state (powder) random lasers more apparent than real. The difference between the two classes of random lasers becomes evident only in rare situations, in which the stimulated emission is supported by intraparticle morphology-dependent resonances (MDR).

8.1.2 Transition from Incoherent Regime of Operation to Coherent Regime of Operation

Laserlike emission in solutions of rhodamine 640 ($5 \times 10^{-3}\,\mathrm{M}$) with different concentrations of ZnO nanoparticles was studied in References [33,34]. Experimentally, 532 nm laser light ($t_{pulse} = 25\,\mathrm{ps}$) was focused onto the sample using a lens with the focal length $f = 10\,\mathrm{cm}$. At a small concentration of scatterers, $2.5 \times 10^{11}\,\mathrm{cm}^{-3}$, a narrowing of the emission band to 5 nm and an increase of the slope of the input–output curve above the threshold, were observed at an increase of the pumping energy. This emission, the behavior of which was similar to that in many experiments discussed in Section 8.1.1, was explained in terms of lasing with nonresonant feedback.

The character of stimulated emission changed dramatically when the concentration of particles was increased to $1 \times 10^{12}\,\mathrm{cm}^{-3}$. In this case, discrete narrow lines ($\Delta\lambda \sim 0.2\,\mathrm{nm}$) appeared on the top of a much broader ($\Delta\lambda \sim 5\,\mathrm{nm}$) emission band above the threshold. When the pumping intensity was increased further, a larger number of sharp emission lines appeared in the spectrum (Figure 8.5).

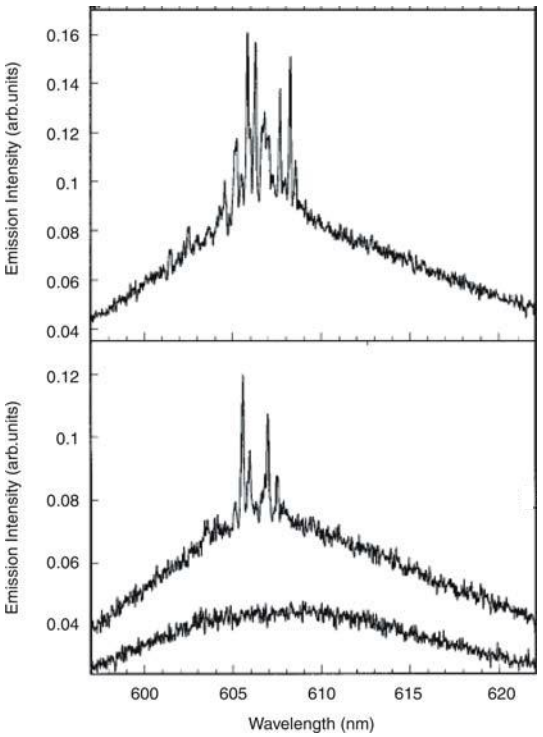

FIGURE 8.5. Emission spectra in the solution of rhodamine 640 laser dye (5×10^{-3} M) with high concentration of ZnO scatterers (1×10^{12} cm^{-3}). The pumping pulse energy is equal to 0.68 μJ (bottom curve), 1.1 μJ (middle curve), and 1.3 μJ (upper curve). (*Source*: Ref. [34].)

Qualitatively, the stimulated emission at high concentration of scatterers appeared to be similar to that in ZnO random lasers; see Chapter 7. Correspondingly, the observed effect was explained in terms of coherent (resonant) feedback, where the interference between scattered waves created a quasi-stationary distribution of electromagnetic field and determined the resonant lasing frequencies. (Note that because of continuous Brownian motion of scattering particles, the positions of the narrow emission lines changed from pulse to pulse.)

The behavior of the stimulated emission was particularly interesting at the intermediate concentration of scatterers, 6×10^{11} cm^{-3}. In this case, as the pumping intensity was increased, a narrowing of the emission band (similar to that in a low-scattering solution) occurred first. Then, at some higher pumping energy threshold, discrete narrow peaks (similar to those in a highly scattering solution) emerged on the top of the narrowed emission band (Figure 8.6).

The experimental results above have been explained [33] in terms of quasi-states, eigenmode solutions of Maxwell equations in a finite-sized random medium. It has been argued that losses in quasi-states are due to (i) losses at the medium–air

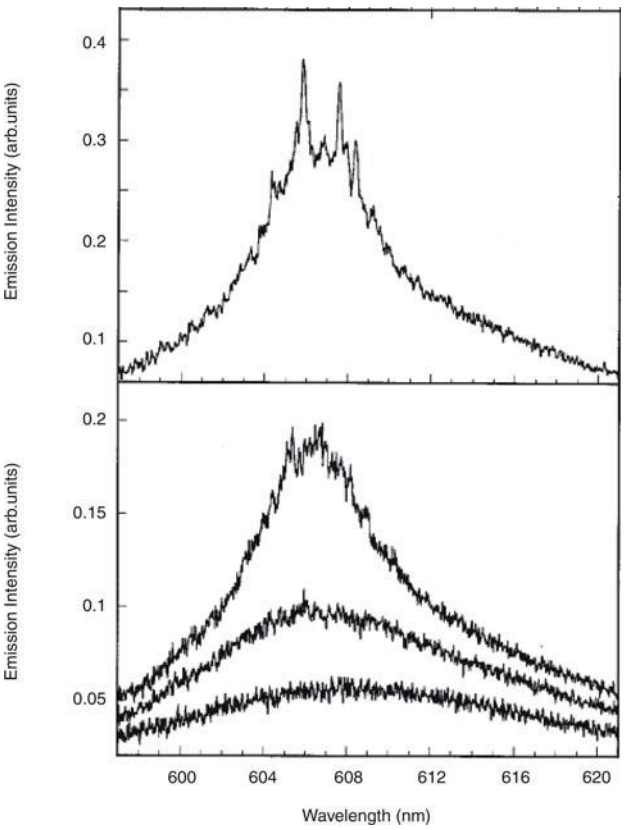

FIGURE 8.6. Emission spectra in the solution of rhodamine 640 laser dye (5×10^{-3} M) with medium concentration of ZnO scatterers (6×10^{11} cm^{-3}). The pumping pulse energy is (from bottom to top) 0.74, 1.35, 1.7, and 2.25 μJ. (*Source*: Ref. [34].)

boundaries and (ii) transfer of energy to other quasi-states. The energy coupling between quasi-states, which according to [33] is stronger at low concentration of scatterers than at high concentration of scatterers, redistributes energy between the quasi-states but does not affect the loss in an ensemble of quasi-states as a whole. Thus, the stimulated emission is first achieved in an ensemble (of stronger or weaker coupled) quasi-states, which has relatively low loss. This corresponds to a regime of nonresonant feedback [10]. According to [33], at some higher energy threshold the laser action occurs in individual quasi-states, which have higher loss. This is the regime of coherent feedback. Following the arguments above (the loss in individual modes decreases with the increase of the concentration of scatterers), the difference between the two thresholds should be smaller at high concentration of scatterers than at low concentration of scatterers. This must determine the difference in the behavior of low-scattering and highly-scattering laser dye solutions.

One should note that discrete (nondegenerate) laser modes, such as those in Figures 8.5 and 8.6, are the states with different photon energies. Thus, the coupling

of quasi-states discussed in [33] is possible only if there is a mechanism by which the frequency of the laser oscillation may change. As possible examples of such mechanisms, acoustic vibrations, Doppler shift due to moving scattering particles, random frequency modulation in the active medium, and the like were discussed in [10]. In liquid dye random lasers studied in [33,34], the average energy difference between laser modes is of the order of several inverse centimeters; however, no physical mechanism that can provide for so large a frequency shift was discussed.

An alternative explanation of narrow-line random laser emission in liquid dye with scatterers has been proposed in Reference [3]. In [35], narrow lines in the emission spectrum have been explained by amplification of stimulated emission in very long but statistically very rare photon paths. It has been argued that introduction of exponential gain in a multiple light scattering process strongly increases the importance of such long light paths, which are often neglected in passive disordered materials.

8.2 Solid-State Polymer Random Lasers with Nonresonant Feedback

8.2.1 Photonic Fibers

The idea of a random laser based on organic dye doped into a solid-state organic host was proposed in Reference [36], in which a "photonic textile fiber" was demonstrated. In [36], rhodamine 590 and rhodamine 640 laser dyes (at typical concentration 2×10^{-3} M) as well as TiO_2 particles were doped in the nylon-6 host, which then was drawn into fibers of different diameters. Nylon fibers doped with pure dye showed morphology-dependent resonances over the entire emission spectrum of dye. However, with addition of scatterers (in concentration $\approx 10^{11}\,\mathrm{cm}^{-3}$) MDRs disappeared completely, and the emission band narrowed and shifted to shorter wavelengths. The dependence of the peak emission intensity on the pumping energy was typical of that in regular lasers, and the emission bandwidth narrowed dramatically above the threshold. Analogous laserlike behavior, similar to that of liquid dyes discussed in Section 8.1.1, was observed in several other technologically important laser materials, including polyester, Kevlar, and Nomex [36]. Proposed applications of the developed fibers included soldier-level identification of friend or foe, search and rescue, anticounterfeiting, and so on. Markers based on organic dyes with scatterers have been used for identification purposes in [37].

8.2.2 Random Laser Action from Semiconducting Polymers with TiO_2 Nanoparticles

Semiconducting conjugated polymers can be used as active media in light emitting diodes [38,39]. The achievement of spectrally narrow polymer laser diodes is an

important goal for polymer photoelectronic devices [40]. The laser action from poly(2-metoxy,5-(2′ethyl-hexiloxy)-1,4-phenylene-vinylene) (MEH-PPV) mixed with TiO_2 nanoparticles in polystyrene has been observed and studied in [40].

Experimentally, 150 to 250 μm free-standing films of polymers have been prepared. The samples were excited with 10 ns laser pulses at $\lambda = 532$ nm or $\lambda = 435$ nm. The significant narrowing of the emission band above the threshold was qualitatively similar to that in liquid dye solutions with scatterers or photonic fibers (see [2] and other examples discussed in Sections 8.1.1 and 8.2.1). At the same time, the stimulated emission threshold was difficult or impossible to achieve in samples without scatterers. The blue shift of the stimulated emission with respect to the maximum of the spontaneous emission, observed in MEH-PPV films with TiO_2 particles [40], was similar to that in the mixture of liquid dyes and scatterers [2,13].

MEH-PPV liquid solutions and solid films demonstrated qualitatively the same type of emission behavior. However, the lasing threshold was nearly an order of magnitude lower in films than in liquid solutions of comparable concentration. The laser threshold in films was much below an onset of the optical damage. The parameters of the MEH-PPV random laser discussed above as well as other polymer random lasers are summarized in Table 8.1.

8.2.3 Laserlike Emission in Variety of Conjugated Polymers

The important difference between conjugated polymers and liquid laser dyes is that liquid dyes undergo concentration quenching and conjugated polymers do not [42]. Accordingly, much higher gain can be achieved in undiluted polymers than in liquid dyes. In [51,52], stimulated emission has been demonstrated in over a dozen different semiconducting polymer films representing a variety of molecular structures with emission wavelengths covering almost the whole visible range. High optical gain and stimulated emission in several other π-conjugated polymers have been reported in [41,43,53–55]. Lasing in microcavities made of PPV and PPV derivative, BuEH-PPV, has been demonstrated in [56,57]. The advances in the development of conjugated polymers for solid-state random lasers have also been reported in [58–60].

Absorption and emission spectra as well as chemical structures of 12 polymers studied in [42] are shown in Figure 8.7. Experimentally, thin-film polymer samples were spin-cast on glass or ITO substrates and excited with 10 ns pulses at 532, 435, or 355 nm. The thickness of the films was smaller than 1 μm. Imperfections in the films provided for scattering of light. No other scatterers were intentionally introduced to the polymers. All polymers depicted in Figure 8.7 demonstrated narrowing of the emission bandwidth above some well-defined threshold, qualitatively similar to that in Figure 8.1. The existence of gain in neat undiluted films of BuEH-PPV under photoexcitation has been confirmed directly in [61], proving that the observed spectral narrowing is, indeed, due to the stimulated emission

process. Blue shifts of the stimulated emission with respect to the maximum of the spontaneous emission, which were observed in many conjugated polymers studied in [42] were qualitatively similar to those in MEH-PPV films and liquid dyes with scatterers [2,13,40].

The indexes of refraction in all polymers depicted in Figure 8.7 are in the range $1.56 < n_{\text{polymer}} < 2$, that is, larger than those in glass ($n_{\text{glass}} = 1.52$) or air ($n_{\text{air}} = 1$). Thus, a waveguide propagation of light is possible in polymer films if the film thickness is greater than some critical cutoff value h_{cutoff}, which is determined by the indexes of refraction of all three media. The width of the emission band at high pumping energy ($>10\,\mu$J), which can be used as an indicator of the stimulated emission, is plotted in Figure 8.8 as a function of the film thickness in the three different polymers studied. In all three materials, the abrupt change of the emission bandwidth corresponds to the value of h_{cutoff} estimated for each polymer based on the value of the refraction index [42]. This experiment proves that laserlike emission in conjugated polymer films occurs in a waveguide regime. Because the coupling between emitting dipoles in the film cannot be altered by merely turning the waveguiding on and off, the superfluorescence, which was proposed in [62] as a possible explanation of laserlike emission in polymer films, cannot be the sole mechanism of a bandwidth narrowing.

In Reference [63], random laser emission characterized by a narrowing of the spectral band has been demonstrated in MEH/PPV/glass waveguide with 20 nm TiO_2 scatterers.

8.2.4 Time-Resolved Studies of Stimulated Emission in Polymer Film

In Reference [44], emission dynamics in thin films of 2,5-dioctyloxy PPV (DOO-PPV) has been studied with femtosecond resolution below and above the threshold for spectral narrowing. The gated upconversion technique used in [44] is described in detail in [64]. Experimentally, the polymer film was excited at 400 nm with 150 fs pulses of second harmonic of Ti-sapphire regenerative amplifier. The fundamental laser beam at 800 nm was used as a gated "clock" pulse. It was mixed in BBO crystal with the photoluminescence signal of the film to generate the sum frequency in the ultraviolet. The signal was detected with a photomultiplier tube attached to the output slit of the spectrometer. This setup allowed for time resolution equal to 300 ps and spectral resolution equal to 2 ns.

In [44], a spin-cast DOO-PPV film had a thickness of 200 nm. The spontaneous emission spectrum of the DOO-PPV film was inhomogeneously broadened, with different decay times in different parts of the spectrum and energy migration within the excitonic state distribution.

Above some critical pumping energy, the emission spectrum narrowed significantly, with the maximum at $\lambda \approx 630$ nm. At the same threshold, (i) the emission lifetime in the film (at $\lambda \sim 630$ nm) shortened from $\sim$250 to $\sim$3 ps, and (ii) the onset of the stimulated emission was delayed in respect to the spontaneous

TABLE 8.1. Parameters of different polymer random lasers[a,b]

Material	Pumping wavelength/ pulsewidth	Scattering particles	Scattering length (μm)	Film thickness (nm)	Pumped spot size
MEH-PPV	532 nm/10 ns	TiO_2, 270 nm, $\sim 10^{11}$ cm^{-3}		$(150–250) \times 10^3$	d $\sim$ 1.5 mm
				126–252	
BuEH-PPV	435 nm/10 ns			87–208	
BCHA-PPV				277–650	
BEH-PPV				300	
MEH-PPV				87–405	
	532 nm/10 ns			355	
				325	
M3O-PPV				310	
BuEH-MEH copolymers: 10:90				330	d $\sim$ 1 mm
70:30				420	
90:10		No intentional		370	
95:5	435 nm/10 ns	scatterers		450	
97.5:2.5				500	
HEH-PF				120	
BDOO-PF	355 nm/10 ns				
CN-PPP				100	
BeEH-PPV	435 nm/10 ns			210	
CN-PPP	355 nm/10 ns			100	
BCHA-PPV	532 nm/10 ns			580	
DOO-PPV	540 nm/150 ps			30–2000	
DOO-PPV	400 nm/150 fs			200	
DOO-PPV			9		
Rhodamine 6G doped gel film	532 nm/100 ps	SiO_2 balls 2×10^{10} cm^{-3}		$\sim 30 \times 10^3$	3 mm $\times$ 30 μm
DOO-PPV				$(0.5–1) \times 10^3$	1 mm $\times$ 30 μm
DOO-PPV		No intentional	>300	$\sim 1 \times 10^3$	1 mm $\times$ 30 μm
DOO-PPV		scatterers	$\sim$15	1×10^3	2 cm $\times$ 100 μm
DOO-PPV			15	$\sim 1 \times 10^3$	2 cm $\times$ 250 μm
PMMA with rhodamine 640 dye and TiO_2 scatterers	532 nm/25 ps	TiO_2, 400 nm.	$\sim$0.3	150×10^3	d $\approx$ 50 μm
			0.9		0.03 mm^2
	532 nm/30 ps	No intentional scatterers		$(0.5–1) \times 10^6$	d $\approx$ 50 μm

[a]Full chemical names of polymers:
MEH-PPV – poly(2-metoxy,5-((2′ethyl-hexil)oxy)-1,4-phenylenevinylene);
BuEH-PPV – poly(2-butyl-5-(2′-etylhexyl)-1,4-phenylenvinylene);
BCHA-PPV – poly(2,5-bis(cholestanoxy)-1,4-phenylenvinylene);
BEH-PPV – poly(2,5-bis((2′-ethylhexyl)oxy)-1,4-phenylenvinylene);
M3O-PPV – poly(2-methoxy-5-(3′-octyloxy)-1,4-phenylenvinylene);
BuEH-MEH – copolymers synthesized from different ratios of BuEH-PPV and MEH-PPV monomers;
HEH-PF – poly(9-hexyl-9-(2′-ethylhexyl)fluorene-2,7-diyl);
BDOO-PF – poly(9,9-bis(3,6-dioxaoctyl)fluorene2,7-diyl);

Wavelength (wavelength range) (nm)	Threshold criterion	Threshold energy (μJ)	Threshold energy density (μJ/cm^2)	Threshold power density (kW/cm^2)	Ref.
570–580		$\sim 2 \times 10^4$	$\sim 1.1 \times 10^{6c}$	$\sim 1.1 \times 10^{5c}$	[40]
520, 560		0.4 ± 0.2	$\sim 51^c$	$\sim 5.1^c$	
		0.2 ± 0.1	$\sim 25^c$	$\sim 2.5^c$	
540, 620		1.0 ± 0.4	$\sim 130^c$	$\sim 13^c$	
580, 650		0.5	$\sim 64^c$	$\sim 6.4^c$	
585, 625		1.1 ± 0.4	$\sim 140^c$	$\sim 14^c$	
		3	$\sim 380^c$	$\sim 38^c$	
		4	$\sim 510^c$	$\sim 51^c$	[41]
530, 620	Narrowing of the emission	4	$\sim 510^c$	$\sim 51^c$	
580, 625	bandwidth	3.2	$\sim 410^c$	$\sim 41^c$	
565, 600		1.0	$\sim 130^c$	$\sim 13^c$	
550, 580		1.0	$\sim 130^c$	$\sim 13^c$	
545, 580		1.6	$\sim 200^c$	$\sim 20^c$	
540, 570		1.0	$\sim 130^c$	$\sim 13^c$	
425, 445		4.2	$\sim 530^c$	$\sim 53^c$	
430, 450, 540		2.3	$\sim 290^c$	$\sim 29^c$	
420		4	$\sim 510^c$	$\sim 51^c$	
555–570		~ 0.6	$\sim 76^c$	$\sim 7.6^c$	
$\sim$420		~ 9	$\sim 1100^c$	$\sim 110^c$	[42]
$\sim$600		~ 2	$\sim 250^c$	$\sim 25^c$	
			~ 60	$\sim 400^c$	[43]
630			< 50	$< 3.3 \times 10^{5c}$	[44]
$\sim$630	Superlinear	0.5			[45]
	increase of	1			
555–565	emission intensity	0.23^c	250^c	2.5×10^3	[46]
625–640		0.03^c	100^c	1×10^3	
625–635		0.05^c	160^c	1.6×10^3	[47]
625–640	Narrow lines	1	50^c	500^c	[48]
630–640	(modes)	< 2	$< 40^c$	$< 400^c$	[49]
		~ 0.07	$\sim 3.6 \times 10^{3c}$	$\sim 1.4 \times 10^{5c}$	[50]
		$\sim 0.75^c$	$\sim 2.5 \times 10^{5c}$	$\sim 1 \times 10^5$	
$\sim$620–625		< 0.98	$\sim 5 \times 10^{4c}$	$\sim 1.7 \times 10^{6c}$	[17]

CN-PPP – poly(2-((6′-cyano-6′methylheptyl)oxy)-1-4-phenylene;
DOO-PPV – poly(2,5-dioctyloxy)-1,4-phenylenvinylene;
PMMA – poly(methyl methacrylate).

[b]When several threshold values were reported in the same publication for different experimental conditions, the smallest of the reported values was used in this table.

[c]The value is calculated by the author (M.N.) from the data reported in the paper. (In calculations, the threshold pumping energy and the threshold pumping power are related via the width of the pumping pulse, but not the spontaneous emission lifetime.)

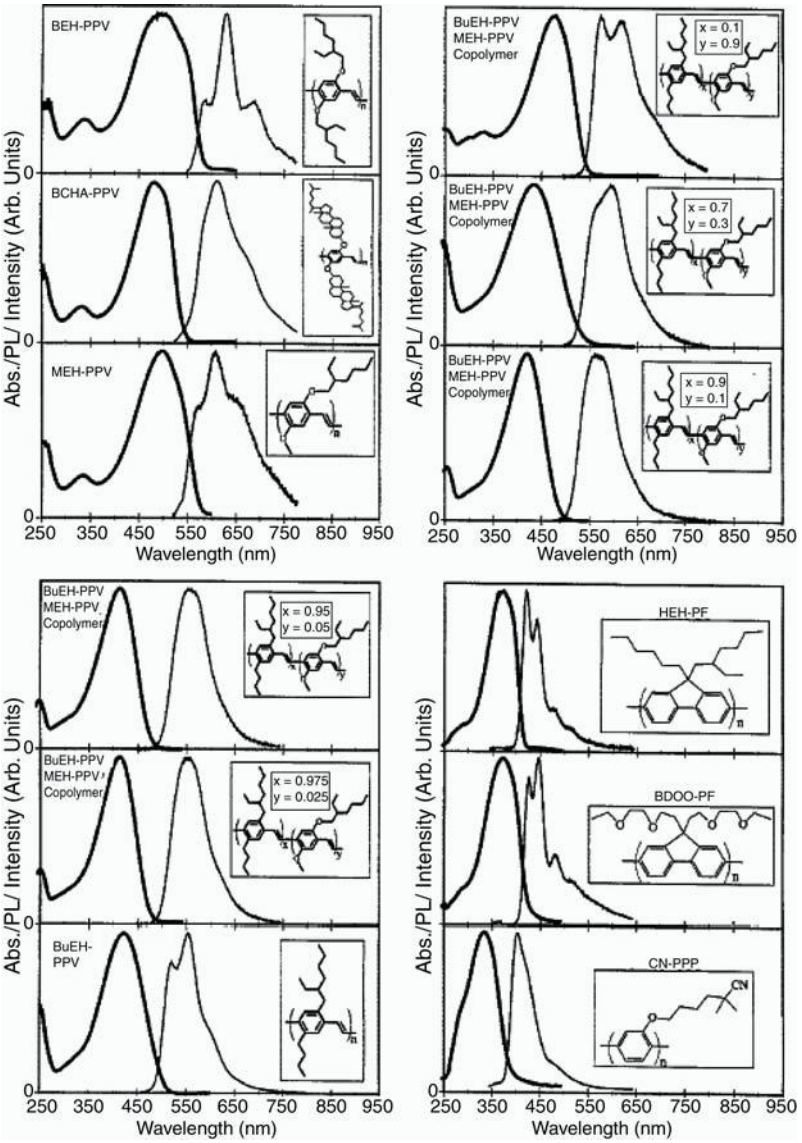

FIGURE 8.7. Absorption (bold smooth curves) and photoluminescence (thin slightly noisy curves) spectra of neat thin films of BuEH-PPV, BCHA-PPV, MEH-PPV, BEH-PPV, BuEH-PPV/MEH-PPV copolymers at different monomer ratios, HEH-PF, BDOO-PF, and CN-PPP. Insets: molecule structures. (*Source*: Ref. [42].)

emission by several picoseconds. These changes in the emission spectra and kinetics were qualitatively similar to those in liquid dyes and polymer films discussed in preceding sections of this chapter. (Note that due to a small variation of the film thickness, the film had high waveguiding efficiency [44], and

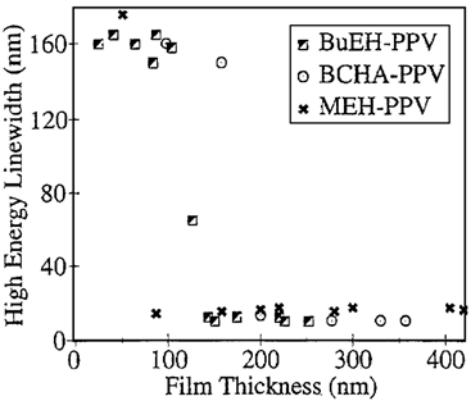

FIGURE 8.8. Bandwidth of the photoluminescence spectrum at high pumping energy ($\geq 10\,\mu$J) as a function of the film thickness for BuEH-PPV (half-filled squares, 435 nm excitation), BCHA-PPV (dotted circles, 532 nm excitation), and MEH-PPV (crosses, 532 nm excitation) films spin-cast on glass substrates. (*Source*: Ref. [42].)

a random laser based on this film was, most likely, two-dimensional rather than three-dimensional.)

Stimulated emission had maximum intensity at $\lambda \sim 630$ nm and was much weaker at all other wavelengths within the spontaneous emission band. As a result, the random laser pulse quickly depopulated excitons corresponding to the stimulated emission wavelength (630 nm), and energy still was stored (long after the end of the pumping pulse) at excitons of other frequencies. With time, which was determined by the rate of spectral energy diffusion, excitons at the stimulated emission wavelength became re-excited due to the energy transfer from excitons of other frequencies, and were able to produce another pulse of stimulated emission (Figure 8.9).

In some sense, the observed multipulse behavior of stimulated emission was nothing else but relaxation oscillations known in conventional lasers [65–67] and random lasers [68–71]. The principal difference between "traditional" relaxation oscillations and those of [44] is that in the majority of lasers, relaxation oscillations sustain only during the pumping pulse, when the population inversion is continuously renewed by pumping. However, in [44], relaxation oscillations were observed after the end of the pumping pulse. This became possible because the energy stored at excitons of nonlasing frequencies continued to "feed" the population inversion at the lasing transition via spectral excitation migration.

As shown in [72], relaxation oscillations observed in the kinetics of stimulated emission can serve as evidence of feedback in a system. Thus the experiment above rules out ASE in open paths as a possible explanation of stimulated emission in the DOO-PPV film in [44] and proves that the observed laserlike behavior is supported by (apparently nonresonant) feedback.

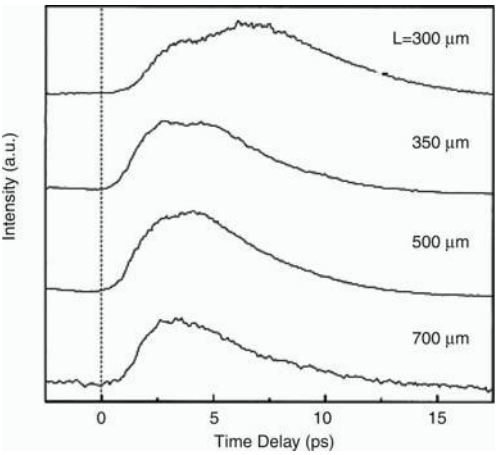

FIGURE 8.9. Picosecond stimulated emission dynamics of DOO-PPV at 630 nm for $I = 300\,\mu\text{Jcm}^{-2}$ per pulse for different lengths L of the excited strip. The second emission bump is clearly seen at $L = 300\,\mu\text{m}$ and $L = 350\,\mu\text{m}$. (*Source*: Ref. [44].)

8.3 Polymer Random Lasers with Resonant Feedback

8.3.1 Transition from Incoherent Regime of Operation to Coherent Regime of Operation

In [45], emission in poly(dioctyl-oxy) phenylevinylene film has been studied in a wide range of pumping intensities. At weak excitation, the emission spectrum is very broad, with the characteristic width equal to 120 nm and the maximum corresponding to 625 nm (Figure 8.10). In this regime, the emission intensity depends linearly on the excitation intensity (region I in Figure 8.11).

At stronger pumping, the emission intensity increases with the increase of the excitation intensity superlinearly (region II in Figure 8.11). Simultaneously, the emission band narrows to less than 8 nm. Qualitatively, the narrowing of the emission band above is similar to that observed by many authors in solutions of liquid dyes with scatterers and polymer thin films (see Sections 8.1 and 8.2). The authors of [45] described this regime of operation in terms of ASE; however, they did not make a distinction between ASE and a random laser with nonresonant feedback.

At even higher pumping intensity (above the second critical threshold), the emission intensity depends on the excitation intensity linearly again (region III in Figure 8.11). Simultaneously, narrow lines appear in the spectrum on the top of a broader band of incoherent stimulated emission (Figure 8.12a). (Much more pronounced narrow emission lines have been observed in DOO-PPV film in Ref. [47]; see Figure 8.12b,c.) Based on the appearance of the multiple-line emission spectrum in Figure 8.12, which resembles that in ZnO random lasers

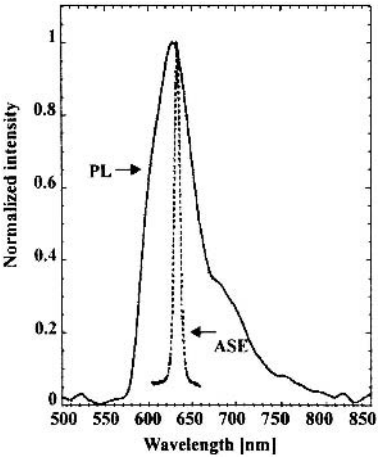

FIGURE 8.10. Emission spectra of a DOO-PPV film at low pumping intensity, solid line, and at higher pumping intensity corresponding to region II in Figure 8.11, dashed line. (*Source*: Ref. [45].)

(Chapter 7), one can conjecture that above the second threshold, the random laser operates in a coherent regime. The validity of this conclusion is proven later in this section.

The evolution of the emission spectrum in DOO-PPV film with the increase of the pumping power resembles that observed in [33] in liquid dye with a medium concentration of scatterers. A qualitatively similar multiple-line emission has been

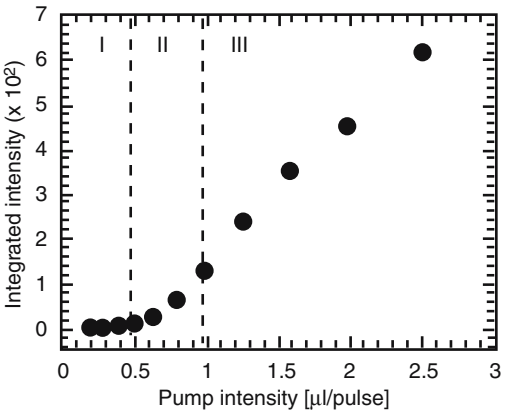

FIGURE 8.11. Emission intensity as a function of the threshold intensity; region I corresponds to the regime of spontaneous emission, region II corresponds to the incoherent random laser regime, and region III corresponds to the coherent random laser regime. (*Source*: Ref. [45].)

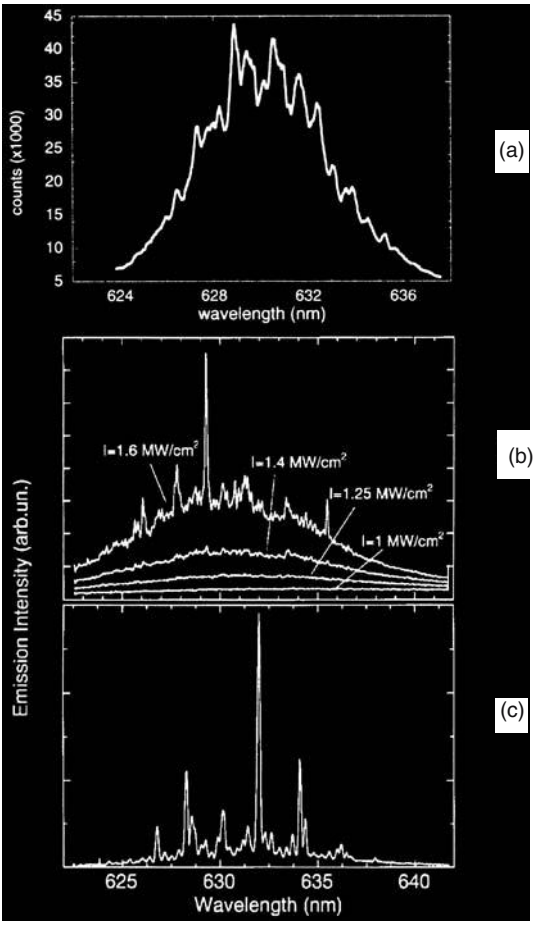

FIGURE 8.12. (a) Random laser emission spectrum of a DOO-PPV film at high excitation intensity (region III in Figure 8.11) showing narrow laser modes on the top of a broader incoherent stimulated emission peak. (*Source*: Ref. [45].) (b) Stimulated emission spectra of DOO-PPV film obtained using a stripelike excitation area with the length of 1 mm and width of 30 μm. (c) Emission from a different area of the same film at pumping density 2 MW/cm^2. (*Source*: Ref. [47].)

observed in gelatin or polymer films doped with laser dye and scatterers [17,46,50] and opals infiltrated with DOO-PPV or rhodamine dye [45,73–75].

8.3.2 Photon Statistics of Polymer Random Lasers

The photon statistics of random laser emission in DOO-PPV thin-film lasers has been studied in [45]. The idea of this type of experiment, originally proposed

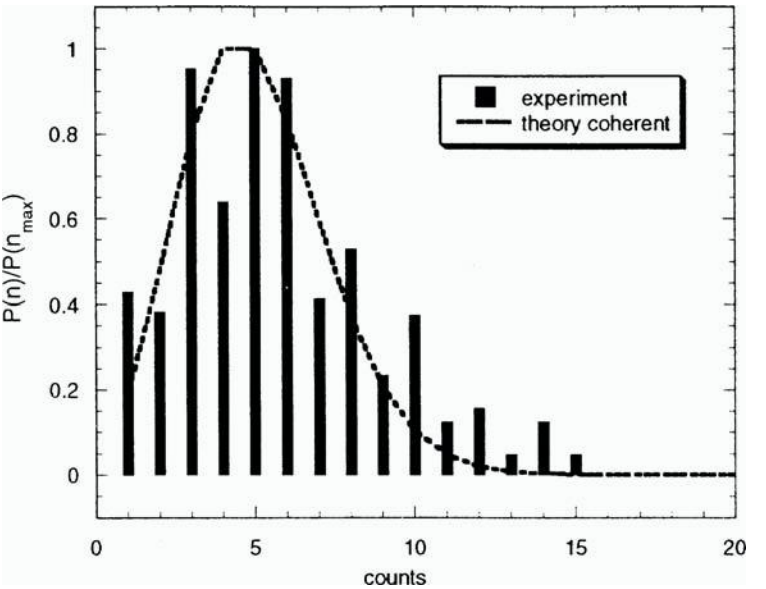

FIGURE 8.13. Normalized photon distribution function, $P(N)$ (full line), of the random laser emission (at the $\lambda = 630$ nm spectral line) shown in Figure 8.12a. The dashed line through the data points is fit using Poisson distribution around $< N >= 5$, proving that the random laser emission is indeed a coherent process. (*Source*: Ref. [45].)

in [76], is described in Section 7.5. According to [77,78], the Poisson photon distribution function corresponds to coherent radiation, and the Bose–Einstein distribution is expected in the case of noncoherent light. In [45], the photon distribution histogram was studied at 630 nm in one of the random laser modes shown in Figure 8.12a. The transient emission kinetics generated by each pulse was divided into time intervals, which were smaller than the emission coherence time. The number of photons N was measured in each time interval and for each pulse, and a photon number histogram $P(N)$ (shown in Figure 8.13) was calculated in order to obtain the probability distribution function. It was found that the data points can be fit with the Poisson distribution $P(N) = \langle N \rangle^N e^{-\langle N \rangle}/N!$, where $\langle N \rangle$ (equal to $\langle N \rangle = 5$ for Figure 8.13) is the mean photon number. Thus, it was concluded that the narrow-line random laser emission, the spectrum of which is depicted in Figure 8.12a, was, indeed, coherent.

In organic random laser media, similar photon-counting experiments have been performed in dye-TiO_2 polymer systems [76] and liquid solution of dye with TiO_2 scatterers [79]. It has been shown that although the random laser emission is coherent in narrow spectral lines (modes) above the threshold, the emission between narrow spectral lines [79] or the emission below the threshold [76] has Bose–Einstein statistics and, thus, is incoherent.

8.3.3 Fourier Transform of the Emission Spectra of Polymer Random Laser

In several publications [45,48,49,79–81], the spectra of coherent stimulated emission in polymer random lasers have been analyzed in terms of the Fourier transform model developed in [48,49,82] for thin-film ring lasers. This model, in turn, is based on the theory formulated for Fabry–Perot resonators that can be applied successfully to microring cavities [83].

The mode spacing $\Delta\lambda$ in Fabry–Perot or microring cavities is given by

$$\Delta\lambda = \frac{\lambda^2}{2nL} = \frac{\lambda^2}{\pi n D}, \tag{8.2}$$

where λ is the wavelength, n is the index of refraction, L is the length of the Fabry–Perot cavity, and D is the diameter of the ring. The quality factor Q of a Fabry–Perot resonator is given by:

$$Q = \frac{2\pi L}{\lambda}\frac{\sqrt{r}}{1-r}, \tag{8.3}$$

where r is the mirror reflectivity. In the case of a laser cavity with gain and loss, the effective value of r can be defined as $R\exp[(\gamma-\alpha)L]$ [73,84], where R is the actual mirror reflectivity, γ is gain per unit length, and α is loss per unit length. [At the laser threshold, when $r = 1$, Eq. (8.3) is no longer valid.] Alternatively, the Q-factor can be defined as

$$Q = \frac{\lambda}{\delta\lambda}, \tag{8.4}$$

where $\delta\lambda$ is the width of a longitudinal emission mode. If $\delta\lambda$ and r are known experimentally, the value nL can be calculated.

The Fourier transform (FT) of the emission spectrum gives a more accurate estimate of nL than the method described above. The Fourier transform consists of a series of equally spaced diminishing lines described by [85,49]:

$$I(d) = |1 - R\exp(2i\Phi)|^2 \sum_{m=0}^{\infty}\sum_{l=0}^{\infty} \frac{R^{l+m}\exp(-2i\Phi(l-m))}{kL(l+m+1)+i(\pi d + nL(l-m))}, \tag{8.5}$$

where k is the wavenumber; $k = 2\pi/\lambda$, d is the conjugate variable to wavevector; l, m are integers; and Φ is the phase change due to reflection from the mirrors. The peaks in the dependence $I(d)$ are produced whenever the imaginary part of the denominator goes to zero. This occurs when d is a multiple of nL/π in the case of a Fabry–Perot cavity or a multiple of $nD/2$ in the case of a circular geometry of a microring. In a simple case of small absorption and short wavelength range [86], the ratio of one Fourier transform peak to the next one is given by r. The experimentally determined value of r can then be substituted to Eq. (8.3) to calculate the value of the Q-factor.

In [49], the experimental samples were made by spin-casting of saturated DOO-PPV solutions in toluene to form approximately 1 μm thick films. The synthesized films were baked at 80°C in nitrogen atmosphere to evaporate the solvent. No

scatterers were intentionally added to the films. Inhomogeneities, for example, local density variations or dust particles, played the role of scattering centers. A frequency-doubled Nd:YAG laser with pulsewidth equal to 100 ps was used to pump the samples. The excitation beam was focused through a cylindrical lens exciting a narrow stripe on the film, approximately 250 μm $\times$ 2 cm. The emission spectrum was collected using a CCD and spectrometer with the overall resolution equal to 0.02 nm.

The spectrum of a coherent random laser emission in DOO-PPV film, characterized by a series of narrow lines on the top of a broader band, was qualitatively similar to those in Figure 8.12 and many other experiments [46,48,50,80,81] (Figure 8.14). This spectrum was reproducible at the fixed position of the pumped spot and the pumping energy and changed at small changes of the excitation intensity or the position of the pumped spot on the sample.

The emission spectrum was analyzed in terms of the Fourier transform discussed in the beginning of this section. The main frame of Figure 8.14 shows the absolute value of the Fourier transform of the emission spectrum depicted in the inset of the same figure. The first peak at $d = 0$ is not interesting in as much as it is merely due to the fact that all emission values are positive. The three dominant peaks in the

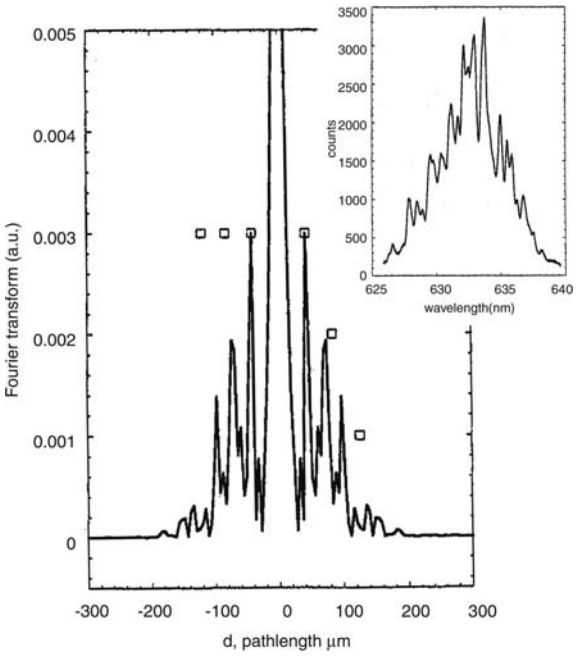

FIGURE 8.14. Main frame: Fourier transform of the DOO-film emission spectrum shown in inset. The square symbols indicate the main peak, twice the main peak, and three times the main peak. Inset: Emission spectrum from a thin film of DOO-PPV at the excitation energy of 2 μJ. (*Source*: Ref. [49].)

Fourier transform spectrum occur at 41, 74, and 97 μm. The discrete spacing of points in the Fourier transform is 4.5 μm. Thus, the second peak can be considered as a multiple of the first harmonic. At the same time, the third peak at 97 μm is not the third multiple of the first peak. If it is related to the resonance at 41 μm, it must be the third peak of a strongly anharmonic cavity. Alternatively, and possibly more likely, this peak corresponds to the first harmonic of some other cavity. The round-trip optical pathlengths of the two cavities in real space (equal to $2\pi D$) are $L = 260\,\mu\text{m}$ and $L = 610\,\mu\text{m}$, respectively. Both of these characteristic lengths are much larger than the film thickness 1 μm, which indicates the alignment of lasing modes in the plane of the film. According to the coherent backscattering measurements, the photon mean free path in the sample is equal to 15 μm. Thus, taking into account the index of refraction in the medium, $n = 1.7$, there are approximately $i = 10$ scattering events per loop in the short cavity and $i = 24$ scattering events per loop in the long cavity.

The value of r, discussed in the beginning of this section, has been evaluated from the analysis of the peak intensities in the Fourier transform spectrum. Substituting to the formula

$$r = R \exp[(\gamma - \alpha)L] \tag{8.6}$$

the values of r and L as well as the values of gain γ and loss α (determined in [49] under the same pumping in a similar film configured to form a microring laser cavity), the authors of [49] calculated the total effective reflectivity of all mirrors in the cavity to be equal to $R = 4.45 \times 10^{-3}$ for a short cavity and $R = 6.55 \times 10^{-7}$ for a long cavity. If the qualitative model of simple ring cavities is accepted (see inset of Figure 7.1a and relevant discussion in Chapter 7), then the reflection coefficient per one scattering center can be calculated as $R_{\text{single}} = R^{1/i}$. The values of R_{single} calculated this way for the short and the long loops were approximately the same, equal to 0.58 and 0.55, respectively.

Note that the model of lasing cavities, which are randomly formed in scattering polymer films, is, in some sense, relevant to the model of spatially localized stimulated emission modes found in ZnO and polymer random lasers in [17]. Surprising and not well understood in the experiments of [49] are (i) the extremely low values of reflectivity, which are still able to support coherent stimulated emission, and (ii) the fact that the contribution from the cavities of only two distinctly different sizes ($i = 10$ and $i = 24$) are seen in the emission spectrum. Note that in [48] only cavities with $i = 15$ and $i = 18$ contributed to the polymer random laser emission and in [45] stimulated emission was supported only by cavities with $i = 20$. In [87], the picture of ring cavities formed by scatterers, which are able to support stimulated emission, was argued to be unrealistic due to very strong scattering out of the loop.

8.3.4 Uniformity of Random Laser Cavities in Polymer Random Lasers

An alternative point of view and an explanation of the coherent stimulated emission in polymer random lasers have been presented in [79–81]. In these works,

the multiline emission spectra of DOO-PPV polymer random lasers have been experimentally obtained and their Fourier transforms have been analyzed.

As discussed in Section 8.3.3, spectral positions of narrow stimulated emission lines change when the pumped spot is moved along the sample. When several tens of emission spectra were averaged, the narrow lines in the spectra smeared out [79–81], producing a nearly featureless band, which was similar to that observed in an incoherent regime at lower pumping energy. At the same time, when the Fourier transforms of many individual emission spectra were averaged, their features did not disappear but, instead, became more obvious and pronounced. The positions of the peaks in the averaged Fourier transform spectra corresponded to only one or two characteristic cavity sizes. At the same time, tens of bright spots (presumably associated with individual localized modes or effective laser cavities) were seen in the near-field emission pattern.

In order to explain this seemingly paradoxical situation, it has been suggested [79–81] that all the resonators, which are responsible for lasing in polymer films, are approximately the same. The nature of such cavities and their uniformity has been described in terms of the model based on long-range fluctuations of the effective index of refraction, which is briefly discussed below. It has been proposed [81] that polymer thin films have thickness inhomogeneities, the shapes of which are circular in a first approximation (Figure 8.15). It has also been assumed that the characteristic (in-plane) linear size of such inhomogeneities is much larger than the photon mean free path l^* determined by scatterers, which, in turn, is much larger than the light wavelength λ. Because light is confined within the film due to waveguiding [42,81], the larger film thickness h leads to a higher in-plane wave vector of the light modes, that is, to higher effectiveness of refraction n_{eff} [81],

$$n_{\text{eff}} = \sqrt{n^2 - (p+1)^2 \left(\frac{\lambda}{2h}\right)}, \tag{8.7}$$

where n is the refraction index of the medium and p is the number of the transverse waveguide mode. By virtue of this mechanism, long-range fluctuations of h can facilitate the formation of microdisk-type resonators [79–81], the properties of which are known in the literature [88,89]. (According to the model presented in

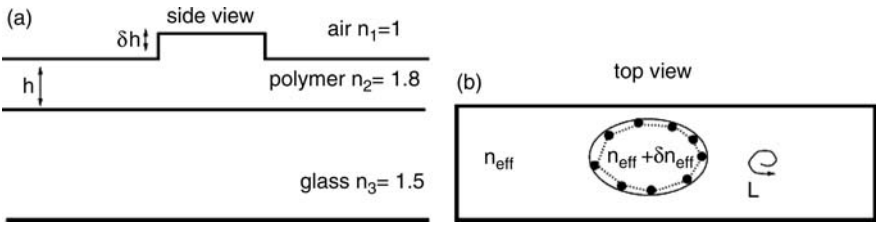

FIGURE 8.15. (a) Schematic illustration of the thickness fluctuation of the polymer film; the refractive indexes of the polymer and glass substrate are given. (b) Schematic illustration of the whispering-gallery-type mode in a resonator formed by a thickness variation δh; L is the round-trip resonator path length. (*Source*: Ref. [81].)

Ref. [87], nearly circular resonators in polymer random lasers can also be formed via correlated arrangements of scatterers.)

It has been argued [80,81] that although the stimulated emission in polymer random lasers and in ZnO random lasers have similar evolution and appearance, the underlying physical mechanisms of the two lasing processes are principally different. According to [81], although scatterers facilitate stimulated emission feedback in ZnO, they detract it in polymer films.

To explain the uniformity of sizes of unintentionally formed microdisk-type resonators, the following model was proposed [81]. For the lasing process to start, the gain in the cavity should exceed loss. For any given value of gain in the medium, there exists a minimum size of microdisk cavity L_γ below which the threshold cannot be reached. On the other hand, it has been argued that the formation of high-quality resonators with the size $L \gg l^*$ is very unlikely and the probability of their existence decreases exponentially with the increase of L due to short-range disorder (scattering). Thus, the size of the resonator is limited by the cut-off value L_γ on the lower end and by a steep exponential decay on the upper end. Thus, the resonator sizes are expected to have a very narrow distribution [79–81].

The other consequence of the effect of scatterers is that the most probable cavity size shortens with the increase of the concentration of scatterers and the positions of peaks in the Fourier transform of the emission spectrum scale with the mean free path l^*. To confirm this prediction, two similar polymer films have been fabricated in [81]: one nominally pure and another with TiO_2 particles. The averaged Fourier transform spectra of the both samples are plotted as functions of distance normalized to l^* in Figure 8.16. The good match of the peaks in the two Fourier transform spectra in Figure 8.16 can serve as proof of the validity of the developed model.

Note that the model developed in References [80,81] does not explain the observation of two (and only two) extremely different cavity sizes in the emission spectra of polymer random lasers, for example, 260 and 610 μm in [49], 56 and 216 μm in [81], and so on. In addition, the strikingly similar appearance of stimulated emission in polymer random lasers [46,79–81], opals infiltrated with dyes [45,73–75], liquid organic dyes [33,34], and ZnO polycrystalline films [33,90,91] calls for an explanation that is common to all these phenomena.

8.3.5 Coherent Polymer Random Lasers Based on PMMA Films Doped with Rhodamine 640 Dye and TiO_2 Particles

Random lasers based on Poly(methyl methacrylate) (PMMA) films doped with rhodamine 640 dye and TiO_2 scatterers were studied in [17,50]. Experimentally, concentrations of dye and scatterers in the samples were varied in a very wide range [50]. The thickness of the films was equal to approximately 150 μm in [50] and 0.5 to 1 mm in [17]. The samples were excited by 25 to 30 ps laser pulses at $\lambda = 532$ nm. The area of the pumped spot in the experiments was varied between approximately 0.002 mm^2 and 0.03 mm^2. The CBS technique was used to characterize the transport mean free path l_t in the system.

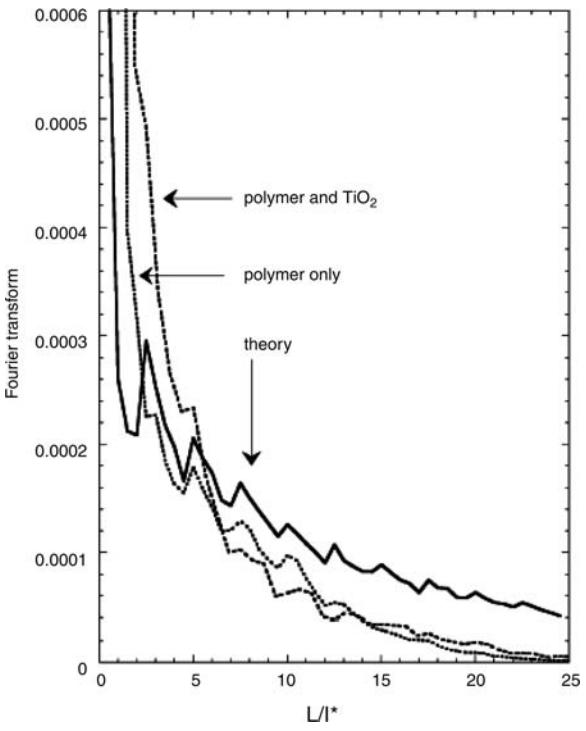

FIGURE 8.16. Average of 125 power Fourier transforms scaled by l^*. Dotted lines are the emission of pure polymer and polymer doped with TiO_2 scatterers, respectively. The solid line is the result of theoretical model developed in Ref. [80]. (*Source*: Ref. [81].)

The behavior of the PMMA-based polymer random laser was similar to that of many other coherent random lasers [17]. Thus, at low pumping intensity the emission spectrum had a single broad spontaneous emission peak. When the pumping energy exceeded a threshold, discrete narrow lines emerged in the emission spectrum. For each spectral peak, the emission intensity fluctuated randomly with the angle. It has been found that [50]:

1. The threshold pumping intensity I_{th} is proportional to the square root of the transport mean free path l_t. [The theoretical explanation of this result [50] was based on the assumption that the frequency spacing between modes in random lasers, characterized by diffusionlike motion of photons, should be larger than the mode linewidths. In Chapter 4, a similar result was derived from the balance of gain and loss in random lasers [92]. (Both theoretical predictions were done for absorbed pumping density. In the experiment of [50], absorbed pumping energy was not much different from incident pumping energy [93].)

2. The number of lasing modes in the emission spectrum increases with the reduction of the transport mean free path l_t. This increase is especially dramatic when l_t approaches the emission wavelength.

3. At constant transport mean free path l_t, the number of lasing modes increases with the increase of the pumping intensity I at relatively small values of I and saturates at high values of I. (The results (2) and (3) are in line with those of [94], where (a) the increase of the number of lasing modes with the increase of the pumping intensity, (b) the repulsion of lasing modes, (c) the saturation of the number of modes for a given size of the system, and (d) the relation between the localization length and the average mode length have been predicted by applying the FDTD computation technique and semi-classical laser model [95,96] to an inhomogeneous random medium.)

4. The threshold pumping intensity I_{th} decreases with the increase of the diameter of the pumped spot d (At $l_t = 0.9\,\mu\text{m}$, I_{th} was proportional to $d^{-1.18}$, and at $l_t = 9\,\mu\text{m}$, I_{th} was proportional to $d^{-1.5}$ [50].) This observation is in line with the results of [19], showing that in random lasers with photon diffusion, the threshold pumping density depends on the diameter of the pumped spot as $\propto 1/d^x + const$, where the value x can vary between 1 and 2, depending on the shape of the pumped volume, its vicinity to the surface of the scattering sample, and so on.

In [17], localized states of stimulated emission in PMMA thin-film random lasers have been examined using a spectrally resolved speckle technique. The method and the experimental setup (Figure 7.11 are discussed in Chapter 7. The spectral image of the emission from the PMMA polymer containing rhodamine 640 dye and TiO_2 particles is shown in Figure 8.17, and the corresponding amplitude of the spatial

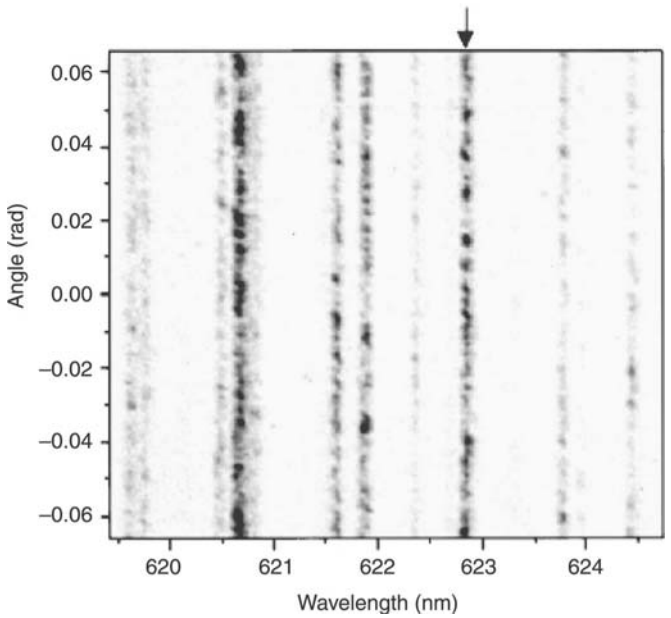

FIGURE 8.17. Fragment of spectrally resolved speckle pattern of emission of PMMA polymer doped with rhodamine 640 dye and TiO_2 particles. (*Source*: Ref. [17].)

field correlation function $lC(x)l$ for the laser line at $\lambda = 622.8\,\text{nm}$ is depicted in Figure 8.18. The emergence of a speckle pattern in the PMMA random laser was direct evidence of a coherent character of narrow-line stimulated emission [17]. It has been argued that the envelope of the spatial field correlation function directly reflects the wave function of a localized state. With the increase of the transport mean free path, the localized states were shown to shrink in size. This experimental observation was in agreement with the theoretical prediction made in [94]. It was finally concluded [17] that individual localized states exist in a random laser medium far from the localization threshold for the whole scattering sample.

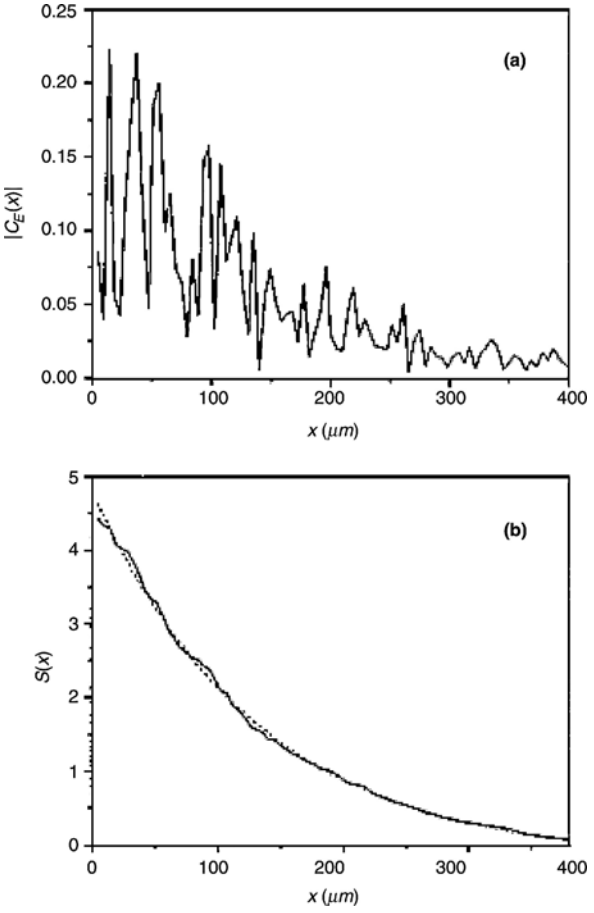

FIGURE 8.18. (a) The amplitude of the spatial field correlation function $|C(x)|$ for the lasing peak at $\lambda = 622.8\,\text{nm}$ in Figure 8.17 (marked by an arrow); (b) the solid line is $S(x)$ obtained by integrating $|C(x)|$ in (a). The dotted line represents the fit of $S(x)$ with an exponential decay function. (*Source*: Ref. [17].)

8.4 Other Random Lasers Based on Dyes and Polymers

Random lasers based on organic gain media are not limited to liquid solutions with scatterers and scattering polymers. Several other interesting realizations of organic random lasers are briefly described below.

Random laser emission from dye-treated animal tissues was observed in [97], where significant narrowing of the emission spectrum and shortening of the emission pulses were observed in optically pumped chicken tissue and pig fat samples treated with rhodamine 640 dye solution. The observed effects were attributed to mirrorless laser action in optically pumped tissue with gain and multiple scattering of emission.

In Reference [98], stimulated emission was obtained in human kidney and colon tissues infiltrated with dye. It has been found that malignant tissues show a much larger number of laser lines compared to healthy tissues taken from the same organ. Consequently, the typical random resonators were found to be different for healthy and cancerous tissues. Proposed potential applications of stimulated emission in (biomedical) tissues include optical imaging, and diagnostic and optotherapeutic treatment of tumors in humans [97,98].

In a number of publications, random laser emission was obtained in opal crystals infiltrated with solutions containing dyes or polymers [45,73–75]. Opals are porous three-dimensional arrays of silica spheres. The face-centered cubic (fcc) lattice of opals usually contains many defects [45]. The emission spectra of opals, which at strong pumping are characterized by a bandwidth narrowing followed by an appearance of narrow lines (modes) on the top of the emission spectrum, have a striking similarity to those of liquid random lasers or thin-film polymer random lasers [45]. However in opals, spectrally narrow lines (modes) of stimulated emission can be observed at the mean free path l^* equal to several hundred wavelengths, ten times longer than those in liquid dyes with scatterers or polymer films demonstrating the same type of behavior.

In Reference [99], porous sintered glass was infiltrated with laser dye dissolved in a liquid crystal. Random laser action was evident as a strong narrowing of the emission spectrum and an abrupt increase of the emission intensity above some critical threshold value. Liquid crystals go through partially ordered phases when heated. Different phases have different indexes of refraction. Thus, when a random laser matrix (sintered glass) is infiltrated with liquid crystal, its diffusion becomes strongly temperature-dependent. Correspondingly, the quality factors of effective cavities formed by scatterers become temperature-dependent too. In [99], this effect was used to switch the random laser emission on and off by changing the temperature. The details of this effect were studied experimentally and theoretically in [100–102]. A random laser effect in a disordered system, in which the multiple scattering feedback mechanism can be switched from a 3D random walk to a quasi-2D type of transport by applying an electric field, is reported in Reference [103]. The phenomenon is observed in dye-doped polymer dispersed liquid crystals and makes use of the strong scattering anisotropies in these materials.

In Reference [104], laser effect has been demonstrated in a stack of glass slides (of slightly varying thickness) with rhodamine 6G dye embedded between the glass slices. Stimulated emission in Reference [104] was supported by long-lived *localized* modes overlapping the localized gain region. Laser emission in a stack of glass slides has been also proposed and theoretically analyzed in Reference [105].

Microlasers based on microspheres, microdisks, or microrings containing dye or polymer have been studied in many publications; see for example, References [47,82,106–113]. The spectra of such lasers are dominated by a periodic series of morphology-dependent resonance lines. The pattern becomes more complicated when an inhomogeneous gain medium with its own resonance frequencies is placed inside a cavity. In [114–116], the emission from submillimeter-sized cylindrical cavities (tubes) filled with solutions of nanostructured fractal aggregate of silver nanoparticles [117–119] and rhodamine 6G dye has been studied. In fractal aggregates, optical excitations are concentrated in regions smaller than the diffraction limit of conventional optics, resulting in strong enhancements of optical fields. Placing an aggregate into a microcavity can further increase the optical fields because of interaction of aggregate modes with cavity resonance modes. As demonstrated in [114–116], this enhancement can result in multiple-mode lasing of dye (with line strengths and line frequencies not fitting any simple pattern) at very low pumping intensity.

As it has been shown in recent Reference [120], the localized surface plasmon resonance of nanostructures exhibits a singularity when surrounded by amplifying medium with critical value of gain. The singularity in enhancement occurs because gain of the amplifying medium can compensate losses in surface plasmons. In this case, the enhancement can be truly gigantic and it is limited only by saturation effects in the amplifying medium. Such composite medium should exhibit strong scattering, leading to light localization effects and low-threshold random laser action. Note that the scattering in such a system will be high in the emission band and low in the absorption band. These are the ideal conditions for the low threshold and high-slope efficiency of random laser because of highly efficient utilization of the pumping energy, low reflection of pumping, and strong feedback at the stimulated emission wavelength [103].

References

1. N.M. Lawandy, A.S.L. Gomes, and R.M. Balachandran, presented at the 1993 International Conference of Luminescence, University of Connecticut, Storrs, CT (1993).
2. N.M. Lawandy, R.M. Balachandran, A.S.L. Gomes, and E. Sauvain, Laser action in strongly scattering medium, *Nature*, **368**: 436–438 (1994).
3. V.M. Markushev, V.F. Zolin, and Ch.M. Briskina, Luminescence and stimulated emission of neodymium in sodium lanthanum molybdate powders, *Sov. J. Quantum Electron.*, **16**: 281–283 (1986).
4. V.M. Markushev, N.È. Ter-Gabriélyan, Ch.M. Briskina, V.R. Belan, and V.F. Zolin, Stimulated emission kinetics of neodymium powder lasers, *Sov. J. Quantum Electron.*, **20**: 772–777 (1990).

5. C. Gouedard, D. Husson, C. Sauteret, F. Auzel, and A. Migus, Generation of spatially incoherent short pulses in laser-pumped neodymium stoichiometic crystals and powders, *J. Opt. Soc. Am. B*, **10**: 2358–2363 (1993).
6. V.S. Letokhov, Stimulated emission of an ensemble of scattering particles with negative absorption, [*ZhETP Pis'ma* **5**: 262–265 (1967) Russian]. *JETP Lett.*, **5**: 212–215, (1967).
7. V.S. Letokhov, Quantum statistics of multi-mode radiation from an ensemble of atoms, [*Zh. Eksp. i Teor. Fiz.*, **53**: 2210–2222 (1967) Russian] *Sov. Phys. JETP*, **26**: 1246–1251 (1968).
8. D.S. Wiersma, M.P. van Albada, and A. Lagendijk, Random laser? *Nature* **373**: 203–204 (1995).
9. V.S. Letokhov, Stimulated radio emission of the interstellar medium, [*Pis'ma Zh. Eksp. i Teor. Fiz.*, **4**: 477–481 (1966) Russian] *JETP Lett.*, **4**: 321–323 (1966).
10. R.V. Ambartsumyan, N.G. Basov, P.G. Kryukov, and V.S. Letokhov, Non-resonant feedback in lasers. In *Progress in Quantum Electronic*, Vol. **1**, J.H. Sanders and K.W.H. Stevens, eds., Pergamon: New York, 107 (1970).
11. V.S. Letokhov, Noncoherent feedback in space masers and stellar lasers, in *Amazing Light, A Volume Dedicated to Charles Hard Townes on his 80th Birthday*, R.Y. Chiao, ed., Springer-Verlag: New York (1996), p. 409.
12. W.L. Sha, C.-H. Liu, and R.R. Alfano, Spectral and temporal measurements of laser action of rhodamine 640 dye in strongly scattering media, *Opt. Lett.*, **19**: 1922–1924 (1994).
13. M.A. Noginov, N.E. Noginova, H.J. Caulfield, P. Venkateswarlu, and M. Mahdi, Line narrowing in the dye solution with scattering centers, *Opt. Commun.*, **118**: 430–437 (1995).
14. G. van Soest, M. Tomita, and A. Lagendijk, Amplifying volume in scattering media, *Opt. Lett.*, **24**: 306–308 (1999).
15. H. Cao, Y.G. Zhao, H.C. Ong, S.T. Ho, J.Y. Dai, J.Y. Wu, and R.P.H. Chang, Ultraviolet lasing in resonators formed by scattering in semiconducor polycrystalline films, *Appl. Phys. Lett.*, **73**: 3656–3658 (1998).
16. H. Cao, Y.G. Zhao, S.T. Ho, E.W. Seelig, Q.H, Wang, and R.P.H. Chang, Random laser action in semiconductor powder, *Phys. Rev. Lett.*, **82**: 2278–2281 (1999).
17. H. Cao, Y. Ling, J.Y. Xu, and A.L. Burin, Probing localized states with spectrally resolved speckle techniques, *Phys. Rev. E*, **66**: 025601 (2002).
18. M. Bahoura, K.J. Morris, and M.A. Noginov, Threshold and slope efficiency of $Nd_{0.5}La_{0.5}Al_3(BO_3)_4$ ceramic random laser: Effect of the pumped spot size, *Opt. Commun.*, **201**: 405–412 (2002).
19. M. Bahoura, K.J. Morris, G. Zhu, and M.A. Noginov, Dependence of the neodymium random laser threshold on the diameter of the pumped spot, *IEEE Journal of Quantum Electronics*, to be published.
20. G. Beckering, S.J. Zilker, and D. Haarer, Spectral measurements of the emission from highly scattering gain media, *Opt. Lett.*, **22**: 1427–1429 (1997).
21. R.M. Balachandran and N.M. Lawandy, Interface reflection effects in photonic paint, *Opt. Lett.*, **20**: 1271–1273 (1995).
22. R.M. Balachandran and N.M. Lavandy, Understanding bichromatic emission from scattering gain media, *Opt. Lett.*, **21**: 1603–1605 (1996).
23. R.M. Balachandran, N.M. Lawandy, and J.A. Moon, Theory of laser action in scattering gain medium, *Opt. Lett.*, **22**: 319–321 (1997).

24. W.L. Sha, C.-H. Liu, F. Liu, and R.R. Alfano, Competition between two laser modes of sulforhodamine 640 in highly scattering media, *Opt. Lett.*, **21**: 1277–1279 (1996).
25. M. Siddique, R.R. Alfano, G.A. Berger, M. Kempe, and A.Z. Genack, Time-resolved studies of stimulated emission from colloidal dye solutions, *Opt. Lett.*, **21**: 450–452 (1996).
26. G.A. Berger, M. Kempe, and A.Z. Genack, Dynamics of stimulated emission from random media, *Phys. Rev. E*, **56**: 6118–6122 (1997).
27. M. Kempe, G.A. Berger, and A.Z. Genack, Stimulated emission from amplifying random media. In *Handbook of Optical Properties*, Vol. II, R.E. Hummel and P. Wißmann, eds. CRC: Boca Raton, FL (1996).
28. S. John and G. Pang, Theory of lasing in a multiple-scattering medium, *Phys. Rev. A*, **54**: 3642–3652 (1996).
29. K. Totsuka, G. van Soest, T. Ito, A. Lagendijk, and M. Tomita, Amplification and diffusion of spontaneous emission in strongly scattering medium, *J. Appl. Phys.*, **87**: 7623–7628 (2000).
30. D.S. Wiersma and A. Lagendijk, Light diffusion with gain and random lasers, *Phys. Rev. E*, **54**: 4256–4265 (1996).
31. G. van Soest, F.J. Poelwijk, R. Sprik, and A. Lagendijk, Dynamics of a random laser above threshold, *Phys. Rev. Lett.*, **86**: 1522–1525 (2001).
32. J. Herrmann and B. Wilhelmi, Mirrorless laser action by randomly distributed feedback in amplifying disordered media with scattering centers, *Appl. Phys. B*, **66**: 305–312 (1998).
33. H. Cao, Random lasers with coherent feedback. In *Optical Properties of Nanostructured Random Media*, V.M. Shalaev, ed., Springer: New York (2002).
34. H. Cao, J.Y. Xu, S.-H. Chang, and S.T. Ho, Transition from amplified spontaneous emission to laser action in strongly scattering medium, *Phys. Rev. E*, **61**: 1985–1989 (2000).
35. S. Mujumdar, M. Ricci, R. Torre, D. Wiersma, Amplified path length modes in random lasers, *Phys. Rev. Lett.*, **93**: 053903/1–4 (2004).
36. R.M. Balachandran, A. Pacheco, and N.M. Lawandy, Photonic textile fibers. In *Conference on Lasers and Electro-Optics*, Vol. 15, 1995 OSA Technical Digest Series, Optical Society of America: Washington, DC (1995), pp. 114–115.
37. S. Larochelle, P. Mathieu, V. Larochelle, and J. Dubois, Long range interrogation of laser paints for identification applications. In *Conference on Lasers and Electro-Optics*, Vol. 11, 1997 OSA Technical Digest Series, Optical Society of America: Washington, DC (1997), p. 143.
38. D. Braun and A.J. Heeger, Visible light emission from semiconducting polymer diodes, *Appl. Phys. Lett.*, **58**: 1982–1984 (1991).
39. R.H. Friend, R.W. Gymer, A.B. Holmes, J.H. Burroughes, R.N. Marks, C. Taliani, D.D.C. Bradley, D.A. Dos Santos, J.L. Brédas, M. Lögdlung, and W.R. Salaneck, Electroluminescence in conjugated polymers, *Nature*, **397**: 121–128 (1999).
40. F. Hide, B.J. Schwartz, M.A. Diaz-Garsia, and A.J. Heeger, Laser emission from solutions and films containing semiconducting polymer and titanium dioxide nanocrystals, *Chem. Phys. Lett.*, **256**: 424–430 (1996).
41. F. Hide, M.A. Días-García, B.J. Schwartz, and A.J. Heeger, New developments in the photonic applications of conjugated polymers, *Acc. Chem. Res.*, **30**: 430–436 (1997).

42. F. Hide, B.J. Schwartz, M.A. Días-García, and A.J. Heeger, Conjugated polymers as solid-state laser materials, *Synth. Metals*, **91**: 35–40 (1997).
43. S.V. Frolov, M. Ozaki, W. Gellerman, Z.V. Vardeny, and K. Yoshino, Mirrorless lasing in conducting polymer poly(2,5-dioctyloxy-pphenylevinylene) films, *Jpn. J. Appl. Phys., Part 2*, **35**: L1371–L1371 (1996).
44. C.W. Lee, K.S. Wong, J.D. Huang, S.V. Frolov, and Z.V. Vardeny, Femtosecond time-resolved laser action in poly(*p*-phenylene vinylene) films: Stimulated emission in an inhomogeneously broadened exciton distribution, *Chem. Phys. Lett.*, **314**: 564–569 (1999).
45. R.C. Polson, A. Chipoline, and Z.V. Vardeny, Random lasing in π-conjugated films and infiltrated opals, *Adv. Mater.*, **13**: 760–764 (2001).
46. S.V. Frolov, Z.V. Vardeny, K. Yoshino, A. Zakhidov, and R.H. Baughman, Stimulated emission in high-gain organic media, *Phys. Rev. B*, **59**: R5284–R5287 (1999).
47. S.V. Frolov, M. Shkunov, A. Fujii, K. Yoshino, and Z.V. Vardeny, Lasing and stimulated emission in π-conjugated polymers, *IEEE J. Quantum Electron.*, **36**: 2–11 (2000).
48. R.C. Polson, J.D. Huang, and Z.V. Vardeny, Random lasers in π-conjugated polymer films, *Synth. Metals*, **119**: 7–12 (2001).
49. R.C. Polson, J.D. Huang, and Z.V. Vardeny, Analysis of random lasers in thin films of π-conjugated polymers. In *Photonic Crystals and Light Localization in the 21st Century*, C.M. Soukoulis, ed., Kluwer: Dordrecht, The Netherlands (2001).
50. Y. Ling, H. Cao, A.L. Burin, M.A. Ratner, X. Liu, and R.P.H. Chang, Investigation of random lasers with resonant feedback, *Phys. Rev. A*, **64**: 063808 (2001).
51. F. Hide, M.A. Días-García, B.J. Schwartz, M.R. Andersson, Q. Pei, and A.J. Heeger, Semiconducting polymers: A new class of solid-state laser materials, *Science*, **273**: 1833–1836 (1996).
52. M.A. Días-García, F. Hide, B.J. Schwartz, M.R. Andersson, A.J. Heeger, and Q. Pei, Plastic lasers: Semiconducting polymers as a new class of solid-state laser materials, *Synth. Metals*, **84**: 455–462 (1997).
53. H.J. Brouwer, V.V. Krasnikov, A. Hilberer, and G. Hadziioannou, Blue superradiance from neat semiconducting alternating copolymer films, *Adv. Mater.*, **8**: 935–940 (1996).
54. G. Gelink, J.W. Warman, M. Remmers, and D. Neher, Narrow band emission in conjugated polymer films, *Chem. Phys. Lett.*, **265**: 320–326 (1997).
55. X. Long, A. Malinowski, D.D.C. Bradley, M. Inbasekaran, and E.P. Woo, Emission processes in conjugated polymer solutions and thin films, *Chem. Phys. Lett.*, **272**: 6–12 (1997).
56. N. Tessler, G.J. Denton, and R.H. Friend, Lasing from conjugated-polymer microcavities, *Nature*, **382**: 695–697 (1996).
57. M.A. Días-García, F. Hide, B.J. Schwartz, M.D. McGehee, M.R. Andersson, and A.J. Heeger, "Plastic" lasers: Comparison of gain narrowing with a soluble semiconducting polymer in waveguides and microcavities, *Appl. Phys. Lett.*, **70**: 3191–3193 (1997).
58. C. Zenz, W. Graupner, S. Tasch, G. Leising, K. Müllen, and U. Scherf, Blue green stimulated emission from a high gain conjugated polymer, *Appl. Phys. Lett.*, **71**: 2566–2568 (1997).
59. S.V. Frolov, M. Shkunov, K. Yoshino, and Z.V. Vardeny, Ring microlasers from conjugated polymers, *Phys. Rev. B*, **56**: R4363-R4366 (1997).

60. S.V. Frolov, Z.V. Vardeny, and K. Yoshino, Cooperative and stimulated emission in poly(p-phenylene-vinylene) thin films and solutions, *Phys. Rev. B*, **57**: 9141–9147 (1998).
61. B.J. Schwartz, F. Hide, M.R. Andersson, and A.J. Heeger, Ultrafast studies of stimulated emission in solid films of conjugated polymers, *Chem. Phys. Lett.*, **265**: 327–333 (1996).
62. S.V. Frolov, W. Gellermann, M. Ozaki, K. Yoshino, and Z.V. Vardeny, Cooperative emission in π-conjugated polymer thin films, *Phys. Rev. Lett.*, **78**: 729–732 (1997).
63. C. Liu, J. Liu, J. Zhang, and K. Dou, Random lasing with scatterers of diameters 20 nm in an active medium, *Optics Communications*, **244**: 299–303 (2005).
64. K.S. Wong, H. Wang, and G. Lanzani, Ultrafast excited-state planarization of the hexamethylsexithiophene oligomer studied by femtosecond time-resolved photoluminescence, *Chem. Phys. Lett.*, **288**: 59–64 (1998).
65. O. Svelto, *Principles of Lasers*, 4th ed., D.C. Hanna, trans. and ed., Plenum: New York (1998).
66. A. Yariv, *Quantum Electronics*, 3d ed., Wiley: New York (1989).
67. W. Koechner, *Solid-State Laser Engineering*, 5th rev. updated ed., Springer-Verlag: New York (1999).
68. V.M. Markushev, N.È. Ter-Gabriélyan, Ch.M. Briskina, V.R. Belan, and V.F. Zolin, Stimulated emission kinetics of neodymium powder lasers, *Sov. J. Quantum Electron.*, **20**: 772–777 (1990).
69. C. Gouedard, D. Husson, C. Sauteret, F. Auzel, and A. Migus, Generation of spatially incoherent short pulses in laser-pumped neodymium stoichiometic crystals and powders, *J. Opt. Soc. Am. B*, **10**: 2358–2363 (1993).
70. M.A. Noginov, N.E. Noginova, H.J. Caulfield, P. Venkateswarlu, T. Thompson, M. Mahdi, and V. Ostroumov, Short-pulsed stimulated emission in the powders of $NdAl_3(BO_3)_4$, $NdSc_3(BO_3)_4$, and $Nd{:}Sr_5(PO_4)_3F$ laser crystals, *J. Opt. Soc. Am. B*, **13**: 2024–2033 (1996).
71. C.M. Soukoulis, X. Jiang, J.Y. Xu, and H. Cao, Dynamic response and relaxation oscillations in random lasers, *Phys. Rev. B*, **65**: 041103 (2002).
72. M.A. Noginov, J. Novak, and S. Williams, Modeling of photon density dynamics in random lasers, *Phys. Rev. A*, **70**: 063810 (2004) (5 pages).
73. S.V. Frolov, Z.V. Vardeny, A.A. Zakhidov, and R.H. Baughman, Laser-like emission in opal photonic crystals, *Opt. Commun.*, **162**: 241–246 (1999).
74. K. Yoshiko, S. Tatsuhara, Y. Kawagishi, M. Ozaki, A. Zakhidov, and Z.V. Vardeny, Amplified spontaneous emission and lasing in conducting polymers and fluorescent dyes in opals as photonic crystals, *Appl. Phys. Lett.*, **74**: 2590–2592 (1999).
75. M.N. Shkunov, Z.V. Vardeny, M.C. DeLong, R.C. Polson, A.A. Zakhidov, and R.H. Baughman, Tunable, gap-state lasing in switchable directions for opal photonic crystals, *Adv. Function. Mater.*, **12**: 21–26 (2002).
76. G. Zacharakis, N.A. Papadogiannis, G. Filippidis, and Th.G. Papazoglou, Photon statistics of laser-like emission from polymeric scattering gain media, *Opt. Lett.*, **25**: 923–925 (2000).
77. J.W. Goodman, *Statistical Optics*, Wiley: New York (2000).
78. R. Loudon, *The Quantum Theory of Light*, 2d ed., Oxford University Press: Oxford (1983).
79. R.C. Polson, M.E. Raikh, and Z.V. Vardeny, Universal properties of random lasers, *IEEE J. Select. Topics Quantum Electron.*, **9**: 120–123 (2003).

80. R.C. Polson, M.E. Raikh, and Z.V. Vardeny, Random lasing from weakly scattering media: Spectrum universality in DOO-PPV polymer films, *Physica E*, **13**: 120–1242 (2002).
81. R.C. Polson, M.E. Raikh, and Z.V. Vardeny, Universality in unintentional laser resonators in p-conjugated polymer films, *C.R. Physique*, **3**: 509–521 (2002).
82. R.C. Polson, G. Levina, and Z.V. Vardeny, Spectral analysis of polymer microring lasers, *Appl. Phys. Lett.*, **76**: 3858–3860 (2000).
83. H.P. Weber and R. Ulrich, A thin-film ring laser, *Appl. Phys. Lett.*, **19**: 38–40 (1971).
84. N.V. Karlov, *Lectures in Quantum Electronics*, CRC: Boca Raton, FL (1993).
85. D. Hofstetter and R.L. Thornton, Loss measurements on semiconductor lasers by Fourier analysis of the emission spectra, *Appl. Phys. Lett.*, **72**: 404–406 (1998).
86. D. Hofstetter and R.L. Thornton, Theory of loss measurements of Fabry–Perot resonators by Fourier analysis of the transmission spectra, *Opt. Lett.*, **22**: 1831–1833 (1997).
87. V.M. Apalkov, M.E. Raikh, and B. Shapiro, Random resonators and prelocalized modes in disordered dielectric films, *Phys. Rev. Lett.*, **89**: 016802 (2002).
88. Y. Yamamoto and R.E. Slusher, Optical processes in microcavities, *Phys. Today*, 66–73 (June 1993).
89. C. Gmachl, F. Capasso, E.E. Narimanov, J.U. Nöckel, A.D. Stone, J. Faist, D.L. Sivko, and A.Y. Cho, High-power directional emission from microlasers with chaotic resonators, *Science*, **280**: 1556–1564 (1998).
90. H. Cao, J.Y. Xu, Y. Ling, S.-H. Chang, S.T. Ho, E.W. Seelig, X. Liu, and R.P.H. Chang, Random lasers with coherent feedback, *Photonic Crystals and Light Localization in the 21st Century*, C.M. Soukoulis, ed., Kluwer: Dordrecht, The Netherlands (2001).
91. H. Cao, Y. Xu, Y. Ling, A.L. Burin, E.W. Seeling, X. Liu, and R.H.P. Chang, Random lasers with coherent feedback, *IEEE J. Quantum Electron.*, **9**: 111–119 (2003).
92. M.A. Noginov, G. Zhu, A.A. Frantz, J. Novak, S.N. Williams, and I. Fowlkes, Dependence of $NdSc_3(BO_3)_4$ random laser parameters on particle size, *JOSA B*, **21**: 191–200 (2004).
93. A.L. Burin, private communication.
94. X. Jiang and C.M. Soukoulis, Time-dependent theory for random lasers, *Phys. Rev. Lett.*, **85**: 70–73 (2000).
95. A.E. Siegman, *Lasers*, University Science Books: Mill Valley, CA (1986), Chapters 2,3,6,13.
96. A. Maitland and H.M. Dunn, *Laser Physics*, North-Holland: Amsterdam (1969), Chapter 9.
97. M. Siddique, L. Yang, Q.Z. Wang, and R.R. Alfano, Mirrorless action from optically pumped dye-treated animal tissues, *Opt. Commun.*, **117**: 475–479 (1995).
98. R.C. Polson and Z.V. Vardeny, Random lasing in human tissues, *Applied Physics Letters*, **85**: 1289–1291 (2004).
99. D.S. Wiersma and S. Cavalierit, Light emission: A temperature-tunable random laser, *Nature*, **414**: 708–709 (2001).
100. D.S. Wiersma, M. Colocci, R. Righini, and F. Aliev, Temperature-controlled light diffusion in random media, *Phys. Rev. B*, **64**: 144208/1–6 (2001).
101. D.S. Wiersma and S. Cavalieri, Temperature-controlled random laser action in liquid crystal infiltrated systems, *Phys. Rev. E*, **66**: 56612/1–5 (2002).
102. S. Cavalieri and D.S. Wiersma, Temperature-tunable random lasing: Numerical calculations and experiments, *JOSA B*, **21**: 201–207 (2004).

103. S. Gottardo, S. Cavalieri, O. Yaroshchuk, and D.S. Wiersma, Quasi-two-dimensional diffusive random laser action, *Phys. Rev. Lett.*, **93**: 263901/1–4 (2004).
104. V. Milner and A.Z. Genack, Photon localization laser, *Phys. Rev. Lett.*, to be published; A.Z. Genack and V. Milner, Photon localization laser, Presented at the SPIE 49th Annual Meeting, 2–4 August, 2004, Denver, CO, paper #5508-32.
105. Y. Feng and K. Ueda, Random stack of resonant dielectric layers as a laser system, *Optics Express*, **12**: #15 (2004).
106. H.-M. Tzeng, K.F. Wall, M.B. Long, and R.K. Chang, Laser emission from individual droplets at wavelengths corresponding to morphology-dependent resonances, *Opt. Lett.*, **9**: 499–501 (1984).
107. H.-B. Lin, A.L. Huston, B.L. Justus, and A.L. Campillo, Some characteristics of a droplet whispering-gallery-mode laser, *Opt. Lett.*, **11**: 614–616 (1986).
108. A. Biswas, H. Latifi, R.L. Armstrong, and R.G. Pinnick, Time-resolved spectroscopy of laser emission from dye-doped droplets, *Opt. Lett.*, **14**: 214–216 (1989).
109. H. Latifi, A. Biswas, R.L. Armstrong, and R.G. Pinnick, Lasing and stimulated Raman scattering in spherical liquid droplets: Time, irradiance, and wavelength dependence, *Appl. Opt.*, **29**: 5387–5392 (1990).
110. A.J. Campillo, J.D. Eversole, and H.-B. Lin, Cavity electrodynamic enhancement of stimulated emission in microdroplets, *Phys. Rev. Lett.*, **67**: 437–440 (1991).
111. R.L. Armstrong, J.-G. Xie, T.E. Ruekgauer, and R.G. Pinnick, Energy-transfer-assisted lasing from microdroplets seeded with fluorescent sol, *Opt. Lett.*, **17**: 943–945 (2002).
112. R.L. Armstrong, J.-C. Xe, T.E. Ruckgauer, J. Gu, R.G. Pinnick, Effect of submicrometer-sized particles on microdroplet lasing, *Opt. Lett.*, **18**: 119–121 (1993).
113. R.C. Polson and Z.V. Vardeny, Multiple resonances in microdisc lasers of π-conjugated polymers, *Appl. Phys. Lett.*, **81**: 1561–1563 (2002).
114. W. Kim, V.P. Safonov, V.M. Shalaev, and R.L. Armstrong, Fractals in microcavities: Giant coupled, multiplicative enhancement of optical resonances, *Phys. Rev. Lett.*, **82**: 4811–4814 (1999).
115. W.T. Kim, V.P. Safonov, V.P. Drachev, V.A. Podolskiy, V.M. Shalaev, and R.L. Armstrong, Fractal-microcavity composites: Giant optical responses. In *Optical Properties of Nanostructured Random Media*, V.M. Shalaev, ed., Springer: New York (2002).
116. V.P. Drachev, W.-T. Kim, V.P. Safonov, V.A. Podolskiy, N.S. Zakovryashin, E.N. Khaliullin, V.M. Shalaev, and R.L. Armstrong, Low-threshold lasing and broad-band multiphoton-excited light emission from Ag aggregate-adsorbate complexes in microcavity, *J. Mod. Opt.*, **49**: 645–662 (2002).
117. V.M. Shalaev, *Nonlinear Optics of Random Media: Fractal Composites and Metal-Dielectric Films*, Springer: New York (2000).
118. V.M. Shalaev, Optical nonlinearities of fractal composites. In *Optical Properties of Nanostructured Random Media*, V.M. Shalaev, ed., Springer: New York (2002).
119. V.P. Drachev, S.P. Perminov, S.G. Rautian, and V.P. Safonov, Nonlinear optical effects and selective photomodification of colloidal silver aggregates. In *Optical Properties of Nanostructured Random Media*, V.M. Shalaev, ed., Springer: New York (2002).
120. N.M. Lawandy, Localized surface plasmon singularities in amplifying media, *Appl. Phys. Lett.*, **85**: 5040–5042 (2004).

9
Other Types of Solid-State Random Lasers

9.1 Praseodymium-Doped Oxisulfide Powder Lasers

Laserlike emission in powders of praseodymium-doped oxisulfides of yttrium, lanthanum, and gadolinium has been reported in References [1,2] under laser pumping (at different wavelengths) and electron beam pumping. The concentration of praseodymium was varied in different experiments between $10^{20}\,\mathrm{cm}^{-3}$ and $10^{21}\,\mathrm{cm}^{-3}$. When the pumping density exceeded its threshold value (which was smaller than in the neodymium random laser, Chapter 2), one of the emission lines strongly increased in comparison with the other spectral lines, its width reduced to 1 Å, and the emission pulsewidth shortened to 8 to 20 ns. This experimental behavior, similar to that in neodymium random lasers [3,4], was explained in terms of stimulated emission.

The stimulated emission wavelength in La_2O_5S-Pr_2O_5S powder was equal to 758.7 nm and that in Y_2O_2S-Pr_2O_2S powder was equal to 768 nm [1]. Both wavelengths were assigned to the Pr^{3+} transition $^3P_0$–$^3F_4$. These wavelengths and the transition were different from those in a Pr:δ-alumina random laser pumped with an electron beam, $\lambda \approx 0.63\,\mu\mathrm{m}$ and $^3P_0$-$^3H_6$, respectively [5].

It was found that the threshold of stimulated emission depended strongly on the particle size, the number of layers of particles in the sample (which provided for the feedback), and the index of refraction. The model explaining the effect, analogous to that in [4], was based on the concept of coupled resonators supported by reflections off microcrystalline facets.

9.2 Ti-Sapphire Random Laser

9.2.1 Experimental Observation of Stimulated Emission in Ti-Sapphire Powder

Stimulated emission in Ti-sapphire powder was obtained in [6]. The two powder samples studied had Ti concentrations equal to 0.1 and 0.2 at.%, which was higher

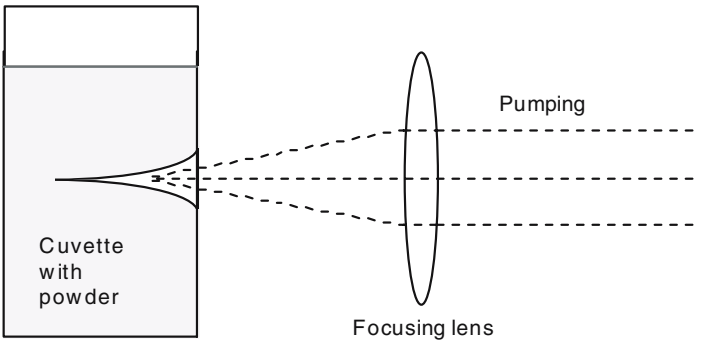

FIGURE 9.1. The channel in the powder volume "drilled" by the pumping laser beam. (*Source*: Ref. [6].)

than in regular Ti-sapphire laser elements.[1] The Ti-sapphire crystals were ground (with the use of a mortar and pestle) to a powder characterized by the mean particle size $\approx 3\,\mu$m. The powder samples were loaded into glass cuvettes and excited with a second-harmonic Q-switched Nd:YAG laser.

Because the absolute output efficiency of stimulated emission in high-density $Nd_{0.5}La_{0.5}Al_3(BO_3)_4$ samples was higher than that in low-density samples (see Section 2), the experiments with Ti-sapphire were started with strongly compressed powders [6]. However, in high-density Ti-sapphire powders, stimulated emission could not be obtained below the damage threshold of the glass wall of the cuvette. Surprisingly, laserlike emission characterized by short pulses and substantial narrowing of the emission spectrum, with the maximum at $\lambda \approx 800$ nm, was relatively easily obtained in a low-density sample, where a focused pumping beam, pushing particles out of its way, "drilled" a narrow channel in the powder volume [6]. (Note that the effect of channel formation was of purely mechanical nature, due to light pressure applied to powder particles. At the pumping densities used in the experiment, no burning, chemical decomposition, melting, or evaporation of the crystalline material was observed.) The diameter of the channel was of the order of 1 mm at the front surface of the cuvette and strongly reduced, down to $\sim 100\,\mu$m, at the depth of 3 to 5 mm (Figure 9.1).

According to Figure 9.2a, showing stimulated emission in Ti-sapphire powder in response to n_1^{th}, n_2^{th}, n_3^{th} ($n_3 > n_2 > n_1$) pumping pulses, which created and continuously increased the hole in the volume of Ti-sapphire powder, the formation of a narrow channel was advantageous for the stimulated emission in this material. (There was not much difference between stimulated emission in 0.1% doped and 0.2% doped Ti-sapphire samples.)

It is interesting to note that the experiment with $Nd_{0.5}La_{0.5}Al_3(BO_3)_4$ powder (3.5 μm mean particle size) demonstrated an opposite behavior: the creation of

[1]The Ti-sapphire crystals were grown by Milan R. Kokta, who was at that time with the Union Carbide Corporation.

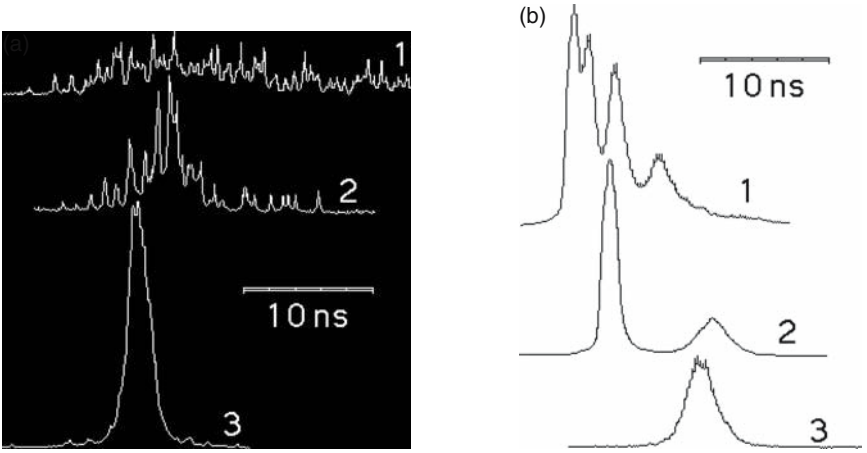

FIGURE 9.2. (a) Evolution of stimulated emission pulses in 0.2% doped Ti-sapphire powder. Traces 1–3 demonstrate the development of stimulated emission pulses along with the increase of the pumping pulse number and the size of the channel. (b) Evolution of stimulated emission pulses in $Nd_{0.5}La_{0.5}Al_3(BO_3)_4$ powder. Traces 1–3 demonstrate the degradation of stimulated emission along with the increase of the pumping pulse number and the size of the channel. At typical pumping energies used in the experiment, traces 1,2,3 corresponded to approximately the third, eighth, and twentieth pulse in the series. The intensity scale is different for different traces. (*Source*: Ref. [6].)

a channel in a powder caused a reduction of the stimulated emission efficiency (Figure 9.2b).

9.2.2 Qualitative Explanation of the Influence of a Channel Formation on Stimulated Emission in Powders

The difference in behavior of Ti-sapphire and $Nd_{0.5}La_{0.5}Al_3(BO_3)_4$ random lasers was explained in terms of the photon absorption and scattering in a gain medium [6].

1. When absorption in powder is weak and scattering is strong (as in the case of Ti-sapphire), only a small fraction of incident pumping light is absorbed in the sample. A much greater amount of energy is diffusely reflected (scattered) off the sample. Thus, the incident pumping energy is utilized very inefficiently. A narrow channel formed in a powder works as a cavity (first approximation to a black body) helping one to reabsorb pumping photons otherwise reflected by the scattering medium. This increases the pumping efficiency and reduces the threshold of stimulated emission.

2. In a medium with relatively strong absorption (such as $Nd_{0.5}La_{0.5}Al_3(BO_3)_4$ powder), the major fraction of incident pumping energy is absorbed in the sample.

TABLE 9.1. Reflection of 532 nm Light off Titanium-Doped and Neodymium-Doped Powders.[a]

Material	Relative reflection
$Nd_{0.5}La_{0.5}Al_3(BO_3)_4$ powder	0.52
Ti-sapphire powder (0.2% of Ti)	0.86
Ti-sapphire powder (0.1% of Ti)	0.88
Al_2O_3 powder	1.0

[a]Reflection is normalized to that off Al_2O_3 powder.
Source: Ref. [6].

The formation of a channel in such a medium practically does not increase the amount of utilized pumping energy, which is already high. On the other hand, a needlelike spatial distribution of the absorbed pumping and the gain is far from optimum (in terms of maximizing the residence time of emission photons in a pumped volume) and determines the high threshold of stimulated emission [6]. [Following this logic, one infers that in Ti-sapphire powder a positive effect of the channel formation (better utilization of the pumping energy) overcomes the negative effect caused by the needle shape of the pumped volume.]

To justify the heuristic model above, the measurements of reflection of Ti-doped and Nd-doped powders at $\lambda = 532$ nm were carried out using the technique described in Section 2.9 [6]. Following the classification of Section 2.9, all powders used in this particular experiment were "medium-dense," filled into cuvettes, and shaken. Because the powder samples were optically thick, the transmission was negligibly small, and all pumping light, which was not reflected, was absorbed in the powder.

As follows from Table 9.1, which summarizes the results of the reflection measurements, there is a large difference between absorption in neodymium-doped and titanium-doped powders. Thus, $Nd_{0.5}La_{0.5}Al_3(BO_3)_4$ powder absorbs nearly half of the incident pumping energy, whereas the absorption in Ti-sapphire powders is as low as 12 or 14%. The reflection off the samples, in which channels were created, was difficult to measure with high accuracy; however, it was evaluated to be smaller than in the samples without channels. These results support the model outlined above [6].

9.2.3 Studies of Light Amplification in Ti-Sapphire Powders

Amplification of backscattered and transmitted light in optically pumped Ti-sapphire powder has been studied in [7–9]. In Reference [8], several Ti-sapphire samples with titanium concentration equal to 0.15 wt.% and transport mean pulse ranging between 10 and 40 μm have been prepared and investigated.

The samples were pumped with 14 ns pulses of Nd:YAG laser focused into a 5 mm spot [8]. The maximum pumping energy was equal to 200 mJ. A Monte

Carlo simulation of light diffusion in Ti(0.15 wt.%):Al_2O_3 powder has predicted the pumping efficiency (absorption efficiency) to be equal to 7.7% [8]. This value is not very far from 12 and 14% experimentally measured in Ti-sapphire powders in Ref. [6]; see Table 9.1.

The pumped spot was probed with low-energy light pulses ($E_{\text{pulse}} = 40\,\mu\text{J}$, $t_{\text{pulse}} = 14\,\text{ns}$) at the wavelength close to the maximum of the gain spectrum. The transmission and the backscattering amplification coefficients were measured by comparing the intensities of, respectively, the transmitted and the backscattering probe lights when the pumping was on and off. The maximum amplification of the transmitted light was equal to 1.42 and that of the backscattered light was equal to 2.55 [8]. The optical gain in excited Ti-sapphire powders caused a significant narrowing of the coherent backscattering cones [7,9]. No lasing effect in Ti-sapphire powders has been reported in [7–9].

In a similar experiment with ruby powder (Cr = 2.1 wt.%), the maximum amplification in transmission was equal to 1.04 [8]. The strong difference between the magnitudes of the effect in ruby and Ti-sapphire is probably due to the fact that the ruby laser operates according to a three-level scheme and the Ti-sapphire laser operates according to a four-level scheme.

9.3 Color Center Powder Laser

The relatively low emission cross section of neodymium-doped and other rare-earth-doped laser crystals and glasses ($\leq 10^{18}\,\text{cm}^2$) determines a relatively high threshold of random lasers based on these materials, which may limit their applications. Color centers (CC) have one of the highest emission cross sections in dielectric solid-state laser materials [10]. Spectroscopic properties of CC:LiF powders, different from those of bulk crystals, as well as efficient stimulated emission of the CC:LiF random laser [11] are discussed in this section.

9.3.1 Experimental Samples and Setup

Experimentally, two crystals of LiF with CCs have been studied in Reference [11]. The crystals were grown by the Kyropolus method in platinum crucibles from nominally pure materials. They were subjected to γ-irradiation with a dose of 1.5×10^8 Rad (Crystal #1) and 1×10^7 Rad (Crystal #2) at a temperature of 293°K. Crystal #1 had high concentration of F_2 CCs characterized by the maximum absorption coefficient of $k_{\text{abs}}^{\max} \approx 200\,\text{cm}^{-1}$; the color of the material was dark red in the bulk form. Crystal #2 was yellow in the bulk form and had relatively low concentration of F_2 CCs ($k_{\text{abs}}^{\max} \approx 25\,\text{cm}^{-1}$). The powder samples were produced by grinding single crystals with a mortar and pestle. The powder of Crystal #1 was yellowish-tan and the powder of Crystal #2 was light yellow. Most

of the experimental results reported in this section were obtained using Crystal #1. Hereafter, by LiF sample we mean Crystal #1 unless otherwise stated. In the experiment, the samples were excited at $\lambda = 532$ nm with Q-switched laser pulses ($t_{\text{pulse}} \approx 15$ ns, 10 Hz repetition rate) or trains of 100 ps pulses ($\approx$12.8 ns between pulses). The emission spectra and emission kinetics were studied at different pumping densities. A Si diode, McPherson 0.3 m monochromator, and a boxcar integrator were used for the spectra acquisition, and a monochromator and a Hamamatsu Streak Camera C4334 were used for the kinetics recording. The transmission spectra of the samples were studied with a UV-VIS Varian spectrophotometer.

9.3.2 Experimental Results

9.3.2.1 Color Centers in Bulk LiF Crystal

The absorption spectrum of a 1.25 cm thick bulk crystal of LiF is shown in Figure 9.3a. According to [10], the strongest absorption band with the maximum at $\approx$445 nm belongs to F_2 CCs; the peak centered at $\approx$380 nm belongs to F_3 CCs; a shoulder at $\approx$550 nm represents N CCs; a weak band at $\approx$800 nm belongs to F_3^- CCs; and an increasing absorbance beyond 900 nm represents the absorption band of F_2^- CCs centered at $\approx$960 nm.

The emission spectra of bulk samples recorded at weak excitation (Figure 9.4, trace 1) correspond to F_2 CCs [10]. At the excitation of bulk samples with a train of weak 100 ps pulses, the emission decay at 673 nm was found to be single-exponential, with the effective lifetime equal to $\approx$16.4 ns in Sample #2 and 15.3 ns in Sample #1 (Figure 9.5, trace #1). These experimental lifetimes are in reasonably good agreement with the 18.3 ± 1.7 ns lifetime reported in [12]. Slight shortening of the emission decay time in the sample with higher CCs concentration (#1) may imply energy migration over F_2 CCs to some quenching centers.

It is known that at strong optical pumping, two-step photoionization converts F_2 CCs into F_2^+ CCs [10,13]. At room temperature, the absorption band of F_2^+ CCs in LiF is centered at 645 nm and has a width equal to $\Delta\nu = 3500\,\text{cm}^{-1}$; this absorption hinders laser emission of F_2 CCs. The maximum of a wide ($\Delta\nu = 2300\,\text{cm}^{-1}$) F_2^+ emission band is at 910 nm [14]. The decay time of F_2^+ luminescence at 77 K is 29 ns [15]. However, the luminescence quantum yield (η) decreases with the increase of the temperature from $\eta = 0.52$ at $T = 90°\text{K}$ to $\eta = 0.15$ at $T = 300°\text{K}$ [16]. F_2^+ CCs in bulk LiF crystal are thermally unstable; at room temperature their effective degradation time is equal to several hours [10].

The emission spectrum of a strongly pumped (at $50\,\text{mJ/cm}^2$) bulk crystal is shown in Figure 9.4 (trace 2). The infrared luminescence band in the spectrum corresponds to F_2^+ CCs. This band is photoinduced, because it is not present at weak excitation of the sample (compare with trace 1). Trace 3 of Figure 9.4 shows the infrared peak alone, calculated as the difference between normalized to unity traces 2 and 1.

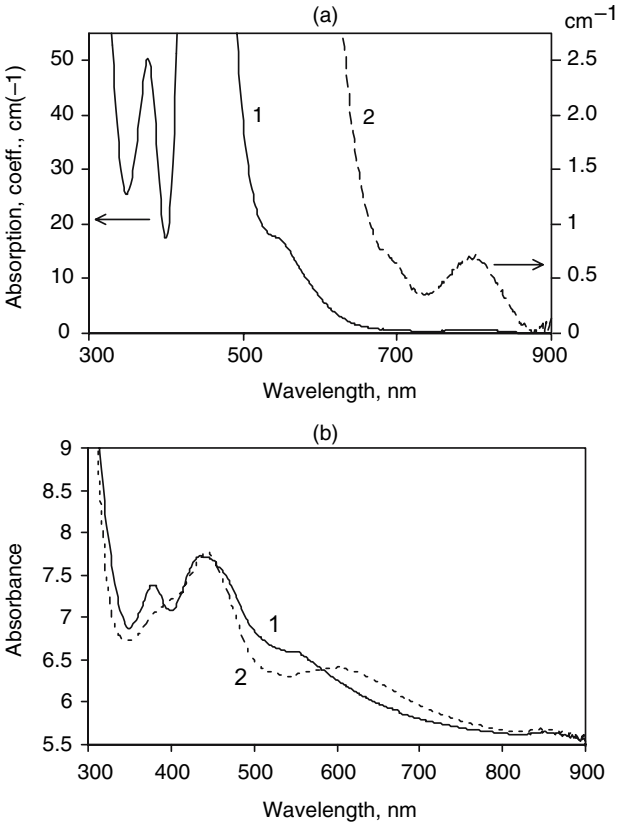

FIGURE 9.3. Absorption spectrum of LiF with color centers (sample #1): (a) bulk sample, $l = 1.25$ mm, trace 1: full spectrum (left scale), trace 2: zoomed infrared bands (right scale); (b) powder samples, trace 1: not exposed, trace 2: preliminary exposed with intense 532 nm laser light. Powder was pressed between two glass slices; the average thickness of the powder layer was equal to 100–200 μm; the thickness of the sample was nonuniform. (*Source*: Ref. [11].)

9.3.2.2 Color Centers in Pulverized Not Strongly Exposed Samples

The absorption spectra of powder samples were taken with the powder compressed between two glass slides. To reduce, to some extent, the effect of scattering, the samples were put very close to the detector port of the spectrophotometer. The thickness of the powder samples was equal to 100 to 200 mm; the uniformity and thickness of the powder layer was difficult to monitor or control. A powder pressed between two glass slides looked porous and had large nonuniformity of the effective thickness. One can argue that in a strongly absorbing sample with strong nonuniformity of the thickness, the ratio of the measured absorption intensity in strong and weak lines is much smaller than the similar ratio in a uniform sample. Although the absorption spectra obtained this way cannot be used for

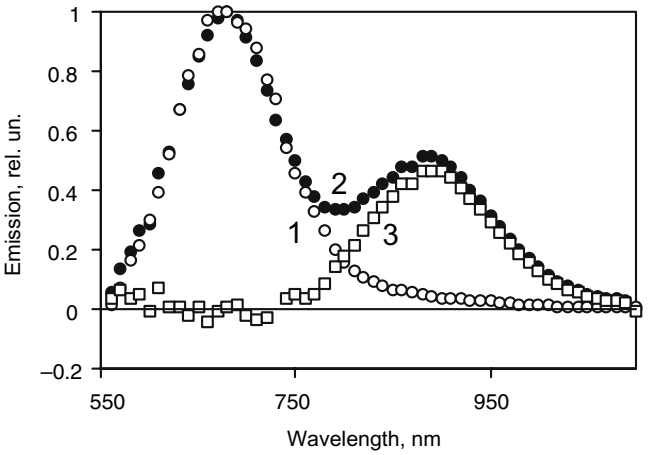

FIGURE 9.4. Emission spectrum of the bulk LiF sample (#1); excitation: 532 nm, Q-switched pulses. Trace 1 (open circles): weak pumping ($<0.1\,\mathrm{mJ/cm^2}$); trace 2 (closed circles): strong pumping ($50\,\mathrm{mJ/cm^2}$); trace 3 (open squares): infrared emission peak alone, calculated as the difference between the normalized to unity traces 2 and 1. (*Source*: Ref. [11].)

precise quantitative analysis, they show the existence and positions of different absorption bands.

The absorption spectrum of an unexposed LiF powder sample is shown in Figure 9.3b, trace 1. The main qualitative differences between the absorption

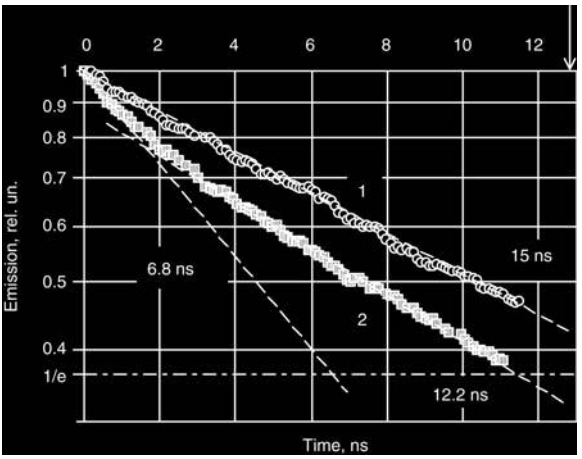

FIGURE 9.5. Kinetics of F_2 luminescence registered at $\lambda = 673$ nm at weak excitation of the samples with a train of 100 ps, 532 nm pulses. The distance between pulses is equal to 12.8 ns. Trace 1 (open circles): bulk material; trace 2 (shaded squares): powder sample. An arrow indicates the position of the next pumping pulse. (*Source*: Ref. [11].)

spectrum of the bulk sample (Figure 9.3a) and that of the powder sample (Figure 9.3b, trace 1) are: (a) the presence in the spectrum of powder of a wide, not well-structured band at ≈600–800 nm and (b) the absence of powder in the spectrum of the band centered at ≈800 nm (F_3^- CCs).

The emission spectrum of a very weakly pumped (0.12 mJ/cm^2) powder sample is shown in Figure 9.6, trace 1. This spectrum consists of two bands. One of them, red, is similar to the emission spectrum of F_2 CCs in the bulk sample (Figure 9.4, trace 1). The second, infrared, band has a maximum at ≈850 nm and is shifted to shorter wavelengths relative to the F_2^+ emission peak in the bulk sample (compare traces 1 and 4 in Figure 9.7). The shape of the emission spectrum of the powder remains unchanged at twice stronger, but still very weak (0.24 mJ/cm^2), excitation. This suggests that CCs responsible for the infrared emission are not photoinduced but created during pulverization of the material. By comparing two powder samples prepared from the same crystal (#1), it was found that the 840 nm infrared peak was stronger in the powder with smaller particles.

The decay kinetics recorded at 673 nm under weak excitation of a fresh (not strongly exposed by 532 nm light) powder sample with a train of weak 100 ps, 532 nm pulses is shown in Figure 9.5, trace 2. This kinetics is shorter than that in bulk material: the initial luminescence decay time is equal to 6.8 ns, and the further decay is characterized by the time-constant equal to 12.2 ns. (Note that because the effective luminescence decay time is comparable to the distance between excitation pulses, the shape of nonexponential kinetics excited with a train of pulses is different from that excited by a single pulse.) The difference between the luminescence decay kinetics (at $\lambda = 673$ nm) in bulk and pulverized samples can be explained by a combination of the following reasons: (a) enhanced energy transfer

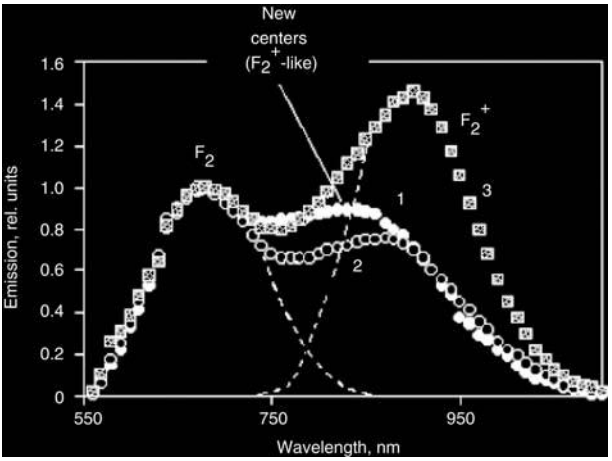

FIGURE 9.6. Emission spectra of the CC:LiF powder sample. Excitation: 532 nm, Q-switched pulses; trace 1 (closed circles): 0.12 mJ/cm^2, trace 2 (open circles): 3.7 mJ/cm^2, trace 3 (shaded squares): 11 mJ/cm^2. (*Source*: Ref. [11].)

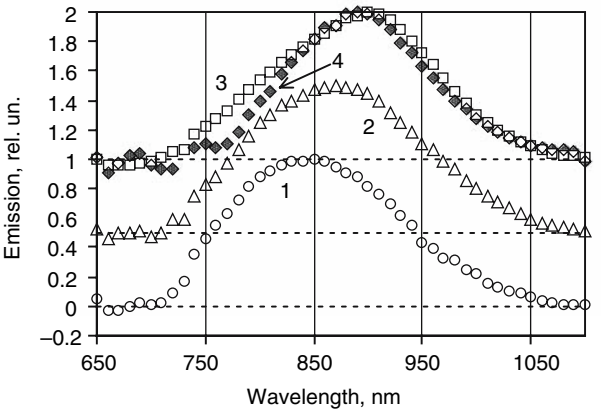

FIGURE 9.7. Infrared emission band, calculated as the difference between the normalized to unity (at 680 nm) experimentally recorded spectrum and extracted emission spectrum of F_2 CCs in the unexposed bulk material (trace 1 in Figure 9.4). Excitation: 532 nm, Q-switched pulses; trace 1 (open circles): powder sample, 0.12 mJ/cm^2; trace 2 (open triangles): powder sample, 3.7 mJ/cm^2; trace 3 (open squares): powder sample, 11 mJ/cm^2; trace 4 (shaded diamonds): bulk crystal, 50 mJ/cm^2. For a more convenient presentation, the zero level of trace 2 is set to be equal to 0.5 and the zero level of traces 3 and 4 is set to be equal to 1. (*Source*: Ref. [11].)

from F_2 CCs to some quenching centers in powder, (b) the presence in the powder of some other CCs, the lifetimes of which are shorter than the lifetime of F_2 CCs, and (c) enhancement of the emission cross section of F_2 CCs in pulverized material.

The luminescence kinetics recorded at $\lambda = 850$ nm at the 100 ps excitation is shown in Figure 9.8, trace 1. This kinetics has a fast component, with the decay time equal to $\approx$2.2 ns, and a long component, with the decay time equal to 14 ± 1.5 ns. The presence of two different components in the kinetics suggests (a) the existence of two different centers emitting at 850 nm or (b) luminescence quenching due to radiationless energy transfer. In any case, the presence of a fast component in the kinetics indicates that emitting centers absorb optical pumping directly. In fact, centers excited via F_2 CCs cannot have the decay time shorter than 12 ns.

The most probable scenario explaining the nature of mechanically produced (by grinding) CCs is as follows. During the grinding process a substantial number of dislocations are created in the material. Generally speaking, those dislocations are traps for electrons. Due to a large affinity to electrons typical of dislocations, an electron belonging to F_2 CC can be attracted and trapped by the dislocation, producing a dislocation-perturbed F_2^{+*} CC. A similar effect was observed in [17], where a γ-irradiated LiF crystal under plastic deformation changed the color from yellow to green due to the reduction of the 450 nm absorption band (F_2 CCs) and creation of the 645 nm absorption band (F_2^{+*} CCs).

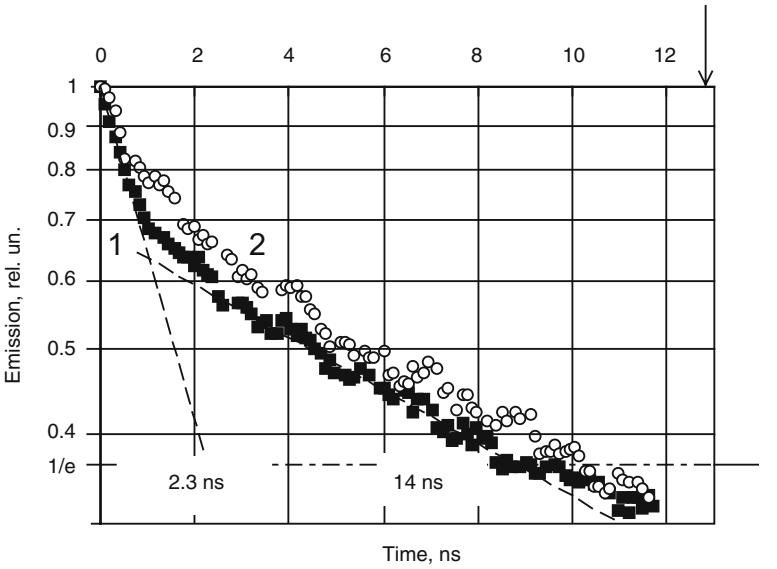

FIGURE 9.8. Trace 1: luminescence kinetics recorded at $\lambda = 850$ nm in fresh (not preliminary exposed) powder. Trace 2: luminescence kinetics recorded at $\lambda = 900$ nm in preliminary strongly exposed, greenish powder. Kinetics taken at weak excitation of the sample with a train of 100 ps, 532 nm pulses. Arrow indicates position of the next pumping pulse. (*Source*: Ref. [11].)

The presence of F_2^+-like CCs in the pulverized material (F_2^{+*}) can explain the presence of a wide absorption band (at 600–800 nm) in the spectrum of powder. Apparently, the perturbation of F_2^+ color centers by dislocations causes the shift of the luminescence band maximum from 900 to 850 nm. The observed 850 nm luminescence decay is also not inconsistent with that expected for F_2^+-like CCs (because the 29 ns decay time at 77 K and the threefold reduction of luminescence quantum yield as the temperature changed from 90 to 300 K were reported in the literature [16]).

The same dislocations can attract and trap electrons from F_3^- CCs, converting them into F_3 CCs. This is the most probable reason why the 800 nm absorption band (F_3^- CCs) is not seen in the spectrum of the powder.

9.3.2.3 Color Centers in Pulverized Samples Exposed by Intense 532 nm Radiation

At stronger excitation of the powder sample (≥ 3.7 mJ/cm^2), the infrared emission peak is slightly shifted to the longer wavelengths and its intensity is reduced relative to the intensity of the red emission peak (Figure 9.6, trace 2 and Figure 9.7, trace 2). At further increase of the pumping density (11 mJ/cm^2), the relative intensity of the infrared peak is significantly increased and its maximum is shifted further to the longer wavelengths (Figure 9.6, trace 3 and Figure 9.7, trace 3). In this

new position, the infrared emission peak of the powder almost resembles that of F_2^+ CCs in a bulk LiF sample. The transformation of the emission spectra above suggests that strong 532 nm excitation reduces the concentration of dislocation-perturbed F_2^{+*} CCs and increases the concentration of color centers emitting at 900 nm (regular F_2^+ CCs).

Note that the emission spectra of the powder did not change immediately after the pumping energy was increased. It took some time—minutes to tens of minutes—for the spectra to transform under exposure. (Simultaneously, the color of the powder changed from yellowish-tan to greenish.) After the change in the material was produced, the emission spectrum (and the color of the sample) did not return back to the original state instantaneously when the pumping density was reduced. At room temperature the produced changes remained in the crystal for a long time, days to weeks. This situation is different from that in bulk LiF, where the room-temperature degradation time of F_2^+ CCs is equal to several hours. Another difference between the bulk and the pulverized LiF samples is that in the powder the pumping energy density required for the $F_2 \rightarrow F_2^+$ conversion is five to ten times lower than that in the bulk material (Figures 9.4 and 9.6).

The absorption spectrum of the powder sample exposed to intense 532 nm radiation is shown in Figure 9.3, trace 2. (The thickness of the exposed sample was close but not equal to the thickness of the unexposed sample, trace 1.) The major differences between the absorption spectra of exposed and unexposed samples are (a) the presence in the spectrum of exposed powder of the pronounced peak centered at ≈650 nm (F_2^+ CCs) and (b) strong reduction in the spectrum of exposed sample of the 380 nm band (F_3 CCs) and the 550 nm band (N CCs).

The luminescence kinetics (recorded at 900 nm, F_2^+ CCs) of strongly exposed greenish powder sample excited with the train of 100 ps, 532 nm pulses is shown in Figure 9.8, trace 2. This kinetics is close but not identical to that at 850 nm (F_2^{+*} CCs), Figure 9.8, trace 1. The initial decay of the 900 nm kinetics is not as fast as that of the 850 nm kinetics and has slightly smaller modulation depth (smaller number of centers decay with short lifetime). The time constant of the slow stage of the 900 nm kinetics (which can be assigned to F_2^+ CCs) within the experimental accuracy matches that of the 850 nm kinetics, 14.0 ± 1.5 ns. The short component in F_2^+ CCs luminescence was not discussed in the literature before. The possible reasons for the two components in 900 nm kinetics are (a) the luminescence quenching and (b) the presence of more than one center emitting at 900 nm. Again, the existence of the short component in the 900 nm kinetics implies direct optical excitation (at least partial) of emitting centers. F_2^+ CCs can be excited by 532 nm light at the short-wavelength wing of their absorption band.

At high pumping density the two-step ionization of F_2 CCs occurs according to the known scheme [10,15] $F_2 + 2h\nu_{0.53} \rightarrow F_2^* + h\nu_{0.53} \rightarrow F_2^+ + e$ (here $h\nu_{0.53}$ is the energy of the pumping photon and F_2^* is the excited F_2 CC). Following the scenario outlined above, one assumes that the photoinduced centers are mostly the F_2 CCs, which have no close dislocations (because F_2 CCs, which have close dislocations, are already converted into dislocation-perturbed F_2^{+*} CCs). Some

electrons released in the process of photoionization of F_2 CCs can be captured by F_2^{+*} CCs. As a result, a part of F_2^{+*} CCs will convert into F_2 CCs (generally, also perturbed by dislocations). Thus, strong exposure of powder with 532 nm light increases the concentration of F_2^+ CCs (900 nm) and decreases the concentration of F_2^{+*} CCs; see Figure 9.6. In principle, the same scenario accounting for dislocation traps in pulverized material can explain the reduction of the effective threshold for the $F_2 \rightarrow F_2^+$ conversion. However, an enhancement of the stability of photoinduced F_2^+ CCs in powders was not completely understood [11].

There is another possible scenario, according to which dislocation traps are ionized by 532 nm light. One can assume that ionized traps do not attract F_2^{+*} CCs any more, and F_2^{+*} CCs can migrate away from dislocations, converting into regular F_2^+ CCs and then, after association with F CCs, converting into F_3^+ CCs ($F_2^+ + F \rightarrow F_3^+$). (The migration of F_2^+ CCs in LiF was discussed in [14].) This scenario can also explain the reduction in F_2^{+*} concentration under exposure of the powder sample with 532 nm radiation.

Under photoexcitation, F_3 CCs (380 nm absorption) and N CCs (550 nm absorption) convert into F_3^+ CCs. The maximum of F_3^+ CCs absorption is at $\approx$460 nm. This band cannot be seen under a strong absorption band of F_2 CCs.

9.3.3 Stimulated Emission in CC:LiF Powder

At strong pumping with Q-switched, 532 nm pulses, the stimulated emission without cavity was observed in CC:LiF powder [11]. Figure 9.9 shows the evolution of emission spectra in the powder sample made of Crystal #1 when the pumping intensity was changed from low to high. After the pumping energy exceeded some critical value, the 900 nm infrared emission band (F_2^+ CCs) shifted to longer wavelengths and narrowed. The change of the spectral position of the emission line stopped when the peak centered at $\approx$936 nm. The further increase of the pumping energy caused a reduction of the linewidth and an increase of the peak emission intensity. A similar spectral behavior is typical of LiF laser operation with F_2^+ CCs in the regular laser cavity [10]. At the pumping density equal to 50 mJ/cm^2 the emission spectrum consisted of a single line with full width at the half height (FWHH) equal to 25 nm (Figure 9.9b).

In CC:LiF powder, the wavelength of stimulated emission was longer than the wavelength of the maximum of spontaneous emission below the threshold. This shift can be explained by a partial overlap of the F_2^+ emission band and the absorption bands of F_2^+ and other CCs. F_2^- CCs, which have a maximum of absorption at 960 nm [10], potentially present a serious problem for the 936 nm stimulated emission. Apparently, excitation of F_2^- CCs via $F_2 \rightarrow F_2^+ \rightarrow F_2^-$ radiation energy transfer followed by photoionization of excited F_2^- centers with the laser light (converting F_2^- CCs into F_2 CCs) strongly bleaches the F_2^- absorption band and makes the laser emission possible.

Figure 9.10 shows the kinetics of stimulated emission in the powder of LiF with color centers close to the threshold (Figure 9.10a) and far above the threshold (Figure 9.10b). As one can see from this figure, when the pumping energy

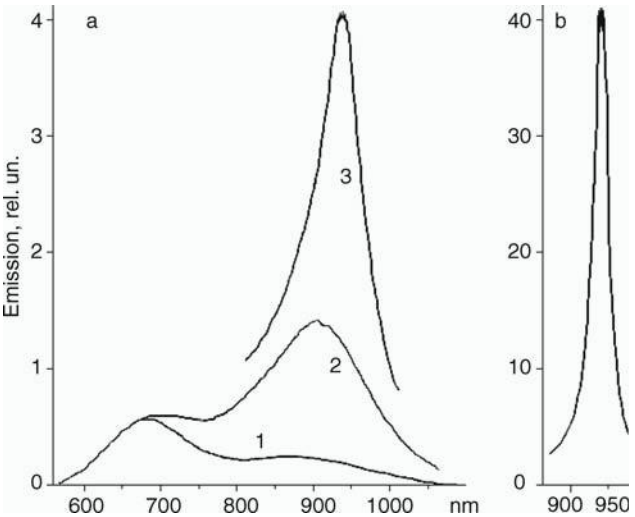

FIGURE 9.9. Evolution of the emission spectra and the stimulated emission in CC:LiF powder. Pumping: Q-switched pulses at 532 nm; (a1): 4.4 mJ/cm^2; (a2): 11 mJ/cm^2; (a3): 23 mJ/cm^2; (b): 50 mJ/cm^2. (*Source*: Ref. [11].)

reaches the threshold, a large number of randomly positioned, overlapped stimulated emission pulses appear in the kinetics at $\lambda = 930$ to 936 nm. As pumping energy increases, the intensity of short emission pulses increases, as well as the number of pulses per unit time. Above a certain pumping energy, the pulses become unresolved and their envelope closely resembles the pumping pulse. This behavior is rather different from that of pulverized Nd doped materials (Figure 2.4).

Trace 2 in Figure 9.10b represents the luminescence kinetics in a preliminary exposed powder sample recorded at 900 nm under weak excitation with a train of 100 ps, 532 nm pulses. According to Figure 9.10b, the duration of individual stimulated emission spikes within the envelope is much shorter than the spontaneous emission decay time and the decay time of luminescence is not longer than the width of the stimulated emission envelope, which resembles the pumping pulse. The latter suggests that the quantum yield of stimulated emission in the CC:LiF random laser is not smaller than that of spontaneous emission.

A typical input–output curve experimentally recorded in a CC:LiF random laser at 936 nm is shown in Figure 9.11. As follows from this figure, the threshold in the LiF powder is not very sharp and the difference between the slopes before and after the threshold is not very large. This type of input–output curve is strongly different from that in neodymium random lasers (Section 2.2), where the emission intensity below the threshold is negligibly small. According to Section 4.3, smooth thresholds are predicted in cw random lasers. Because in the CC:LiF random laser

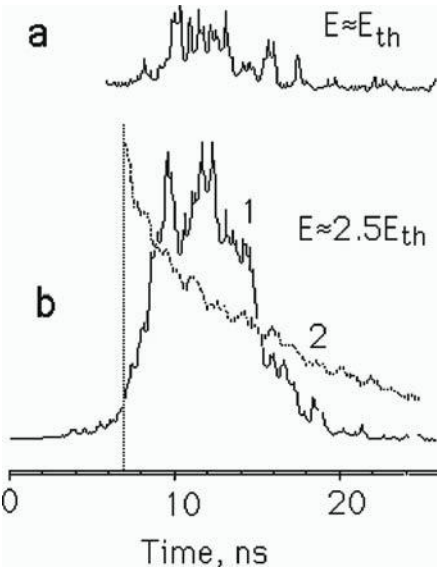

FIGURE 9.10. (a) stimulated emission pulse in LiF powder close to the threshold ($E_{\text{pump}} \approx E_{th}$), excitation: Q-switched, 532 nm pulse, registration: 930–936 nm; (b) trace 1: stimulated emission pulse at 936 nm in the same powder sample at $E_{\text{pump}} \approx 2.5E_{th}$; trace 2 (dotted line): luminescence kinetics recorded in the same sample at 900 nm, at excitation with a train of 100 ps, 532 nm pulses. (*Source*: Ref. [11].)

the duration of the pumping pulse is comparable to the spontaneous emission lifetime, its regime of operation is close to cw. The threshold pumping density in the CC:LiF random laser, $\approx$25 mJ/cm^2, is smaller than in neodymium random lasers (Chapter 2) and larger than in semiconductor (Chapter 7) or polymer (Chapter 8) random lasers.

9.4 Mid-Infrared Eye-Safe Random Lasers Based on Cr^{2+}:ZnS and Cr^{2+}:ZnSe

In the mid'90s there appeared a new class of laser materials, emitting transition metal-doped zinc chalcogenides [18] in the mid-infrared. These materials are characterized by a relatively low saturation intensity resulting in an intrinsically low lasing threshold as well as by some other attractive spectroscopic features. It is therefore not a surprise that they have evolved in the past few years to the active media of broadly tunable (over 1100 nm around 2.5 μm), highly efficient, and high-power continuous-wave, Q-switched, and mode-locked lasers [19].

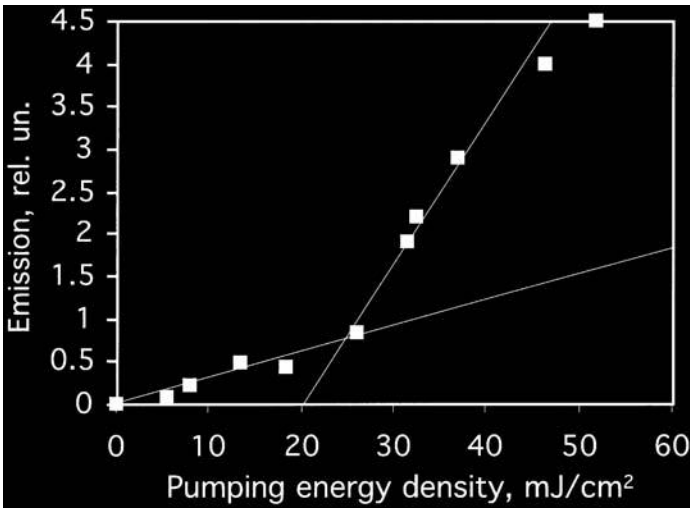

FIGURE 9.11. Input–output curve of stimulated emission in CC:LiF powder sample measured at 936 nm. Pumping: Q-switched pulses at 532 nm. (*Source*: Ref. [11].)

Random lasers based on the two most successful members of the Cr^{2+}-doped II–VI compounds, Cr^{2+}:ZnSe [18] and Cr^{2+}:ZnS [20], have been reported in [21,22]. Experimentally several samples of Cr:ZnSe and Cr:ZnS powders made by mechanically grinding the single crystals with the concentration of Cr^{2+} ions varying between 5×10^{18} cm^{-3} and 2×10^{19} cm^{-3} have been studied. The particle sizes in different samples ranged from submicron to tens of micrometers. Each powder sample was loaded into a cylindrical glass container, with inner diameter equal to 1 mm and outer diameter equal to 1.5 mm, and illuminated by 15 ns sub-mJ pulses of an optical parametric oscillator (OPO). The diameter of the pumped spot was varied between 0.7 mm and 1.1 mm. In the emission kinetics measurements, the samples were pumped near the absorption peak of Cr^{2+} at 1780 nm in the case of Cr:ZnSe powder and 1700 nm in the case of Cr:ZnS powder. In the spectral studies, the samples were pumped at 1594 nm and 1570 nm, respectively.

At the pumping energy fluence comparable to the absorption saturation fluence, ($J_{sat} \equiv h\nu_{pump}/\sigma_{abs}$) of bulk Cr:ZnSe and Cr:ZnS (i.e., between 0.3 and 0.5 J_{sat}), the dramatic shortening of the emission lifetime (Figure 9.12a), the thresholdlike input–output behavior of the emission intensity (Figure 9.12b), and the radical narrowing of the emission spectrum at gain peak (Figure 9.13) have been observed. The spectral linewidth of the main peak in Figure 9.13 was limited by the resolution of the apparatus. Note that the measurements presented in Figures 9.12 and 9.13 were done at different pumping wavelengths and different diameters of the pumped spot, which determined the difference in the threshold energies.

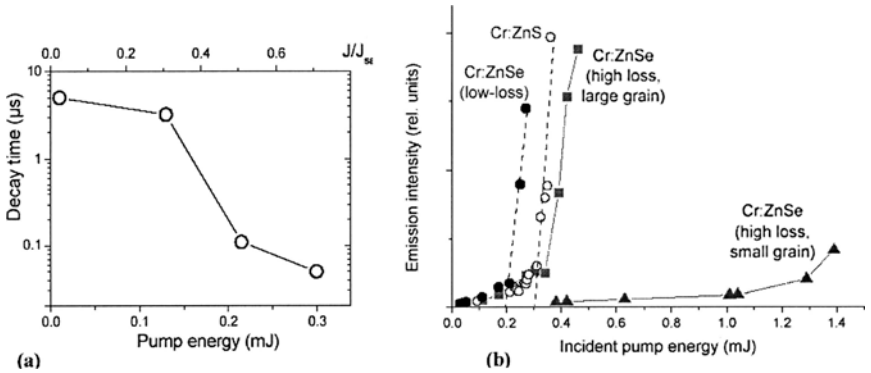

FIGURE 9.12. (a) Dependence of the Cr^{2+} emission decay time on the pumping energy in Cr^{2+}:ZnSe powder (excitation wavelength $\approx$ 1780 nm, pumped spot diameter $\approx$ 0.7 mm). A qualitatively similar dependence was observed in the Cr^{2+}:ZnS powder. (b) Emission intensity versus pumping energy for different samples (excitation wavelength 1780 nm, pumped spot diameter $\approx$ 1.1 mm). (*Source*: Ref. [22].)

The threshold pumping energy density as low as $\sim$20 mJ/cm^2 could be observed in Cr:ZnSe and a factor of 1.5 higher in Cr:ZnS. This difference corresponds to the higher threshold of Cr:ZnS in the bulk form [20]. The two powder samples, the input–output curves of which are shown in Figure 9.12b, were prepared from the same bulk crystal (with relatively high absorption loss). The mean particle size of one powder ("small grain") was smaller than half of the emission wavelengths and the mean particle size of the other powder ("large grain") was comparable to the wavelength. As follows from Figure 9.12b, the stimulated emission threshold in the coarse powder was much smaller than that in the fine (subwavelength-size) powder. This result is in line with the theoretical predictions made for random lasers with diffusion character of photon motion (Section 4.7) and the experimental observations done in neodymium random lasers [23,24]. Note that strongly irregular shapes of the powder particles excluded the possibility of stimulated emission supported by resonances in individual granules.

The threshold energy densities in Cr:ZnSe and Cr:ZnS powder (random) lasers were comparable to those in regular lasers based on single crystals of the same materials (e.g., in the case of Cr:ZnSe $\sim$20 mJ/cm^2 in powder versus 8 to 62 mJ/cm^2 in various regular lasers). This suggests that the efficiency of feedback in random lasers is comparable to that in regular lasers. (Note that the typical output coupling in Cr:ZnSe lasers is about 7.5% [18].)

It is important to note that the random lasers based on Cr^{2+}:ZnS and Cr^{2+}:ZnSe powders are eye-safe and eye-safe-pumped. This opens a broad range of applications of mid-infrared random lasers in search and rescue; identification, including identification of friend and foe (IFF); and so on.

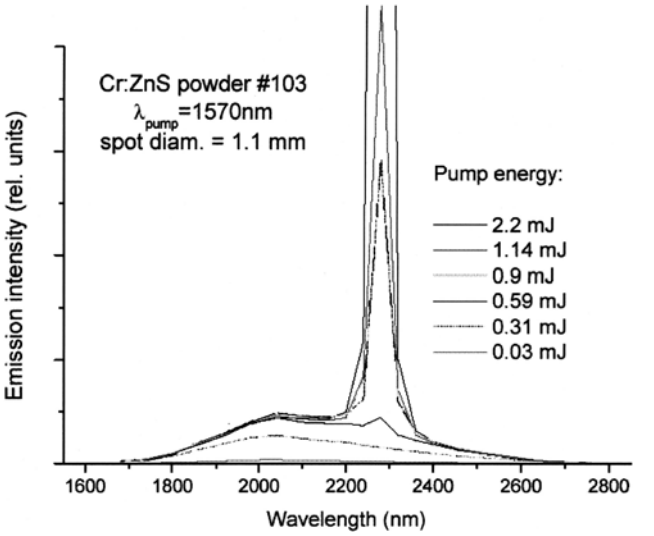

FIGURE 9.13. Emission spectra of Cr^{2+}:ZnS powder at various pumping pulse energies (1570 nm). A qualitatively similar evolution of spectra was observed in Cr^{2+}:ZnSe powder. (*Source*: Ref. [22].)

9.5 Superradiance and Superfluorescence in Random Laser Materials

9.5.1 Properties of Cooperative Emission

As outlined in References [25,26], three types of coherent emission effects taking their roots in spontaneous emission are superradiance (SR), superfluorescence (SF), and amplified spontaneous emission [27–30]. The criteria allowing one to distinguish among these three effects have been formulated in [26,29].

In the case of SR, the ensemble of coherently excited atoms in volume $<\lambda^3$ emits spontaneously as one collective dipole. The cooperative state of SR is organized through the interaction of atoms with the coherent pumping field. SF can occur in volumes $>\lambda^3$. The pumping in this case is incoherent, and organization of emitting atoms into a cooperative state comes through their coupling via the emitted field. The stimulated emission process (collective but not cooperative), which does not involve a formation of collective dipole, is referred to as ASE.

All three phenomena above are characterized by spectral line narrowing, shortening of emission pulses (or multiple-pulsed emission) [30–32], and some sort of threshold [25]. The quadratic dependence of the emission intensity on the population inversion density is the characteristic signature of the SR and SF effects. (The classification above did not take into account the existence of the cavity providing for feedback, which strongly changes the emission properties.)

Although the majority of laserlike effects commonly observed in random lasers can be described in a first approximation in terms of stimulated emission, SF and SR always persist as alternative explanations of the phenomenon. The volume of random lasers typically exceeds λ^3 and the pumping is not highly coherent, therefore SF is more probable than SR. According to [25,26], SF exists and predominates over ASE when $L_T \ll L \ll L_c$, and ASE predominates over SF at $L > L_c$. Here L is the size of the pumped medium, $L_T = L\tau_{SF}/T_2$ is the threshold length, $L_c = (\tau_{SF} Lc)^{1/2}$ is the Arecchi and Courtens [33] cooperative length, T_2 is the phase relaxation time, $\tau_{SF} = 8\pi\tau_0/(3\rho\lambda^2 L)$ is the SF decay time for inversion density ρ and radiative decay rate τ_0^{-1}, and c is the speed of light [25,26]. When $L \approx L_c$, an oscillatory behavior of emission is predicted [25].

The cooperative decay of incoherently pumped atoms (SF) in a disordered medium was studied theoretically in [34]. It has been shown that SF in a diffusive medium can be interpreted as an independent cooperative decay of many subsystems of atoms that are grouped along different diffusion trajectories. In the limit of large radiation decay time L^2/D (D is the diffusion coefficient), atoms exchange energy with the field many times. Thus, the stimulated emission becomes important, and the system exhibits oscillatory behavior, which is qualitatively similar to that observed in many experiments. A multipulse emission was predicted in superradiance of two-component media in [32].

The cooperative emission from an ensemble of incoherently pumped classical oscillators confined within a volume much smaller than the cubic wavelength, was studied in [35]. It has been shown that when the oscillator frequencies are randomly distributed around a central frequency ω_0 with some characteristic width Ω ($0 < \Omega \ll \omega_0$), the emission peak splits into a system of random narrow spectral peaks. In the presence of disorder, the emission spectrum of a large number of oscillators develops a fine structure, which, in the first approximation, resembles the spectra of coherent ZnO random lasers (Chapter 7) or polymer random lasers (Chapter 8).

9.5.2 Experimental Observations of Superradiance and Superfluorescence in Random Laser Materials

In [36], narrowing of the emission band and shortening of the emission pulses in strongly pumped DOO-PPV film, qualitatively similar to those discussed in Section 8.2, were explained in terms of SF. However, according to [37], the observation of waveguiding properties in similar polymer films proves that SF is not the sole mechanism responsible for the observed laserlike emission.[2]

In [38], the cone of laserlike emission (similar to the coherent backscattering cone, although at the wavelength of stimulated emission and without any probe light beam at the emission wavelength) was observed in liquid dye with scatterers. It

[2]The explanation in terms of SF was not used in the further publications of the authors of Ref. [36].

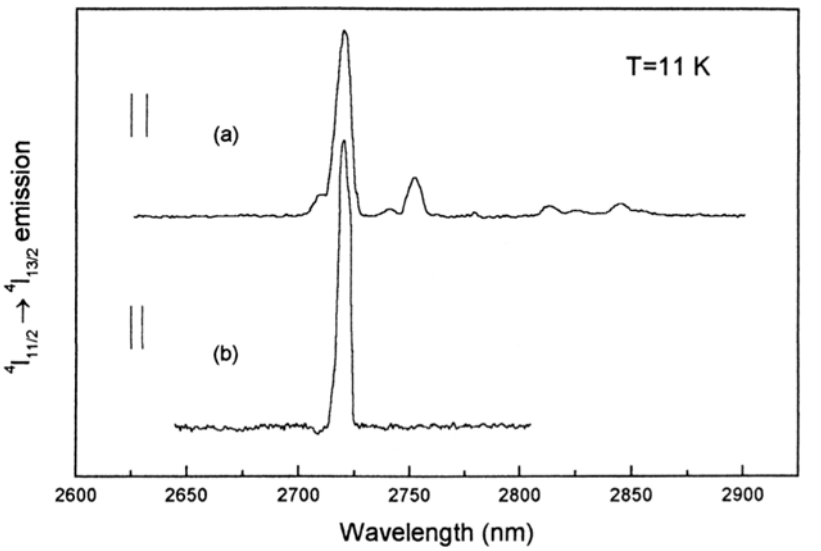

FIGURE 9.14. Emission spectra of a single layer of Er:$YLiF_4$ powder with particle size about 30 μm (a) below the threshold and (b) above the threshold. (*Source*: Ref. [39].)

has been argued [38] that this not completely understood phenomenon originates from SF, the possibility of which was predicted theoretically in random lasers in [34].

The effect of superfluorescence was observed in powders of Er(1%):$YLiF_4$ laser crystal in [25,39]. (Qualitatively similar effects were observed in bulk Er:$LiYF_4$ in Ref. [40].) In [25], large-grain powders of Er:$YLiF_4$ (with mean particle size larger than 100 μm) have been excited with a cw krypton laser at $\lambda = 6470$ Å. In [39], the particle size was reduced to 30 μm and the powder sample was excited with a cw Ti-sapphire laser at $\lambda = 9666$ Å. The emission at the transition $^4I_{11/2}$–$^4I_{13/2}$ was studied in the spectral range 2650 to 2900 nm at cryogenic temperatures (<60 K in Ref. [25] and 11 K in Ref. [39]).

Above a certain power density threshold, 827 W/cm^2 in [39], the emission spectrum of Er:$YLiF_4$ powder changed dramatically; see Figure 9.14. Such transformation of the spectrum was qualitatively similar to that in neodymium random lasers (Figure 2.4). (However, as argued below, the nature of this narrowing is quite different.) Exciting the sample with long, 80 ms, rectangular laser pulses below the threshold, one could observe only regular spontaneous luminescence decay. At the same time, a much shorter emission spike was observed in the end of the pumping pulse above the threshold (Figure 9.15). The intensity of this spike quadratically depended on the pumping power (Figure 9.16). A qualitatively similar emission behavior was observed in [25] at the Krypton laser pumping.

The thresholds in Er^{3+}:$YLiF_4$ powders were remarkably low, $<10^3$ W/cm^2 [25,39]. Evaluating the spontaneous emission lifetime of $^4I_{11/2}$ Er^{3+} to be equal to ≈5 ms [39] and calculating the threshold energy according to Eq. (4.15), one can

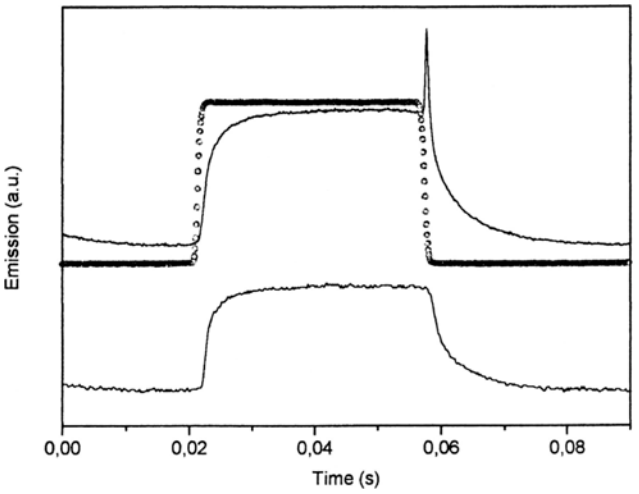

FIGURE 9.15. Kinetics of $^4I_{11/2}$ emission below the threshold (lower trace) and above the threshold (upper trace). The trace with open dots is the pumping intensity. (*Source*: Ref. [39].)

estimate the threshold energy density to be $<5\ \mathrm{mJ/cm^2}$. This value is much smaller than the threshold energy densities in neodymium random lasers, $\geq 100\ \mathrm{mJ/cm^2}$; see Table 1.1. The short-spike emission could be observed only at low Er concentrations and low temperature, $<10^{20}\ \mathrm{cm^{-3}}$ and <60 K, respectively [25,39]. These are the experimental conditions, which maximize the dephasing time T_2 in the medium.

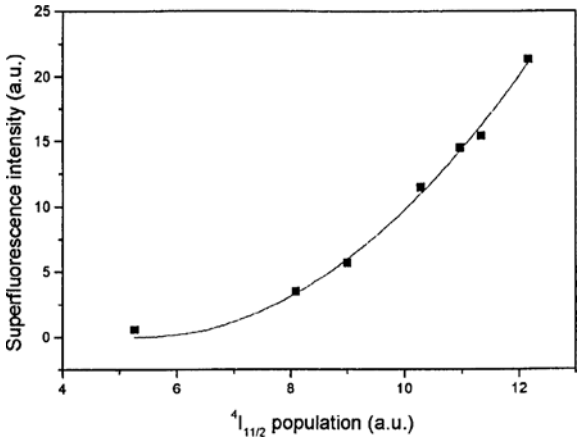

FIGURE 9.16. Integrated intensity of the short superfluorescence pulse of Figure 9.15 plotted against relative population density of emitting level $^4I_{11/2}$. The continuous line is a quadratic fit. (*Source*: Ref. [39].)

The experimental facts listed above point to superfluorescence or superradiance in the Dicke–Bonifacio sense [27,29], for which the principal condition is the existence of a long dephasing time T_2, longer than the characteristic times of SF or SR emission.

It has been concluded that SF takes place at the pumping of the upper state $^4F_{9/2}$ Er^{3+} with a Krypton laser [25,39]. In this case, excitation reaches the metastable state $^4I_{11/2}$ via a combination of incoherent relaxation processes and the phasing of the spontaneous emission becomes self-organized. In contrast, at the direct excitation of the state $^4I_{11/2}$ with a Ti-sapphire laser, the interaction of Er ions with coherent pumping light facilitates the phasing of emission from the lowest emitting Stark level (SR). This difference explains the higher efficiency of the Ti-sapphire laser excitation in comparison with the Krypton laser excitation [25,39].

Note that the neodymium random lasers discussed in Chapter 2 benefit from high Nd concentration and can be operated at room temperature. This suggests that the emission of neodymium random lasers is not owing to SF or SR, but rather due to a regular stimulated emission.

References

1. V.F. Zolin, A.A. Lichmanov, and N.P. Soshchin, *Abstracts of Reports to the First International Conference on Chemistry and Technology of Luminophores*, Institute of Luminophores: Stavropol (1988).
2. V.F. Zolin, The nature of plaser-powdered laser, *J. Alloys Compounds*, **300–301**: 214–217 (2000).
3. V.M. Markushev, V.F. Zolin, and Ch.M. Briskina, Luminescence and stimulated emission of neodymium in sodium lanthanum molybdate powders, *Sov. J. Quantum Electron.*, **16**: 281–283 (1986).
4. V.M. Markushev, N.È. Ter-Gabriélyan, Ch.M. Briskina, V.R. Belan, and V.F. Zolin, Stimulated emission kinetics of neodymium powder lasers, *Sov. J. Quantum Electron.*, **20**: 772–777 (1990).
5. G. Williams, B. Bayram, S.C. Rand, T. Hinklin, and R.M. Laine, Laser action in strongly scattering rare-earth-doped dielecric nanophosphors, *Phys. Rev. A*, **65**: 013807 (2001).
6. M.A. Noginov, N. Noginova, S.U. Egarievwe, H.J. Caulfield, C. Cochrane, J.C. Wang, M.R. Kokta, and J. Paitz, Study of the pumping regimes in Ti-sapphire and $Nd_{0.5}La_{0.5}Al_3(BO_3)_4$ powders, *Opt. Mater.*, **10**: 297–303 (1998).
7. D.S. Wiersma, M.P. van Albada, and A. Lagendijk, Coherent backscattering of light from amplifying random media, *Phys. Rev. Lett.*, **75**: 1739–1742 (1995).
8. D.S. Wiersma and A. Lagendijk, Light diffusion with gain and random lasers, *Phys. Rev. E*, **54**: 4256–4265 (1996).
9. D.S. Wiersma and A. Lagendijk, Interference effects in multiple light scattering with gain, *Physica A*, **241**: 82–88 (1997).
10. T.T. Basiev and S.B. Mirov, *Room Temperature Color Center Lasers*, Laser Science and Technology Book Series, An International Handbook, Vol. 16, Gordon and Breach Science/Harwood Academic (1995), pp. 1–160.

11. M.A. Noginov, N.E. Noginova, S.U. Egarievwe, H.J. Caulfield, P. Venkateswarlu, A. Williams, and S.B. Mirov, Color-center powder laser: The effect of pulverization on color-center characteristics, *J. Opt. Soc. Am. B*, **14**, 2153–2160 (1997).
12. T.T. Basiev, F.A. Vakhidov, Yu.K. Voron'ko, P.G. Zverev, V.A. Konyushkin, S.B. Mirov, Yu.B. Orlovsky, and V.V. Osiko, Optical and nonlinear characteristics of color centers in LiF crystals and their practical applications. In *Proceedings of IVth Conference on Tunable Lasers*, V.P. Chebotaev, ed., Novosibirsk, USSR, December (1983), pp. 77–82.
13. T.T. Basiev, S.B. Mirov, and V.B. Ter-Mikirtychev, Two-step photoionization and photophysics of color centers in LiF crystals, *SPIE Proceedings*, **1839**: 292 (1992).
14. J. Nahum, Optical properties and mechanism of formation of some F^- aggregate centers in LiF, *Phys. Rev.*, **158**: 814–825 (1967).
15. L. Bosi, C. Bussolati, and C.G. Spin, Life-time of the first excited state of the F_2^+ center in LiF, *Phys. Lett.*, **32A**: 159–160 (1970).
16. I.A. Parfianovich, V.M. Hulugurov, B.D. Lobanov, and N.T. Maximova, Luminescence and stimulated emission of color centers in LiF, *Bull. Acad. Sci. USSR, Phys. Ser.*, **43**: 20–27 (1979).
17. T.T. Basiev, S.B. Mirov, A.N. Stepanov, and A.M. Shirokov, N-absorption band increasing in γ-irradiated LiF crystals under plastic deformation and its polarization properties, *Zhurnal Prikladnoi Spectroscopii*, **45**: 505–509, Russian (1986).
18. L.D. DeLoach, R.H. Page, G.D. Wilke, S.A. Payne, and W.P. Krupke, Transition metal-doped zinc chalcogenides: Spectroscopy and laser demonstration of a new class of gain media, *IEEE J. Quantum Electron.*, **32**: 885–895 (1996).
19. I.T. Sorokina, Mid-infrared crystalline solid-state lasers. In *Solid-State Mid-IR Laser Sources*, Springer: Berlin (2003), pp. 255–348,
20. I.T. Sorokina, E. Sorokin, S. Mirov, V. Fedorov, V. Badikov, V. Panyutin, and K. Schaffers, Broadly tunable compact continuous-wave Cr^{2+}:ZnS laser, *Opt. Lett.*, **27**: 1040–1042 (2002).
21. I.T. Sorokina, E. Sorokin, V.G. Shcherbitsky, N.V. Kuleshov, G. Zhu, A. Frantz, and M.A. Noginov, Room-temperature lasing in nanocrystalline Cr^{2+}:ZnSe random laser. In *Technical Digest: Advanced Solid-State Photonics, Nineteenth Topical Meeting and Tabletop Exhibit* Paper # WB14, ISBN # 1-55752-764-4 (2004).
22. I.T. Sorokina, E. Sorokin, V. Shcherbitsky, N.V. Kuleshov, G. Zhu, A. Frantz, and M.A. Noginov, First mid-infrared eye-safe random lasers based on Cr^{2+}:ZnS and Cr^{2+}:ZnSe. In *International Quantum Electronics Conference, paper #IThG22, CD ROM 2004 CLEO/IQEC Technical Digest*, ISBN # 1-55752-770-9 (2004).
23. N.È. Ter-Gabriélyan, V.M. Markushev, V.R. Belan, Ch.M. Briskina, O.V. Dimitrova, V.F. Zolin, and A.V. Lavrov, Stimulated radiation emitted by lithium neodymium tertaphosphate $LiNd(PO_3)_4$ and neodymium pentaphosphate NdP_5O_{14} powders, *Sov. J. Quantum Electron*, **21**, 840–841 (1991).
24. M.A. Noginov, G. Zhu, A. Frantz, J. Novak, S. Williams, and I. Fowlkes, Dependence of the $NdSc_3(BO_3)_4$ random laser parameters on the particle size, *JOSA B*, **21**: 191–200 (2004).
25. F. Auzel, S. Hubert, and D. Meichenin, Very low threshold CW excitation of superfluorescence at 2.72 μm in Er^{3+}, *Europhys. Lett.*, **7**: 459–462 (1988).
26. F. Auzel, Properties of highly populated excited states in solids: Superfluorescence, hot luminescence, excited state absorption. In *Optical Properties of Excited States in Solids*, B. DiBartolo, ed., Plenum: New York (1992), pp. 305–347.
27. R.H. Dicke, Coherence in spontaneous radiation process, *Phys. Rev.*, **93**: 99–110 (1954).

28. T. Waite, Size-dependent spontaneous energy loss in lasers due to self-stimulated emission, *J. Appl. Phys.*, **35**: 1680–1682 (1964).
29. R. Bonifacio and L.A. Lugiato, Cooperative radiation processes in two-level systems: Superfluorescence, *Phys Rev. A*, **11**: 1507–1521 (1975).
30. H.M. Gibbs, Q.H.F. Vrehen, and H.M.J. Hikspoors, Single-pulse superfluorescence in cesium, *Phys. Rev. Lett.*, **39**: 547–550 (1977).
31. J.C. MacGillivray, and M.S. Feld, Limits of superradiance as a process of achieving short pulses of high energy, *Phys. Rev. A*, **23**: 1334–1349 (1981).
32. A.V. Andreev and P.V. Polevoy, Superradiance of two-component media, *Quantum Opt.*, **6**: 57–72 (1994).
33. F.T. Arecchi and E. Courtens, Cooperative phenomena in resonant electromagnetic propagation, *Phys. Rev. A*, **2**: 1730–1737 (1970).
34. A. Yu. Zyuzin, Superfluorescence of photonic paint, *J. Exper. Theor. Phys.*, **86**: 445–449 (1998).
35. T.V. Shahbazyan, M.E. Raikh, and Z.V. Vardeny, Mesoscopic cooperative emission from a disordered system, *Phys. Rev. B*, **61**: 13266–13276 (2000).
36. S.V. Frolov, W. Gellermann, M. Ozaki, K. Yoshino, and Z.V. Vardeny, Cooperative emission in π-conjugated polymer thin films, *Phys. Rev. Lett.*, **78**: 729–732 (1997).
37. F. Hide, B.J. Schwartz, M.A. Días-García, and A.J. Heeger, Conjugated polymers as solid-state laser materials, *Synth. Metals*, **91**: 35–40 (1997).
38. M. Shukri and R.L. Armstrong, Coherent, directional, laserlike emission from random gain media, *Appl. Opt.*, **39**: 4300–4305 (2000).
39. F. Auzel and P. Goldner, Coherent light sources with powder: Stimulated amplification versus super-radiance, *J Alloys Compounds*, **300–301**: 11–17 (2000).
40. S. Hubert, D. Meichenin, and F. Auzel, Thermal behaviour of low temperature coherent emission in $LiYF_4:Er^{3+}$, *J. Lumin*, **45**: 434–436 (1990).

10
Applications of Random Lasers

The proposed potential applications of random lasers are, as a rule, based on their properties (described below), which are different from the properties of regular lasers. All applications will benefit from low cost of random laser materials and robustness of operation.

The feedback in random lasers is not supported by conventional resonators. Correspondingly, the emission wavelength (in random lasers with incoherent feedback) is determined by the gain spectrum and should not be sensitive to vibrations of absent mirrors. Therefore, it was proposed in Reference [1] to use random lasers with incoherent feedback as highly stable optical frequency standards. The same idea was later discussed in [2,3].

Low coherence of random lasers with incoherent feedback and low contrast of a speckle pattern is attractive in applications requiring high uniformity of the field distribution. As proposed in [4,3], low coherent random laser sources can be advantageous in holography, laser inertial confinement fusion (driver sources for megajoule lasers), transport of energy in fibers for medical applications, and other applications, where the coherent properties of conventional lasers present a severe drawback by degrading the luminescence uniformity. In fact, the basic idea of beam-smoothing techniques used in laser fusion is the incoherent superposition of uncorrelated speckle patterns. Such superposition is naturally generated by random lasers with incoherent (nonresonant) feedback. According to References [5,6], the absence of speckle in random laser emission can facilitate large-area, submicron optical lithography. Other applications of speckleless radiation of random lasers include "low-noise" imaging, communication, displays, and new lighting systems [7].

Uniqueness of the stimulated emission wavelengths, which serve as fingerprints of particular random laser materials, in combination with remote alignment-free pumping and low cost allow one to use random lasers for identification, marking, and machine vision.

Narrow-linewidth emission signatures of random lasers make them ideal for producing wavelength-domain photonic codes [2]. If N slightly different random laser materials with overlapped absorption bands and spectrally resolvable stimulated emission lines are available, they can be used to construct 2^N identification

markers with unique spectral characteristics (at $N = 10$, $2^N \approx 1000$, at $N = 20$, $2^N \approx 1{,}000{,}000$, etc.). The information encoded in such markers can be read with a single nanosecond laser pulse from a short or long distance.

Short-range applications include encoding of documents and credit cards [2,8], photonic barcodes, machine vision [9], sorting parts on conveyer belts [9], and so on. The combination of wavelength signatures with geometrical pattern signatures can strongly increase the number of encrypted codes [2].

Long-range applications include search and rescue and military identification of friend and foe (IFF) [2,9]. Random laser markers can enable search craft to identify downed vehicles and survivors by a unique wavelength-coded return signal emanating from painted fuselages, hulls, tarps, sails, life jackets, and marker plaques attached to various objects [9]. A similar concept can be used in IFF.

The successful field-testing of the proposed long-range systems has been demonstrated when the distance between the interrogation platform (containing laser and detector [10]) and the target was equal to 1000 ft [2] and 1 km [10]. In [10], random laser material in a target plaque was placed in a focal plane of a lens, which (a) focused pumping and (b) formed 1 mrad beam of random laser emission propagating in the direction of the interrogation platform. All long-range identification applications require eye-safe-pumped and eye-safe-emitting random laser materials, similar to those recently demonstrated in [11,12].

Embedding of random laser materials (dye and scatterers) into textile fibers was proposed in [13]. Textiles and papers marked with lasing fibers can be used for soldier-level IFF, search and rescue, anticounterfeiting, and so on [13]. A commercial product containing random laser textile fibers was presented at the CLEAN-99 exhibition (Orlando, FL) [14]. It was demonstrated that laser paint thread can be used to track garments and linens in commercial and institutional laundries. Costing from U.S. \$0.60 to \$0.80, fiber markers can be inserted into textiles and garments. The information encoded in fibers is easily retrievable, even when the garment is out of sight or distorted by twisting. The system has been tested after 100 washes, and has shown no degradation. Laundry management can track and recall individual items from a conveyor system, or even in a bundle.

On a different note, random microlasers [15,16] can be used to monitor the flow of liquids by adding a small amount of ZnO clusters to the liquid and detecting the laser emission over large flow distances [8]. Alternatively, microscopic random lasers may be used as optical tags in biological and medical studies.

The typically high slope efficiency of dye random lasers ($\approx$50%) in combination with high-energy density of emission and relatively narrow linewidth ($\approx$4 nm) make them ideal for photodynamic therapy, dermatology, and medical imaging (tumor detection) [2,9,17,18]. In the former, drugs that selectively bind to rapidly dividing cancer cells, such as photofrin and benzophoryn derivatives, are activated by laser light to destroy these target cells by free radical processes [2]. In dermatology, specific wavelengths are used to treat port wine stains and remove unwanted tattoos [2]. Because this application is a contact process, the absence of a collimated laser beam is not a drawback. Alternatively, high-brightness stimulated emission obtained in the tissue volume [17] can increase the contrast of medical

imaging. According to Reference [18], healthy and malignant human colon tissues infiltrated with dye have significantly different spectra of random laser emission. This may lead to application of random lasers in cancer diagnostics.

Because of omnidirectional output, high spectral brightness, fast response, higher quantum yield of stimulated emission in comparison with spontaneous emission, and possibility of electron beam pumping, numerous applications for laser phosphors can be imagined in displays and lighting [5–7,9,19–21].

Although the brightness of existing phosphors in televisions, fluorescent lights, plasma, and field emission displays is strictly limited by the spontaneous emission rate, this limitation can be overcome with stimulated emission [6]. As predicted in Reference [7], electron-pumped random laser emission can be obtained not only by using traditional bulky electron-accelerating tubes, but also much more compact field-emission cathodes. Multicolor displays can potentially be made by combining random laser materials emitting in blue, green, and red.

Some applications require emitting displays with unique advanced characteristics. For example, for the development of optical correlators for pattern recognition, one should have displays with single-frequency emission (linewidth $\approx$0.1 to 0.2 nm) and pulse duration of one nanosecond [21]. Powder lasers can be a promising solution for this application. According to [22], where the temperature control of random laser emission has been demonstrated, random lasers may find applications in active temperature-sensitive displays and screens.

Sensitivity of random laser emission to temperature or other environmental factors would allow the use of random lasers as sensors. As proposed in [22], because the threshold of certain tunable random lasers can be set to specific temperatures, random lasers may find application in remote temperature sensing, for example, in investigations of biological processes.

Random lasers can also potentially be used as biochemical sensors. In principle, chemical or biological agents can change the refractive index or introduce absorption loss in the vicinity of the stimulated emission line and thus shift frequency of a random laser. Many random lasers have very narrow spectral peaks, so small frequency shifts can be easily detected, providing for a high sensitivity. The application of random lasers as sensors for atmospheric pollutants and toxic gases has been discussed in [5,19]. Note that the sensing application (based on the change of the laser frequency) and the frequency standard application (discussed in the beginning of this chapter) exclude each other, the former requiring high sensitivity and the latter requiring high stability of the laser wavelength.

Another group of proposed applications of random lasers is aimed to complement conventional laser technology. Thus, it was proposed in [1,23] to use random lasers for the study of laser action in substances, which could not be produced in the form of homogeneous large crystals. According to [24], the measurement (under standard conditions) of the random laser threshold in pulverized or highly scattering samples can be put in the basis of an express-testing of potential solid-state laser materials, which require significant time and effort to be grown in the form of high-quality laser crystals. In addition, in frequency ranges where high-reflectivity

mirrors are not available (e.g., gamma-rays, x-rays), scattering can be used as an alternative way of providing feedback for lasers.

Another group of applications of random lasers is determined by their miniature sizes. As early as 1971, it was proposed that miniature light sources, powder lasers, could find applications in integrated circuit networks [25]. (Note that stimulated emission in Reference [25] occurred in individual powder granules.) As single random lasers can be made as tiny as a grain of tens of micrometers in diameter (or even much smaller, comparable to a wavelength), they can find application in nanophotonics devices [16,22]. Thus, there is a growing effort to develop photonic crystals, which can guide and switch lightwaves in the way that electronic devices control electric currents. As proposed in Reference [8], random microlasers can play the important role of the active elements or miniature light sources in such crystals.

In [21], the principle of operation of a proposed memory cell was based on the following properties of random lasers: (a) random lasers have two distinct states, luminescence and stimulated emission; (b) the transition from one state to another has a sharp threshold; and (c) the threshold depends on the coupling between particles. It was proposed to control intergranule coupling and, correspondingly, the state of the random laser by using photosensitive powders, the index of refraction of which depends on photoexcitation [21].

In [26,27], strong (Anderson) localization of light in highly scattering random laser materials was discussed as an underlying mechanism of optical energy storage elements or "optical batteries." According to [6], confinement of light within subwavelength regions may mediate new or enhanced nonlinear phenomena associated with ultraslow light, recurrent scattering, and surface resonances.

Superradiance and superfluorescence have been reported in laser powders in Reference [3]. Because sources of cooperative emission are based on synchronization of spontaneous emission, which constitutes the basic noise limitation in optical amplifiers, noise-suppressed amplifiers (similar to those discussed in Ref. [28]) can potentially be realized in laser powders.

References

1. V.S. Letokhov, Stimulated emission of an ensemble of scattering particles with negative absorption [*Pis'ma Zh. Eksp. i Teor. Fiz.*, **5**: 262–265 (1967) Russian], *JETP Lett.*, **5**: 212–215 (1967).
2. R.M. Balachandran, D.P. Pacheco, and N.M. Lawandy, Laser action in polymeric gain media containing scattering particles, *Appl. Opt.*, **35**: 640–643 (1996).
3. F. Auzel and P. Goldner, Coherent light sources with powder: Stimulated amplification versus super-radiance, *J. Alloys Compounds*, **300–301**: 11–17 (2000).
4. C. Gouedard, D. Husson, C. Sauteret, F. Auzel, and A. Migus, Generation of spatially incoherent short pulses in laser-pumped neodymium stoichiometic crystals and powders, *J. Opt. Soc. Am. B*, **10**: 2358–2363 (1993).

5. G. Williams, S.C. Rand, T. Hinklin, and R.M. Laine, Blue and infrared laser action in strongly scattering Nd:alumina nanopowders. In *Conference on Lasers and Electro-Optics*, OSA Technical Digest, Optical Society of America: Washington, DC (1999), p. 483.
6. G. Williams, B. Bayram, S.C. Rand, T. Hinklin, and R.M. Laine, Laser action in strongly scattering rare-earth-doped dielecric nanophosphors, *Phys. Rev. A.*, **65**: 013807 (2001).
7. V.S. Letokhov and S.K. Sekatskii, Cavityless powder lasers pumped by field-emission cathodes as a new class of monochromatic spatially incoherent radiation sources, *Quantum Electron.*, **32**(11): 1007–1008 (2002).
8. D.S. Wiersma, The smallest random laser, *Nature*, **406**: 132–133 (2000).
9. N.M. Lawandy, 'Paint-on lasers' light the way for new technologies, *Photon. Spectra*, 119–127 (July 1994).
10. S. Larochelle, P. Mathieu, V. Larochelle, and J. Dubois, Long range interrogation of laser paints for identification applications. In *Conference on Lasers and Electro-Optics*, Vol. 11, 1997 OSA Technical Digest Series, Optical Society of America: Washington, DC (1997), p. 143.
11. I.T. Sorokina, E. Sorokin, V.G. Shcherbitsky, N.V. Kuleshov, G. Zhu, A. Frantz, and M.A. Noginov, Room-temperature lasing in nanocrystalline Cr^{2+}:ZnSe random laser. In *Technical Digest: Advanced Solid-State Photonics, Nineteenth Topical Meeting and Tabletop Exhibit.* Paper # WB14, ISBN # 1-55752-764-4 (2004).
12. I.T. Sorokina, E. Sorokin, V. Shcherbitsky, N.V. Kuleshov, G. Zhu, A. Frantz, and M.A. Noginov, Fiber-coupled random laser. In *International Quantum Electronics Conference, paper #IThG22, CD ROM 2004 CLEO/IQEC Technical Digest*. ISBN # 1-55752-770-9 (2004).
13. R.M. Balachandran, A. Pacheco, and N.M. Lawandy, Photonic textile fibers. In *Conference on Lasers and Electro-Optics*, Vol. 15, 1995 OSA Technical Digest Series, Optical Society of America: Washington, DC (1995), pp. 114–115.
14. N. Schiff, Chemistry at CLEAN'99" http://search.netscape.com/ns/boomframe.jsp?query=%22Laser+paint%22&page=3&offset=0 &result_url=redir%3Fsrc%3Dwebsearch%26requestId%3Dbfca7b7a65ff95a%26clickedItemRank%3D21%26userQuery%3D%2522Laser%2Bpaint%2522%26clickedItemURN%3Dhttp%253A%252F%252Fwww.schiff-consulting.com%252FCHEMISTRYATCLEAN%252799.HTM%-26invocationType%3Dnext%26fromPage%3DNSCPNextPrev%26amp%3BampTest-%3D1&remove_url=http%3A%2F%2F www.schiff-consulting.com%2FCHEMISTRYATCLEAN%252799.HTM.
15. H. Cao, J.Y. Xu, D.Z. Zhang, S.-H. Chan, S.T. Ho, E.W. Seelig, X. Liu, and R.P.H. Chang, Spatial confinement of laser light in active random media, *Phys. Rev. Lett.*, **84**: 5584–5587 (2000).
16. H. Cao, J.Y. Xu, E.W. Seeling, and R.P. Chang, Microlaser made of disordered media, *Appl. Phys. Lett.*, **76**: 2997–2999 (2000).
17. M. Siddique, L. Yang, Q.Z. Wang, and R.R. Alfano, Mirrorless action from optically pumped dye-treated animal tissues, *Opt. Commun.*, **117**: 475–479 (1995).
18. R.C. Polson and Z.V. Vardeny, Random lasing in human tissues, *Applied Physics Letters*, **85**: 1289–1291 (2004).
19. G. Williams, S.C. Rand, T. Hinklin, and R.M. Laine, Ultraviolet laser action in strongly scattering Ce:alumina nanoparticles. In *Conference on Lasers and Electro-Optics*, OSA Technical Digest, Optical Society of America: Washington, DC (1999), p. 90.

20. V.F. Zolin, The nature of plaser-powdered laser, *J. Alloys Compounds*, **300–301**: 214–217 (2000).
21. A.A. Lichmanov, Ch.M. Briskina, N.P. Soshchin, and V.F. Zolin, Lasing in powders and its use for data processing, *Bulletin of the Russian Academy of Sciences. Physics* [*Izvestiya Rossiiskoi Akademii Nauk. Seriya Fizicheskaya*], **63**: 922–926 (1999).
22. D.S. Wiersma and S. Cavalierit, Light emission: A temperature-tunable random laser, *Nature*, **414**: 708–709, (2001).
23. V.S. Letokhov, Generation of light by a scattering medium with negative resonance absorption [*Zh. Eksp. i Teor. Fiz.*, **53**: 1442–14452 (1967) Russian], *Sov. Phys. JETP*, **26**: 835–840 (1968).
24. V.M. Markushev, V.F. Zolin, and Ch.M. Briskina, Luminescence and stimulated emission of neodymium in sodium lanthanum molybdate powders, *Sov. J. Quantum Electron.*, **16**: 281–283 (1986).
25. F. Varsanyi, Surface lasers, *Appl. Phys. Lett.*, **19**: 169–171 (1971).
26. S.C. Rand, Strong localization of light and photonic atoms, *Can. J. Phys.*, **78**: 625–637 (2000).
27. S.C. Rand, Bright storage of light, *Opt. Photon. News*, 32–37 (May 2004).
28. F. Auzel, Properties of highly populated excited states in solids: Superfluorescence, hot luminescence, excited state absorption. In *Optical Properties of Excited States in Solids*, B. DiBartolo, (ed.), C. Beckwith, (assist. ed.), Plenum: New York (published in cooperation with NATO Scientific Division) (1992), pp. 305–347.

Index

absorption length, 87, 158
amplified spontaneous emission (ASE), 12, 86, 178, 215, 216
amplifiers, noise-suppressed, 225
Anderson localization, 89, 123, 130, 141–142, 149, 156
angular distribution, of emission, 15–16, 137–139, 150
anti-Stokes solid-state laser, 159
ASE; *see* amplified spontaneous emission

backscattering coefficient, 4, 202
blue shift, 25, 149, 167, 168, 172, 173

cavity; *see* resonator
cavity mode; *see* resonator mode
cerium (Ce), trivalent, energy levels, 121
coherence
  degree of, 33, 34, 144, 150
  longitudinal, 30–33
  speckle pattern analysis, 33–35
  transversal, 35–39
coherent backscattering (CBS), 15, 39, 57–61
coherent regime of operation, 157
  transition from incoherent regime, 168–171
color center powder laser, 202–212
cooperative emission, 215–219
cooperative length, 216
cosmic laser effect, 11
coupled resonators, 198
  intraparticular, 35, 75, 95–97
coupling coefficient, 97
cw regime of operation (of random laser), 78–79

degree of coherence, 33, 34, 144, 150
dermatology, 223
diffusion, 59
diffusion approximation; *see* diffusion model
diffusion coefficient, 2, 87
diffusion model
  random laser
    application to stimulated emission in mixture of powders, 71–72
    calculation of random laser threshold in, 86–89
    comparison with experiment, 89–91
    spectrum narrowing, 70–71
    stimulated emission prediction, 69–70
displays, 224
distribution diagram
  angular, 15–16
  of particle sizes, 44

eigenmode, 104, 169
electron beam pumped random laser, 120–132
  Ce:δ-alumina random laser, 120–124
  Nd:δ-alumina random laser, 126–130
  Nd:YAG pumped with electron beam via scintillator, 131–132
  Pr:δ-alumina random laser, 125–126, 198
emission cross-section, 70, 72, 167
emission decay kinetics; *see* emission kinetics
emission energy density, 72, 73
emission kinetics, 12, 44, 73, 75, 148–149, 154, 181, 213

emission spectrum, 5
  Ce:δ-alumina cathodoluminescence, 123
  color center powder laser, 205, 206, 207, 211
  Cr^{2+}:ZnS, 215
  dependence on pumping current, 121–122, 125, 127, 129, 132
  Er:$YLiF_4$ powder, 217
  GaAs random laser, 159
  GaAsN random laser, 155, 156
  LiF crystal/powder samples, 203, 206, 208–209
  liquid dye random lasers, 165, 167, 169, 170
  narrowing of; *see* spectrum narrowing
  neodymium random lasers, 6, 14, 25, 26, 84, 102, 109, 127, 130
  polymer random lasers, 176, 179, 180, 183
  Pr:δ-alumina cathodoluminescence, 125
  ZnO random lasers, 136, 139, 142, 143, 144, 152
enhancement factor, 60–61
erbium random laser, 217–219
excitation spectrum, 30

Fabry–Perot resonator, 1, 182
feedback, 86
  coherent, 170
  external, 140
  intraparticle, 97
  nonresonant; *see* nonresonant feedback
fiber markers, 223
finite-difference time-domain (FDTD) method, 142, 148, 149, 188
Fourier transform, of laser emission spectra, 142, 182–184, 185, 186
fractal aggregate, of silver nanoparticles, 191
frequency-doubling materials, 108
Fresnel coefficients, 92, 93
Fresnel equations, 63, 64

GaAs random laser, 135, 155–159
  Anderson localization, 156
  input–output curve, 156–157
  slope efficiency, 158–159
  stimulated emission, 158
GaAsN random laser, 135, 154–155
  emission kinetics, 154
  relaxation oscillations, 154
  stimulated emission, 154–155
gadolinium oxisulfide, praseodymium-doped, 198
gain, 69–70
  threshold, 69, 94
galaxy laser (stellar laser), 4
galaxy maser, 4, 166

holography, 222

identification, 222–223
incoherent regime of operation; *see* nonresonant feedback
index of refraction; *see* refractive index
information processing, 132
input–output curve (input–output dependence)
  color center powder lasers, 211–212
  electron beam pumped random lasers, 122, 126, 127, 129
  GaAs random lasers, 156–157
  liquid dye random lasers, 164, 168
  mid-infrared eye-safe random lasers, 213
  neodymium random lasers, 5, 10, 14–15, 43, 46, 78–79
    with external mirror, 104
    with fiber-pumping, 106
  second-harmonic powder lasers, 108, 112
  ZnO random lasers, 137, 140, 152
intraparticle resonances, 27, 35, 75, 95–97
Ioffe-Regel criterion, 141–142, 149

Kubelka–Munk model, 52–54, 87

lanthanum oxisulfide, praseodymium-doped, 198
laser cavity/resonator; *see* resonator
laser emission spectra; *see* emission spectra
laser inertial confinement fusion, 222
laser with nonresonant feedback; *see* nonresonant feedback
laser threshold; *see* stimulated emission, threshold
lifetime of photon in cavity, 73
lighting, 224
linewidth, 32–33, 95, 152
Liouville equation, 96
liquid flow monitors, 223
localized mode, 85–86, 130–131, 142
luminescence (decay) kinetics, 44, 206–208, 209, 211

marking, random laser, 222
medical imaging, 223–224
memory cells, 225
2-methyl-4-nitroaniline; *see* MNA
microdisk resonator/cavity, 185, 186, 191
microring resonator/cavity, 182, 191
microsphere resonator/cavity, 191
mid-infrared eye-safe random laser, 212–215
Mie scattering, 65, 66, 97
MNA (2-methyl-4-nitroaniline), 107–108
  concentration optimization, 115–116
  refractive index, 111
mode attraction, 149
mode density, 146
mode saturation, 143, 148
mode spacing, 148, 182, 187
mode width; *see* linewidth
morphology-dependent resonances (MDR), 168
multimode laser, 1
multiple resonators, 137

near-field emission distribution, 141, 142
neodymium (Nd), trivalent, energy levels, 121
neodymium random lasers
  basic properties, 11–16
  coherence studies, 30–39
    interferometric measurements of longitudinal coherence, 30–33
    interferometric studies of transversal coherence, 35–39
    speckle pattern analysis, 33–35
  controlled by external seeding light, 101
  electron beam pumped, 126–130
  Nd:YAG pumped with electron beam via scintillator, 131–132
  propagation of pumping light, 52–57
  spectroscopic properties, 22
  stimulated emission
    dependence on powder particle size, 44–47
    dependence on powder volume density, 41–44
    dependence of threshold on diameter of pumped spot, 39–41, 91–95
    in different materials and types of samples, 16–23
    first observation in neodymium-doped powders, 10–11
    influence of channel formation, 200–201
    in mixtures of powders, 23–25, 71–72
    modeling of dynamics, 72–75
    prediction, 69–70
    quantum yield, 27–30
    supported by large regularly shaped particles, 25–27
  summary of properties of materials, 17–21
  theoretical modeling, 68–97
    see also coupled resonators; diffusion model; spectral dynamics; threshold pumping energy/energy density
  transport mean free path determination; *see* transport mean free path
nonresonant feedback (incoherent feedback), 1, 33, 164–168, 170, 172–178
  transition to coherent regime, 168–171

omnidirectional emission, 131
opal crystals, random laser emission in, 190
optical energy storage elements, 225
optical frequency standards, 222
optical imaging, 190
optical lithography, 222
optical modes, in arrays of dielectric particles, 228

particle size
  average, 58
  correlation with transport mean free path, 61–66
  dependence of stimulated emission on, 44–47
  distribution, 44
penetration depth
  of electron beam pumping, 120, 126
  of optical pumping, 4, 57, 87, 156
photodynamic therapy, 223
photoluminescence upconversion, 154
photon diffusion; *see* diffusion model
photon localization
  one-dimensional (1D), 149–151
  two-dimensional (2D), 85
  see also Anderson localization
photon mean free path; *see* transport mean free path
photon number probability distribution, 143, 228
  see also photon statistics

photon residence time, 87–88
effective, 73, 74
mean, 86
model and Monte Carlo simulation, 92–93
calculation results, 93–95
photon statistics
Bose–Einstein, 1, 143, 144, 181
Poisson, 1, 143, 144, 181
in polymer random laser, 180–181
in ZnO random laser, 143–145
photon walks, 92–93
one-dimensional (1D), 83–85
three-dimensional (3D), 92–93, 190
two-dimensional (2D), 85, 190
photonic crystals, 225
photonic fibers, 171
PMMA films, rhodamine-doped, 186–189
polymer films, 129, 155, 173–178
polymer random laser, 129, 150
with nonresonant feedback, 171–178
laserlike emission in conjugated polymers, 172–173
photonic fibers, 171
semiconducting polymers with TiO_2 nanoparticles, 171–172
time-resolved studies of stimulated emission in polymer film, 173–178
with resonant feedback, 178–189
based on PMMA films doped with rhodamine 640 dye and TiO_2 particles, 186–189
Fourier transform of emission spectra, 182–184, 185, 186
photon statistics, 180–181
transition from incoherent to coherent regime, 178–180
polymers
conjugated, 172–173
semiconducting, 171–172
population inversion, 3, 73, 74, 127, 156, 167, 177, 215
powder laser, 2, 4
see also random laser
praseodymium (Pr), trivalent, energy levels, 121
propagating mode, 130
pulsed regime of operation, 79–82
pumping light
propagation, 52–57
comparison of model predictions with experimental results, 55–57
Kubelka–Munk two-flux model, 52–54, 87
transmission and reflection measurements in powders, 54–55
pumping power density, 72

Q-factor (quality factor), 90–91, 95, 105
in electron beam pumped random laser, 126
of Fabry–Perot resonator, 182
in fiber-coupled random laser, 107
quantum efficiency, 27
quantum yield of emission, 27–30, 140
quantum yield of luminescence, 78
quasi-states, 147, 169–170, 171

random laser, 2
applications of, 124, 132, 190, 214, 222–225
based on dye-infiltrated biological tissues, 190–191
based on photonic crystals, 151
cerium (Ce), 120–124
coherent, 153
color center; *see* color center powder laser
controlled by external seeding light, 101
Cr^{2+}:ZnS and Cr^{2+}:ZnSe (eye-safe), 212–215
cw, 78–79
diffusion model; *see* diffusion model, random laser
early experiments, 4–7
electron beam pumped; *see* electron beam pumped random laser
erbium (Er), 217–219
with external mirror, 101–105, 140
fiber-coupled, 105–107
GaAs, 135, 155–159
GaAsN, 135, 154–155
GaN, 137
incoherent regime of operation, 157
transition to coherent regime, 168–171
liquid crystal, 190
liquid dye, 83, 102, 164–171
with nonresonant feedback, 164–168
transition from incoherent to coherent regime, 166–171
microlaser, 140–143, 191
neodymium (Nd); *see* neodymium random lasers
one-dimensional (1D), 83–85

random laser (*cont.*)
photon localization; *see* photon localization
polymer; *see* polymer random laser
praseodymium (Pr), 125–126, 198
pulsed, 79–82
ruby powder, 202
second-harmonic, 107–118
comparison of theory and experiment, 109–118
experimental results, 108–109
experimental samples, 107–108
semiconductor; *see* semiconductor random laser
thin-film, 91
Ti:Al_2O_3 (Ti-sapphire), 198–202
two-dimensional (2D), 146–147
ZnO; *see* ZnO random laser
random laser film; *see* polymer films; random laser, thin-film; semiconductor random laser
random photon walk, 83, 168
rate equations, 69, 70, 72, 83, 96, 111
Rayleigh scattering, 65
Rayleigh–Jeans formula, 3
red shift of emission, 26, 103, 149, 167
reflection coefficients, 53, 55, 63, 85, 95–96, 184
refractive index, 63, 64, 74, 88, 156
polymers, 173, 185
relaxation oscillations, 3, 70, 72, 75, 86
damped, 107
in GaAsN random laser, 154
in polymer random lasers, 177
in ZnO random lasers, 149
residence time of photon; *see* photon residence time
resonant (coherent) feedback, 1, 149, 153, 169, 170, 178–189
resonator mode, 27
ring resonator/cavity, 137, 153
ruby powder random laser, 202

scattering coefficient, 53, 55
scattering efficiency, 57
scattering mean free path, 61–63
search and rescue, 214, 223
second-harmonic generation, 107–118
comparison of theory and experiment, 109–118
conversion efficiency, 111, 112, 114–115
experimental results, 108–109
experimental samples, 107–108
optimization, 117–118
second-order correlation coefficient (G_2), 144
semiconductor random laser, 105
Cr^{2+}:ZnS and Cr^{2+}:ZnSe (eye-safe), 212–215
GaAs, 135, 155–159
GaAsN, 135, 154–155
GaN, 137
ZnO; *see* ZnO random laser
sensors, 224
slope efficiency (output efficiency), 28, 29, 47, 78
in fiber-coupled random laser, 105–106
in GaAs random laser, 158–159
Snell's law, 64
space maser; *see* galaxy maser
spatial coherence; *see* coherence
spatial field correlation function, 150, 188–189
speckle pattern, 1, 149, 188–189, 222
analysis, 33–35
spectral dynamics, of neodymium random lasers, 82–83
spectrum narrowing, 12–14, 70–71, 83, 121–123, 125–129, 135–137, 152, 154–159, 164–173, 178–180, 210–215, 216–219
spontaneous emission, 12–14, 79
see also amplified spontaneous emission
stellar laser; *see* galaxy laser
stimulated emission, 4
in color center powder lasers, 210–212
in cw regime, 79
in different materials and types of samples, 16–23
effect of external mirror on, 101–105, 140
with feedback, 164–165
in GaAs random lasers, 158
in GaAsN random lasers, 154–155
influence of channel formation, 200–201
in mixtures of powders, 23–25, 71–72
modeling of dynamics, 72–75
in one-dimensional array of coupled lasing volumes, 83–86
in polymer random lasers, 172, 186
time-resolved studies, 173–178
powder particle size dependence, 44–47
powder volume density dependence, 41–44
prediction, 69–70

in pulsed regime, 79–82
quantum yield, 27–30, 140
spectra; *see* emission spectra
supported by large regularly shaped particles, 25–27
threshold (laser threshold), 4
dependence on diameter of pumped spot, 39–41, 91–95, 147
in powders compared with single crystals, 22, 24
in Ti-sapphire random laser, 198–202
stochastic resonator, 3, 33
superfluorescence (SF), 132, 173, 215–219
experimental observations, 216–219
properties, 215–216
superradiance (SR), 215–216, 219
experimental observations, 219
properties, 215–216

third-order nonlinear optical effect, 149
Thouless number, 141
threshold pumping energy/energy density, 41, 47, 75
absorbed, 89, 90
color center powder laser, 212
Er:$YLiF_4$ random lasers, 217–218
fiber-coupled random laser, 105–106
GaAs random laser, 159
incident, 88–89
invariance in different pumping regimes, 75–82
liquid dye random laser, 166
mid-infrared eye-safe random laser, 214
polymer random laser, 187, 188
random laser in cw regime, 78–79
random laser in pulsed regime, 79–82
regular laser, 77
ZnO random laser, 137, 144, 146
threshold pumping power, 78
Ti-sapphire random laser
light amplification studies, 201–202
stimulated emission
experimental observation, 198–200
influence of channel formation, 200–201
transport mean free path, 87
correlation with (mean) particle size, 61–66
determination, 57–66
experimental results, 60–61
experimental samples, 58
experimental setup, 59–60
in electron beam pumped random laser, 121, 125, 129
in polymer random laser, 187, 188
in ZnO random laser, 65, 151
tumor treatment, 190

volume density of powder, 53, 91
dependence of stimulated emission on, 41–44

waveguide, 173, 176
waveguide mode(s), 185

yttrium oxisulfide, praseodymium-doped, 198

ZnO random laser, 135–153
emission dynamics, 148–149
external feedback effect, 140
with external reflector, 104
intuitive model, 137
microlaser, 140–143
new technological realizations, 153
phenomenological description, 135–137
photon statistics, 143–145
pumped area effect on operation, 145–148
relaxation oscillations, 149
spectrally resolved speckle studies, 149–151
stimulated emission, 97, 129, 186
angular distribution study, 137–139
from 3D photonic crystals of ZnO colloidal spheres, 151
quasi cw, in ZnO pellet, 151–153
strong spatial confinement of, 140–143
transport mean free path, 65, 151

Additional Notes and References

Different chapters of this book were finalized between January and June of 2004. Correspondingly, a number of relevant papers published in 2004 and 2005 were not referenced in the text submitted to the publisher. These references have been added to the book at proof. Many of them are incorporated into the corresponding chapters. Several theoretical works are briefly overviewed below.

The dependence of the size of the threshold gain volume and the threshold energy on the saturation absorption, dye concentration, transport mean free path, and spectroscopic parameters of the optical gain material have been studied in Reference [1] in a scattering random laser medium.

Resonant modes within (cylindrical) particles and ensembles of particles have been theoretically studied in Reference [2]. It has been demonstrated that (i) internal resonances of individual particles can strongly influence the emitted intensity and (ii) optimal tuning of the size and separation of the particles can enhance the quality factor by more than four orders of magnitude. The potential applications of this work include optimization of random lasers *via* appropriate engineered design.

In a relevant work [3], optical modes in finite partially ordered low-dimensional arrays of dielectric particles have been investigated in a coupled dipole approximation. High-quality modes have been predicted under the condition of small enough interparticle distances. The analytical and numerical studies have revealed the dependence of these modes on the system size, dimensionality, and the extent of disorder.

In References [4,5], the photon number probability distribution of light emitted from random scattering medium was derived using a generalized master equation that followed from a diffusion model with gain (originating from a more general coherence propagation theory for the electric field). It has been demonstrated that with stronger scattering, the pumping threshold for the transition from chaotic to isotropic coherent light emission decreases and the local second-order coherence, above the threshold, increases. In this approach, coherence properties of random lasers have been derived without direct use of wave equations, which are employed by many authors in modeling of random lasers with resonant feedback.

A quantum (photon) theory of random laser, which was consistent with a semiclassical theory, was developed in Reference [6] without use of the first-principle

approach. Scaled Fano factors have been calculated under the assumption of an open system model.

References

1. T. Ito and M. Tomita, Analysis of gain volume in random laser in a spherical multiple scattering medium, *Optical Review*, **11**: 7–11 (2004).
2. J. Ripoll, C.M. Soukoulis, and E.N. Economou, Optimal tuning of lasing modes through collective particle resonance, *J. Opt. Soc. Am.*, **21**: 141–149 (2004).
3. A.L. Burin, H. Cao, G.C. Schatz, and M.A. Ratner, High-quality optical modes in low-dimensional arrays of nanoparticles: application to random lasers, *J. Opt. Soc. Am. B*, **21**: 121–131 (2004).
4. L. Florescu and S. John, Photon statistics and coherence in light emission from a random laser, *Phys. Rev. Lett.*, **93**: 013602/1–4 (2004).
5. L. Florescu and S. John, Theory of photon statistics and optical coherence in a multiple-scattering random-laser medium, *Phys. Rev. E*, **69**: 46603/1–16 (2004).
6. V. Perinova, A. Luks, and J. Krepelka, Quantum and semiclassical models for a random laser, *Journal of Optics B*, **6**: S104–S110 (2004).